

## AN ABSTRACT OF THE THESIS OF

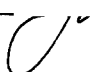
Thana Sornchamni for the degree of Doctor of Philosophy in Chemical Engineering, presented on March 18, 2004.

Title: Magnetically Assisted Liquid-Solid Fluidization in A Gradient Magnetic Field: Theory and Application.

Abstract approved:

Redacted for Privacy

---

 Goran M. Jovanovic

Development of efficient methods for the destruction of solid wastes and recovery of valuable resources is needed to support long-duration manned missions in space. In particular, these technologies are required for deployment in hypogravity and microgravity environments, such as at the lunar or Martian surfaces. Gradient Magnetically Assisted Fluidized Bed (G-MAFB) technology is under development in this study to serve as an operating platform for fluidized bed operations in the space environments. The G-MAFB technology has been specifically tailored for microgravity, hypogravity and variable gravity operating conditions. In addition, this study also focuses on the feasibility of the G-MAFB operation as a renewable filter used in the solid waste destruction process.

The fluid dynamic behavior of the G-MAFB in a non-uniform magnetic field is experimentally observed in this study. The magnetic field is designed to have a stronger field intensity at the bottom of the bed, and gradually decreases toward the top of the bed. The magnetic field gradient is kept constant throughout the

bed. This change in the magnetic field strength along the fluidization column varies the magnitude of the magnetic force,  $F_m$ , from the bottom to the top of the column. As a result, the particle holdup, or inversely the bed voidage, at any location varies along the column to reflect the equilibrium of all the forces involved (drag force, gravitational force, buoyancy force, and magnetic force).

These experimental investigations covering four different magnetic field gradients, ( $dH_z/dz = -14,663$  A/m/m,  $-18,289$  A/m/m,  $-20,543$  A/m/m and  $-33,798$  A/m/m) and three different fluid flow rates ( $U_0 = 0.0176$  m/s,  $0.0199$  m/s and  $0.0222$  m/s) have revealed that increases in magnetic field gradient and magnetic field intensity result in the decrease in height of the fluidized bed, and therefore, in the decrease of bed voidage. The experimentally observed dynamic pressure drop  $\Delta P_{f(d)}$  is measured, and then converted to the bed voidage. A Two-Continuum Phase (TCP) method mathematical model, based on the equations of motion and the equations of continuity for both liquid and solid phases, is developed with the help of Discrete Particle Method (DPM) algorithms to theoretically evaluate the voidage distribution in the G-MAFB. Experimentally obtained bed voidage data in both, laboratory experiments (1g) and on board of the NASA KC-135 aircraft (0g) indicate good agreement with the proposed model.

As part of an effort to apply the G-MAFB in the solid waste destruction process in a closed-loop life support system, a series of filtration experiments is conducted using the G-MAFB with a fixed magnetic field gradient of  $-38,817$  A/m/m and the flow velocities varying between  $0.0054$  and  $0.0134$  m/s. The biomass waste particles suspended in an aqueous stream are recirculated between

a holding tank and the G-MAFB, and the particulate concentration in the holding tank is monitored by changes in optical density of the suspension. A mathematical model describing the filtration of micron-sized solid waste particles from a liquid stream is developed. The experimental data are in good agreement with the model predictions.

© Copyright by Thana Sornchamni  
March 18, 2004  
All Rights Reserved



Magnetically Assisted Liquid-Solid Fluidization  
in A Gradient Magnetic Field: Theory and Application

by

Thana Sornchamni

A THESIS

Submitted to

Oregon State University

in partial fulfillment of  
the requirements for the  
degree of

Doctor of Philosophy

Presented March 18, 2004  
Commencement June 2004

Doctor of Philosophy thesis of Thana Sornchamni presented March 18, 2004

APPROVED:

Redacted for Privacy

---

Major Professor, representing Chemical Engineering

Redacted for Privacy

---

Head of the Department of Chemical Engineering

Redacted for Privacy

---

Dean of the Graduate School

I understand that my thesis will become part of the permanent collection of Oregon State University libraries. My signature below authorizes release of my thesis to any reader upon request.

Redacted for Privacy

---

Thana Sornchamni, Author

## ACKNOWLEDGEMENTS

This research could not have been completed without all the support of many people. I wish to express my sincere gratitude to the following people and organizations:

First of all, I am very grateful to my major advisor, Dr. Goran Jovanovic, for all his valuable advice, support and time he spent with me from the beginning to the completion of my thesis. His encouragement and guidance really helped me to overcome any difficulties I had during my stay at OSU. I also wish to thank the other members of my Graduate Committee: Dr. Shoichi Kimura, Dr. Adel Faridani, Dr. Todd Palmer, and Dr. Richard Vong. Their comments, suggestions and time are very much appreciated.

Special thanks to James Atwater, Dr. James Akse, and Richard Wheeler from Umpqua Research Company for their advice and support in doing this research. I would also like to thank Steven Adam from the Mechanical Engineering Department for training and helping me to construct the fluidized bed.

I also gratefully acknowledge the National Aeronautics and Space Administration (NASA) for their financial support, and the Reduced Gravity Student Flight Opportunities program for allowing us to perform our experiments in the zero-g environment.

Finally, I would like to thank my family in Thailand, Dr. Eric Henry, my fellow graduate students, and the professors in the Chemical Engineering Department for their encouragement and support.

## TABLE OF CONTENTS

	<u>Page</u>
Chapter 1    Introduction.....	1
1.1    Thesis overview .....	1
1.2    Goals and objectives.....	7
Chapter 2    Theoretical Background .....	10
2.1    Mass and momentum conservation equations.....	16
2.1.1    Mass conservation equation for liquid and solid phase .....	16
2.1.2    Momentum conservation equation for liquid and solid phase .....	16
2.2    Constitutive relationships .....	17
2.2.1    Interaction force between fluid and particles.....	17
2.2.2    Magnetic force on the ferromagnetic particle .....	19
2.2.3    Particle pressure, the particle stress tensor and elastic modulus in the G-MAFB.....	20
2.3    Magnetic filtration theory .....	26
2.3.1    Fundamental of filtration in the G-MAFB .....	27
2.3.2    Filtration mechanisms .....	32
Chapter 3    Experimental Apparatus and Materials.....	37
3.1    Fluidization column.....	37
3.1.1    Fluidization column for voidage distribution experiments...	38
3.1.2    Fluidization column for experiments on board NASA's KC-135 aircraft.....	41
3.1.3    Fluidization column for filtration experiments .....	44

## TABLE OF CONTENTS (Continued)

	<u>Page</u>
3.2 Magnetic field generator (Helmholtz ring).....	47
3.2.1 Magnetic field generator for voidage distribution experiments.....	47
3.2.2 Magnetic field generator for experiments on board NASA's KC-135 aircraft.....	48
3.2.3 Magnetic field generator for filtration experiments.....	48
3.3 Water supply system .....	49
3.3.1 Water supply system for voidage distribution experiments.....	49
3.3.2 Water supply system for experiments on board NASA's KC- 135 aircraft.....	50
3.3.3 Water supply system for filtration experiments.....	50
3.4 Instrumentation .....	51
3.4.1 Dynamic pressure measuring system.....	51
3.4.2 Gaussmeter .....	52
3.4.3 Particle concentration detector .....	53
3.4.4 Stirrer plate.....	57
3.5 Ferromagnetic particles.....	57
3.5.1 Ferromagnetic sodium alginate mixture suspension .....	59
3.5.2 Ferromagnetic particle generator .....	60
3.5.3 Calcium chloride cross-linking solution.....	60
3.6 Biomass waste particles .....	64
3.6.1 Intermediate size screen analysis.....	64
3.6.2 Centrifugal sedimentation particle size analysis .....	65
3.6.3 Optical microscope analysis .....	67
3.6.4 Summary of biomass particle diameter .....	69

## TABLE OF CONTENTS (Continued)

	<u>Page</u>
Chapter 4 Mathematical Modeling and Experimental Method .....	70
4.1 Voidage distribution model .....	70
4.2 Voidage distribution experimental method .....	78
4.3 Filtration model .....	82
4.4 Filtration experimental method .....	84
Chapter 5 Experimental Data and Results .....	85
5.1 Voidage distribution experimental data and results.....	85
5.1.1 Effect of magnetic force on the gradient-magnetically assisted fluidized bed.....	85
5.1.2 Voidage distribution experimental data from laboratory experiments .....	89
5.1.3 Voidage distribution experimental results from laboratory experiments .....	90
5.1.4 Experimental data on board NASA's KC-135 aircraft.....	99
5.1.5 Experimental results on board NASA's KC-135 aircraft.....	100
5.2 Filtration experimental data and results.....	108
5.2.1 Filtration experimental data .....	108
5.2.2 Filtration experimental results.....	110
Chapter 6 Discussion, Conclusions, and Recommendations .....	123
6.1 Discussion .....	123
6.1.1 Discussion of voidage distribution experiments.....	123
6.1.2 Discussion of filtration experiments .....	126

## TABLE OF CONTENTS (Continued)

	<u>Page</u>
6.2 Conclusions .....	133
6.3 Recommendations.....	138
Bibliography .....	140
Appendices .....	144



## LIST OF FIGURES

<u>Figure</u>	<u>Page</u>
2.1 Balance of forces acting on a fluidized particle in a conventional fluidized bed (liquid media-solid particles) .....	12
2.2 Balance of forces acting on a ferromagnetic fluidized particle in a gradient magnetically fluidized bed (liquid media-solid particles).....	13
2.3 Balance of forces acting on a fluidized particle containing ferromagnetic material in a) a fluidized bed in microgravity in the absence of a magnetic field, and b) a gradient magnetically assisted fluidized bed in microgravity .....	14
2.4 Magnetic interparticle forces: a) attractive force when two ferromagnetic particles approach along the dipole moment line, and b) repulsive force when two ferromagnetic particles approach perpendicular to the dipole moment line .....	23
2.5 Distance between two particles in adjacent layers.....	24
2.6 Elastic modulus of particle A in the G-MAFB, $dH_z/dz = -20,543 \text{ A/m/m}$ , $U_0 = 0.0222 \text{ m/s}$ , and $H_{bed} = 0.190 \text{ m}$ .....	26
2.7 Schematic representation of the pilot G-MAFB System.....	28
2.8 G-MAFB pilot system for filtration and destruction of solid waste.....	29
2.9 Schematic representation of the G-MAFB for filtration experiment .....	30
2.10 Schematic diagram of the G-MAFB filtration system .....	31
2.11 Streamlines and particle trajectories approaching filter element .....	34
3.1 Schematic representation of the experimental apparatus used in this study.....	38
3.2 Schematic diagram and photograph of the G-MAFB used in voidage distribution experiments.....	40

## LIST OF FIGURES (Continued)

<u>Figure</u>	<u>Page</u>
3.3 Schematic diagram and photograph of distributor plate used in voidage distribution experiments.....	41
3.4 Schematic diagram and photograph of G-MAFB used on board NASA's KC-135 aircraft .....	43
3.5 Schematic diagram and photograph of the G-MAFB used in filtration experiments .....	45
3.6 Schematic diagram and photograph of distributor plate used in filtration experiment .....	46
3.7 Schematic representation of the inclined manometer .....	52
3.8 Schematic diagram of laser-photodiode detector.....	55
3.9 Visual Designer system block diagram .....	56
3.10 Visual Designer <i>FlowGram</i> used in filtration experiments .....	57
3.11 Schematic diagram of the particle generator .....	58
3.12 Photo of the particle generator apparatus .....	59
3.13 Schematic model for gel formation in alginates.....	61
3.14 Schematic representation of magnetic susceptibility measurement .....	63
3.15 Modified TGA setup for the susceptibility measurement.....	63
3.16 Biomass waste particles (wheat straw particles). ....	65

## LIST OF FIGURES (Continued)

<u>Figure</u>		<u>Page</u>
5.1	Bed expansion as a function of superficial fluid velocity for the different magnetic field intensities and field gradient ( $d_{p,A} = 2.16$ mm and $d_{p,B} = 2.5$ mm) .....	88
5.2	Bed expansion as a function of the magnetic field gradient for different superficial fluid velocities .....	88
5.3	Dynamic pressure drop of particle A in the G-MAFB $dH_z/dz = - 20,543$ A/m/m, $U_0 = 0.0222$ m/s, and $h_{bed} = 0.190$ m .....	89
5.4	Voidage distribution of particle A in the G-MAFB $dH_z/dz = - 20,543$ A/m/m, $U_0 = 0.0222$ m/s, and $h_{bed} = 0.190$ m .....	90
5.5	Voidage distribution of particle A in the G-MAFB, $dH_z/dz = -20,543$ A/m/m, $U_0 = 0.0176$ m/s, and $h_{bed} = 0.220$ m .....	92
5.6	Voidage distribution of particle A in the G-MAFB, $dH_z/dz = - 14,663$ A/m/m, $U_0 = 0.0222$ m/s, and $h_{bed} = 0.220$ m .....	93
5.7	Voidage distribution of particle A in the G-MAFB, $dH_z/dz = - 18,289$ A/m/m, $U_0 = 0.0222$ m/s, and $h_{bed} = 0.205$ m .....	93
5.8	Voidage distribution of particle A in the G-MAFB, $dH_z/dz = - 20,543$ A/m/m, $U_0 = 0.0222$ m/s, and $h_{bed} = 0.190$ m .....	94
5.9	Voidage distribution of particle A in the G-MAFB, $dH_z/dz = - 14,663$ A/m/m, $U_0 = 0.0176$ m/s, and $h_{bed} = 0.130$ m .....	94
5.10	Voidage distribution of particle A in the G-MAFB, $dH_z/dz = - 18,289$ A/m/m, $U_0 = 0.0176$ m/s, and $h_{bed} = 0.120$ m .....	95
5.11	Voidage distribution of particle A in the G-MAFB, $dH_z/dz = - 20,543$ A/m/m, $U_0 = 0.0176$ m/s, and $h_{bed} = 0.110$ m .....	95
5.12	Voidage distribution of particle A in the G-MAFB, $dH_z/dz = - 20,543$ A/m/m, $U_0 = 0.0199$ m/s, and $h_{bed} = 0.130$ m .....	96

## LIST OF FIGURES (Continued)

<u>Figure</u>	<u>Page</u>
5.13 Voidage distribution of particle A in the G-MAFB, $dH_z/dz = - 33,798 \text{ A/m/m}$ , $U_o = 0.0199 \text{ m/s}$ , and $h_{bed} = 0.115 \text{ m}$ .....	96
5.14 Voidage distribution of particle B in the G-MAFB, $dH_z/dz = - 14,663 \text{ A/m/m}$ , $U_o = 0.0222 \text{ m/s}$ , and $h_{bed} = 0.187 \text{ m}$ .....	97
5.15 Voidage distribution of particle B in the G-MAFB, $dH_z/dz = - 18,289 \text{ A/m/m}$ , $U_o = 0.0222 \text{ m/s}$ , and $h_{bed} = 0.178 \text{ m}$ .....	97
5.16 Voidage distribution of particle B in the G-MAFB, $dH_z/dz = - 20,543 \text{ A/m/m}$ , $U_o = 0.0222 \text{ m/s}$ , and $h_{bed} = 0.165 \text{ m}$ .....	98
5.17 Voidage distribution of particle B in the G-MAFB, $dH_z/dz = - 20,543 \text{ A/m/m}$ , $U_o = 0.0222 \text{ m/s}$ , and $h_{bed} = 0.217 \text{ m}$ .....	98
5.18 Comparison of the calculated mass obtained from model and experiment with the exact mass .....	99
5.19 Prediction of the voidage distribution of particle C in the 0g environment, $U_{o,bottom} = 0.0000 \text{ m/s}$ , $d_p = 0.0024 \text{ m}$ , and $h_{bed} = 0.160 \text{ m}$ .....	102
5.20 Prediction of the voidage distribution of particle C in the 0g environment, $U_{o,bottom} = 0.0010 \text{ m/s}$ , $d_p = 0.0024 \text{ m}$ , and $h_{bed} = 0.160 \text{ m}$ .....	103
5.21 Prediction of the voidage distribution of particle C in the 0g environment, $U_{o,bottom} = 0.0055 \text{ m/s}$ , $d_p = 0.0024 \text{ m}$ , and $h_{bed} = 0.195 \text{ m}$ .....	103
5.22 Prediction of the voidage distribution of particle C in the 0g environment, $U_{o,bottom} = 0.0076 \text{ m/s}$ , $d_p = 0.0024 \text{ m}$ , and $h_{bed} = 0.200 \text{ m}$ .....	104
5.23 Prediction of the voidage distribution of particle C in the 0g environment, $U_{o,bottom} = 0.0110 \text{ m/s}$ , $d_p = 0.0024 \text{ m}$ , and $h_{bed} = 0.210 \text{ m}$ .....	104
5.24 Prediction of the voidage distribution of particle D in the 0g environment, $U_{o,bottom} = 0.0000 \text{ m/s}$ , $d_p = 0.0015 \text{ m}$ , and $h_{bed} = 0.180 \text{ m}$ .....	105
5.25 Prediction of the voidage distribution of particle D in the 0g environment, $U_{o,bottom} = 0.0010 \text{ m/s}$ , $d_p = 0.0015 \text{ m}$ , and $h_{bed} = 0.208 \text{ m}$ .....	105

## LIST OF FIGURES (Continued)

<u>Figure</u>	<u>Page</u>
5.26 Comparison between the height of the bed obtained from the model and the height of the bed obtained from the experimental observations.....	106
5.27 Comparison between the predicted mass and the exact mass of particles in the bed .....	106
5.28 G-MAFB apparatus used in filtration experiments .....	109
5.29 Change of biomass concentration in the holding tank, $d_p = 2.5$ mm, $D_p = 73.52$ $\mu$ m, $dH_z/dz = - 38,817$ A/m/m, and packed bed condition....	109
5.30 Change of biomass concentration in the holding tank, $d_p = 2.5$ mm, $D_p = 73.52$ $\mu$ m, $dH_z/dz = - 38,817$ A/m/m, $C_0 \sim 0.12$ [mg/cm <sup>3</sup> ], and packed bed condition .....	110
5.31 Change of biomass concentration in the holding tank, $d_p = 2.5$ mm, $D_p = 73.52$ $\mu$ m, $dH_z/dz = - 38,817$ A/m/m, $C_0 \sim 0.33$ [mg/cm <sup>3</sup> ], and packed bed condition .....	111
5.32 Change of biomass concentration in the holding tank, $d_p = 2.5$ mm, $D_p = 73.52$ $\mu$ m, $dH_z/dz = - 38,817$ A/m/m, $C_0 \sim 0.51$ [mg/cm <sup>3</sup> ], and packed bed condition .....	111
5.33 Change of biomass concentration in the holding tank, $d_p = 2.5$ mm, $D_p = 114.68$ $\mu$ m, $dH_z/dz = - 38,817$ A/m/m, $C_0 \sim 0.30$ [mg/cm <sup>3</sup> ], and packed bed condition .....	112
5.34 Change of biomass concentration in the holding tank, $d_p = 2.5$ mm, $D_p = 114.68$ $\mu$ m, $dH_z/dz = - 38,817$ A/m/m, $C_0 \sim 0.22$ [mg/cm <sup>3</sup> ], and packed bed condition .....	112
5.35 Change of biomass concentration in the holding tank, $d_p = 3.5$ mm, $D_p = 73.52$ $\mu$ m, $dH_z/dz = - 38,817$ A/m/m, $C_0 \sim 0.18$ [mg/cm <sup>3</sup> ], and packed bed condition .....	113
5.36 Change of biomass concentration in the holding tank, $d_p = 3.5$ mm, $D_p = 73.52$ $\mu$ m, $dH_z/dz = - 38,817$ A/m/m, $C_0 \sim 0.35$ [mg/cm <sup>3</sup> ], and packed bed condition .....	113

## LIST OF FIGURES (Continued)

<u>Figure</u>	<u>Page</u>
5.37 Change of biomass concentration in the holding tank, $d_p = 3.5$ mm, $D_p = 73.52$ $\mu$ m, $dH_z/dz = -38,817$ A/m/m, $C_0 \sim 0.53$ [mg/cm <sup>3</sup> ], and packed bed condition .....	114
5.38 Change of biomass concentration in the holding tank, $d_p = 3.5$ mm, $D_p = 114.68$ $\mu$ m, $dH_z/dz = -38,817$ A/m/m, $C_0 \sim 0.20$ [mg/cm <sup>3</sup> ], and packed bed condition .....	114
5.39 Change of biomass concentration in the holding tank, $d_p = 3.5$ mm, $D_p = 114.68$ $\mu$ m, $dH_z/dz = -38,817$ A/m/m, $C_0 \sim 0.31$ [mg/cm <sup>3</sup> ], and packed bed condition .....	115
5.40 Change of biomass concentration in the holding tank, $d_p = 3.5$ mm, $D_p = 114.68$ $\mu$ m, $dH_z/dz = -38,817$ A/m/m, $C_0 \sim 0.40$ [mg/cm <sup>3</sup> ], and packed bed condition .....	115
5.41 Change of biomass concentration in the holding tank at different pH, $d_p = 3.5$ mm, $D_p = 114.68$ $\mu$ m, $U_0 = 0.00825$ m/s, and $dH_z/dz = -38,817$ A/m/m, and packed bed condition .....	116
5.42 Correlation for the accumulation coefficient ( $k_f$ ) obtained from intermediate size screen analysis .....	118
5.43 Correlation for the accumulation coefficient ( $k_f$ ) obtained from centrifugal sedimentation particle size analysis .....	119
5.44 Correlation for the accumulation coefficient ( $k_f$ ) obtained from centrifugal sedimentation particle size analysis .....	119
5.45 Correlation for the detachment coefficient ( $k_2$ ) .....	122
6.1 Voidage distribution and elastic modulus of particle A in the MAFB $dH_z/dz = -20,543$ A/m/m, $U_0 = 0.0222$ m/s, and $h_{bed} = 0.190$ m .....	125
6.2 Change of biomass concentration in the holding tank, $d_p = 2.5$ mm, $D_p = 73.52$ $\mu$ m, $dH_z/dz = -38,817$ A/m/m and packed bed condition .....	127

## LIST OF FIGURES (Continued)

<u>Figure</u>	<u>Page</u>
6.3 Changes of media particle diameter inside the G-MAFB with time, $d_{p,0} = 0.0025 \text{ m}$ .....	127
6.4 Changes of biomass concentration deposited inside the G-MAFB with time .....	128
6.5 Change of voidage in the G-MAFB with time, $\varepsilon_0 = 0.46$ .....	128
6.6 Comparison of mass obtain from experiment and proposed model in the G-MAFB system .....	129
6.7 Predicted changes of biomass concentration in the holding tank ( $d_p = 2.7 \text{ mm}$ , $C_0 = 0.782 \text{ mg/cm}^3$ , $V_{\text{tank}} = 8,000 \text{ cm}^3$ , $U_0 = 0.01957 \text{ m/s}$ , and $h_{\text{bed}} = 0.35 \text{ m}$ ).....	130
6.8 Predicted changes of media particle diameter in the G-MAFB with time ( $d_p = 2.7 \text{ mm}$ , $C_0 = 0.782 \text{ mg/cm}^3$ , $V_{\text{tank}} = 8,000 \text{ cm}^3$ , $U_0 = 0.01957 \text{ m/s}$ , and $h_{\text{bed}} = 0.35 \text{ m}$ ).....	131
6.9 Predicted changes of mass deposited in the G-MAFB with time ( $d_p = 2.7 \text{ mm}$ , $C_0 = 0.782 \text{ mg/cm}^3$ , $V_{\text{tank}} = 8,000 \text{ cm}^3$ , $U_0 = 0.01957 \text{ m/s}$ , and $h_{\text{bed}} = 0.35 \text{ m}$ ).....	131
6.10 Predicted changes of voidage distribution in the G-MAFB with time ( $d_p = 2.7 \text{ mm}$ , $C_0 = 0.782 \text{ mg/cm}^3$ , $V_{\text{tank}} = 8,000 \text{ cm}^3$ , $U_0 = 0.01957 \text{ m/s}$ , and $h_{\text{bed}} = 0.35 \text{ m}$ ).....	132
6.11 Predicted changes of mass in the G-MAFB system with time ( $d_p = 2.7 \text{ mm}$ , $C_0 = 0.782 \text{ mg/cm}^3$ , $V_{\text{tank}} = 8,000 \text{ cm}^3$ , $U_0 = 0.01957 \text{ m/s}$ , and $h_{\text{bed}} = 0.35 \text{ m}$ ).....	132

## LIST OF TABLES

<u>Table</u>	<u>Page</u>
1.1 Summary of the studies of the magnetically stabilized fluidized bed .....	2
1.2 Summary of the studies of the magnetically fluidized bed in a non-uniform magnetic field .....	5
3.1 Helmholtz ring dimensions .....	49
3.2 Specifications of the gaussmeter .....	53
3.3 Specification of the laser module .....	55
3.4 Ferromagnetic particle properties .....	62
3.5 Median size, standard deviation, and specific surface area measured by the centrifugal sedimentation particle size analyzer .....	66
3.6 Size distribution of biomass waste particles measure by the centrifugal sedimentation particle size analyzer .....	67
3.7 Size distribution of biomass waste particles by microscopic analysis .....	68
3.8 Nominal diameter of biomass waste particle .....	69
5.1 Bed height at different fluid flow rates and different magnetic field gradients for ferromagnetic particles A and B .....	86
5.2 Bed height at a fixed magnetic field strength for different flow rates .....	100
5.3 Values of parameters in the accumulation correlation .....	118
5.4 Values of parameter in the detachment correlation .....	121



## LIST OF APPENDICES

	<u>Page</u>
Appendix A    The derivation of mass and momentum equations .....	145
A.1      Mass conservation equation.....	145
A.1.1    Mass conservation equation for fluid phase .....	145
A.1.2    Mass conservation equation for particle phase....	147
A.2      Momentum conservation equation .....	147
A.2.1    Momentum conservation equation for fluid phase.....	147
A.2.2    Momentum conservation equation for particle phase .....	151
Appendix B    Derivation of the attractive interparticle magnetic force .....	152
Appendix C    Preparation of ferro-sodium alginate mixture .....	156
Appendix D    Properties of materials.....	158
Appendix E    Calibration of instruments .....	160
E.1      Gaussmeter calibration.....	160
E.2      G-MAFB flow rate calibration .....	160
E.3      Rheostat resistance calibration .....	162
E.4      Laser photo-diode detector calibration.....	163
Appendix F    Magnetic field intensity .....	164
Appendix G    Magnetic susceptibility measurement .....	168

## LIST OF APPENDICES (Continued)

	<u>Page</u>
Appendix H    Visual designer flowgram .....	171
Appendix I    Dimensional analysis .....	173
Appendix J    Optimization program for evaluating $k_1$ and $k_2$ .....	176
Appendix k    Dynamic pressure drop and voidage data .....	180
Appendix L    Filtration experimental data .....	194

## LIST OF APPENDIX FIGURES

<u>Figure</u>	<u>Page</u>
A.1 Stationary volume element $\Delta x \Delta y \Delta z$ through which fluid and particles are flowing .....	145
A.1 Stationary volume element $\Delta x \Delta y \Delta z$ through in which the x momentum component is transported through the surface.....	147
B.1 Repulsive and attractive magnetic force between two ideal dipoles under the influence of a uniform external magnetic field, $\mathbf{B}_0$ . The forces $F_r$ and $F_\theta$ acting on particle 1 are of the same magnitude but opposite direction.....	152
E.1 Flow rotameter calibration for voidage distribution experiment.....	161
E.2 Flow rotameter calibration curve for a special flow meter used on board NASA's KC-135 aircraft .....	161
E.3 Flow rotameter calibration curve for filtration experiments.....	162
E.4 Rheostat resistant calibration curve .....	162
E.5 Laser photo-diode detector calibration curve .....	163
F.1 Magnetic field intensity in the bed used in the voidage distribution experiments at 1.0 volt across power supply .....	164
F.2 Magnetic field intensity in the bed used in the voidage distribution experiments at 2.0 volt across power supply .....	165
F.3 Magnetic field intensity in the bed used in the voidage distribution experiments at 3.0 volt across power supply .....	165
F.4 Magnetic field intensity in the bed used in the voidage distribution experiments at 4.0 volt across power supply .....	166
F.5 Magnetic field intensity used for the experiments on board NASA's KC-135 aircraft at 1.0 volt across power supply.....	166

## LIST OF APPENDIX FIGURES (Continued)

<u>Figure</u>	<u>Page</u>
F.6     Magnetic field intensity in the bed used in the filtration experiments .....	167
G.1     Magnetic field intensity used with the TGA .....	170
H.1     Schematic diagram of <i>FlowGram</i> in Visual Designer® software .....	171

## LIST OF APPENDIX TABLES

<u>Table</u>	<u>Page</u>
D.1 Properties of Sodium Alginate Powder.....	158
D.2 Physical and chemical properties of microsphere balloons.....	158
D.3 Composition and properties of ferromagnetic powder.....	159
D.4 Properties of Gellan Gum.....	159
G.1 Calculation of magnetic susceptibility of ferromagnetic particle .....	170
H.1 Parameter Setting on pAnalogInput 1 .....	172
I.1 Dimensions of variables.....	173
K.1 Experimental dynamic pressure drop and voidage of particle A in the G-MAFB, $dH_z/dz = -20,543 \text{ A/m/m}$ , $U_0 = 0.0176 \text{ m/s}$ , $h_{bed} = 0.220 \text{ m}$ , and $h_{in} = 0.135 \text{ m}$ .....	180
K.2 Experimental dynamic pressure drop and voidage of particle A in the G-MAFB, $dH_z/dz = -14,663 \text{ A/m/m}$ , $U_0 = 0.0222 \text{ m/s}$ , $h_{bed} = 0.220 \text{ m}$ , and $h_{in} = 0.135 \text{ m}$ .....	182
K.3 Experimental dynamic pressure drop and voidage of particle A in the G-MAFB, $dH_z/dz = -18,289 \text{ A/m/m}$ , $U_0 = 0.0222 \text{ m/s}$ , $h_{bed} = 0.205 \text{ m}$ , and $h_{in} = 9.5 \text{ cm}$ .....	183
K.4 Experimental dynamic pressure drop and voidage of particle A in the G-MAFB, $dH_z/dz = -20,543 \text{ A/m/m}$ , $U_0 = 0.0222 \text{ m/s}$ , $h_{bed} = 0.190 \text{ m}$ , and $h_{in} = 9.5 \text{ cm}$ .....	184
K.5 Experimental dynamic pressure drop and voidage of particle A in the G-MAFB, $dH_z/dz = -14,663 \text{ A/m/m}$ , $U_0 = 0.0176 \text{ m/s}$ , $h_{bed} = 0.130 \text{ m}$ , and $h_{in} = 6.5 \text{ cm}$ .....	185

## LIST OF APPENDIX TABLES (Continued)

<u>Table</u>	<u>Page</u>
K.6      Experimental dynamic pressure drop and voidage of particle A in the G-MAFB, $dH_z/dz = - 18,289 \text{ A/m/m}$ , $U_o = 0.0176 \text{ m/s}$ , $h_{bed} = 0.125 \text{ m}$ , and $h_{in} = 6.5 \text{ cm}$ .....	186
K.7      Experimental dynamic pressure drop and voidage of particle A in the G-MAFB, $dH_z/dz = - 20,543 \text{ A/m/m}$ , $U_o = 0.0176 \text{ m/s}$ , $h_{bed} = 0.110 \text{ m}$ , and $h_{in} = 6.5 \text{ cm}$ .....	187
K.8      Experimental dynamic pressure drop and voidage of particle A in the G-MAFB, $dH_z/dz = - 20,543 \text{ A/m/m}$ , $U_o = 0.0199 \text{ m/s}$ , $h_{bed} = 0.130 \text{ m}$ , and $h_{in} = 6.5 \text{ cm}$ .....	188
K.9      Experimental dynamic pressure drop and voidage of particle A in the G-MAFB, $dH_z/dz = - 33,798 \text{ A/m/m}$ , $U_o = 0.0199 \text{ m/s}$ , $h_{bed} = 0.115 \text{ m}$ , and $h_{in} = 6.5 \text{ cm}$ .....	189
K.10     Experimental dynamic pressure drop and voidage of particle A in the G-MAFB, $dH_z/dz = - 14,663 \text{ A/m/m}$ , $U_o = 0.0222 \text{ m/s}$ , $h_{bed} = 0.187 \text{ m}$ , and $h_{in} = 13.5 \text{ cm}$ .....	190
K.11     Experimental dynamic pressure drop and voidage of particle A in the G-MAFB, $dH_z/dz = - 18,289 \text{ A/m/m}$ , $U_o = 0.0222 \text{ m/s}$ , $h_{bed} = 0.178 \text{ m}$ , and $h_{in} = 13.5 \text{ cm}$ .....	191
K.12     Experimental dynamic pressure drop and voidage of particle A in the G-MAFB, $dH_z/dz = - 20,543 \text{ A/m/m}$ , $U_o = 0.0222 \text{ m/s}$ , $h_{bed} = 0.165 \text{ m}$ , and $h_{in} = 13.5 \text{ cm}$ .....	192
K.13     Experimental dynamic pressure drop and voidage of particle A in the G-MAFB, $dH_z/dz = - 20,543 \text{ A/m/m}$ , $U_o = 0.0222 \text{ m/s}$ , $h_{bed} = 0.217 \text{ m}$ , and $h_{in} = 17.0 \text{ cm}$ .....	193

## LIST OF APPENDIX TABLES (Continued)

<u>Table</u>	<u>Page</u>
L.1 Filtration experimental data in Figure 5.29, $d_p = 2.5$ mm, $D_p = 73.52$ $\mu$ m, and $h_{bed} = 0.20$ m .....	194
L.2 Filtration experimental data in Figure 5.30, $d_p = 2.5$ mm, $D_p = 73.52$ $\mu$ m, and $h_{bed} = 0.20$ m .....	195
L.3 Filtration experimental data in Figure 5.31, $d_p = 2.5$ mm, $D_p = 73.52$ $\mu$ m, and $h_{bed} = 0.20$ m .....	196
L.4 Filtration experimental data in Figure 5.32, $d_p = 2.5$ mm, $D_p = 114.68$ $\mu$ m, and $h_{bed} = 0.15$ m .....	197
L.5 Filtration experimental data in Figure 5.33, $d_p = 2.5$ mm, $D_p = 114.68$ $\mu$ m, and $h_{bed} = 0.15$ m .....	198
L.6 Filtration experimental data in Figure 5.35, $d_p = 3.5$ mm, $D_p = 73.52$ $\mu$ m, and $h_{bed} = 0.20$ m .....	199
L.7 Filtration experimental data in Figure 5.36, $d_p = 3.5$ mm, $D_p = 73.52$ $\mu$ m, and $h_{bed} = 0.20$ m .....	200
L.8 Filtration experimental data in Figure 5.37, $d_p = 3.5$ mm, $D_p = 73.52$ $\mu$ m, and $h_{bed} = 0.20$ m .....	201
L.9 Filtration experimental data in Figure 5.38, $d_p = 3.5$ mm, $D_p = 114.68$ $\mu$ m, and $h_{bed} = 0.15$ m .....	202
L.10 Filtration experimental data in Figure 5.39, $d_p = 3.5$ mm, $D_p = 114.68$ $\mu$ m, and $h_{bed} = 0.15$ m .....	203
L.11 Filtration experimental data in Figure 5.40, $d_p = 3.5$ mm, $D_p = 114.68$ $\mu$ m, and $h_{bed} = 0.15$ m .....	204

## NOTATION

Symbol	Description	Units
$a$	Parameter in Equation (2-20) and (5-3)	[-]
$a'$	Particle surface per unit volume of the bed	[m <sup>2</sup> surface/m <sup>3</sup> bed]
$A_p$	Particle cross sectional area	[m <sup>2</sup> ]
$b$	Parameter in Equation (2-20) and (5-3)	[-]
$B$	Magnetic flux density	[Wb/m <sup>2</sup> ]
$c$	Parameter in Equation (5-3)	[-]
$c_s$	Cunningham's correction factor	[-]
$C$	Virtual mass coefficient defined in Equation (2-5)	[-]
$C^*(x, t)$	Biomass concentration in the fluidized bed	[kg/m <sup>3</sup> ]
$C_d$	Fluid drag coefficient	[-]
$d_p$	Ferromagnetic particle diameter	[m]
$D_p$	Biomass (straw) particle diameter	[m]
$D_{col}$	Fluidization column diameter	[m]
$D_{BM}$	Diffusion coefficient	[m <sup>2</sup> /s]
$d_{scr}$	Screen size diameter	[m]
$e$	Parameter in Equation (5-4)	[-]
$E$	Elastic coefficient of the fluidized bed	[N/m <sup>2</sup> ]
$f$	Parameter in Equation (5-4)	[-]
$f_d^*$	Fluid drag force acting on a single particle	[N]



## NOTATION (Continued)

<b>Symbol</b>	<b>Description</b>	<b>Units</b>
$f_m$	Interparticle magnetic force	[N/m <sup>3</sup> ]
$F_{\text{I}}, F_d$	Interface interaction force between fluid and particle	[N/m <sup>3</sup> ]
$F_b$	Buoyancy force acting on the particle	[N/m <sup>3</sup> ]
$F_g$	Gravitational force acting on the particle	[N/m <sup>3</sup> ]
$F_m$	Magnetic force acting on the particle	[N/m <sup>3</sup> ]
$g$	Parameter in Equation (5-4)	[-]
$g$	Acceleration of gravity	[m/s <sup>2</sup> ]
$h$	Height of the bed	[m]
$h_{in}$	Initial height of the bed	[m]
$H$	Magnetic field intensity	[A/m]
$H_r$	Magnitude of magnetic field intensity in r direction	[A/m]
$H_z$	Magnitude of magnetic field intensity in z direction	[A/m]
$H_\theta$	Magnitude of magnetic field intensity in $\theta$ direction	[A/m]
$k_1$	Accumulation coefficient	[m <sup>3</sup> liquid/m <sup>3</sup> bed-s]
$k_2$	Detachment coefficient	[1/s]
$K_{EC}$	Parameter defined in Equation (2-31)	[-]
$K_{EI}$	Parameter defined in Equation (2-32)	[-]

## NOTATION (Continued)

Symbol	Description	Units
$K_{EM}$	Parameter defined in Equation (2-34)	[-]
$K_{ES}$	Parameter defined in Equation (2-36)	[-]
$L$	Height of the fluidization bed	[m]
$m$	Parameter defined in Equation (2-24)	[-]
$\mathbf{M}_b$	Magnetization of bed medium	[A/m]
$M_p$	Magnetization of the particle	[A/m]
$n$	Parameter defined in Equation (2-24)	[-]
$\Delta P_f$	Pressure drop between any two given points	[Pa]
$\Delta P_d$	Dynamic pressure drop	[Pa]
$\Delta P_p$	Particle pressure	[Pa]
$t$	Time	[s]
$Q$	Electrical charge	[Coulomb]
$r$	Radius or distance between two magnetic particles in adjacent layers	[m]
$U$	Interaction energy between two dipoles	[J]
$\mathbf{U}$	Velocity of fluid phase	[m/s]
$U_0$	Superficial fluid velocity	[m/s]
$u_x, u_y, u_z$	Interstitial fluid velocity in $x$ , $y$ and $z$ components	[m/s]
$u_{mf}$	Minimum fluidizing velocity	[m/s]
$\mathbf{V}$	Velocity of particle phase	[m/s]

## NOTATION (Continued)

Symbol	Description	Units
$v_x, v_y, v_z$	Interstitial fluid velocity in x, y and z components	[m/s]
$V_p$	Volume of the particle	[m <sup>3</sup> ]
$x_1$	Distance between center of rotation and sedimentation plane	[m]
$x_2$	Distance between center of rotation and measuring plane	[m]
$x_i$	Fraction of particle in each range	[-]
$x, y, z$	Cartesian coordinate	[-]
$\tau_f$	Fluid stress tensor	[N/m <sup>2</sup> ]
$\tau_p$	Particle stress tensor	[N/m <sup>2</sup> ]
$\mu$	Magnetic permeability of the particle	[kg m/A <sup>2</sup> s <sup>2</sup> ]
$\mu_0$	Magnetic permeability of free space ( $4\pi \times 10^{-7}$ )	[kg m/A <sup>2</sup> s <sup>2</sup> ]
$\mu_b$	Magnetic permeability of the bed mixture	[kg m/A <sup>2</sup> s <sup>2</sup> ]
$\mu_f$	Viscosity of the fluid phase	[N s/m <sup>2</sup> ]
$\chi$	Particle magnetic susceptibility	[-]
$\beta$	Friction coefficient defined in Equation (2-5)	[-]
$\alpha$	Constant defined in Equation (4-16)	[-]
$\varphi$	Constant defined in Equation (4-17)	[-]
$\lambda$	Constant defined in Equation (4-18)	[-]

## NOTATION (Continued)

Symbol	Description	Units
$\gamma$	Constant defined in Equation (4-19)	[-]
$\gamma_c$	Constant defined in Equation (2-35)	[-]
$\gamma_p$	Constant defined in Equation (2-33)	[-]
$\omega(t)$	Rotational angular velocity	[radian/sec]
$\eta_o$	Viscosity coefficient of dispersion medium	[-]
$\eta$	Empirical coefficient defined in Equation (2-11)	[-]
$\sigma$	Biomass concentration on the media particles	[kg/m <sup>2</sup> surface]
$\rho_f$	Fluid density	[kg/m <sup>3</sup> ]
$\rho_p$	Ferromagnetic particle density	[kg/m <sup>3</sup> ]
$\rho_{str}$	Biomass wheat straw density	[kg/m <sup>3</sup> ]
$\varepsilon$	Void fraction of bed	[-]
$\varepsilon_c$	Dielectric constant of collector	[-]
$\varepsilon_f$	Dielectric constant of fluid	[-]
$\varepsilon_p$	Dielectric constant of particle	[-]

# **Magnetically Assisted Liquid-Solid Fluidization in A Gradient Magnetic Field: Theory and Application**

## **CHAPTER 1**

### **INTRODUCTION**

#### **1.1 Thesis overview**

Magnetically Stabilized Fluidized Beds (MSFB) are among the most recent and novel chemical engineering developments in the area of fluid-solid contacting operations. The fluid dynamic characteristics and the stability of MSFB performance in a uniform magnetic field have been investigated by several researchers. Rosensweig (1979), Rosensweig *et al.* (1983), and Conan (1996) proposed mathematical models to predict the stability of the MSFB in a uniform magnetic field. Hristov (1996) also studied the effect of field line orientation on the stability of a bed of ferromagnetic particles. In addition, Arnaldos *et al.* (1985) and Wu *et al.* (1997) studied a MSFB containing a mixture of magnetic and non-magnetic particles. Table 1.1 summarizes the most relevant studies of the MSFB.

Normally, the fluidization conditions are based on the balance of gravitational, buoyancy, and drag forces. In the absence of normal gravity, or under microgravity and variable gravity conditions, the gravitational force must be

**Table 1.1** Summary of the studies of magnetically stabilized fluidized bed

Author	Particles	Density [kg/m <sup>3</sup> ]	Size [μm]	Fluidization System	Type of Magnetic Field	Type of study
Graham, L, J. (1998)	a) Alginate-ferrite	1,173	2,000	Liquid-Solid	Uniform	Dechlorination of p-Chlorophenol on Bimetallic Pd/Fe Catalyst in a MSFB
Rhee, Brian K. (1998)	a) Alginate-ferrite + active carbon	1,515	3,000	Liquid-Solid	Uniform	Enhancement of Mass Transfer Coefficient in A Three-Phase MSFB
Al-Mulhim (1995)	a) Alginate-ferrite + active carbon	1,370	1,500	Liquid-Solid	Uniform	Enhancement of Mass Transfer Coefficient in a MSFB
Wu W.Y. <i>et al.</i> (1997)	a) Iron b) Copper	7,831 8,920	1,416 935	Gas-Solid	Uniform	Hydrodynamic Characteristics of Magnetic and Non-magnetic Particles
Conan J. Fee (1996)	a) Poly-Acrylamide-Magnetic (PAM)	1,800	-	Liquid-Solid	Uniform	The Stability of The Liquid-Fluidized Magnetically Stabilized Fluidized Bed
	b) Calcium Alginate-Magnetic (CAM)	1,200	-			
Jordan Y. Hristov (1996)	a) Magnetite b) Iron Powder c) Fe Catalyst	5,200 7,800 -	100-400 100-200 200-315	Gas-Solid	Uniform	The Effect of Field Line Orientation on Bed Stability
Zhu Qingshan Hongzhong Li (1995)	a) Reduced iron powder (Fe)	7,810	12.92	Gas-Solid	Uniform	Study on Magnetic Fluidization Behavior of Group C Powders
	b) α-FeO (OH)	3,290	7.02			
	c) SiO <sub>2</sub>	2,490	13.56			

**Table 1.1** Summary of the studies of magnetically stabilized fluidized bed (Continued)

Author	Particles	Density [kg/m <sup>3</sup> ]	Size [μm]	Fluidization System	Type of Magnetic Field	Type of study
Saxena S.C. S. Shrivastava (1991)	a) Steel Shots	7,029	262 624 1,491	Gas-Solid	Uniform	Hydrodynamic investigation of the MSFB
Siegell J.H. (1987)	a) Composite of Non-Magnetic with Stainless Steel b) Stainless Steel	2,700 & 1,900 7,750	- - -	Liquid-Solid	Uniform	Liquid-fluidized magnetically stabilized beds
Arnaldos, J. <i>et al.</i> (1985)	a) Steel b) Nickel c) Copper d) Silica	7,500 5,870 8,890 2,670	350-420 177-400 350-420 630-890	Gas-Solid	Uniform	The stability of the mixture of magnetic and non- magnetic particles
Rosensweig <i>et al.</i> (1983)	a) Ceramic Ferrite	1,880	-	Gas-Solid	Uniform	The mechanics of the MSFB
Rosensweig (1979)	-	-	-	Gas-Solid	Uniform	The stability of the MSFB

replaced by an alternative force to restore fluidization. To reinstate fluidization conditions in the absence of gravity using magnetic forces, ferromagnetic solid phase media and a non-uniform magnetic field are required. Table 1.2 summarizes the recent studies of a magnetically fluidized bed in a gradient magnetic field. Our work has shown that, given a suitable variable field design, the resulting magnetic field gradient can create sufficient magnetic force acting upon the ferromagnetic particles to replace or supplement the gravitational force. Furthermore, the magnetic force can be put to work in ordinary fluidized beds to enhance or create new operational features, and thus create a degree of freedom that can be creatively used to control the operation of the bed. We term this variation of MSFB as a Gradient Magnetically Assisted Fluidized Bed (G-MAFB).

In our study, the feasibility of using the G-MAFB in a microgravity environment is considered. To accomplish this task, the magnetic field inside the fluidization column must be changed from a uniform to a **non-uniform** magnetic field. The magnetic field gradient creates a magnetic force on ferromagnetic particles, replacing the gravitational force, and hence, the fluidization conditions can be restored.

In the G-MAFB fluidization, forces acting on the particles are composed of the drag force, the gravitational force, the magnetic force, and the buoyancy force. These forces must be in balance to maintain stable fluidization. The gravitational force and the buoyancy force are dependent on the density and the volume of fluidized particles. The drag force is a function of the relative velocity



**Table 1.2** Summary of the studies of magnetically fluidized bed in a non-uniform magnetic field

Author	Particles	Density [kg/m <sup>3</sup> ]	Size [mm]	Fluidization System	Type of Magnetic Field	Type of study
Jovanovic, G. <i>et al.</i> (2003b)	a) Alginate-Ferrite b) Alginate-ZrO c) Alginate-Ferrite	1,340 1,430 1,440	1.84 1.84 2.5, 3.5	Liquid-solid	Non-uniform	Development of enabling technologies for magnetically assisted gasification of solid wastes
Sornchamni, T. <i>et al.</i> (2003)	a) Alginate-Ferrite	1,440	2.5, 3.5	Liquid-solid	Non-uniform	Biomass waste filtration experiments in liquid-solid magnetically assisted fluidized Bed (MAFB)
Jovanovic, G. <i>et al.</i> (2003a)	a) Alginate-Ferrite	1,119 1,302 1,502 1,090	2.2 2.5 2.4 1.5	Liquid-solid	Non-uniform	Study the behavior of non-uniform magnetic fluidized bed and Voidage distribution
Espinoza, J. (2002)	a) Alginate-Ferrite b) Alginate-ZrO	1,340 1,430	1.84 1.84	Liquid-solid	Non-uniform	Dynamic behavior of ferromagnetic particles in a liquid-solid MAFB
Jovanovic, G. <i>et al.</i> (1999)	a) Alginate-Ferrite	-	1.5, 2.4, 4.9	Liquid-solid	Non-uniform	Magnetically assisted gasification of solid waste

of fluid and particles and the viscosity of fluid, as well as, the diameter of particles and bed voidage. The magnetic force is not only dependent on the magnetic field gradient, but also on the magnetic field intensity and on the magnetic susceptibility of particles. In the experimental investigation in this study, the magnetic field is designed to have a stronger field intensity at the bottom of the bed, and decreases gradually-linearly toward the top of the bed. This change in the magnetic field strength along the fluidization column varies the magnitude of the magnetic force from the bottom to the top of the column. As a result, the particle holdup at any location varies along the column to reflect the equilibrium of all of the forces involved.

The nature of the magnetic forces produced in conventional MSFB versus G-MAFB systems is quite different. In MSFB systems, the externally applied magnetic field intensity is uniform within the column, and the magnetic force that appears in this bed is only the magnetic force between the particles. On the other hand, in G-MAFB systems the magnetic field intensity within the fluidization column varies from the bottom to the top of the bed. In addition to the interparticle magnetic forces, the magnetic field and field gradient produce a direct force acting upon all ferromagnetic media. This is the first study, to the best of our knowledge, which takes into account both types of magnetic forces in the modeling of magnetically assisted fluidized bed. The application of suitably designed magnetic field gradients makes feasible a fluidization operation in the absence of gravity or a creative enhancement of fluidized bed performance in normal or variable gravity. The possibilities for the development of gradient

magnetically assisted fluidized bed space-flight applications include Advanced Life Support - ALS and *In Situ* Resource Utilization - ISRU (Jovanovic *et al.*, 1999), energy conversion, and various chemical and biochemical reaction processes.

## **1.2 Goals and objectives**

The main goals of this study are as follows:

1. to gain new knowledge of fluidization fundamentals related to external and interparticle magnetic forces,
2. to expand fluidized bed applications (unit operations, chemical processes and bio processes) to the space environment where microgravity is the most predominant operating factor,
3. to develop a new paradigm for investigating fluidized bed fluid dynamic behavior (including interparticle forces) by implementing two investigative approaches; the Discrete Particle Method (DPM) and the Two-Continuum Phase (TCP) method.

To accomplish these goals, the following objectives have to be realized:

1. design and construct the magnetically assisted fluidized bed,
2. produce and characterize ferromagnetic particles suitable for the G-MAFB demonstration application,

3. investigate the fluid dynamic behavior of the G-MAFB, and measure the variation of the bed porosity in the axial direction under different experimental conditions,
4. develop a model that can predict the voidage distribution in axial directions as a function of process parameters, such as the magnetic field and its gradient, particle properties, fluid properties, and flow conditions,
5. perform a filtration experiment for particles of interest for NASA's advanced life support program,
6. develop a filtration model that can predict the performance of the filtration operation in both 0g and 1g environments.

Voidage distribution in the G-MAFB is of primary interest because voidage is the most important parameter among all fluidization parameters, and it fundamentally determines fluidized bed performance. The degree of consolidation or fluidization of ferromagnetic media can be controlled by the magnetic force. In the study of the voidage distribution, we propose that the Discrete Particle Method (DPM) approach can be used as an investigative tool for the Two-Continuum Phase representation of fluidized beds. We do not consider DPM and TCP as two competing modeling approaches but rather as two complementary synergetic methods of representation of fluidized beds. We demonstrate this synergetic relationship by using DPM as an investigative tool for the advancement of the Two-Continuum Phased fluidized bed representation. This approach is particularly

helpful in incorporating interparticle forces into consideration of operating behavior of fluidized beds. Interparticle forces are a topic that is particularly hard to address within the TCP. We also propose the G-MAFB as a promising operating platform for fluidized bed operations in the space environment by demonstrating the practical implementation of the G-MAFB in the filtration and destruction of solid biomass waste particles from liquid streams.

## **CHAPTER 2**

### **THEORETICAL BACKGROUND**

Fluidization is the process by which a bed of solid particles is transformed into a fluid-like state by suspension in a gas or liquid. When a fluid is passed through a bed of particles at a low flow rate, the fluid will move through the void spaces between particles without affecting the structure of the bed (fixed bed). If the fluid flow increases, the particles will start rearranging their positions with a few vibrations and the height of the bed will slightly increase. At an even higher velocity, a point is reached where the friction forces between the particles and fluid counterbalance the buoyant weight of all particles in the bed. This point is referred to as an incipient fluidization (Kunii and Levenspiel, 1991). This simplified picture of the incipient fluidization does not include any secondary and tertiary factors such as momentum transfer at the distributor plate, friction losses at walls, etc.

Liquid-solid fluidization in the MSFB has limited importance from an industrial point of view. A number of studies and research projects (Burns and Graves (1985,1986), Terranova and Burns (1990), and Siegel (1987)) have been performed to improve fluidization operations for various possible industrial applications. It is particularly interesting to note that the studies by Al-Mulhim (1995) and Rhee (1998) showed that the mass transfer coefficient for MSFB systems could be greatly enhanced in a liquid-solid fluidized bed. This fact may

substantially influence the operation of, for example, fluidized bed bioreactors with immobilized cells.

However, no study of liquid-solid fluidization has ever been conducted in microgravity or variable gravity conditions (e.g., Space Station, interplanetary travel, Moon or Mars). The possibilities for the development of fluidized bed applications in space may include Advanced Life Support Systems (Jovanovic *et al.*, 1999), In Situ Resource Recovery, biochemical reaction processes, and energy conversion. This study, therefore, focuses on: a) liquid-solid fluidization in the G-MAFB with constant gradient magnetic field, and b) the feasibility of fluidization operation in the absence of the gravitational field. The bed voidage, which is one of the most important fluid dynamic parameters for predicting performance of the fluidized bed reaction process or unit operations, is the focal point of the experimental and modeling work.

In either conventional fluidized beds or magnetically stabilized fluidized beds, the fluidization conditions result from the interaction of forces acting on fluidized particles. This can be illustrated through a balance of three characteristic forces, the gravitational force,  $F_g$ , the buoyancy force,  $F_b$ , and the drag force,  $F_d$ , as shown in Figure 2.1.

The equilibrium of forces in Figure 2.1 represents the fluidization condition in the region that is far enough from the distributor plate or wall of the fluidization column. At the distributor plate, the fluid jets transfer momentum to the particles, while at the walls, momentum is transferred from particles to the fluidization

column. These effects are eventually, through collision of particles, distributed throughout the bed. In this study, we do not explicitly address these phenomena.

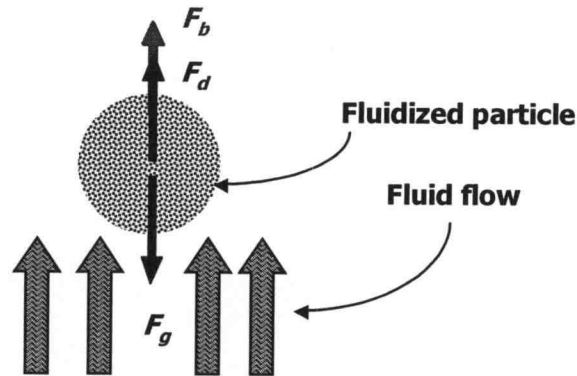


**Figure 2.1** Balance of forces acting on a fluidized particle in a conventional fluidized bed (liquid media-solid particles).

However, magnetic force can be added to this balance of forces. The magnitude and orientation of this force depends primarily on the orientation, strength and gradients of the field as well as on the magnetization properties of the fluidization particles. Figure 2.2 schematically illustrates one such example. Simple quantitative analysis of these forces shown in Figure 2.2 points to some obvious consequences. For example, to sustain the same quality of fluidization (i.e. similar voidage distribution), one has to increase fluid velocity in order to create sufficient drag force to balance the magnetic force. This, in turn will increase the relative velocity of particles and fluid, which should increase mass transfer (Al-Mulhim, 1995) between particles and fluid.



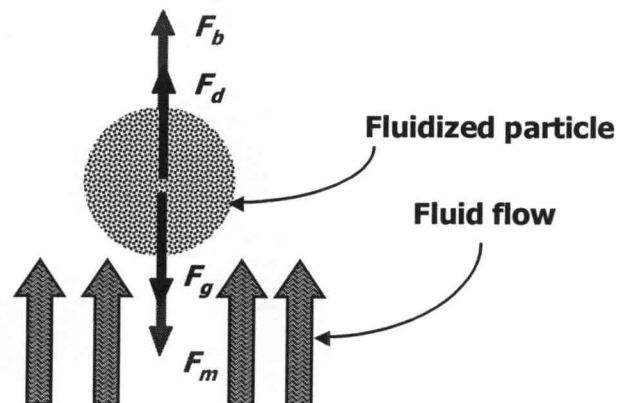


**Figure 2.2** Balance of forces acting on a ferromagnetic fluidized particle in a gradient magnetically fluidized bed (liquid media-solid particles).

Moreover, under microgravity conditions where the gravitational force is no longer significant, the drag force still acts on fluidized particles as shown in Figure 2.3a. Under these conditions the balance of forces no longer exists, and the particles in the fluidized bed will immediately be swept away in the direction of the fluid flow. Fluidization conditions can be restored by introducing an additional force, such as a magnetic force,  $F_m$ , to reinstate the balance of forces on the fluidized particle. Such a magnetic force acting on the ferromagnetic particles can be created simply by placing magnetically susceptible particles into a non-uniform magnetic field, as shown in Figure 2.3b.

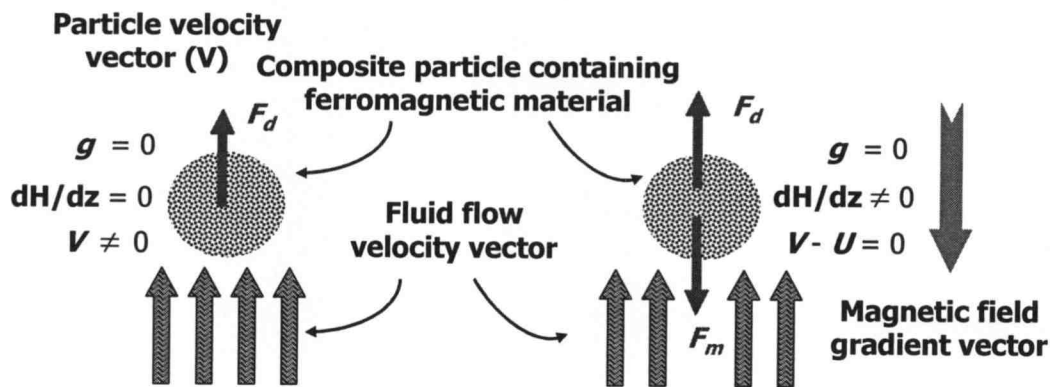


**Figure 2.3** Balance of forces acting on a fluidized particle containing ferromagnetic material in a) a fluidized bed in microgravity in the absence of a magnetic field, and b) a gradient magnetically assisted fluidized bed in microgravity.

Voidage distribution throughout the bed reflects the influence of all the above-mentioned forces, and therefore, lends itself as a suitable tool for the investigation of G-MAFB fluid dynamic phenomena. In gradient magnetically assisted fluidization, the forces acting on fluidization particles are the drag force, the gravitational force, the external magnetic force, and the buoyancy force. These forces must be in balance at the fluidization condition. Aside from this external magnetic force, which is created in the interaction between an external gradient magnetic field and magnetically susceptible particles, there are also interparticle magnetic forces. Interparticle magnetic forces are created between magnetized particles and they depend on the characteristics of the magnetic field and particles. Simply magnetized particles can attract or repel each other depending on their magnetizations and relative positions. It is interesting to note

that the interparticle magnetic forces can be created even in the uniform external magnetic field, in which the external magnetic forces cannot be established ( $\nabla H=0$  and  $\mathbf{F}_m=0$ ). Furthermore, the resultant local average value of interparticle magnetic forces acting on any given particle in the bed is zero. One of the consequences of this situation is that interparticle magnetic forces do not contribute directly to the local average balance of forces. However, these forces contribute to the solid phase stress tensor. In other words, interparticle magnetic forces increase the internal solid phase stress and therefore indirectly change the voidage of the fluidized bed, which in turn influences the drag force and overall fluidization condition. This phenomenon is intensively studied by Pinto-Espinoza (2002) and we incorporate the results of this study in determining the voidage distribution of the bed. Our basic approach in this study is to use TCP modeling for representation of the G-MAFB and complement it with the results of the DPM investigation by converting these results into a form suitable for the TCP modeling approach.

According to the TCP modeling approach, the motion of fluid and particles in the bed can be described by four fundamental equations, namely, the equations of continuity and the equations of motion for solid and liquid phases. These equations describe the motion of the fluid and particles at each point in the column. The fluidized bed is viewed as a two-continuous-phase flow system in which the fluid phase and the particle phase freely penetrate and interact with each other.

## 2.1 Mass and momentum conservation equations

The point mechanical variables, such as the fluid velocity, pressure, and stress components, are interpreted as local average values over a region that is large compared to the particle spacing, but remains small compared to the scale of macroscopic variation from point to point in the system. Anderson and Jackson (1967) were the first to develop the equations of continuity and the equations of motion for a system of fluidized particles. These equations in vector notation are described below.

### 2.1.1 Mass conservation equation for liquid and solid (particle) phase

$$\text{Fluid phase:} \quad \frac{\partial \varepsilon}{\partial t} + \nabla \cdot \varepsilon \mathbf{U} = 0 \quad (2-1)$$

$$\text{Particle phase:} \quad \frac{\partial (1-\varepsilon)}{\partial t} + \nabla \cdot (1-\varepsilon) \mathbf{V} = 0 \quad (2-2)$$

### 2.1.2 Momentum conservation equation for liquid and solid (particle) phase

$$\text{Fluid phase:} \quad \rho_f \varepsilon \left( \frac{\partial \mathbf{U}}{\partial t} + (\mathbf{U} \cdot \nabla) \mathbf{U} \right) = -\varepsilon \nabla P_f - \varepsilon \nabla \tau_f + \rho_f \varepsilon \mathbf{g} - \varepsilon \mathbf{F}_1 \quad (2-3)$$

$$\begin{aligned} \text{Particle phase:} \quad \rho_p (1-\varepsilon) \left( \frac{\partial \mathbf{V}}{\partial t} + (\mathbf{V} \cdot \nabla) \mathbf{V} \right) = & -(1-\varepsilon) \nabla P_f - (1-\varepsilon) \nabla P_p - (1-\varepsilon) \nabla \cdot \tau_p \\ & + \rho_p (1-\varepsilon) \mathbf{g} + \varepsilon \mathbf{F}_1 + \mathbf{F}_m \end{aligned} \quad (2-4)$$

The momentum conservation equation for the particle phase is augmented with the magnetic force,  $\mathbf{F}_m$ , which depends on the magnetic field intensity, the magnetization of the particles, and the magnetic field gradient. The drag force is a function of the velocity and the viscosity of the fluid, as well as the particle diameter and bed voidage. These sets of equations cannot be solved unless the expressions for  $\mathbf{F}_1$ ,  $\nabla P_p$ ,  $\nabla \tau_p$ , and  $\mathbf{F}_m$  in terms of the fluid flow and magnetic properties are defined. With the magnetic term coupling in the momentum conservation equation for the particle phase, the magnetic field equations will be reviewed, and then applied in this modeling process.

## 2.2 Constitutive relationships

### 2.2.1 Interaction force between fluid and particle, $\mathbf{F}_1$

The main contributors to the interaction between fluid and particles are the buoyancy force, the drag force, and the virtual mass force. The gravitational force and the buoyancy force are dependent on the density and the volume of fluidized particles. The virtual mass force is due to acceleration of the relative velocity ( $\mathbf{U} - \mathbf{V}$ ) and relates to the force required to accelerate the surrounding fluid (Crowe *et al.*, 1998). The buoyancy force of fluid on the particle is included in the first term of Equation (2-4),  $(1-\varepsilon)\nabla P_f$ . The expression for the drag force and the virtual mass force,  $\mathbf{F}_1$ , is given by Anderson and Jackson (1967) as:

$$\mathbf{F}_1 = \beta(\varepsilon)(\mathbf{U} - \mathbf{V}) + \frac{(1-\varepsilon)}{\varepsilon} C(\varepsilon) \rho_f \frac{d(\mathbf{U} - \mathbf{V})}{dt} \quad (2-5)$$

The drag force is assumed to act in the direction of the relative velocity, and depends on the void fraction and on the relative velocity of the two phases. The drag force is proportional to the magnitude of  $\mathbf{U} - \mathbf{V}$  and the particle to fluid drag coefficient,  $\beta$ , and is assumed to be dependent on the voidage. The form of the coefficient  $\beta$ , for flow through a bed of particles, can be presented as:

$$\beta(\varepsilon) = \frac{150(1-\varepsilon)\mu_f}{d_p^2 \varepsilon^2} + \frac{1.75(1-\varepsilon)|\mathbf{U} - \mathbf{V}| \rho_f}{d_p \varepsilon^2} \quad (2-6)$$

This expression was proposed by Ergun (1952) who cleverly combined the Kozeny-Carman equation for flow in the viscous regime and the Burke-Plummer equation for the turbulent regime. The characteristic Reynolds number,  $Re_p$ , is defined as:

$$Re_p = \frac{d_p U_0 \rho_f}{\mu_f} \quad (2-7)$$

When  $Re_p < 20$ , the viscous loss term dominates and can be used alone with negligible error. On the other hand, when  $Re_p > 1000$ , only the turbulent loss term is needed. The virtual mass coefficient,  $C$ , is suggested to be equal to 0.5 for an isolated spherical particle (Jackson, 1985). There is another form of the description of the drag force, which is used in the recent fluidization literature. Di Felice (1994) proposed the expression of the fluid drag force action on a single particle as:

$$\mathbf{F}_1 = f_d^* \varepsilon^{-\eta} \quad (2-8)$$

$f_d^*$  represents the fluid drag force acting on a single particle in the absence of other particles and it can be written as:

$$f_d^* = \frac{1}{2} C_d \rho_f A_p |\mathbf{U} - \mathbf{V}| (\mathbf{U} - \mathbf{V}) \quad (2-9)$$

where  $A_p$  is the particle cross sectional area, and  $C_d$  is the fluid drag coefficient, which can be expressed by the following equation,

$$C_d = \left( 0.063 + \frac{4.8}{\text{Re}_p^{0.5}} \right)^2 \quad (2-10)$$

The empirical coefficient,  $\eta$ , is found to be a function of particle Reynolds number as follows:

$$\eta = 3.7 - 0.65 \exp \left[ - \frac{(1.5 - \log \text{Re}_p)^2}{2} \right] \quad (2-11)$$

In this study, we chose the former approach due to its simplicity.

### 2.2.2 Magnetic force on the ferromagnetic particles, $\mathbf{F}_m$

The magnetic force is computed with the assumption that the fluidization particles contain a soft (i.e., easily magnetized and demagnetized) ferromagnetic material. The magnetization of the fluidized bed as a whole,  $\mathbf{M}_b$ , is assumed to be collinear with the magnetic field intensity,  $\mathbf{H}$ . Cowley and Rosensweig (1967)

defined the magnetic body force acting on a magnetic medium in a non-uniform magnetic field as:

$$\mathbf{F}_m = \mu_0 \mathbf{M}_b \nabla \mathbf{H} \quad (2-12)$$

Rosensweig (1979) proposed the magnetic equation of state for a uniformly fluidized bed.

$$\frac{\mathbf{M}_b}{|\mathbf{M}_p|} = (1 - \varepsilon) \frac{\mathbf{H}}{|\mathbf{H}|} \quad \text{and} \quad |\mathbf{M}_p| = \chi |\mathbf{H}| \quad (2-13)$$

He assumed that the magnetization of the bed is collinear with the direction of the magnetic field and proportional to the solid content in the bed.

### 2.2.3 Particle pressure, the particle stress tensor ( $\nabla P_p$ and $\tau_p$ ) and elastic modulus in the G-MAFB

The effect of interparticle forces (van der Waals force) and magnetic interparticle forces on the fluidized bed is well documented. The experimental series by Rietema *et al.* (1977, 1990 and 1993) demonstrated that the van der Waals interparticle force is accounted for as the particle pressure and the particle stress tensor in the momentum conservation equation. In the experiment performed by Rietema and Muster (1977), finely dispersed solids were fluidized in a quasi-two dimensional bed with 10×4 cm horizontal dimensions. The gas flow rate was increased to produce the condition in which the bed was expanded but gas bubbles did not appear. It was shown that the bed could be tilted up to a certain angle without the powder sliding, the surface remaining perpendicular to



the direction of flow. Rosensweig *et al.* (1983) also suggested that the interparticle magnetic force has an effect on the magnetically stabilized fluidized bed. Rosensweig claimed that magnetized particles in MSFB systems that are in close contact with neighboring particles form a "magnetic gel" exhibiting a measurable yield stress. The yield stress was measured in the MSFB by noting the force required to withdraw a vertical flat plate having surfaces roughened with glued-on bed particles. The experiments showed that the yield stress became higher with increased applied magnetic field intensity, due to magnetization and mutual attraction and repulsion of particles. It is easy to picture how interparticle magnetic forces give rise to a mechanical structure that has a certain elasticity. This phenomenon must be included in the equation of motion in terms of the particle pressure and the particle stress tensor. Rietema (1993) defined the particle pressure and the particle shear stress in the  $z$  direction in terms of an elastic modulus represented by the following expression,

$$-\frac{\partial P_{p,zz}}{\partial z} - \frac{\partial \tau_{p,zz}}{\partial z} = E \frac{\partial \varepsilon}{\partial z} \quad (2-14)$$

As already mentioned, in the G-MAFB, there are two types of magnetic forces acting on the ferromagnetic particles, namely, the external magnetic force  $\mathbf{F}_m$  due to the magnetic field gradient (Equation (2-12)) and the interparticle magnetic force  $\mathbf{f}_m$  due to the magnetization of ferromagnetic particles. As a consequence of interparticle magnetic forces in the G-MAFB, terms describing the elasticity of the solid bed structure must be introduced into momentum equations of the particle phase. The magnetic interparticle forces, which are necessarily

defined in the Discrete Particle Method (DPM), can be transformed into a continuous solid phase property that we define as the modulus of elasticity. First, we define the elastic modulus as

$$E = \frac{d_p}{A_p} \frac{df_{m,z}}{dz} \quad (2-15)$$

Pinto-Espinoza (2002) described all interparticle forces created in the G-MAFB. When the ferromagnetic particles are present in the magnetic field, they will be magnetized. The interparticle forces between ferromagnetic particles can be either attractive or repulsive depending on the position of the particles. If two particles approach each other along the line of their dipole moment, the force is attractive (Figure 2.4a). If two particles approach each other along the perpendicular direction of the dipole moment line, the force is repulsive (Figure 2.4b). The derivation of attractive interparticle magnetic forces by Pinto-Espinoza (2002) is shown in Appendix B.

Villers (1998) observed that when ferromagnetic particles were magnetized and fluidized in the presence of a homogeneous magnetic field, these particles trended to form a chain oriented along the magnetic field line (z-direction in this study). From his observations, we can conclude that the magnetic interparticle force in the direction of the magnetic field line is the most dominant magnetic interparticle force. The fully attractive interparticle magnetic force between two particles in the z-direction is derived as

$$f_{m,z} = \frac{-6(\chi V_p \mu_0 H_z)^2}{\mu_0} \left[ \frac{2\pi^2 r^5 + \chi V_p r^2}{(2\pi r^3 - \chi V_p)^3} \right] \quad (2-16)$$

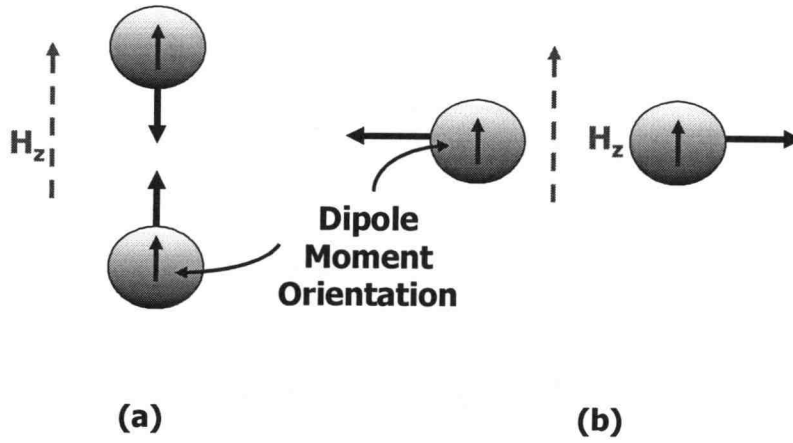


**Figure 2.4** Magnetic interparticle forces: a) attractive force when two Ferromagnetic particles approach along the dipole moment line, and b) repulsive force when two ferromagnetic particles approach perpendicular to the dipole moment line.

By differentiation of Equation (2-16) with respect to  $z$ , one obtains

$$\frac{df_{m,z}}{dz} = \frac{12(\chi V_p \mu_0 H_z)^2 \pi r (8\pi^2 r^6 + 12\pi r^3 \chi V_p + \chi^2 V_p^2)}{\mu_0 (-2\pi r^3 + \chi V_p)^4} \quad (2-17)$$

which is then inserted into Equation (2-15) to yield;

$$E = \frac{d_p}{A_p} \frac{12(\chi V_p \mu_0 H_z)^2 \pi r (8\pi^2 r^6 + 12\pi r^3 \chi V_p + \chi^2 V_p^2)}{\mu_0 (-2\pi r^3 + \chi V_p)^4} \quad (2-18)$$

The distance between two magnetic particles in adjacent layers, at distance  $r$ , can be derived as follows:

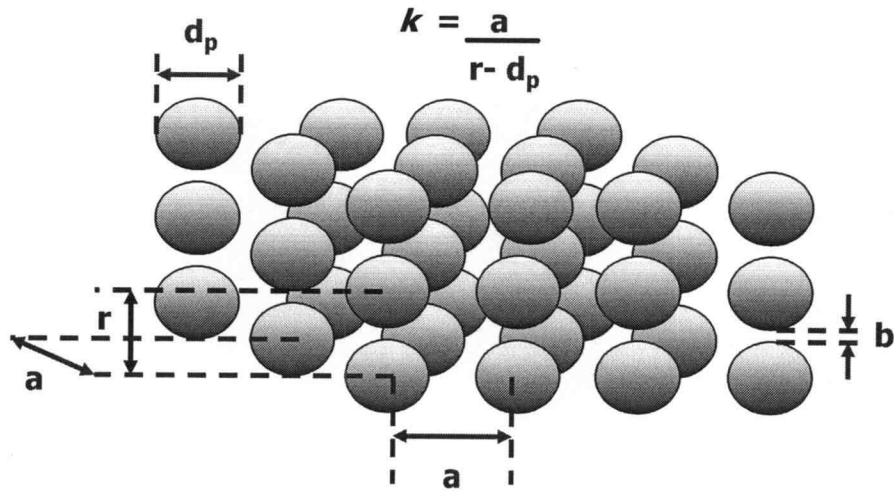


**Figure 2.5** Distance between two particles in adjacent layers.

From Figure 2.5, the volume occupied by solid particles in a cube is defined as

$$(1-\epsilon) = \frac{\text{particle volume}}{\text{total volume}} = \frac{\frac{1}{6} \pi d_p^3}{b \times a^2 + d_p \times a^2} \quad (2-19)$$

Define  $k$  as a distance ratio between two adjacent particles and two particle layers as shown in Figure 2.5.

$$k = \frac{a}{b} \quad (2-20)$$

Equation (2-19) can be rewritten as

$$(1-\varepsilon) = \frac{\frac{1}{6} \pi d_p^3}{k^2 b^3 + d_p k^2 b^2} \quad (2-21)$$

Assume that  $b \ll d_p$ , Equation (2-21) is reduced to

$$b = \frac{d_p}{k} \sqrt{\frac{\pi}{6(1-\varepsilon)}} \quad (2-22)$$

Therefore, the distance between two magnetic particles in adjacent layers can be obtained as;

$$r = d_p + b = d_p + \frac{d_p}{k} \sqrt{\frac{\pi}{6(1-\varepsilon)}} \quad (2-23)$$

The distance ratio,  $k$ , is obviously a function of bed voidage and to some degree depends upon the spatial order of particles. We suggest that the ratio of  $k$  is a function of voidage as follows:

$$k = \frac{m}{(\varepsilon - \varepsilon_0)^n} \quad (2-24)$$

Figure 2.6 demonstrates an example of the elastic modulus, Equation (2-18), found in our study.

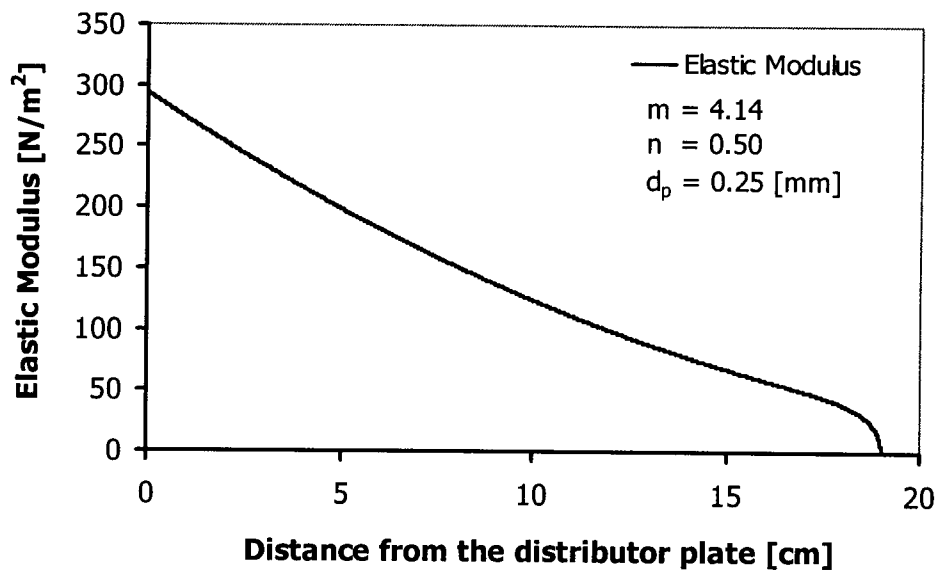


**Figure 2.6** Elastic modulus of particle A in the G-MAFB,  $dH_z/dz = -20,543 \text{ A/m/m}$ ,  $U_o = 0.0222 \text{ m/s}$ , and  $H_{bed} = 0.190 \text{ m}$ .

### 2.3 Magnetic Filtration Theory

The conversion of solid waste into useful resources in support of long-duration manned missions in space presents serious technological challenges. Several technologies, including supercritical water oxidation, microwave-powered combustion and fluidized bed incineration, have been tested for the conversion of solid waste. However, none of these technologies are compatible with microgravity or hypogravity operating conditions. In this study, the Gradient Magnetically

Assisted Fluidized Bed is proposed as a promising operating platform for fluidized bed operations in the space environment. Our experimental and theoretical work has evolved into both: a) the development of a theoretical model based on fundamental principles for the design of the G-MAFB, and b) the practical implementation of the G-MAFB in filtration and destruction of solid biomass waste particles from liquid streams. Figure 2.7 is a schematic representation of the pilot system for filtration and destruction of solid waste built at OSU during this project. Figure 2.8 is a photo of the same system shown schematically in Figure 2.7. Gasification of the solid waste with high temperature steam is beyond the scope of this thesis, although it is a part of this project and is currently under detailed investigation (NASA-NAG-9-1181).

### 2.3.1 Fundamentals of filtration in the G-MAFB

In this study, we used the G-MABF as a renewable filter to separate solid waste particles (wheat straw) from liquid waste streams. A schematic representation of the G-MAFB filtration process is shown in Figure 2.9. Filtration experiments are performed in two different experimental setups. Although these setups are different in size and details of operation, the nature of the filtration experiment is almost identical. For the modeling proposed, one can represent the experimental apparatus in the form depicted in Figure 2.10. The system boundary (I) represents the region of the experimental apparatus (including holding tank, pump and flow meter) where the only particles present are biomass waste.

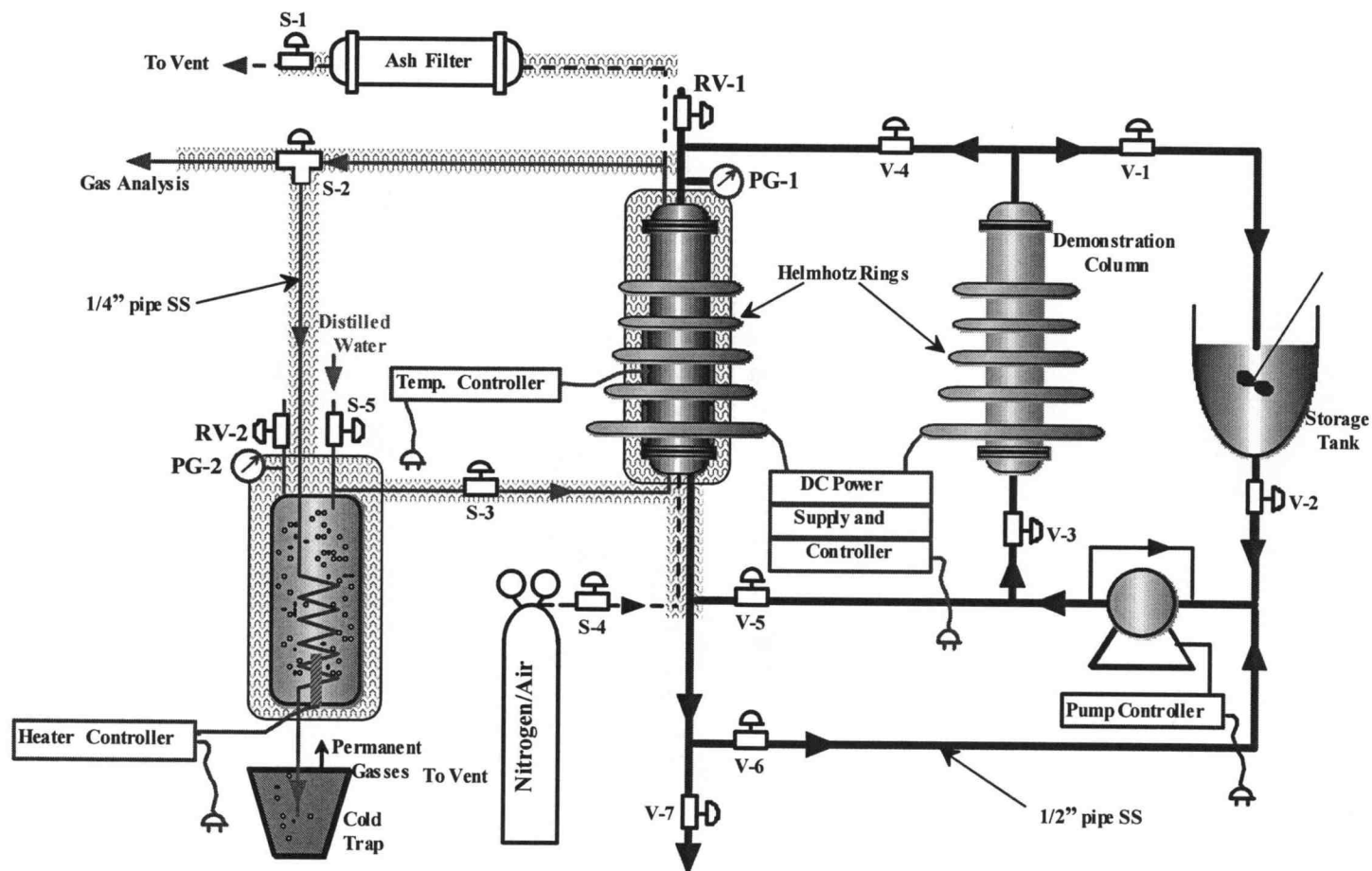


**Figure 2.7** Schematic representation of the pilot G-MAFB System.



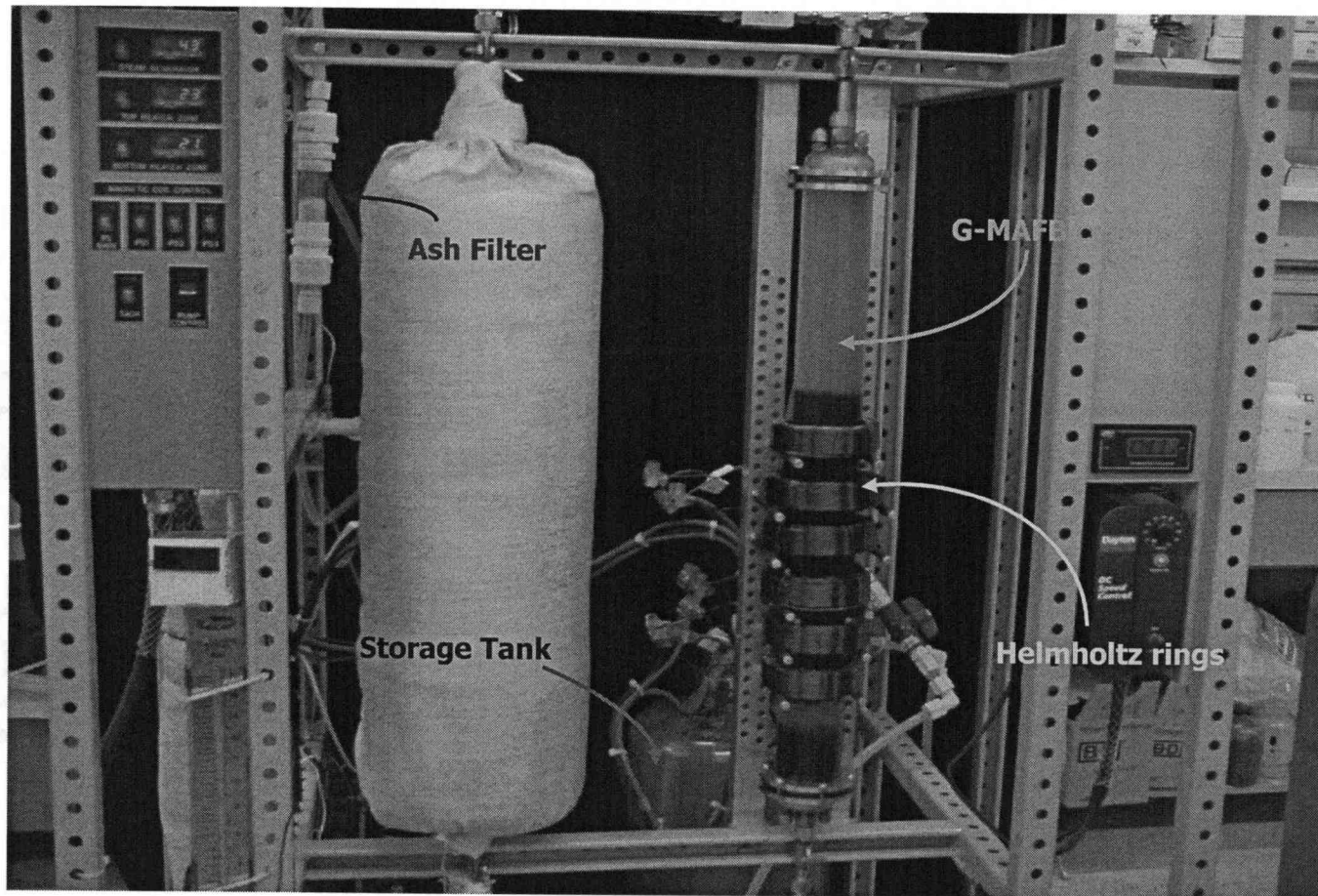


**Figure 2.8** G-MAFB pilot system for filtration and destruction of solid waste.

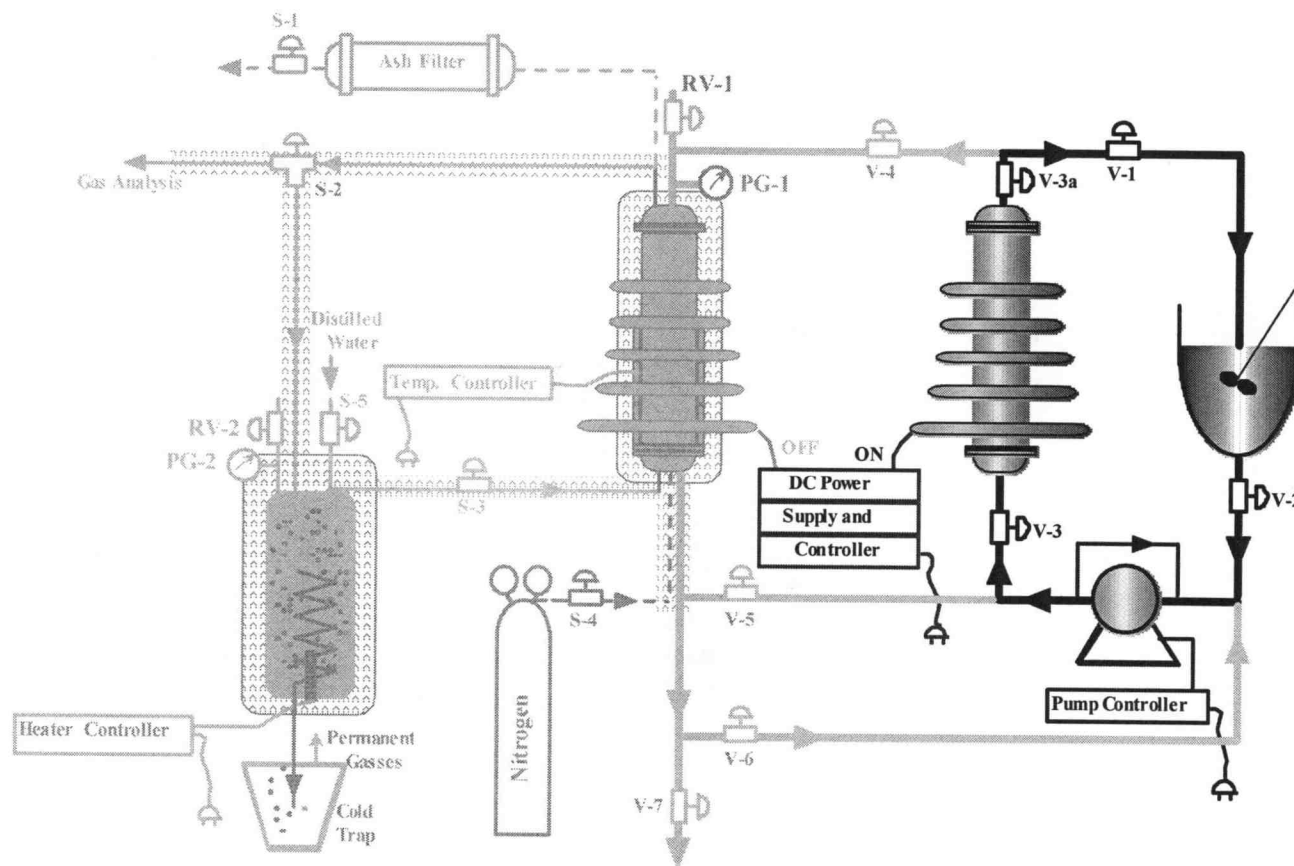


**Figure 2.9** Schematic representation of the G-MAFB for filtration experiment.

It is assumed that in this volume the fluid is very well mixed and hence the biomass concentration is uniform. System boundary (II) is the section of our system where the filtration process takes place.

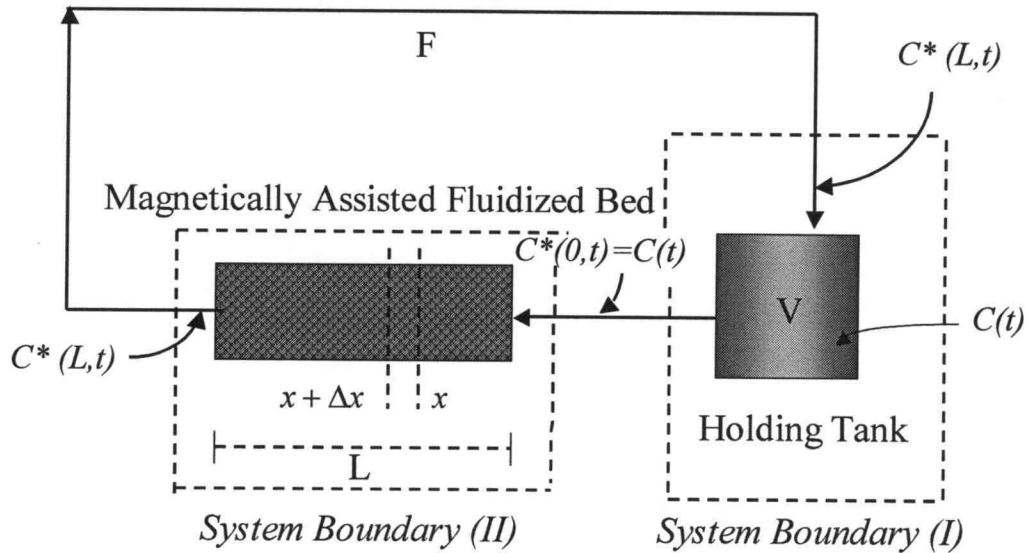


**Figure 2.10** Schematic diagram of the G-MAFB filtration system.

The material balance in both system boundaries can be written in the form of partial-differential equations in the axial symmetric filter bed as the followings;

$$\text{The holding tank: } FC^*(L,t) - FC^*(0,t) = V_{\text{tank}} \frac{\partial C^*(0,t)}{\partial t} \quad (2-25)$$

$$\text{Initial Conditions: } C^*(0,0) = C_0$$

The G-MAFB: 
$$-v \frac{\partial C^*(x,t)}{\partial x} - a' \frac{\partial \sigma}{\partial t} = \frac{\partial(\epsilon C^*(x,t))}{\partial t} \quad (2-26)$$

*Initial Conditions:*  $C^*(x,0) = 0; \quad t = 0, \quad 0 < x \leq L$

*Boundary Conditions:*  $C^*(0,t) = C(t); \quad x = 0, \quad t > 0$

$C^*(0,0) = C(0); \quad x = 0, \quad t = 0$

The rate of filtration: 
$$\frac{\partial \sigma}{\partial t} = \frac{k_1 C^*(x,t)}{a'} - k_2 \sigma \quad (2-27)$$

*Initial Conditions:*  $\sigma(x,0) = 0; \quad 0 \leq x \leq L$

$C^*(x,0) = 0; \quad t = 0, \quad 0 < x \leq L$

We postulate that the rate of filtration is a balance between two first order processes: 1) the rate of accumulation of waste particles in the bed, and 2) the rate of detachment of already accumulated particles from the bed. Both rates are assumed to be first order with respect to the respective concentrations of waste particles ( $C^*, \sigma$ ).

### 2.3.2 Filtration mechanisms

A fundamental study of a filtration process requires an analysis of possible filtration mechanisms. Such an analysis must include consideration of all the forces that operate between the waste particles and the collecting fluidization media. The primary mechanisms by which collection of waste particles (filtration)

may take place are: *Interception*, *Inertial Impaction*, *Brownian Diffusion*, and *Electrostatic Attraction*. These mechanisms are discussed in detailed reviews by Black (1966) and Tien (1989), and are briefly presented here.

### 1. Interception

Consider the case in which all the forces acting on the particle (relevant for the filtration mechanisms) in a fluid stream are negligible. Whenever the streamline along which the particle approaches a filter element passes within a distance of one-half the particle diameter from the element, interception of particle by the filter element will occur. The parameter that characterizes the importance of interception (Black, 1966) as a mechanism for particle deposition is  $N_R$ , defined as

$$N_R = \frac{D_p}{d_p} \quad (2-28)$$

The streamlines and particle trajectories approaching a filter medium are shown in Figure 2.11.

### 2. Inertial Impaction

The parameter that characterizes the importance of inertial impaction as a mechanism for particle deposition in the filter is the Stokes number  $N_{St}$ , defined as

$$N_{st} = \frac{\rho_{str} U_0 D_p^2}{18 \mu_f d_p} \quad (2-29)$$

This inertial impact parameter arises out of the force balance of fluid resistance opposing the motion of the particle.

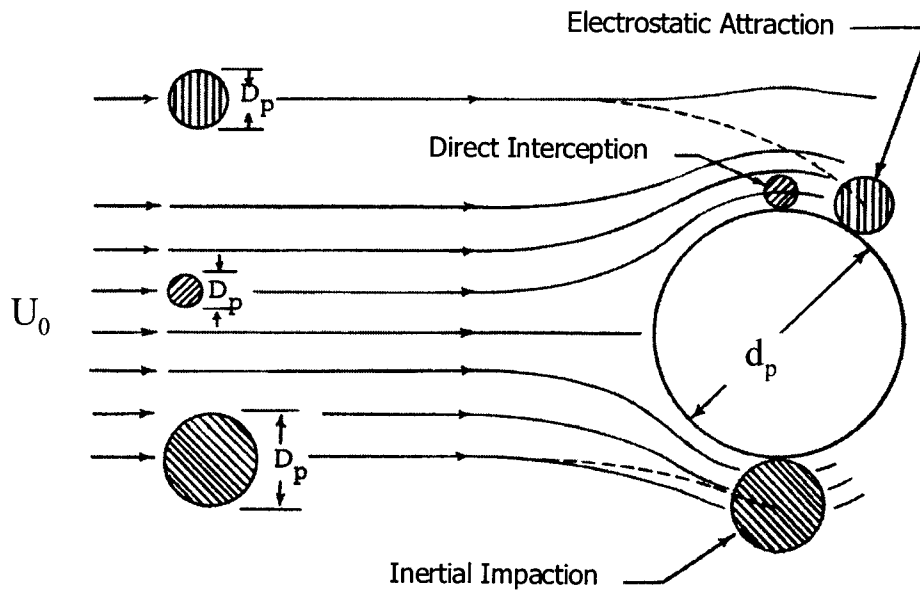


**Figure 2.11** Streamlines and particle trajectories approaching filter element (Black, 1966).

### 3. Brownian Diffusion

The Peclet number is used to characterize the importance of Brownian movement in a filtration process. It is defined as follows:

$$N_{Pe} = \frac{U_0 d_p}{D_{BM}} \quad (2-30)$$

The parameter  $N_{Pe}$  is the ratio of the fluid resistance to the diffusive force caused by random thermal motion.

#### 4. Electrostatic Attraction

If a particle and a filtration medium carry electrostatic charges, the filtration process may be influenced by the electrostatic force between the particles. Four typical types of electric force acting on particles moving toward a filter medium are presented as the following (Tien, 1989).

4.1 When both the particles and medium are charged, the Coulomb force can be attractive or repulsive, depending upon whether the particles and medium have like or unlike charges. The parameter that characterizes the Coulomb force is defined as:

$$K_{EC} = \frac{c_s Q_p Q_c}{3\pi^2 \epsilon_f d_p^2 D_p \mu_f U_0} \quad (2-31)$$

4.2 If the filter medium is charged, it may induce an image opposite charge on the surface of the particles. As a result, an additional electrostatic force on the particle is created. The parameter that characterizes the charged medium image force is defined as:

$$K_{EI} = \frac{2\gamma_p c_s Q_c^2 D_p^2}{3\pi^2 \epsilon_f d_p^5 \mu_f U_0} \quad (2-32)$$

$$\gamma_p = (\epsilon_p - \epsilon_f) / (\epsilon_p + 2\epsilon_f) \quad (2-33)$$

4.3 If the particles are charged, they may induce an image opposite charge on the filter medium. This causes an additional force on the particles. The parameter that characterizes the charged particle image force is defined as:

$$K_{EM} = \frac{\gamma_c c_s Q_p^2}{3\pi^2 \epsilon_f d_p^2 \mu_f U_0 D_p} \quad (2-34)$$

$$\gamma_c = (\epsilon_c - \epsilon_f) / (\epsilon_c + 2\epsilon_f) \quad (2-35)$$

4.4 The particles produce a repulsive force among themselves. This effect is known as the space charge effect. The parameter that characterizes the charge particle force is defined as:

$$K_{ES} = \frac{\gamma_c c_s Q_p^2 d_p C}{18\pi \epsilon_f \mu_f U_0 D_p} \quad (2-36)$$

Each mechanism mentioned above will contribute to removal efficiency of small particles in the fluidization media.



## **CHAPTER 3**

### **EXPERIMENTAL APPARATUS AND MATERIALS**

A typical schematic diagram of the experimental apparatus used in this study is shown in Figure 3.1. The experimental apparatus and materials consist of the following elements:

- 3.1 Fluidization Column
- 3.2 Magnetic Field Generator (Helmholtz rings)
- 3.3 Water Supply System
- 3.4 Instrumentation
- 3.5 Ferromagnetic Particles
- 3.6 Biomass Waste Particles

#### **3.1 Fluidization column**

There are three different types of fluidization column used in this study: a) a fluidization column for voidage distribution experiments (1g), b) a fluidization column for experiments on board the NASA KC-135 aircraft (0g), and c) a fluidization column for filtration experiments (1g).

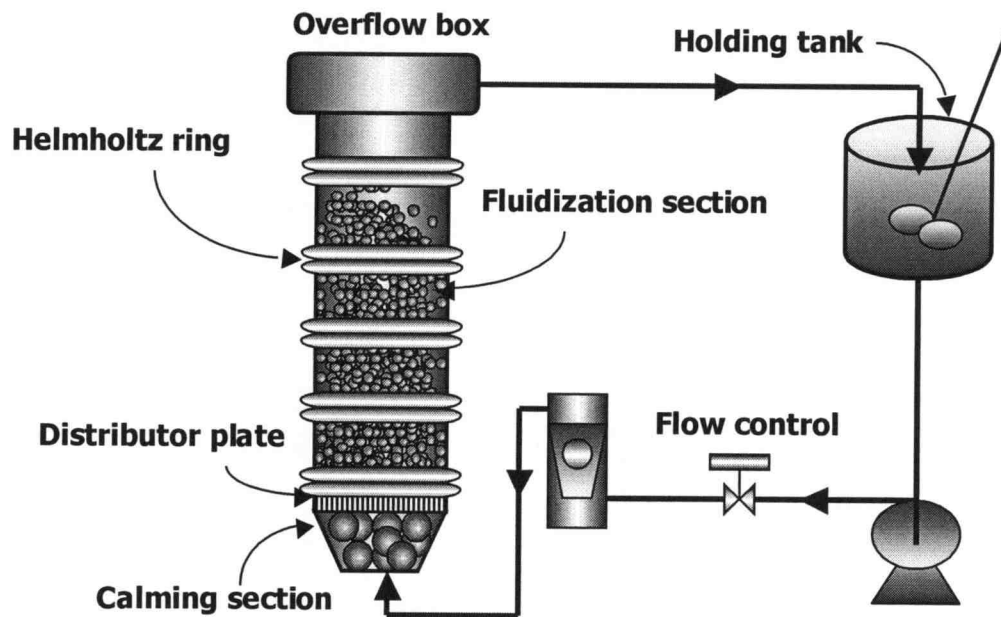


**Figure 3.1** Schematic representation of the experimental apparatus used in this study.

### 3.1.1 Fluidization column for voidage distribution experiments

The fluidization column in which the particles are fluidized is made of Plexiglas™, allowing for visual observation through the wall. The fluidization column is made of three removable parts: a) the fluidization section, b) the calming section, and c) the overflow box.

a) Fluidization section

This section is a 35.0 cm long cylindrical clear Plexiglas™ tube. It has an inside diameter of 4.5 cm and outside diameter of 5.1 cm. A circular distributor plate is located at the bottom of the fluidization section and it can be easily removed or repositioned to any location along the fluidization section. The distributor plate is responsible for evenly distributing the flow over the entire area of the column. A schematic representation and a photograph of the fluidization column are shown in Figure 3.2.

b) Calming section

This section is composed of 1.2 cm diameter marbles which fill the cylinder under the distributor plate. It provides a uniform upward flow of liquid to the fluidization section. This section is designed to dissipate large liquid jets which may form at the entrance of the fluidization apparatus. The calming and the fluidization sections are separated by the distributor plate, which is made of a 0.3 cm thick clear Plexiglas™ plate. The distributor plate is 4.5 cm in diameter, with one hundred and forty-six 2.0 mm uniformly distributed circular holes. The open area is approximately 30% of the total area of the distributor plate. A schematic representation and a photo of the distributor plate are shown in Figure 3.3.

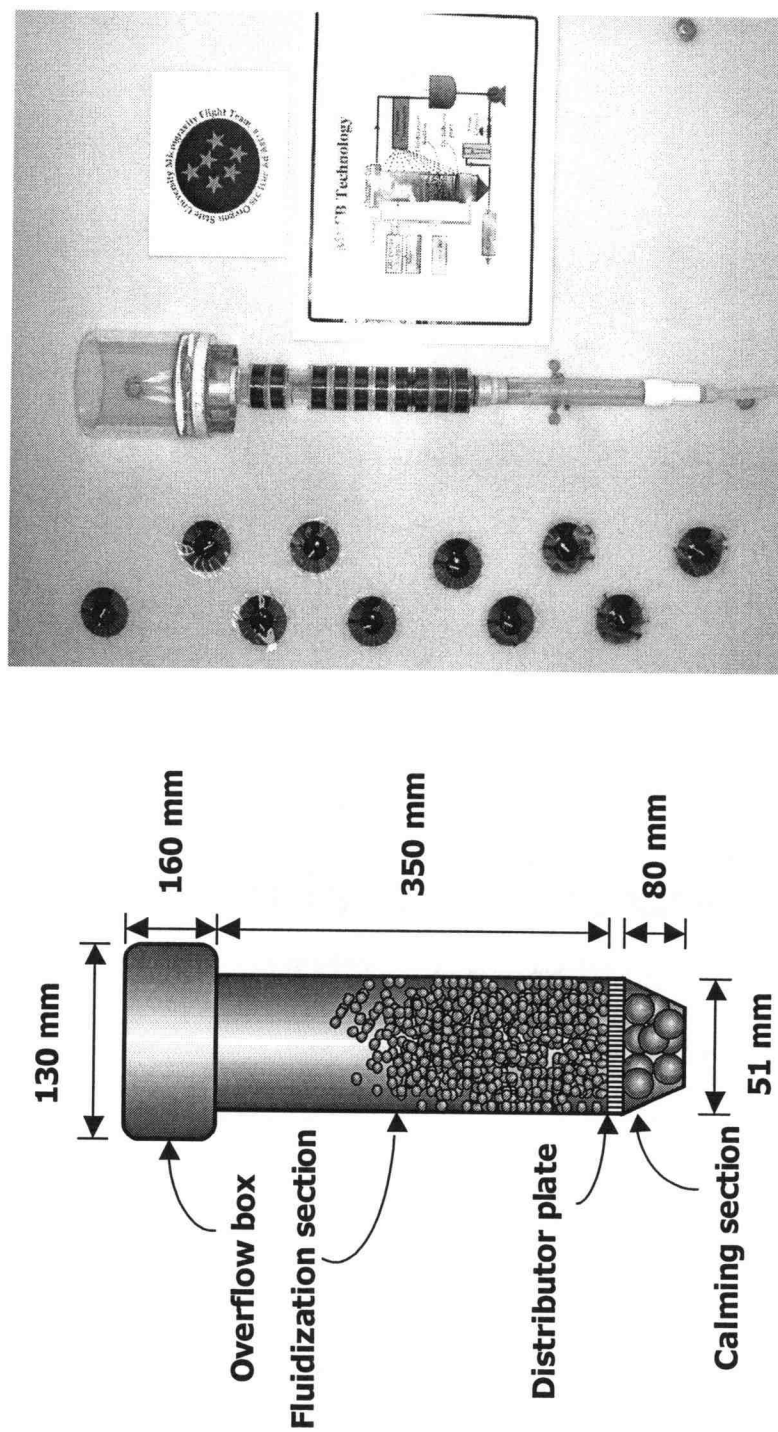


**Figure 3.2** Schematic diagram and photograph of the G-MAFB used in voidage distribution experiments.

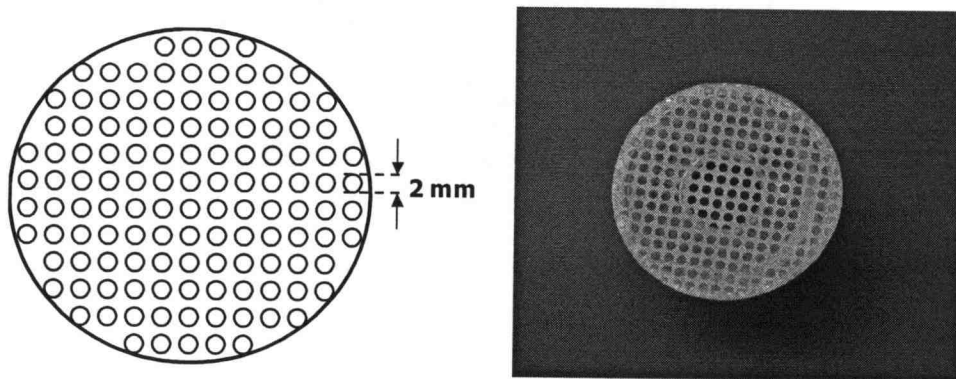


**Figure 3.3** Schematic diagram and photograph of the distributor plate used in voidage distribution experiments.

c) Overflow box

The overflow box is a cylinder 13.0 cm in diameter and 16.0 cm in height, mounted on the top of the fluidization section. The side outlet from the overflow box is covered with a plastic screen to prevent occasional extraneous particles from leaving the fluidization section, thus protecting the water recirculating system. The open surface of the fluid in the overflow box provides a "reference" 1.0 atm pressure in the system.

### 3.1.2 Fluidization column for experiments on board NASA's KC-135 aircraft

The schematic flow diagram of the G-MAFB apparatus used on board the NASA KC-135 aircraft (0g flight) is similar to the G-MAFB operated in the

laboratory (Figure 3.1). A notable difference is the shape of the fluidization column.

a) Fluidization section

The experiments in 0g are conducted in a two-dimensional, square cross-section, tapered fluidization column, as shown in Figure 3.4. The design of the fluidization column is unique and we could not find any previous references describing a similar apparatus. The tapered shape is introduced to provide additional stability for the fluidization process. The stability of the fluidization operation depends on the local intensity of drag and magnetic forces. The tapered shape of the column relates with both forces. Namely, at the bottom of the column, the magnetic force is highest and the smallest cross-sectional area of the column makes the drag force highest as well. Both drag and magnetic forces decrease as the height of the column increases.

b) Calming section

This section is composed of small marbles enclosed in the small rectangular volume under the distributor plate. The calming and the fluidization sections are separated by the distributor plate, which is made of a 0.3 cm thick, 3.0 cm by 5.0 cm, clear Plexiglas™ plate covered with a fabric mesh to provide a uniform upward flow of the liquid stream to the fluidization section.

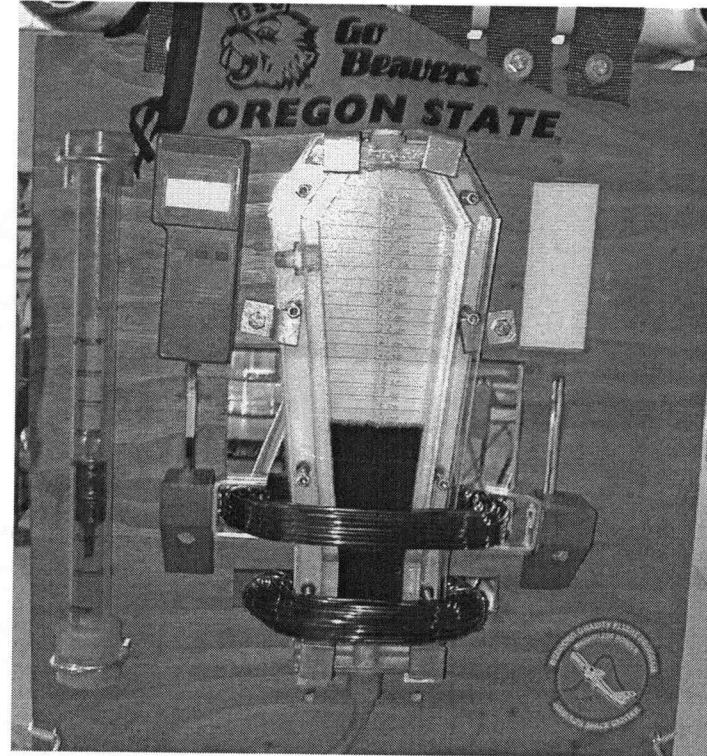
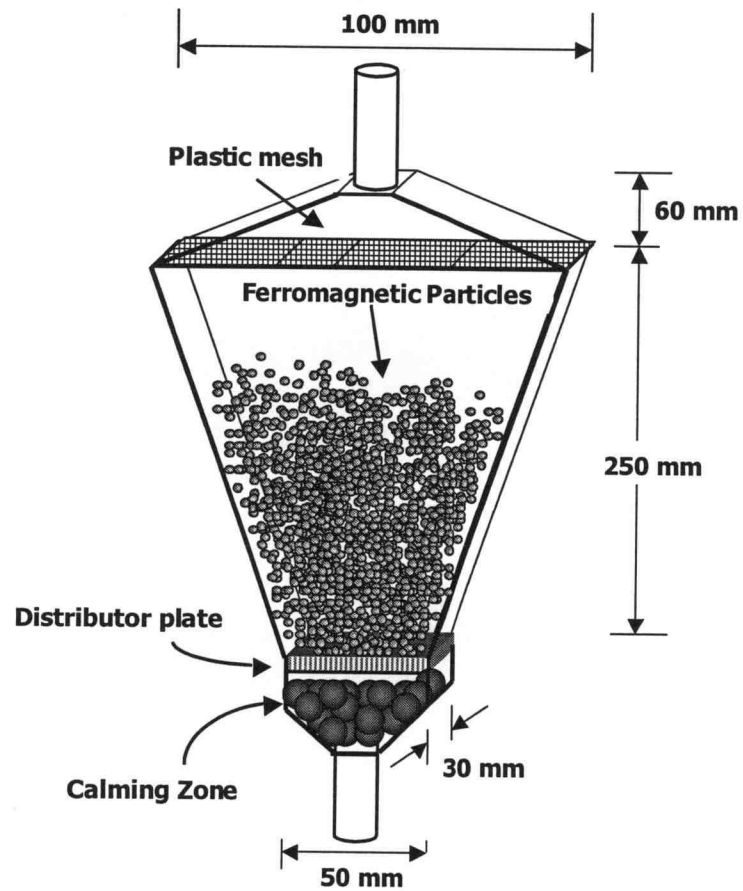


**Figure 3.4** Schematic diagram and photograph of G-MAFB used on board NASA's KC-135 aircraft.

c) Expansion chamber

In the experimental set up used in 0g experiments, the role of the overflow box is replaced with an expansion chamber. A small balloon is enclosed inside a closed container, providing a reference pressure to the system.

### 3.1.3 Fluidization column for filtration experiments

The filtration experiments are conducted in a closed recirculating G-MAFB system with a constant magnetic field gradient. During the filtration process, the bed is kept in a packed condition and biomass waste particles are deposited in the void spaces among the ferromagnetic particles. Some parts of the G-MAFB system used in voidage distribution experiments are replaced with newer components as follows:

a) Fluidization column

The apparatus used for laboratory filtration experiments is a cylindrical bed. The fluidization column is made of polycarbonate, allowing visual observation through the wall. The column has an inside diameter of 5.0 cm and an outside diameter of 5.8 cm. A schematic diagram of the fluidization column is shown in Figure 3.5.



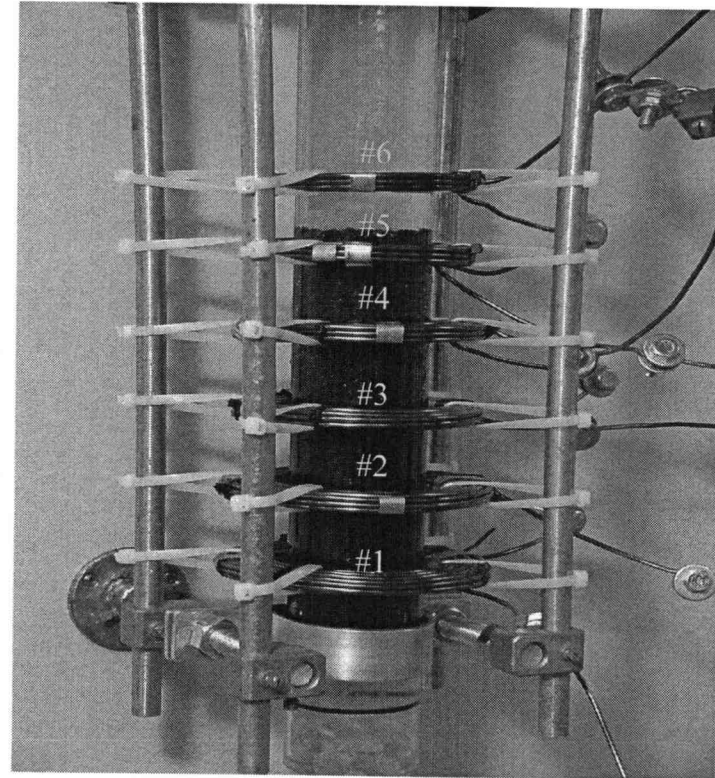
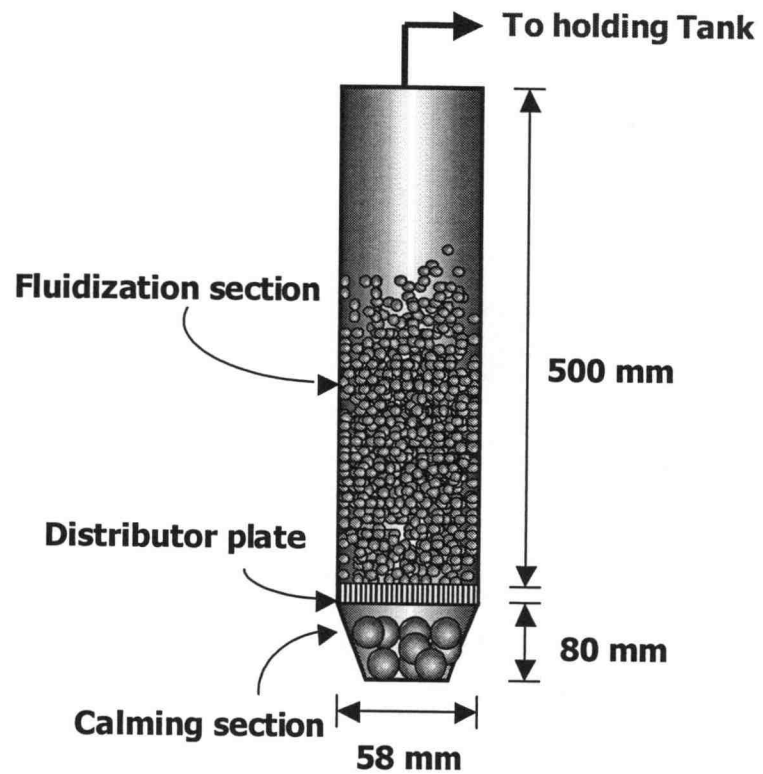


**Figure 3.5** Schematic diagram and photograph of the G-MAFB used in filtration experiments.

b) Calming section

This section is composed of small marbles enclosed in a small cylinder under the distributor plate. The distributor plate is made of 7-Mesh Plastic Canvas manufactured by Quick-Count®. The distributor plate has one hundred and forty-six, 2.0 by 2.0 mm uniformly distributed square holes. This hole size is chosen to prevent undesired biomass particle deposition on the distributor plate. A schematic representation and a photo of the distributor plate are shown in Figure 3.6.

c) Overflow box

In this experimental set up, an 8-liter Plexiglas™ holding tank is open to the atmosphere and acts as an overflow box to provide a reference pressure to the system.

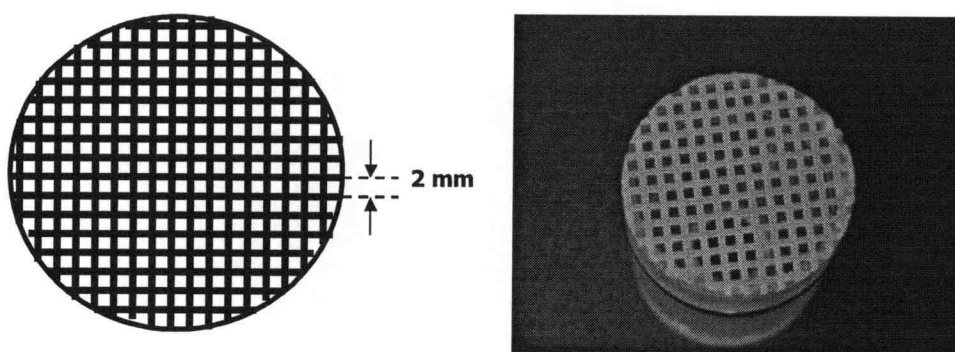


**Figure 3.6** Schematic diagram and photograph of the distributor plate used in filtration experiments.

### **3.2 Magnetic field generator (Helmholtz ring)**

#### **3.2.1 Magnetic field generator for voidage distribution experiments**

An Acme Electric Corporation™ Model AQA 5-220 direct current (DC) power supply is connected with ten parallel Helmholtz rings and ten rheostats. This DC power supply has an AC input of 230 volts. It can provide 0-5 volts and up to 220 amps of current to the system. The output voltage is manually controlled by a voltage control knob. Each Helmholtz ring is made of a copper wire manufactured by MWS™. The nominal wire diameter is 1.0 mm. This copper wire is coated with a polyester-imide resin that withstands temperatures up to 180 °C. Each Helmholtz ring consists of two 10 turn layers of copper wire, which are fixed around a 2.5 cm long, 5.1 cm outside diameter Plexiglas™ ring (Figure 3.2). The Helmholtz ring can be positioned at any axial location along the fluidization column. The magnetic field orientation is parallel to the direction of fluid flow.

The rheostats, connected in series with the Helmholtz rings, are used to control the current in each Helmholtz ring. Each rheostat can be maintained at 0-0.5 Ohms and manually controlled by adjusting a control knob. The calibration of rheostat resistance is given in Appendix E. The overall magnetic field intensity within the fluidized bed is the summation of the magnetic field intensities generated from each Helmholtz ring. The magnetic field intensity is strongest at the bottom of the bed, and decreases gradually linearly toward the top of the bed. This change in the magnetic field strength along the fluidization column varies the

magnitude of the magnetic force from the bottom to the top of the column. As a result, the particle holdup at any location varies along the column reflecting the equilibrium of forces. In this study, a constant magnetic field gradient ( $dH/dz = \text{constant}$ ) is produced by adjusting the currents and the spacing between the ten Helmholtz rings. The magnetic field intensity inside the fluidized bed is measured directly using a gaussmeter (see section 3.4.2).

### 3.2.2 Magnetic field generator for experiments on board NASA's KC-135 aircraft

Two short rectangular solenoid coils are used in this experiment. All coils are made of copper wire gauge 10 (HAPT) manufactured by MWS<sup>™</sup>. The diameter of the copper wire is 2.7 mm. The first solenoid coil has dimensions of 10.0 cm by 15.0 cm and the second has dimensions of 10.0 cm by 20.0 cm (Figure 3.4). Both coils have six layers with five turns of wire per layer. The bottom of the fluidization column is located between two solenoid coils where the magnetic field intensity is the highest.

### 3.2.3 Magnetic field generator for filtration experiments

The magnetic field generator is composed of three direct current (DC) power supplies (Sorensen<sup>™</sup> Model DCS8-125E) connected to six parallel Helmholtz rings (Solenoid). Each power supply has an AC input of 115 volts and a maximum current load of 20 amps. The DC output may be varied between 0-8 volts with a

current load between 0-125 amps. The Helmholtz rings are made of a copper wire gauge 10 (HAPT) manufactured by MWS™. The diameter of the copper wire is 2.7 mm. The Helmholtz rings can be positioned at any point along the fluidization column to obtain a desired magnetic field gradient. The overall magnetic field intensity within the fluidized bed is the summation of the magnetic field intensities generated from each Helmholtz ring. A photograph of these Helmholtz rings is found in Figure 3.5. The Helmholtz ring dimensions are list in Table 3.1

**Table 3.1** Helmholtz ring dimensions

Helmholtz ring number	# turns	# Layers
1	8	3
2	7	3
3	6	3
4	5	3
5	4	3
6	3	3

### 3.3 Water supply system

#### 3.3.1 Water supply system for voidage distribution experiments

Water circulation is driven by a 1/3 Hp, 2600/3000 rpm centrifugal pump (Little Giant Pump Co™ Model 4-MD-SC). The pump discharge is connected to a flow rotameter, Gilmont Instrument™ Model E-2448, and it is directed to the

fluidization column. The fluid flow is regulated by a valve mounted upstream of the rotameter. The calibration of the superficial fluid velocity,  $U_o$ , corresponding to a rotameter reading is given in Appendix E. A 15-liter holding tank containing deionized water ( $\text{pH} \approx 7.0$ ) is used in the G-MAFB water supply system. The water is periodically replaced to reduce ablation and fungal growth.

### 3.3.2 Water supply system for experiments on board NASA's KC-135 aircraft

Water circulation is driven by a 1/40 Hp, 3000 rpm centrifugal pump (MARCH MFG™ Model AC-2CP-MD). A special innovative flow rotameter (developed at OSU) is used to measure the liquid flow rate in the absence of gravity. The plastic bar inside the rotameter is replaced with a neutrally buoyant magnetic bar. A ring of permanent magnet is located at the top of the flow meter, positioned coaxially in such a way that it creates a normal repulsive magnetic force acting on the float, thus pushing the magnetic bar away from the top of the flow meter. As the liquid flow rate increases, the ball will move closer to the top of the flow meter. The calibration of this unique flow-measuring instrument is given in Appendix E.

### 3.3.3 Water supply system for filtration experiments

Water circulation is driven by a 1/8 Hp, 3000 rpm centrifugal pump (MARCH MFG™ Model TE-5C-MD). The pump discharge is connected to a flow

rotameter (Gilmont Instrument™, Model E-2448), and it is directed to the fluidization column. The fluid flow is regulated by a valve, mounted downstream of the rotameter. The calibration of the superficial fluid velocity,  $U_o$ , corresponding to a rotameter reading is given in Appendix E. An 8-liter Plexiglas™ holding tank containing deionized water (pH  $\approx$  7) is used in the G-MAFB water supply system.

### **3.4 Instrumentation**

System instrumentation consists of the dynamic pressure measuring system, gaussemeter, particle concentration detector, and stirrer plate. The details of this equipment are as follows:

#### **3.4.1 Dynamic pressure measuring system**

The pressure measuring system consists of a water filled clear glass tube connected to an aluminum probe. The glass tube has an internal diameter of 2.0 mm. The aluminum probe is 1.0 mm in diameter and 80.0 cm in length. The aluminum probe is inserted into the fluidized column and is used to measure the pressure every 0.5 centimeter from the bottom of the bed. The pressure values obtained from this measurement are called the dynamic pressures. The water level shown in the inclined glass tube indicates the dynamic pressure at the given

location in the bed. The distance in the  $z$  direction is obtained by the following equation:

$$\Delta z = \Delta x \tan \theta \quad (3-1)$$

A schematic representation of this inclined manometer is shown in Figure 3.7.

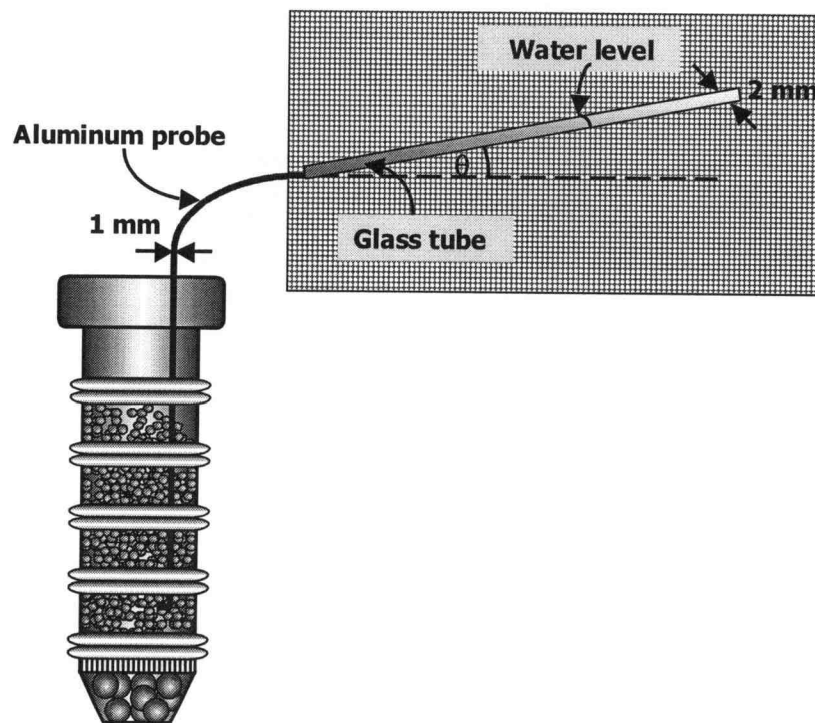


**Figure 3.7** Schematic representation of the inclined manometer.

### 3.4.2 Gaussmeter

The magnetic field intensity inside the fluidized bed is measured directly using a gaussmeter (Lake Shore Cryotronics, Inc. Model 410 gaussmeter). It is a



hand-held, field-portable unit that provides measurement of AC or DC magnetic fields. The two main parts of the gaussmeter are the gaussmeter and the axial probe. The axial probe (Cal No. 897) is connected directly to the gaussmeter unit by a probe extension cable, which allows the probe to be extended three meters from the unit. The important specifications of gaussmeter are listed in Table 3.2.

**Table 3.2** Specifications of the gaussmeter

<b>Display</b>	LCD, 3 ½ digits
<b>Resolution</b>	0.1 gauss (200 gauss range)
<b>Range</b>	2T, 200 mT, 20 mT
<b>DC Accuracy</b>	2% of reading (at 25 °C)
<b>Frequency Response</b>	DC and 20 Hz to 20 kHz
<b>Temperature Range</b>	0 to 50 °C

#### 3.4.3 Particle concentration detector

A laser-photodiode detector is used for measuring the concentration of biomass waste particles in the holding tank. The laser module is manufactured by RadioShack®; the specifications are listed Table 3.3. The photodiode is supplied by RS Component Limited. A schematic diagram of the laser-photodiode detector is shown in Figure 3.8. The biomass waste concentration is measured by recording a voltage signal response from the photodiode which is inversely proportional to the density of solid waste particles traversed by the laser beam. The calibration curve of concentration and voltage response is shown in Appendix

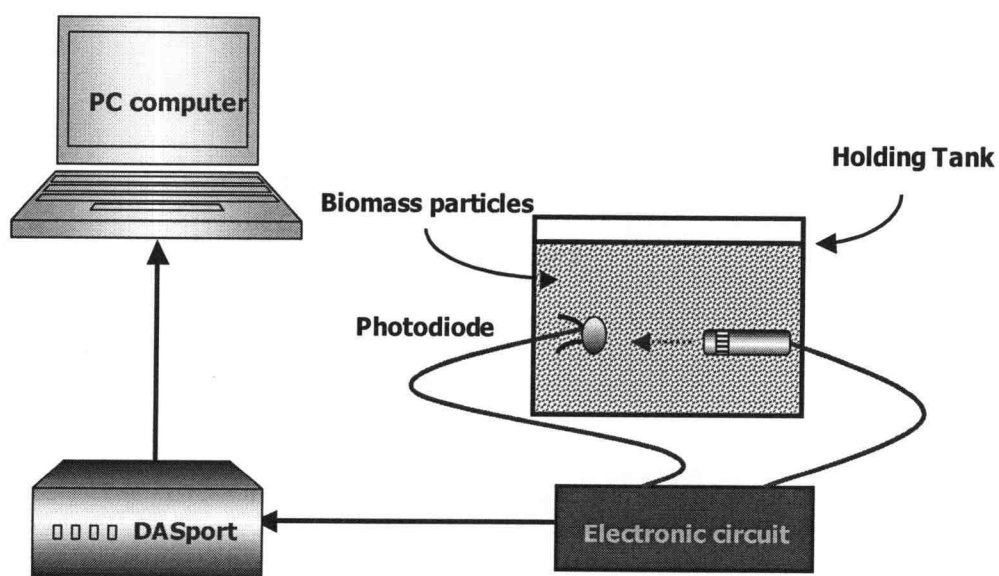
E. The voltage signal is sent to the DASport parallel port interface multifunction data acquisition system (Intelligent Instrument™ Model PCI-20450P Series). At this data acquisition port, the voltage signal is sent to the computer and displayed on the screen using Visual Designer® Software.

The DASport acquisition system is a portable data acquisition card that communicates with a PC through a Standard, Enhanced or Extended (PS/2 type) parallel port interface. The analog input channels can be selected as 16 single-ended or 8 differential analog input channels. The DASport card can receive analog input signals in either a 0-10 V or  $\pm 10$  V range and the analog output is in the  $\pm 10$  V range.

The Visual Designer® Software is a very useful program for analyzing the data obtained from our filtration experiments. This software is constructed based on a block diagram structure. It allows the user to design or customize the data acquisition, analysis, display and control program to meet the specific needs. A block diagram called *FlowGram* is built and saved. *FlowCode* is created just before the program is executed by the *Run* command. A schematic diagram of the operation of Visual Designer® software (Intelligent Instrument™, 1993) is shown in Figure 3.9. The *FlowGram* for biomass concentration measurement is given in Figure 3.10. The details of *FlowGram* used in this study are presented in Appendix H.

**Table 3.3** Specifications of the laser module

<b>Wavelength</b>	650 nm
<b>Current</b>	60 mA max
<b>Laser class</b>	Class II (FDA regulation)
<b>Focus</b>	Fixed
<b>Pattern</b>	6 mm point (at 3 m distance)
<b>Lens</b>	Single plastic collimated
<b>Optical power</b>	< 1 mW at 3V DC

**Figure 3.8** Schematic diagram of the laser-photodiode detector.

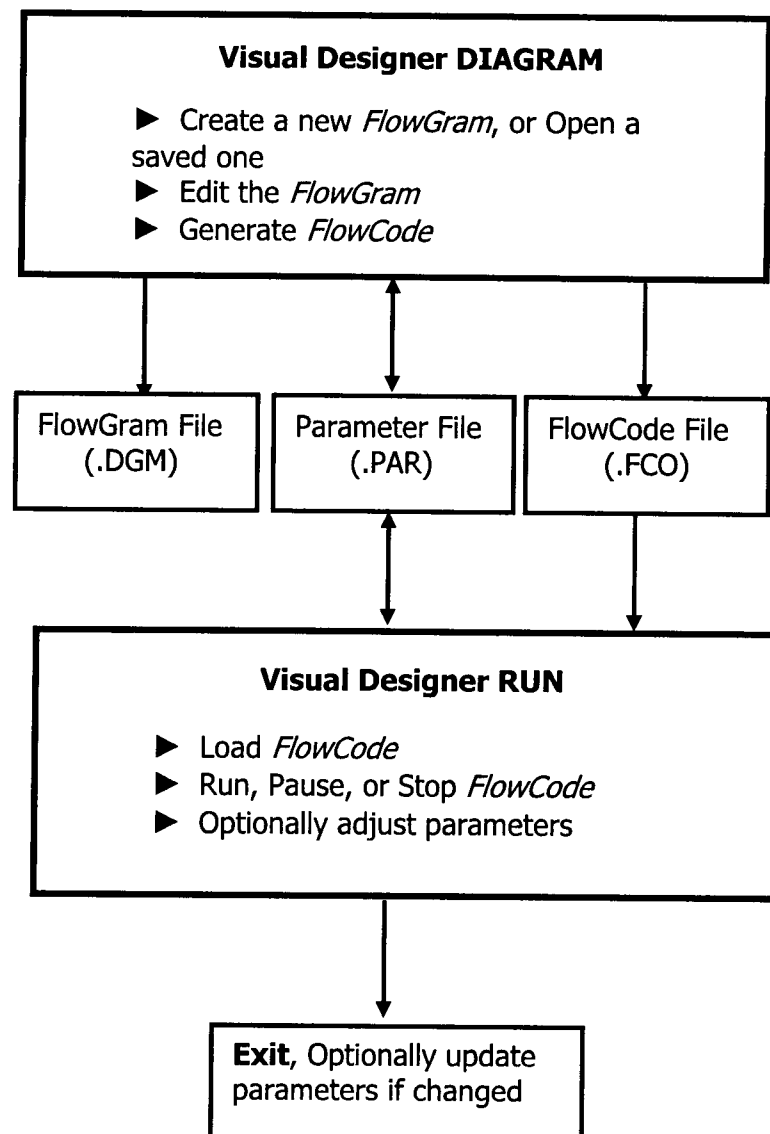


**Figure 3.9** Visual Designer system block diagram.

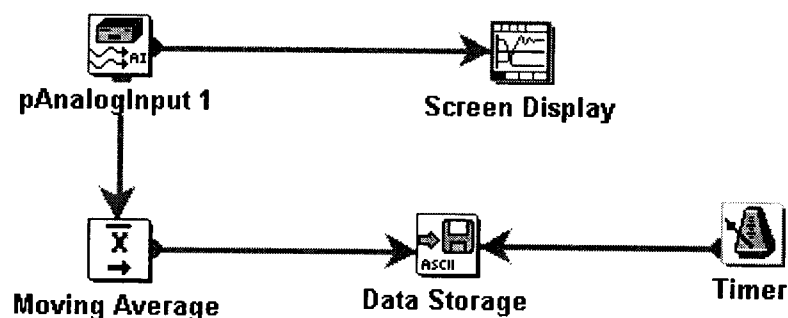


**Figure 3.10** Visual Designer *FlowGram* used in filtration experiments.

#### 3.4.4 Stirrer plate

A magnetic stirrer plate with a magnetic stir bar is placed under the holding tank to prevent biomass particles from settling and keep the uniform particle concentration in the holding tank.

### 3.5 Ferromagnetic particles

Ferromagnetic particles are one of the most important components in our studies. Ferromagnetic particles are produced from sodium alginate solution, ferromagnetic powder, microsphere balloons (sodium borosilicate), and Gellan gum. A schematic diagram of the particle generator and a ferromagnetic particle

is shown in Figure 3.11. Figure 3.12 shows a photograph of the particle generation equipment used in this study.

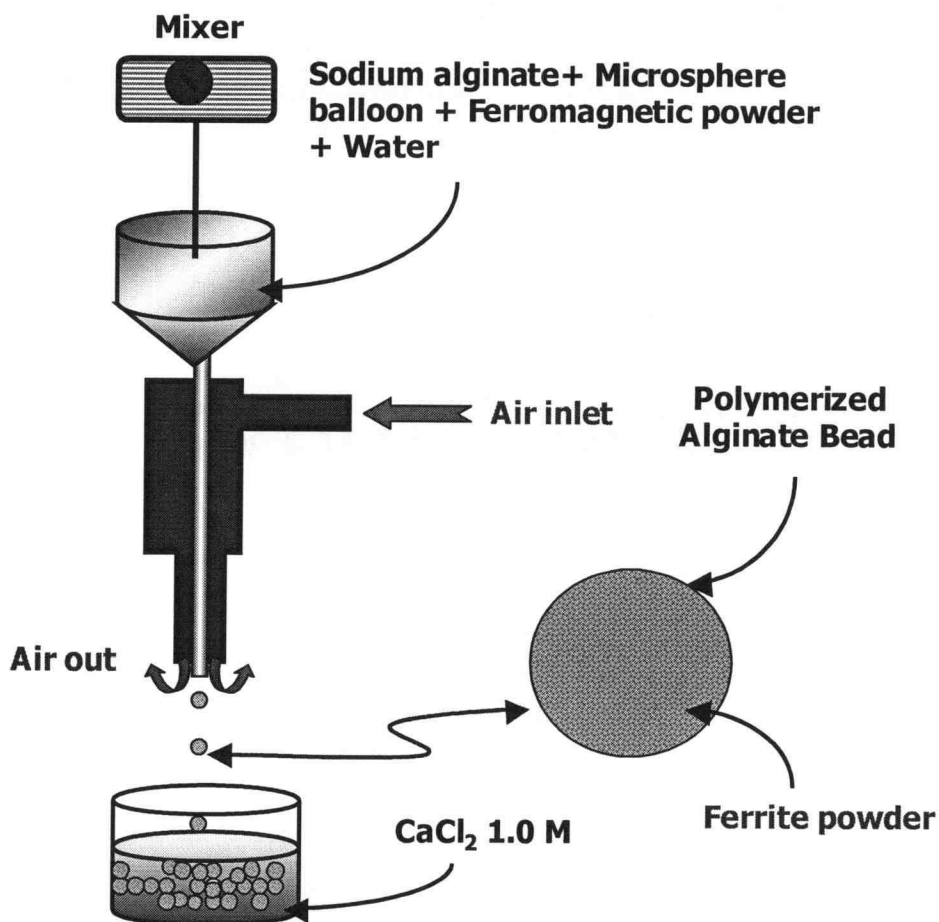


**Figure 3.11** Schematic diagram of the particle generator.

The following is the description of the ferromagnetic sodium alginate mixture suspension, the particle generator, and calcium chloride cross-linking, used in our experiments.

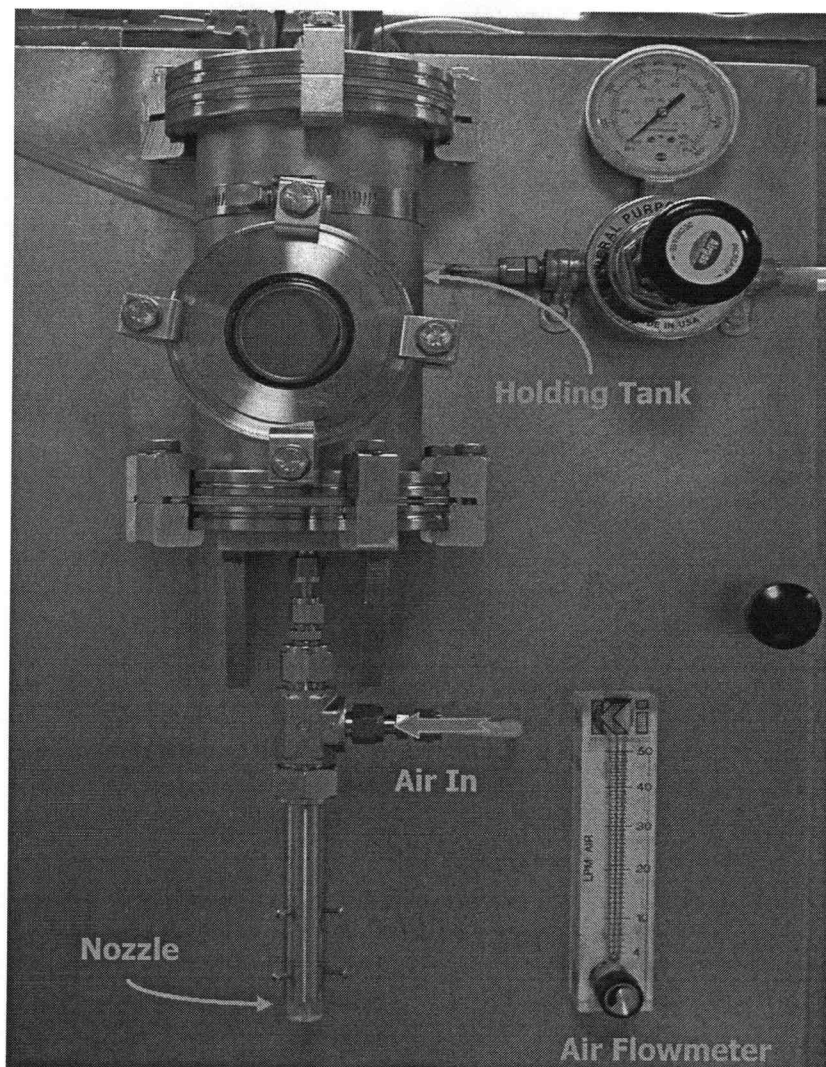


**Figure 3.12** Photo of the particle generation apparatus.

### 3.5.1 Ferromagnetic sodium alginate mixture suspension

1.75% wt sodium alginate solution is prepared beforehand. The ferromagnetic powder and microsphere balloons are then added to the solution,

respectively. The preparation of the ferro-sodium alginate mixture is described in Appendix C. The compositions and properties of ferromagnetic powder and microsphere balloons are given in Appendix D.

### 3.5.2 Ferromagnetic particle generator

The particle generator consists of a nozzle, which is connected to the bottom of a steel column. When the ferromagnetic alginate mixture is poured at the top of the column, it slowly flows through the nozzle and finally drops into a 1.0 M calcium chloride solution. The particle size can be adjusted by regulating the air pressure at the top of the column, and the airflow at the tip of the nozzle, which shears off the particles. The stirrer is mounted on top of the steel column and is connect to a variable speed motor (Ika Labortechnik™, Model RW20 DZM.n). The ferromagnetic alginate mixture is continuously stirred to avoid the sedimentation of ferromagnetic powder during the particle generation process.

### 3.5.3 Calcium chloride cross-linking solution

A 1.0 M calcium chloride solution is used to cross-link the ferromagnetic sodium alginate droplets coming out from the tip of the nozzle. Calcium chloride immediately reacts with sodium alginate, and forms calcium alginate on the surface of the droplets. The gel formation reaction is represented by:

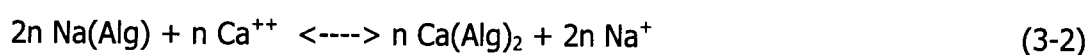
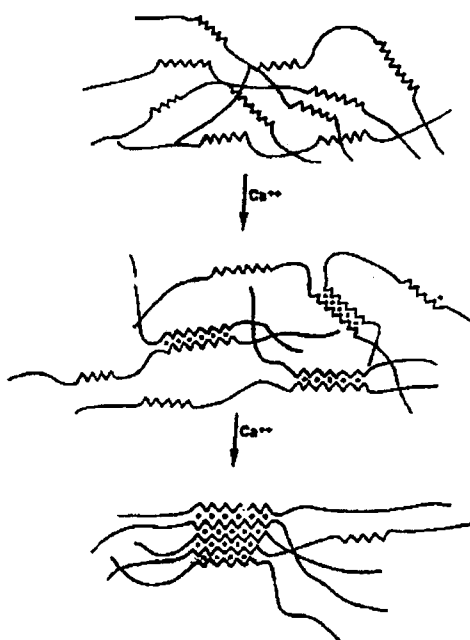




Figure 3.13 shows a model of gel formation in alginates. At the beginning, only the surface of the Sodium Alginate droplet reacts with the calcium ions. When the droplet is left in the calcium chloride solution over a period of time, calcium ions diffuse toward the center of the bead, and form a complete calcium alginate gel structure throughout the droplet. The particles are briefly rinsed with deionized water, and stored in a low concentration calcium chloride solution at room temperature.



**Figure 3.13** Schematic model for gel formation in alginates.

The properties of the ferromagnetic particles used in our studies are listed in Table 3.4. Particles A and B are used in voidage distribution experiments, particles C and D are used in experiments onboard the NASA KC-135 aircraft, and particles E and F are used in filtration experiments. The magnetic susceptibility of

ferromagnetic powder is measured separately by a custom-modified Thermalgravimetric Analysis (TGA) apparatus (TA Instruments™ Model 2950). A schematic diagram of the magnetic susceptibility measurement system is shown in Figure 3.14.

**Table 3.4** Ferromagnetic particle properties

Particle	A	B	C	D	E	F
<b>Diameter [mm]</b>	2.16	2.5	2.4	1.5	2.5	3.5
<b>Density [kg/m<sup>3</sup>]</b>	1119	1302	1502	1090	1351	1351
<b>Ferrite [w/w]</b>	20%	20%	30%	20%	35%	35%
<b>Microsphere balloon [w/w]</b>	8%	2%	0%	9%	3.5%	3.5%
<b>Gellan Gum [w/w]</b>	0%	0%	0%	0%	0.3%	0.3%
<b>1.75% Alginate solution [w/w]</b>	72%	78%	70%	71%	61.2%	61.2%
<b>Minimum fluidization velocity <math>U_{mf}</math> [m/s]</b>	0.0042	0.0110	0.0151	0.0017	0.0123	0.0174
<b>Magnetic susceptibility <math>\chi_r</math> [/]</b>	2.79	3.12	5.21	2.75	5.80	5.80

In this magnetic susceptibility measurement setup, a single solenoid is placed underneath a small ceramic canister that contains ferromagnetic particles. The solenoid creates a magnetic field gradient that results in a magnetic force acting on the ferromagnetic particles toward the center of the coil. The magnitude of magnetic force is equal to the change of the particle apparent weight. The details of the magnetic susceptibility measurement procedure and susceptibility calculations are shown in Appendix G. Figure 3.15 shows the custom-modified TGA setup.

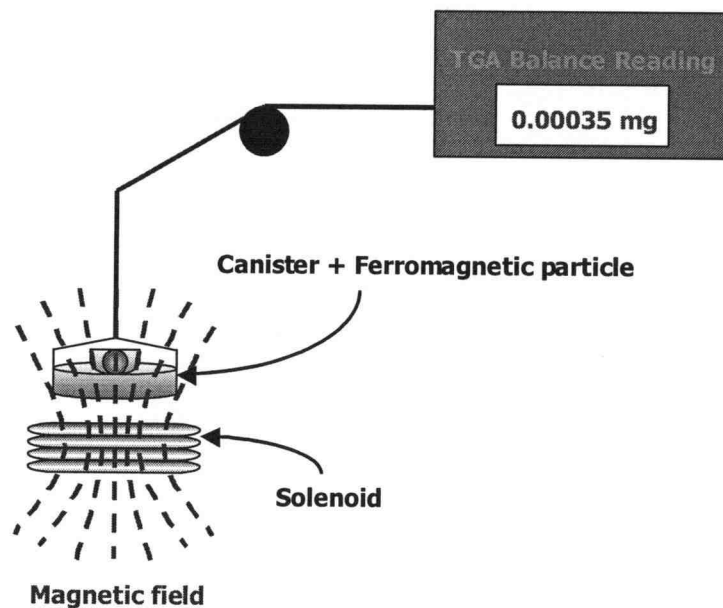


**Figure 3.14** Schematic representation of the magnetic susceptibility measurement device.

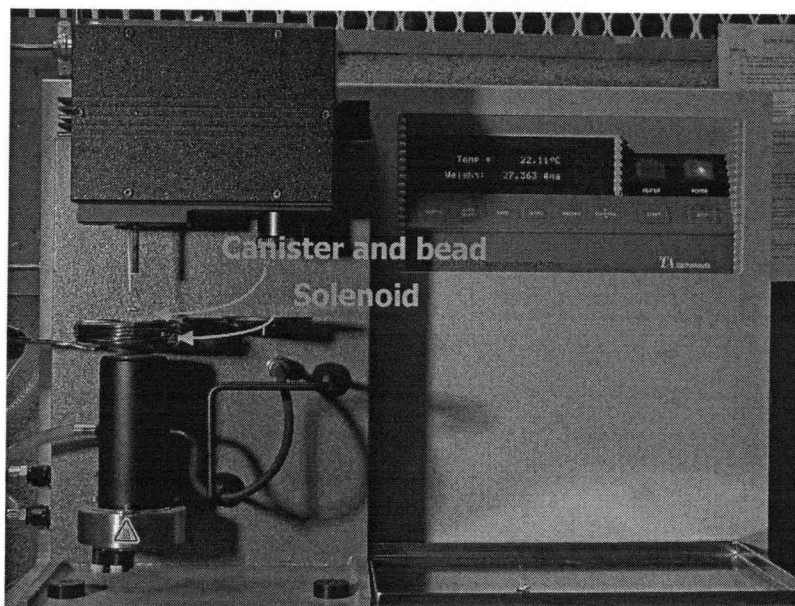


**Figure 3.15** Modified TGA setup for susceptibility measurements (photo by Pinto-Espinoza, 2002).

### 3.6 Biomass waste particles

Two different size ranges of biomass waste particles (wheat straw particles) are used in the filtration experiments. The smaller biomass particles (batch #1) are the particles which pass through a 180  $\mu\text{m}$  standard sieve size and are retained on a 149  $\mu\text{m}$  standard sieve size. The larger biomass particles (batch #2) are the particles with diameters between 180  $\mu\text{m}$  and 295  $\mu\text{m}$  standard sieve sizes. The concentration of biomass particles in the holding tank is monitored online using a laser-photodiode detector (section 3.4.3). The biomass particles have a cylindrical shape with different lengths. Figure 3.14 shows the typical shape of wheat straw particles. The density of dry wheat straw is 261.9  $\text{kg/m}^3$  and the density of suspended wheat straw is 1089.6  $\text{kg/m}^3$ . Because of the long-thin fiber shape of biomass particles, three different size measurement methods are proposed as follows;

#### 3.6.1 Intermediate size screen analysis

When particles settle between two adjacent standard sieve sizes, a screen size diameter can be calculated as;

$$d_{scr} = \frac{(d_{upper-sieve} + d_{lower-sieve})}{2} \quad (3-3)$$

Therefore, the smaller biomass particles that are held between 149  $\mu\text{m}$  and 180  $\mu\text{m}$  standard sieve sizes have the screen size diameter of 164.5  $\mu\text{m}$ . The bigger

biomass particles between 180  $\mu\text{m}$  and 295  $\mu\text{m}$  standard sieve sizes have a screen size diameter of 237.5  $\mu\text{m}$ .

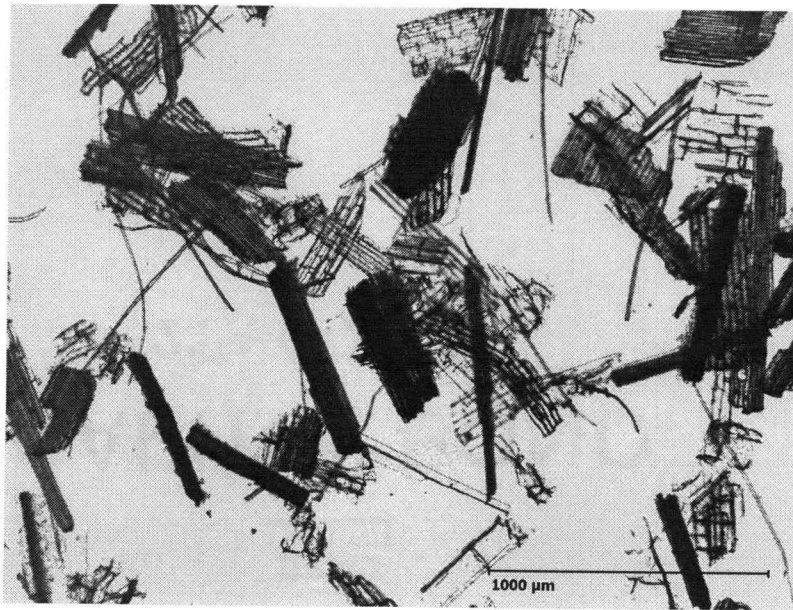


**Figure 3.16** Biomass waste particles (wheat straw particles).

### 3.6.2 Centrifugal sedimentation particle size analysis

The nominal particle size distribution is measured by a particle size distribution analyzer (Horiba™ Model CAPA-700). This method relies on the

principle of liquid-phase sedimentation. According to the Stokes sedimentation law (Horiba Instruction Manual), for particles of equivalent density, particles with a larger diameter settle first, followed by successively smaller particles. Because of the time required for very small particles to settle naturally, centrifugal sedimentation is applied to reduce analysis time. In this method, the long-thin fiber particles are represented by the spherically shaped particle diameter that has the same sedimentation time. The relationship between the particle diameter and centrifugal sedimentation time is expressed as;

$$D_p = \left[ \frac{18\eta_0 \ln(x_2 / x_1)}{(\rho_{straw} - \rho_f) \omega^2 (t)} \right]^{\frac{1}{2}} \quad (3-4)$$

Median diameter, standard deviation and specific surface area are listed in Table 3.5 and the size distribution results are shown in Table 3.6.

**Table 3.5** Median size, standard deviation, and specific surface area measured by the centrifugal sedimentation particle size analyzer

Batch#	Median diameter [ $\mu\text{m}$ ]	Standard Deviation [ $\mu\text{m}$ ]	Specific Surface Area [ $\text{m}^2/\text{g}$ ]
1	73.52	34.72	0.064
2	114.68	39.98	0.045

**Table 3.6** Size distribution of biomass waste particles measure by the centrifugal sedimentation particle size analyzer

Diameter [ $\mu\text{m}$ ]	Batch#1		Batch#2	
	Frequency [%]	Cumulative Distribution [%]	Frequency [%]	Cumulative Distribution [%]
400-300	0.00	100.00	0.00	100.00
300-200	0.00	100.00	0.00	100.00
200-100	15.90	100.00	58.60	100.00
100-90	9.90	84.20	4.30	41.40
90-80	12.50	74.30	14.85	37.10
80-70	18.20	61.80	7.05	22.25
70-60	18.20	43.60	7.10	15.20
60-50	13.20	25.40	3.35	8.10
50-40	6.90	12.20	3.05	4.75
40-30	3.40	5.30	1.10	1.70
30-20	1.40	1.90	0.20	0.60
20-10	0.20	0.50	0.10	0.40
10-0	0.30	0.30	0.30	0.30

### 3.6.3 Optical microscope analysis

The size of biomass particle is measured by Electron microscope (Leica® DM-IL). As shown in Figure 3.16, biomass particles have an irregular shape, therefore, the characteristic size of particles is defined as the distance between the extreme left and right tangents that are perpendicular to the reference line. This characteristic length is known as Ferret's diameter (Hinds 1999). Table 3.7 shows the size distribution of each particle batch.

**Table 3.7** Size distribution of biomass waste particles by microscopic analysis

Diameter [μm]	Batch#1:		Batch#2	
	Weight percent [%]	Accumulation [%]	Weight percent [%]	Accumulation [%]
1001-1050	0.00	100.00	1.16	100.00
951-1000	0.00	100.00	0.88	98.84
901-950	0.00	100.00	3.68	97.96
851-900	0.00	100.00	3.87	94.28
801-850	1.76	100.00	6.40	90.41
751-800	0.80	98.24	11.85	84.01
701-750	1.52	97.44	8.70	72.16
651-700	1.29	95.92	6.90	63.46
601-650	4.98	94.63	15.56	56.56
551-600	6.83	89.65	13.96	41.00
501-550	15.69	82.82	7.19	27.04
451-500	14.43	67.13	11.97	19.85
401-450	19.41	52.70	4.72	7.88
351-400	16.25	33.29	1.44	3.16
301-350	12.06	17.04	1.18	1.72
251-300	3.58	4.98	0.54	0.54
201-250	1.40	1.40	0.00	0.00
151-200	0.00	0.00	0.00	0.00

The average particle diameter in this analysis can be calculated as follows (Levenspiel 1998);

$$D_p = \frac{1}{\sum \frac{x_i}{D_{p,i}}} \quad (3-5)$$



The average diameter of biomass particles in Batch #1 and #2 is found to be 430.40  $\mu\text{m}$  and 609.11  $\mu\text{m}$ , respectively.

#### 3.6.4 Summary of biomass particle diameter

The nominal diameter of biomass waste particles in each measurement method can be summarized in Table 3.8.

**Table 3.8** Nominal diameter of biomass waste particles

Measurement Method	Batch #1	Batch #2
Screen Analysis	164.5 $\mu\text{m}$	237.5 $\mu\text{m}$
Centrifugal Sedimentation Analysis	73.52 $\mu\text{m}$	114.68 $\mu\text{m}$
Microscopical Analysis	430.40 $\mu\text{m}$	609.11 $\mu\text{m}$

We are not certain which of these three diameters most appropriately serves the modeling effort, therefore, we will keep all of diameters and use them in Chapter 5.

## CHAPTER 4

### MATHEMATICAL MODELING AND EXPERIMENTAL METHOD

This chapter covers the derivation of the voidage distribution model and the filtration model. In addition, the experimental methods for both voidage experiment and filtration experiment are presented.

#### 4.1 Voidage distribution model

The voidage distribution model for a liquid-solid fluidization in a gradient magnetic field can be derived from the four fundamental equations, namely, equations of continuity and equations of motion, presented in Chapter 2. All the governing equations and their constitutive relationships can be summarized as:

The Equations of Continuity:

$$\text{Fluid phase:} \quad \frac{\partial \varepsilon}{\partial t} + \nabla \cdot \varepsilon \mathbf{U} = 0 \quad (2-1)$$

$$\text{Particle phase:} \quad \frac{\partial (1 - \varepsilon)}{\partial t} + \nabla \cdot (1 - \varepsilon) \mathbf{V} = 0 \quad (2-2)$$

The Equations of Motion:

$$\text{Fluid phase:} \quad \rho_f \varepsilon \left( \frac{\partial \mathbf{U}}{\partial t} + (\mathbf{U} \cdot \nabla) \mathbf{U} \right) = -\varepsilon \nabla P_f - \varepsilon \nabla \tau_f + \rho_f \varepsilon \mathbf{g} - \varepsilon \mathbf{F}_1 \quad (2-3)$$

$$\begin{aligned} \text{Particle phase:} \quad \rho_p (1-\varepsilon) \left( \frac{\partial \mathbf{V}}{\partial t} + (\mathbf{V} \cdot \nabla) \mathbf{V} \right) = & -(1-\varepsilon) \nabla P_f - (1-\varepsilon) \nabla P_p - (1-\varepsilon) \nabla \cdot \tau_p \\ & + \rho_p (1-\varepsilon) \mathbf{g} + \varepsilon \mathbf{F}_1 + \mathbf{F}_m \end{aligned} \quad (2-4)$$

where  $\mathbf{F}_1$  is the force between fluid and particles and is defined as

$$\mathbf{F}_1 = \beta(\varepsilon)(\mathbf{U} - \mathbf{V}) + \frac{(1-\varepsilon)}{\varepsilon} C(\varepsilon) \rho_f \frac{d(\mathbf{U} - \mathbf{V})}{dt} \quad (2-5)$$

Using the Ergun expression,  $\beta(\varepsilon)$  is given by

$$\beta(\varepsilon) = \frac{150(1-\varepsilon)\mu_f}{d_p^2 \varepsilon^2} + \frac{1.75(1-\varepsilon)|\mathbf{U} - \mathbf{V}| \rho_f}{d_p \varepsilon^2} \quad (2-6)$$

$\mathbf{F}_m$  is the magnetic force acting on the ferromagnetic particles which is defined as follows:

$$\mathbf{F}_m = \mu_0 M_b \nabla H = \mu_0 (1-\varepsilon) M_p \nabla H \quad (2-12)$$

The magnetization of the particle is collinear with the field intensity and is given as

$$M_p = \chi H \quad (2-13)$$

This set of equations can also be written in a cylindrical coordinate system as:

### The Equations of Continuity:

*Fluid Phase:*

$$\frac{\partial \varepsilon}{\partial t} + \frac{1}{r} \frac{\partial (r \varepsilon u_r)}{\partial r} + \frac{1}{r} \frac{\partial (\varepsilon u_\theta)}{\partial \theta} + \frac{\partial (\varepsilon u_z)}{\partial z} = 0$$

$$\frac{\partial \varepsilon}{\partial t} + \frac{\varepsilon u_r}{r} + u_r \frac{\partial \varepsilon}{\partial r} + \varepsilon \frac{\partial u_r}{\partial r} + \frac{1}{r} u_\theta \frac{\partial \varepsilon}{\partial \theta} + \frac{1}{r} \varepsilon \frac{\partial u_\theta}{\partial \theta} + u_z \frac{\partial \varepsilon}{\partial z} + \varepsilon \frac{\partial u_z}{\partial z} = 0 \quad (4-1)$$

*Particle Phase:*

$$\frac{\partial (1-\varepsilon)}{\partial t} + \frac{1}{r} \frac{\partial (r(1-\varepsilon)v_r)}{\partial r} + \frac{1}{r} \frac{\partial ((1-\varepsilon)v_\theta)}{\partial \theta} + \frac{\partial ((1-\varepsilon)v_z)}{\partial z} = 0$$

$$-\frac{\partial \varepsilon}{\partial t} + \frac{(1-\varepsilon)v_r}{r} - v_r \frac{\partial \varepsilon}{\partial r} + (1-\varepsilon) \frac{\partial v_r}{\partial r} - \frac{v_\theta}{r} \frac{\partial \varepsilon}{\partial \theta} + (1-\varepsilon) \frac{\partial v_\theta}{\partial \theta} - v_z \frac{\partial \varepsilon}{\partial z} + (1-\varepsilon) \frac{\partial v_z}{\partial z} = 0 \quad (4-2)$$

### The Equations of Motion:

*Fluid Phase:*

$$\rho_f \varepsilon \left( \frac{\partial u_r}{\partial t} + u_r \frac{\partial u_r}{\partial r} + \frac{u_\theta}{r} \frac{\partial u_r}{\partial \theta} + u_z \frac{\partial u_r}{\partial z} - \frac{u_\theta^2}{r} \right) = -\varepsilon \frac{\partial P_f}{\partial r} - \frac{\varepsilon}{r} \frac{\partial (r \tau_f)}{\partial r} - \rho_f \varepsilon g_r - \varepsilon F_{1,r}$$

$$\rho_f \varepsilon \left( \frac{\partial u_\theta}{\partial t} + u_r \frac{\partial u_\theta}{\partial r} + \frac{u_\theta}{r} \frac{\partial u_\theta}{\partial \theta} + u_z \frac{\partial u_\theta}{\partial z} + \frac{u_r u_\theta}{r} \right) = -\frac{\varepsilon}{r} \frac{\partial P_f}{\partial \theta} - \frac{\varepsilon}{r} \frac{\partial \tau_f}{\partial \theta} - \rho_f \varepsilon g_\theta - \varepsilon F_{1,\theta}$$

$$\rho_f \varepsilon \left( \frac{\partial u_z}{\partial t} + u_r \frac{\partial u_z}{\partial r} + \frac{u_\theta}{r} \frac{\partial u_z}{\partial \theta} + u_z \frac{\partial u_z}{\partial z} \right) = -\varepsilon \frac{\partial P_f}{\partial z} - \varepsilon \frac{\partial \tau_f}{\partial z} - \rho_f \varepsilon g_z - \varepsilon F_{1,z} \quad (4-3)$$

*Particle Phase:*

$$\rho_p (1-\varepsilon) \left( \frac{\partial v_r}{\partial t} + v_r \frac{\partial v_r}{\partial r} + \frac{v_\theta}{r} \frac{\partial v_r}{\partial \theta} - \frac{v_\theta^2}{r} \right) = -(1-\varepsilon) \frac{\partial P_f}{\partial r} - (1-\varepsilon) \frac{\partial P_p}{\partial r} - \frac{(1-\varepsilon)}{r} \frac{\partial (r \tau_p)}{\partial r}$$

$$\begin{aligned}
& -\rho_p(1-\varepsilon)g_r + \varepsilon F_{1,r} + F_{m,r} \\
\rho_p(1-\varepsilon) & \left( \frac{\partial v_\theta}{\partial t} + v_\theta \frac{\partial v_\theta}{\partial r} + \frac{v_\theta}{r} \frac{\partial v_\theta}{\partial \theta} + v_z \frac{\partial v_\theta}{\partial z} + \frac{v_r v_\theta}{r} \right) = -\frac{(1-\varepsilon)}{r} \frac{\partial P_f}{\partial \theta} - \frac{(1-\varepsilon)}{r} \frac{\partial P_p}{\partial \theta} \\
& -\frac{(1-\varepsilon)}{r} \frac{\partial \tau_p}{\partial \theta} - \rho_p(1-\varepsilon)g_\theta + \varepsilon F_{1,\theta} + F_{m,\theta} \\
\rho_p(1-\varepsilon) & \left( \frac{\partial v_z}{\partial t} + v_r \frac{\partial v_z}{\partial r} + \frac{v_\theta}{r} \frac{\partial v_z}{\partial \theta} + v_z \frac{\partial v_z}{\partial z} \right) = -(1-\varepsilon) \frac{\partial P_f}{\partial z} - (1-\varepsilon) \frac{\partial P_p}{\partial z} - (1-\varepsilon) \frac{\partial \tau_p}{\partial z} \\
& -\rho_p(1-\varepsilon)g_z + \varepsilon F_{1,z} + F_{m,z} \tag{4-4}
\end{aligned}$$

The magnetic field intensity,  $\mathbf{H}$ , has three components  $H_r, H_z, H_\theta$ .

Therefore, the magnetic force acting on the particles in a cylindrical coordinate system can be written as follows:

$$\begin{aligned}
F_{m,z} &= \mu_0(1-\varepsilon)\chi \left( H_r \frac{\partial H_r}{\partial z} + H_z \frac{\partial H_z}{\partial z} + H_\theta \frac{\partial H_\theta}{\partial z} \right) \\
F_{m,r} &= \mu_0(1-\varepsilon)\chi \left( H_r \frac{\partial H_r}{\partial r} + H_z \frac{\partial H_z}{\partial r} + H_\theta \frac{\partial H_\theta}{\partial r} \right) \\
F_{m,\theta} &= \mu_0(1-\varepsilon)\chi \left( H_r \frac{\partial H_r}{\partial \theta} + H_z \frac{\partial H_z}{\partial \theta} + H_\theta \frac{\partial H_\theta}{\partial \theta} \right) \tag{4-5}
\end{aligned}$$

In order to ease experimental work and to simplify the computation of the bed voidage using the above model, three experimental conditions are introduced and simplifying assumptions are made.

The following specific experimental conditions were used in this study:

1. The magnetic field intensity is highest at the bottom of the bed and

decreases linearly with the height of the bed ( $\partial H/\partial z = \text{constant}$ ). The system is symmetric in the  $\theta$  direction (cylindrical column).

Therefore, any derivative with respect to  $\theta$  can be neglected,

2. This system is at steady state,  $\partial ()/\partial t = 0$ .

The following are the simplifying assumptions used in this study.

1. The mean particle velocity is assumed to be zero,  $\mathbf{V} = 0$ . With this assumption, all terms that include the particle velocities,  $v_r$ ,  $v_\theta$ , and  $v_z$  or their derivatives are negligible.
2. The fluid phase is treated as an inviscid flow except for mutual interaction with the particle phase. Therefore, the stress tensor terms ( $\tau_f$ ) in the liquid phase can be ignored in Equation (4-3).
3. The magnetic field intensity in the  $r$  and  $\theta$  directions are much smaller than the magnetic field intensity in the  $z$  direction. Therefore, the magnetic field intensity in the  $r$  and  $\theta$  directions can be ignored.
4. The virtual mass force due to the relative acceleration between fluid and particle is small compared to the force due to gravity, so the second term in Equation (2-5) can be neglected. The momentum terms due to the change of fluid velocity (fluid acceleration/deceleration term) are small compared to the other forces (the gravitational force, the drag force, and the magnetic force). Therefore, the terms on the left-hand side of Equation (4-3) can be ignored.
5. The distribution of flow inside the column is assumed to be plug flow

( $u_r$  and  $u_\theta$  are much smaller than  $u_z$ ), therefore, any terms in Equation (4-3), including the velocity in the  $r$  and  $\theta$  directions, can be neglected.

6. The magnetic forces in the  $r$  and  $\theta$  directions are small compared to the magnetic force in the  $z$  direction. Therefore, the magnetic force terms,  $F_{m,r}$  and  $F_{m,\theta}$  can be ignored in Equation (4-4). In addition, the particle stress tensor due to the magnetic interparticle force in the  $r$  and  $\theta$  directions can be ignored.

7. There is no gravitational acceleration component in the  $r$  and  $\theta$  directions. As a result, the terms containing  $g_\theta$  and  $g_r$  in Equation (4-3) and Equation (4-4) can be neglected.

With the assumptions and specific experimental conditions listed above, Equation (4-1) reduces to:

$$\frac{\partial(\epsilon u_z)}{\partial z} = 0 \quad (4-6)$$

Equation (4-2) is automatically satisfied because the mean velocity of the particle is assumed to be equal to zero.

The equations of motion for the fluid and particle phases in the  $z$  direction are reduced to:

The fluid phase:

$$0 = -\epsilon \frac{\partial P_f}{\partial z} - \rho_f \epsilon g_z + \epsilon F_{1,z} \quad (4-7)$$

The particle phase:

$$0 = -(1-\epsilon) \frac{\partial P_f}{\partial z} - (1-\epsilon) \frac{\partial P_p}{\partial z} - (1-\epsilon) \frac{\partial \tau_p}{\partial z} - \rho_p (1-\epsilon) g_z + \epsilon F_{1,z} + F_{m,z} \quad (4-8)$$

One can rearrange Equation (4-7) to obtain:

$$\frac{\partial P_f}{\partial z} = -\rho_f g_z - F_{1,z} \quad (4-9)$$

By substituting Equation (4-9) into Equation (4-8) and rearranging the terms

$$0 = -(1-\varepsilon)(-\rho_f g_z - F_{1,z}) - (1-\varepsilon)\left(\frac{\partial P_p}{\partial z} + \frac{\partial \tau_p}{\partial z}\right) - \rho_p(1-\varepsilon)g_z + \varepsilon F_{1,z} + F_{m,z} \quad (4-10)$$

$$0 = (1-\varepsilon)\rho_f g_z + (1-\varepsilon)F_{1,z} - (1-\varepsilon)\left(\frac{\partial P_p}{\partial z} + \frac{\partial \tau_p}{\partial z}\right) - \rho_p(1-\varepsilon)g_z + \varepsilon F_{1,z} + F_{m,z} \quad (4-11)$$

With the help of Equation (2-14), one can write Equation (4-11) as:

$$0 = -(\rho_p - \rho_f)(1-\varepsilon)g_z + F_{1,z} + (1-\varepsilon)E\frac{\partial \varepsilon}{\partial z} + \mu_0(1-\varepsilon)\chi H_z \frac{\partial H_z}{\partial z} \quad (4-12)$$

The constitutive expression for the drag force,  $F_{1,z}$  is given by the following equations:

$$\mathbf{F}_1 = \beta(\varepsilon)(\mathbf{U} - \mathbf{V}) \quad (4-13)$$

$$\beta(\varepsilon) = \frac{150(1-\varepsilon)\mu_f}{d_p^2 \varepsilon^2} + \frac{1.75(1-\varepsilon)|\mathbf{U} - \mathbf{V}|\rho_f}{d_p \varepsilon^2} \quad (4-14)$$

Then, Equation (4-12) can be written as:

$$0 = -(\rho_p - \rho_f)(1-\varepsilon)g_z + \frac{150(1-\varepsilon)^2 \mu_f U_0}{d_p^2 \varepsilon^3} + \frac{1.75(1-\varepsilon)\rho_f U_0^2}{d_p \varepsilon^3} + (1-\varepsilon)E\frac{\partial \varepsilon}{\partial z} + \mu_0(1-\varepsilon)\chi H_z \frac{dH_z}{dz} \quad (4-15)$$



The elastic modulus is defined by Equation (2-18) as follows:

$$E = \frac{d_p}{A'} \frac{12(\chi V_p \mu_0 H_z)^2 \pi r (8\pi^2 r^6 + 12\pi r^3 \chi V_p + \chi^2 V_p^2)}{\mu_0 (-2\pi r^3 + \chi V_p)^4} \quad (2-18)$$

where  $r = d_p + \frac{d_p}{k} \sqrt{\frac{\pi}{6(1-\varepsilon)}}$  and  $k = \frac{m}{(\varepsilon - \varepsilon_0)^n}$

We define  $\alpha = \frac{150\mu_f U_0}{d_p^2 (\rho_p - \rho_f) g}$  (4-16)

$$\varphi = \frac{1.75\rho_f u U_0^2}{d_p (\rho_p - \rho_f) g} \quad (4-17)$$

$$\lambda = \frac{1}{(\rho_p - \rho_f) g L} \quad (4-18)$$

$$\gamma = \frac{\mu_0 \chi}{(\rho_p - \rho_f) g} \frac{dH_z}{dz} \quad (4-19)$$

It is important to remember that in all these experiments,  $\partial H_z / \partial z$  is constant, otherwise this function must be supplied separately. Equation (4-15) can be rewritten as:

$$\frac{\partial \varepsilon}{\partial z/L} = \frac{\varepsilon^3 - \alpha(1-\varepsilon) - \varphi - \gamma H_z \varepsilon^3}{\lambda E \varepsilon^3} \quad (4-20)$$

with boundary conditions  $z/L = 1, \varepsilon = 1$

Equation (4-20) is used to determine the corresponding voidage at any given fluid velocity, magnetic field intensity, and magnetic field gradient. In order to determine the voidage distribution in G-MAFB systems, the values of process parameters, such as fluid velocity, magnetic field intensity and size of the particles must be known.

In the absence of gravity (0g), the first term on the right hand side of Equation (4-15) vanishes and after rearranging we obtain:

$$\frac{\partial \varepsilon}{\partial z} = \frac{-\alpha(1-\varepsilon) - \varphi - \gamma H \varepsilon^3 \frac{\partial H}{\partial z}}{E \varepsilon^3} \quad (4-21)$$

$$\alpha = \frac{150 \mu_f U_0}{d_p^2} \quad (4-22)$$

$$\varphi = \frac{1.75 \rho_f U_0^2}{d_p} \quad (4-23)$$

$$\gamma = \mu_0 \chi \quad (4-24)$$

## 4.2 Voidage distribution experimental method

The magnetic field intensity is measured beforehand by using the gaussmeter (see Appendix F). The pressure drop,  $\Delta P_{f(d)}$ , in the column is measured by using the pressure probe as described in Section 3.4.1. The

pressure probe is inserted vertically into the top of the column and moved axially to measure the dynamic pressure every 0.5 centimeters from the bottom to the top of the bed.

The dynamic pressure is defined as the total vertical pressure corrected for the hydrostatic head (static pressure  $\rho_f g dz$ ) of the fluid. It is expressed as:

$$-\frac{dP_f}{dz} = -\frac{dP_{f(d)}}{dz} + \rho_f g \quad (4-25)$$

The total vertical pressure drop through the bed is strongly related to the holdup of each phase and the magnetic force acting on the particle phase. It is defined as:

$$-\frac{dP_f}{dz} = (\varepsilon \rho_f + (1-\varepsilon) \rho_p) g + \mu_0 (1-\varepsilon) \chi H_z \frac{\partial H_z}{\partial z} + (1-\varepsilon) E \frac{\partial \varepsilon}{\partial z} \quad (4-26)$$

In Equation (4-26), we assumed that the frictional loss on the wall is negligible. Substituting Equation (4-26) into Equation (4-25), one obtains:

$$-\frac{dP_{f(d)}}{dz} = (1-\varepsilon) (\rho_p - \rho_f) g + \mu_0 (1-\varepsilon) \chi H_z \frac{\partial H_z}{\partial z} + (1-\varepsilon) E \frac{\partial \varepsilon}{\partial z} \quad (4-27)$$

With the help of Equation (4-15), one can rearrange Equation (4-27) as:

$$-\frac{dP_{f(d)}}{dz} = \frac{150(1-\varepsilon_{\text{exp}})^2 \mu_f U_0}{d_p^2 \varepsilon_{\text{exp}}^3} + \frac{1.75(1-\varepsilon_{\text{exp}}) \rho_p U_0^2}{d_p \varepsilon_{\text{exp}}^3} \quad (4-28)$$

By measuring the pressure drop,  $\Delta P_{f(d)}$ , for a small interval  $\Delta z$ , the corresponding voidage at any location in the bed can be evaluated with Equation (4-28).

The voidage distributions obtained from the experiments are compared with those obtained from the voidage distribution model. The numerical data for the dynamic pressure drop,  $\Delta P_{f(d)}$ , at any location in the bed, for different flow rates and different magnetic field gradients, are found in Appendix K.

The experiments in the 0g environment are conducted on board the NASA KC-135 aircraft. The trajectory flown on each maneuver provides approximately 25 seconds of zero-gravity conditions for experiments. Particles C and D are fluidized in a square two-dimensional fluidization column with a fixed magnetic field gradient at different liquid flow rates. Because each maneuver provides only 25 seconds for an experimental run, the only experimental data that are recorded, the height of the bed at any given liquid flow rate, are filmed by a video camera. The trajectory is shown in Figure 4.1. Figure 4.2 shows a photo of experiments performed on the aircraft.

The Reduced Gravity Student Flight Opportunities program is sponsored by NASA and administered by the Texas Space Grant Consortium. By flying a series of parabolic trajectories, NASA's Boeing KC-135 aircraft provides a true three-dimensional "weightless" environment. This airplane has been widely used as a platform for testing in reduced-gravity environments and for the training of US astronauts.

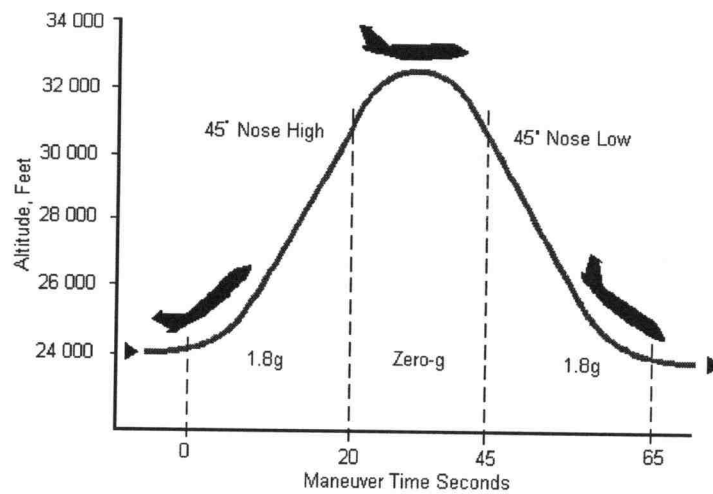


**Figure 4.1** Trajectory of the Boeing NASA KC-135 aircraft.



**Figure 4.2** Experiments in 0g conditions onboard the NASA KC-135 aircraft.

### 4.3 Filtration model

The material balances for waste particles in the G-MFAB and in the holding tank are presented in Chapter 2. A summary of these material balances for both control volumes of the system is shown below:

$$\text{The holding tank:} \quad FC^*(L, t) - FC^*(0, t) = V_{\text{tank}} \frac{\partial C^*(0, t)}{\partial t} \quad (2-25)$$

$$\text{Initial Conditions:} \quad C^*(0, 0) = C_0$$

$$\text{The G-MAFB:} \quad -U_0 \frac{\partial C^*(x, t)}{\partial x} - a' \frac{\partial \sigma}{\partial t} = \frac{\partial (\varepsilon C^*(x, t))}{\partial t} \quad (2-26)$$

$$\text{Initial Conditions:} \quad C^*(x, 0) = 0; \quad t = 0, \quad 0 < x \leq L$$

$$\text{Boundary Conditions:} \quad C^*(0, t) = Q(t); \quad x = 0, \quad t > 0$$

$$C^*(0, 0) = Q(0); \quad x = 0, \quad t = 0$$

$$\text{The rate of filtration} \quad \frac{\partial \sigma}{\partial t} = \frac{k_1 C^*(x, t)}{a'} - k_2 \sigma \quad (2-27)$$

$$\text{Initial Conditions:} \quad \sigma(x, 0) = 0; \quad 0 \leq x \leq L$$

$$C^*(x, 0) = 0; \quad t = 0, \quad 0 < x \leq L$$

In our study, we assume that once the biomass particles are deposited on the surface of the magnetic media bed particles, they will form a thin layer of

biomass waste on the particle surface, hence, the actual media diameter may increase as the biomass is deposited. The variation in the media nominal diameter as the waste mass is deposited can be expressed as:

$$d_p(x,t) = d_p(x,0) + \frac{\sigma(x,t)}{\rho_{\text{straw}}} \quad (4-29)$$

The primary effect of this correction is actually related to the voidage of the bed, at any given time, which can be presented as:

$$\varepsilon = 1 - (1 - \varepsilon_0) \frac{d_p^3(x,t)}{d_p^3(x,0)} \quad (4-30)$$

With the help of Equation (4-29) and (4-30), Equation (2-26) can be rewritten as

$$\begin{aligned} -U_0 \frac{\partial C^*(x,t)}{\partial x} - a' \frac{\partial \sigma(x,t)}{\partial t} = & \left[ 1 - (1 - \varepsilon_0) \frac{d_p^3(x,t)}{d_p^3(x,0)} \right] \frac{\partial C^*(x,t)}{\partial t} \\ & - \frac{3(1 - \varepsilon_0)}{\rho_{\text{straw}}} \frac{d_p^2(x,t)}{d_p^3(x,0)} \frac{\partial \sigma(x,t)}{\partial t} \end{aligned} \quad (4-31)$$

Equations (2-25), (2-27) and (4-31) are solved numerically, and accumulation and detachment coefficients,  $k_1$  and  $k_2$ , are evaluated using an optimization procedure (a Fortran program provided in Appendix J).

#### **4.4 Filtration experimental method**

A series of filtration experiments is conducted in the G-MAFB system presented in Chapter 3. A magnetic field inside the filtration column is set such that the field intensity is highest at the bottom of the bed, and decreases toward the top of the bed. This arrangement produces a direct magnetic force on the ferromagnetic filter medium, which is oriented downward toward the distributor plate and fixes the bed in position. In our filtration experiments, the magnetic field gradient is fixed and flow velocities are varied between 0.54 and 1.34 cm/s. At the beginning of the filtration experiment, the bed is fluidized at a fluid velocity greater than the minimum fluidization velocity and the magnetic field is still off at this point. The biomass waste particles are uniformly distributed through out the system. Then, the magnetic field is turned on and the fluid velocity is set to a desired flow rate. At this point, the bed media is packed and biomass (wheat straw particles), which are suspended in an aqueous stream recirculating between the holding tank and the magnetically consolidated filter bed, starts to deposit in the bed. Loading of the filter is monitored by the reduction in particulate concentration within the holding tank as a function of time, which is determined by changes in the optical density of the suspension. The holding tank is stirred with a magnetic stir plate placed underneath to prevent settling of the biomass particles.



## **CHAPTER 5**

### **EXPERIMENTAL DATA AND RESULTS**

This chapter presents experimental results from voidage distribution experiments and filtration experiments. The voidage distribution model presented in Chapter 4 is verified with the experimental data obtained both in the laboratory and in the 0g environment on board NASA's KC-135 aircraft. The filtration experimental data are compared with the filtration model, and the characteristics of the accumulation and detachment coefficients are discussed.

#### **5.1 Voidage distribution experimental *Data and Results***

##### **5.1.1 Effect of magnetic force on the gradient-magnetically assisted fluidized bed**

As mentioned in Chapter 2, the ferromagnetic particles are subjected to a magnetic force when they are placed in a gradient magnetic field. A magnetic field inside the column is created such that the field intensity is highest at the bottom of the bed, and decreases linearly toward the top of the bed at a constant rate ( $dH_z/dz=\text{constant}$ ). As a result, magnetic force on the ferromagnetic particles is oriented downward toward the distributor plate and against the drag force. The magnetic field intensities used in the experiments are provided in Appendix F.

Table 5.1, Figure 5.1, and Figure 5.2 represent the effects of the magnetic forces on bed expansion within the magnetically assisted fluidized bed. Two general observations can be made at a given magnetic field intensity and field gradient: the height of the bed increases as the superficial fluid velocity increases, and vice versa, at a given superficial fluid velocity, the height of the bed decreases as the magnetic field intensity and field gradient increase.

**Table 5.1** Bed height at different fluid flow rates and different magnetic field gradients for ferromagnetic particles A and B

Particle	Flow rate [m/s]	$dH_z/dz$ [A/m/m]	$H_z$ at the bottom [A/m]	Packed Bed Height [m]	Fluidized Bed Height [m]
A	0.0176	0	0	0.065	0.145
A	0.0176	-14663	4276.5	0.065	0.130
A	0.0176	-18289	5334.3	0.065	0.120
A	0.0176	-20543	6262.1	0.065	0.110
A	0.0222	0	0	0.095	0.240
A	0.0222	-14663	4276.5	0.095	0.220
A	0.0222	-18289	5334.3	0.095	0.205
A	0.0222	-20543	6262.1	0.095	0.190
B	0.0222	0	0	0.170	0.252
B	0.0222	-14663	4276.5	0.170	0.240
B	0.0222	-18289	5334.3	0.170	0.230
B	0.0222	-20543	6262.1	0.170	0.217

Compositions and characteristics of particles A and B are presented in section 3.5.

It is clear that the magnetic field intensity and field gradient have a significant effect on the bed height. Experimental observations show that there are three distinct regions that appear in the magnetic fluidized bed. The first is the region adjacent to the distributor plate. The water coming through the distributor plate has a high velocity, and creates small jets above the distributor plate. These jets exchange momentum with the surrounding fluid and particles. As a result, the particles in this region move vigorously, with visible vibrations. For a given fluid velocity, the length of this zone depends on the magnetic field intensity and the field gradient. This zone is longer at lower magnetic field intensities, and can diminish or even disappear if the magnetic field intensity is substantially increased.

Above this jetting zone is the region where the particles are packed and the jets no longer influence movement of the particles. This region is established whenever the magnetic forces are stronger than the drag forces acting on the particles. In most of our laboratory studies, this zone was eliminated by carefully choosing the appropriate fluid flow rate and field intensity.

The third region, usually observed at the top of the bed, is characterized as "normal/usual" fluidization. In this region, magnetic forces are well balanced with other forces to allow particulate fluidization.

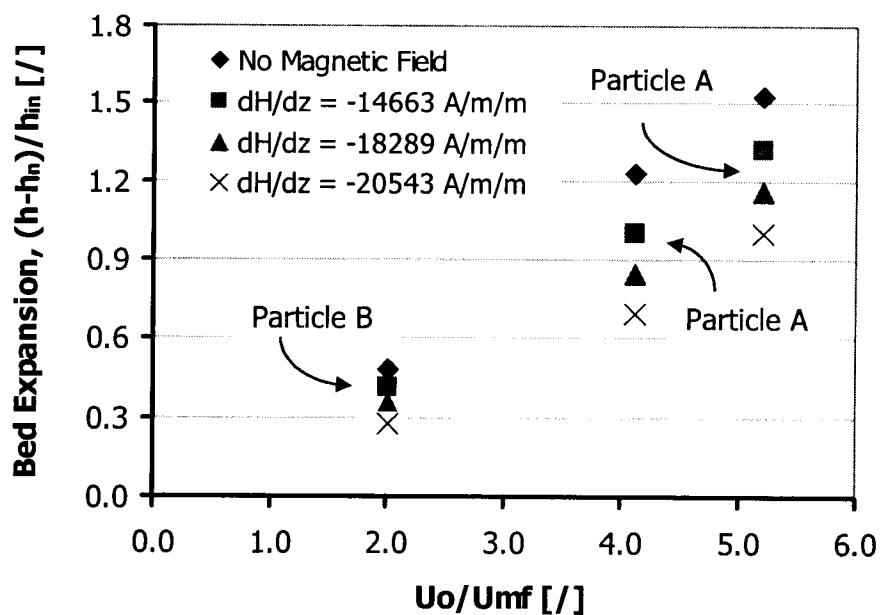


**Figure 5.1** Bed expansion as a function of superficial fluid velocity for the different magnetic field intensities and field gradients ( $d_{p,A} = 2.16$  mm and  $d_{p,B} = 2.5$  mm).

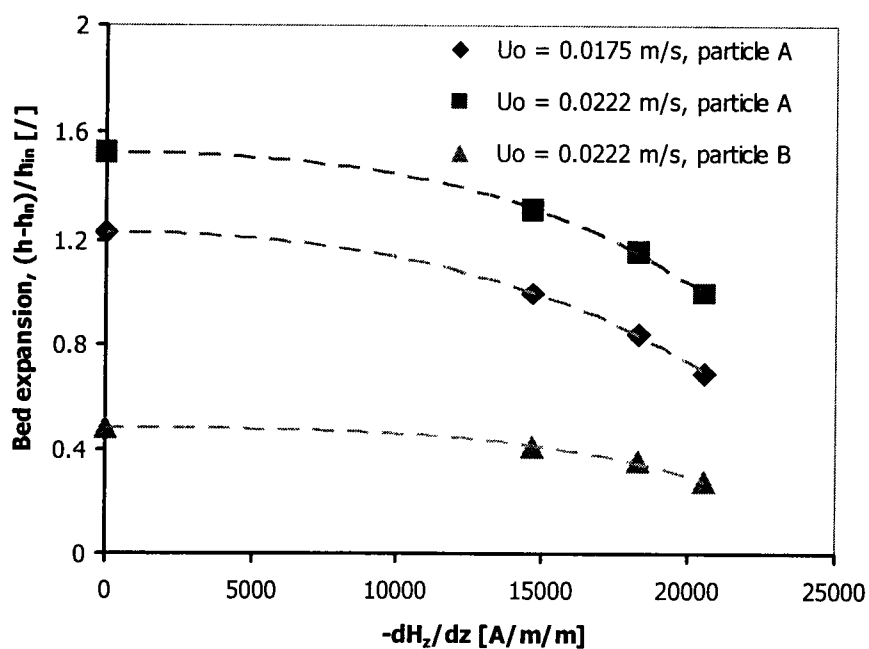


**Figure 5.2** Bed expansion as a function of the magnetic field gradient for different superficial fluid velocities.

### 5.1.2 Voidage distribution experimental data from laboratory experiments

In laboratory experiments, the dynamic pressure,  $\Delta P_{f(d)}$ , is measured every 5 millimeters from the bottom to the top of the column. The corresponding voidage at any location in the bed can be evaluated with Equation (4-28).

$$-\frac{dP_{f(d)}}{dz} = \frac{150(1-\varepsilon_{\text{exp}})^2 \mu_f U_0}{d_p^2 \varepsilon_{\text{exp}}^3} + \frac{1.75(1-\varepsilon_{\text{exp}}) \rho_p U_0^2}{d_p \varepsilon_{\text{exp}}^3} \quad (4-28)$$

Figure 5.3 illustrates the dynamic pressure drop obtained in the G-MAFB containing particle A, and Figure 5.4 shows the corresponding voidage.

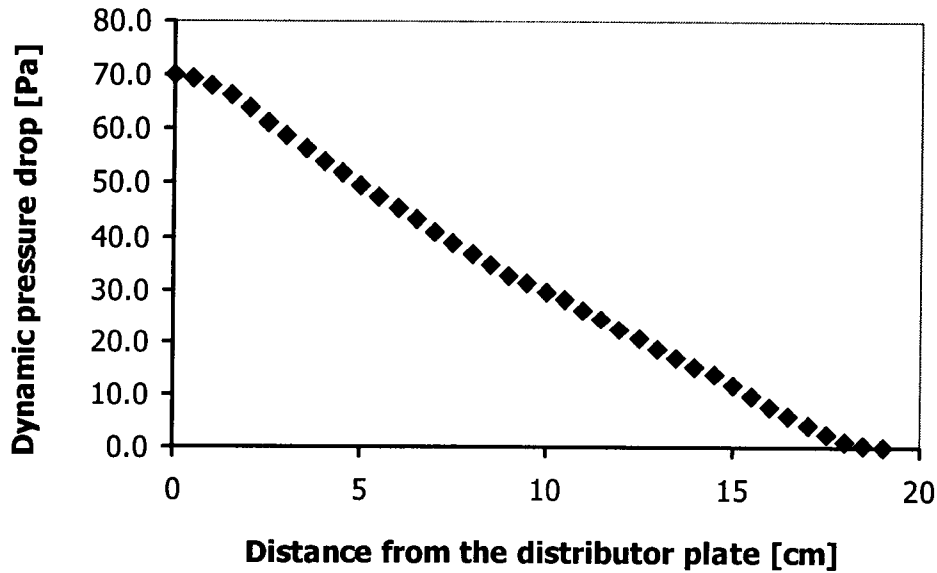


**Figure 5.3** Dynamic pressure drop of particle A in the G-MAFB  $dH_z/dz = -20,543 \text{ A/m/m}$ ,  $U_0 = 0.0222 \text{ m/s}$ , and  $h_{\text{bed}} = 0.190 \text{ m}$ .

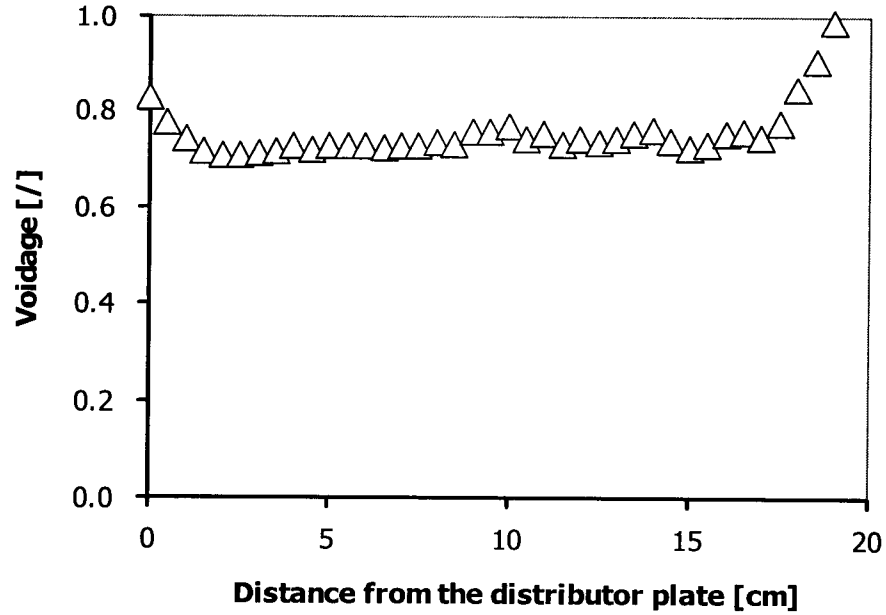


**Figure 5.4** Voidage distribution of particle A in the G-MAFB  $dH_z/dz = -20,543$  A/m/m,  $U_o = 0.0222$  m/s, and  $h_{bed} = 0.190$  m.

The complete numerical data for the dynamic pressure drop,  $\Delta P_{f(d)}$  and corresponding experimental voidage, at any location in the bed, for different flow rates and different magnetic field gradients, are listed in Appendix K.

### 5.1.3 Voidage distribution experimental results from laboratory experiments

The voidage distribution obtained from the model presented in Chapter 4 is here compared to the voidage distribution obtained from the experiments. In the voidage distribution model, the final height of the bed, the superficial fluid

velocity, and the magnetic field intensity at any given magnetic field gradient, are needed to predict the voidage distribution in the column. This is done by integration of the model, Equation (4-20). Once again, the voidage distribution model is represented by:

$$\frac{\partial \varepsilon}{\partial z/L} = \frac{\varepsilon^3 - \alpha(1 - \varepsilon) - \varphi - \gamma H_z \varepsilon^3}{\lambda E \varepsilon^3} \quad (4-20)$$

with boundary conditions:  $z/L = 1, \varepsilon = 1$

The parameters in Equation (4-20) are defined as:

$$\alpha = \frac{150 \mu_f U_0}{d_p^2 (\rho_p - \rho_f) g} \quad (4-16)$$

$$\varphi = \frac{1.75 \rho_f U_0^2}{d_p (\rho_p - \rho_f) g} \quad (4-17)$$

$$\lambda = \frac{1}{(\rho_p - \rho_f) g L} \quad (4-18)$$

$$\gamma = \frac{\mu_0 \chi}{(\rho_p - \rho_f) g} \frac{dH_z}{dz} \quad (4-19)$$

$$E = \frac{d_p}{A_p} \frac{12 (\chi V_p \mu_0 H_z)^2 \pi r (8 \pi^2 r^6 + 12 \pi r^3 \chi V_p + \chi^2 V_p^2)}{\mu_0 (-2 \pi r^3 + \chi V_p)^4} \quad (2-18)$$

$$r = d_p + \frac{d_p}{k} \sqrt{\frac{\pi}{6(1 - \varepsilon)}} \quad (2-23)$$

$$k = \frac{m}{(\varepsilon - \varepsilon_0)^n} \quad (2-24)$$

Figures 5.5 to 5.17 represent the voidage distribution experimental data and values predicted from the voidage distribution model. The values of  $m$  and  $n$  in Equation (2-24) are evaluated using an optimization procedure, and they are found to be 4.14 and 0.50, respectively. In addition, the calculated total mass of particles in the bed, using both experimental data and calculated voidage is compared with the measured mass of particles in the bed (Figure 5.18). These data provide insight into the applicability of the model and the resolution of our experiments.

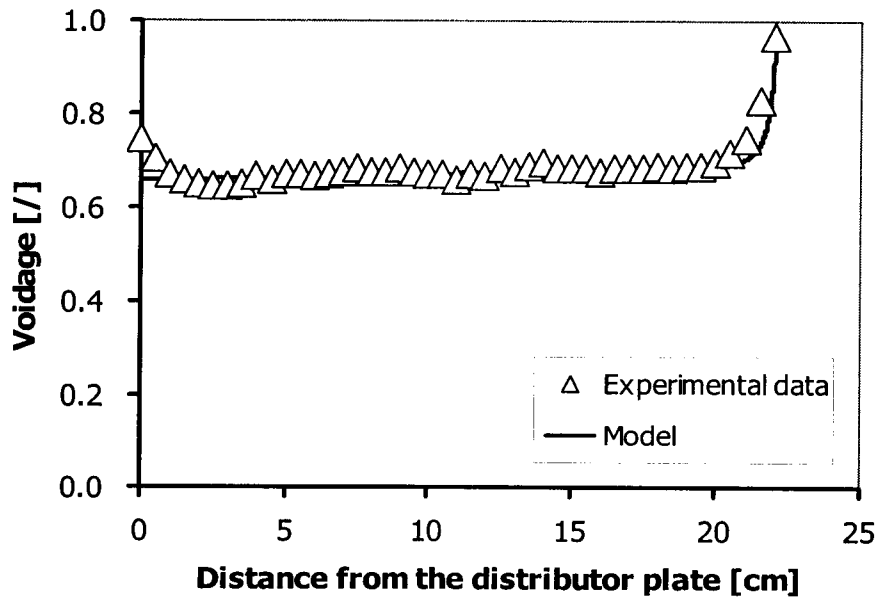


**Figure 5.5** Voidage distribution of particle A in the G-MAFB,  $dH_z/dz = -20,543 \text{ A/m/m}$ ,  $U_o = 0.0176 \text{ m/s}$ , and  $h_{\text{bed}} = 0.220 \text{ m}$ .



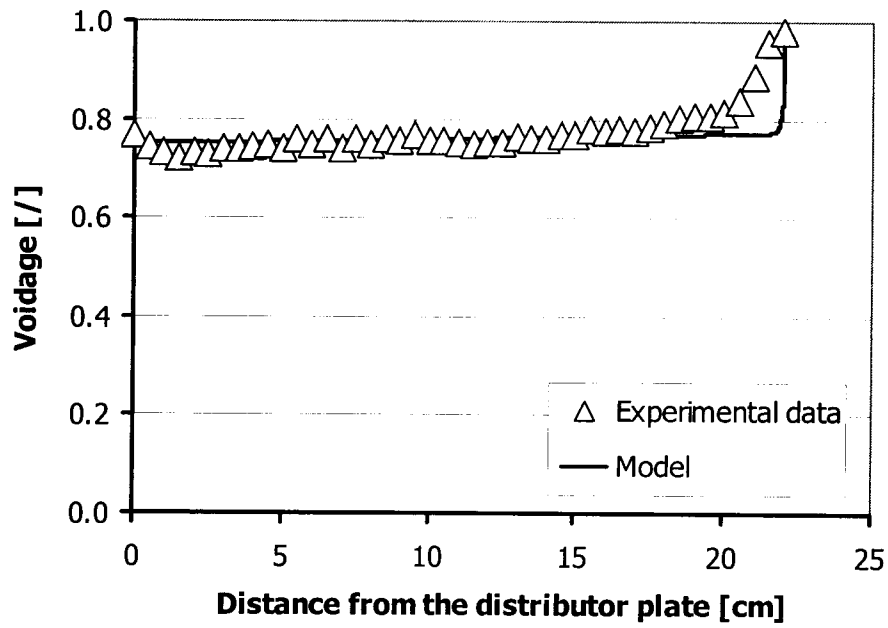


**Figure 5.6** Voidage distribution of particle A in the G-MAFB  $dH_z/dz = -14,663 \text{ A/m/m}$ ,  $U_0 = 0.0222 \text{ m/s}$ , and  $h_{bed} = 0.220 \text{ m}$ .

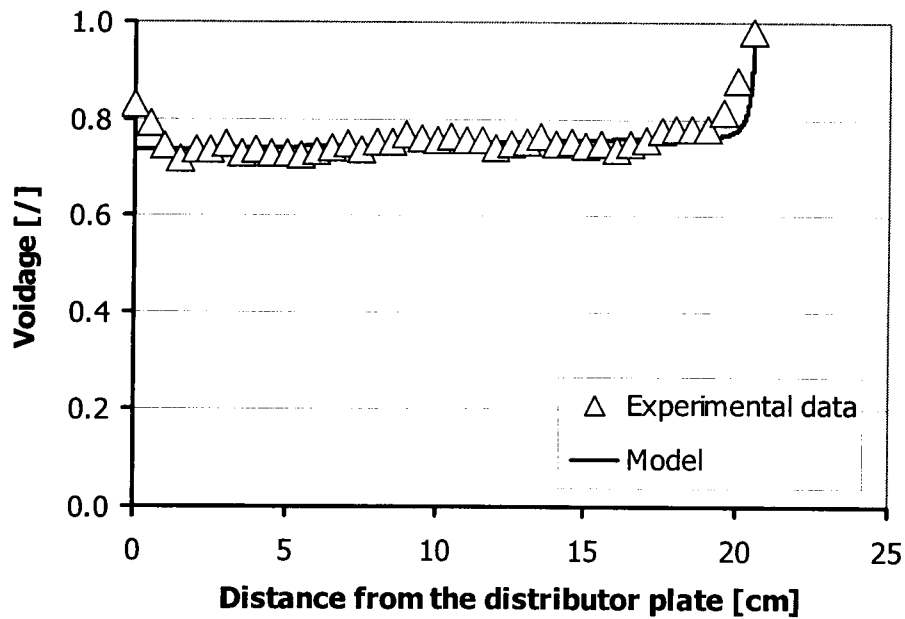


**Figure 5.7** Voidage distribution of particle A in the G-MAFB  $dH_z/dz = -18,289 \text{ A/m/m}$ ,  $U_0 = 0.0222 \text{ m/s}$ , and  $h_{bed} = 0.205 \text{ m}$ .

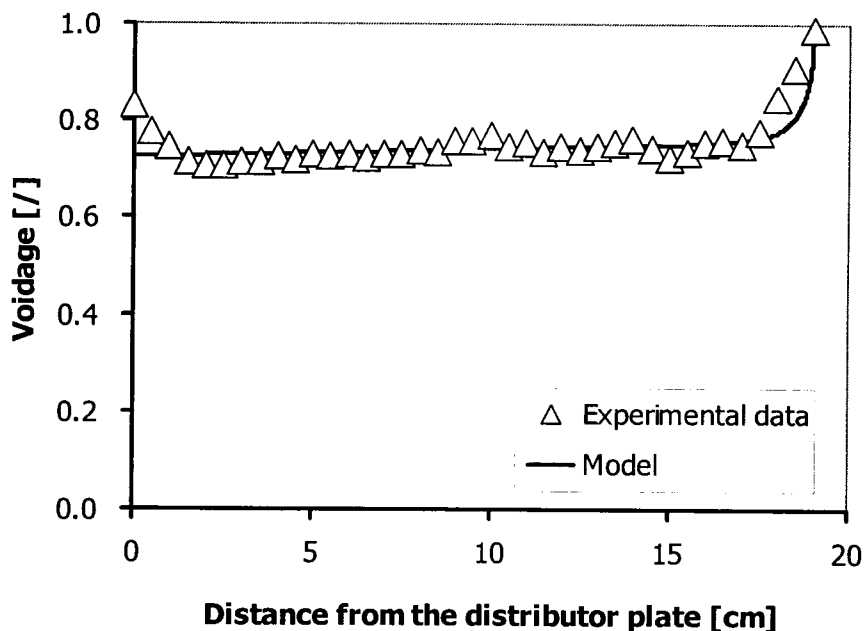


**Figure 5.8** Voidage distribution of particle A in the G-MAFB  $dH_z/dz = -20,543 \text{ A/m/m}$ ,  $U_0 = 0.0222 \text{ m/s}$ , and  $h_{\text{bed}} = 0.190 \text{ m}$ .

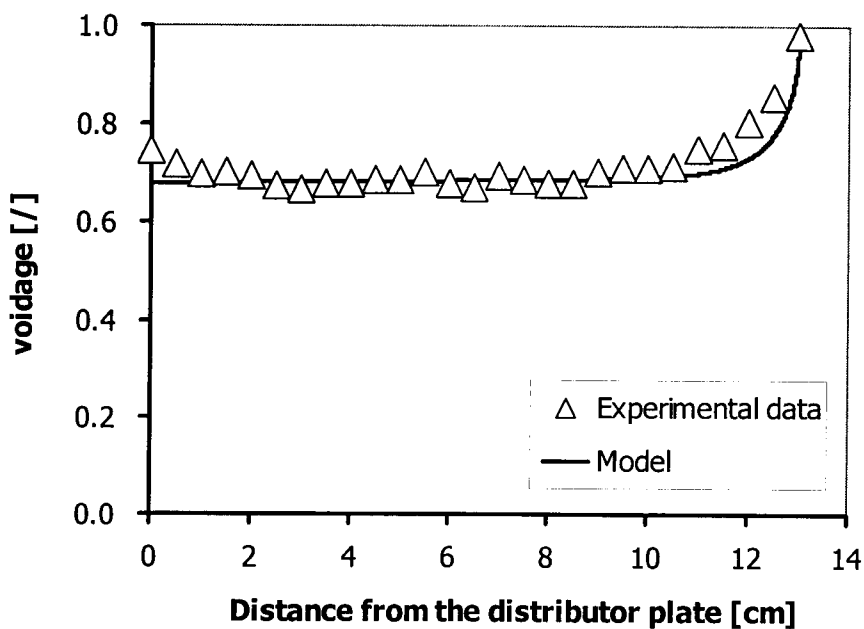


**Figure 5.9** Voidage distribution of particle A in the G-MAFB  $dH_z/dz = -14,663 \text{ A/m/m}$ ,  $U_0 = 0.0176 \text{ m/s}$ , and  $h_{\text{bed}} = 0.130 \text{ m}$ .

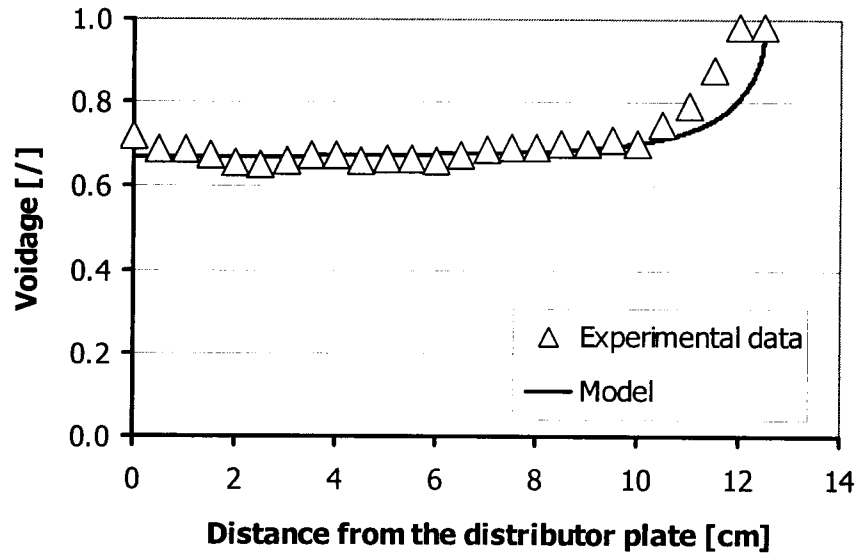


**Figure 5.10** Voidage distribution of particle A in the G-MAFB  $dH_z/dz = -18,289 \text{ A/m/m}$ ,  $U_0 = 0.0176 \text{ m/s}$ , and  $h_{\text{bed}} = 0.120 \text{ m}$ .

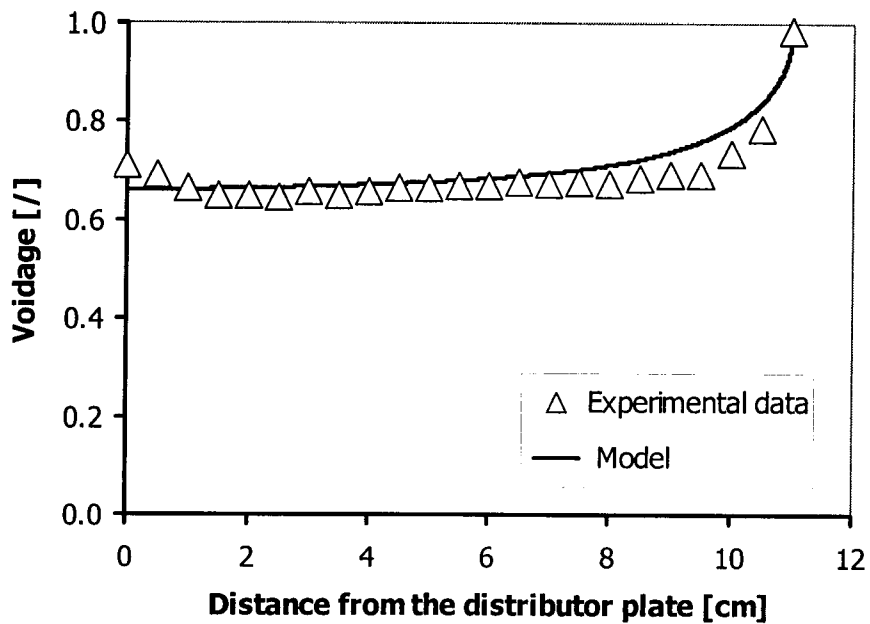


**Figure 5.11** Voidage distribution of particle A in the G-MAFB  $dH_z/dz = -20,543 \text{ A/m/m}$ ,  $U_0 = 0.0176 \text{ m/s}$ , and  $h_{\text{bed}} = 0.110 \text{ m}$ .

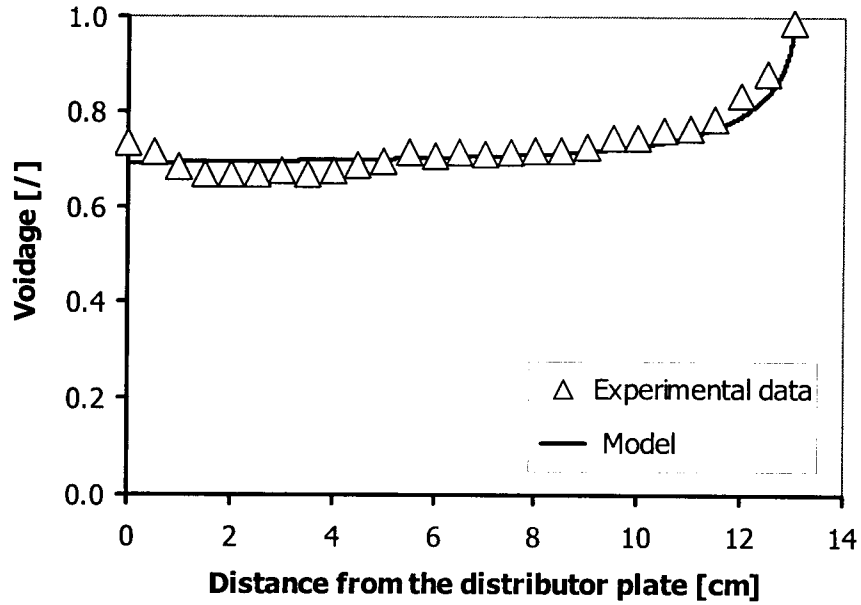


**Figure 5.12** Voidage distribution of particle A in the G-MAFB  $dH_z/dz = -20,543$  A/m/m,  $U_o = 0.0199$  m/s, and  $h_{bed} = 0.130$  m.

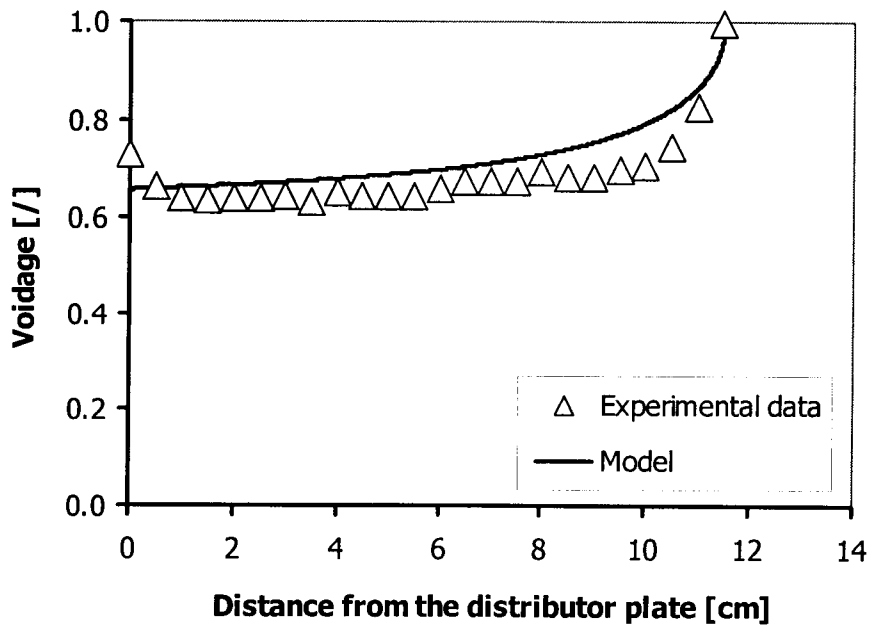


**Figure 5.13** Voidage distribution of particle A in the G-MAFB  $dH_z/dz = -33,798$  A/m/m,  $U_o = 0.0199$  m/s, and  $h_{bed} = 0.115$  m.

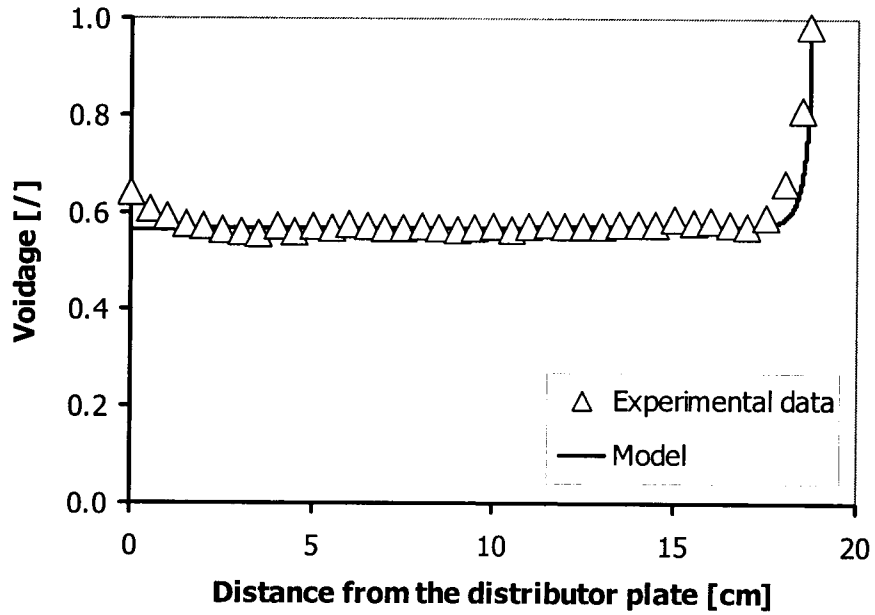


**Figure 5.14** Voidage distribution of particle B in the G-MAFB  $dH_z/dz = -14,663 \text{ A/m/m}$ ,  $U_o = 0.0222 \text{ m/s}$ , and  $h_{\text{bed}} = 0.187 \text{ m}$ .

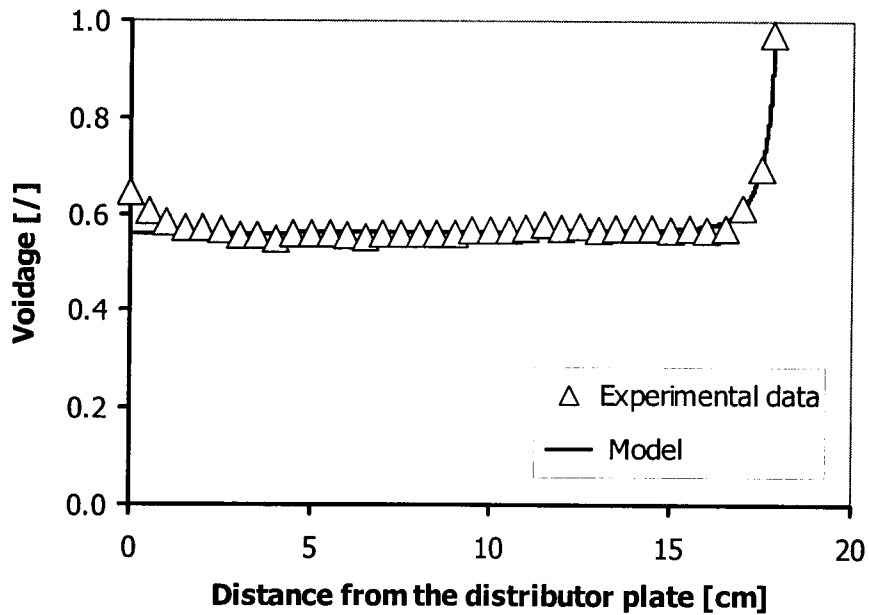


**Figure 5.15** Voidage distribution of particle B in the G-MAFB  $dH_z/dz = -18,289 \text{ A/m/m}$ ,  $U_o = 0.0222 \text{ m/s}$ , and  $h_{\text{bed}} = 0.178 \text{ m}$ .

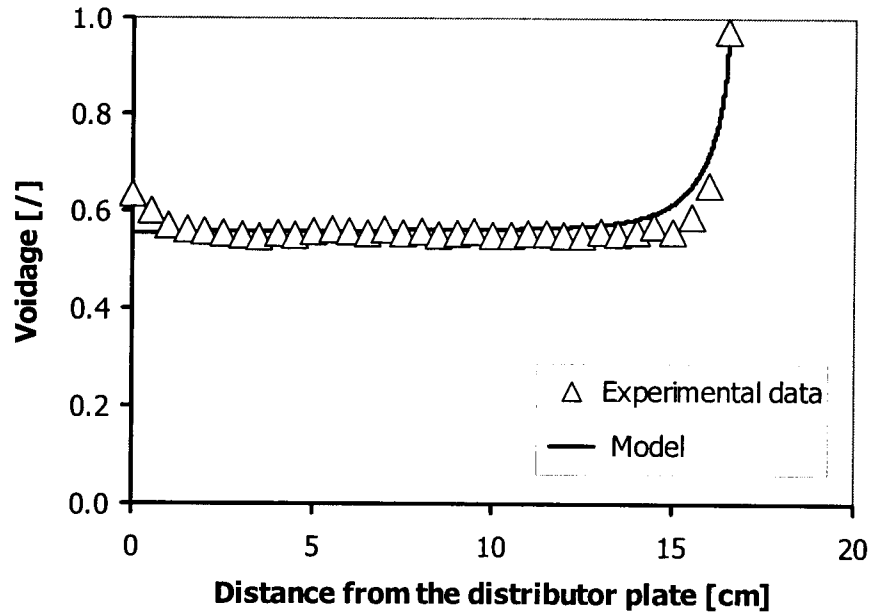


**Figure 5.16** Voidage distribution of particle B in the G-MAFB  $dH_z/dz = -20,543 \text{ A/m/m}$ ,  $U_o = 0.0222 \text{ m/s}$ , and  $h_{bed} = 0.165 \text{ m}$ .

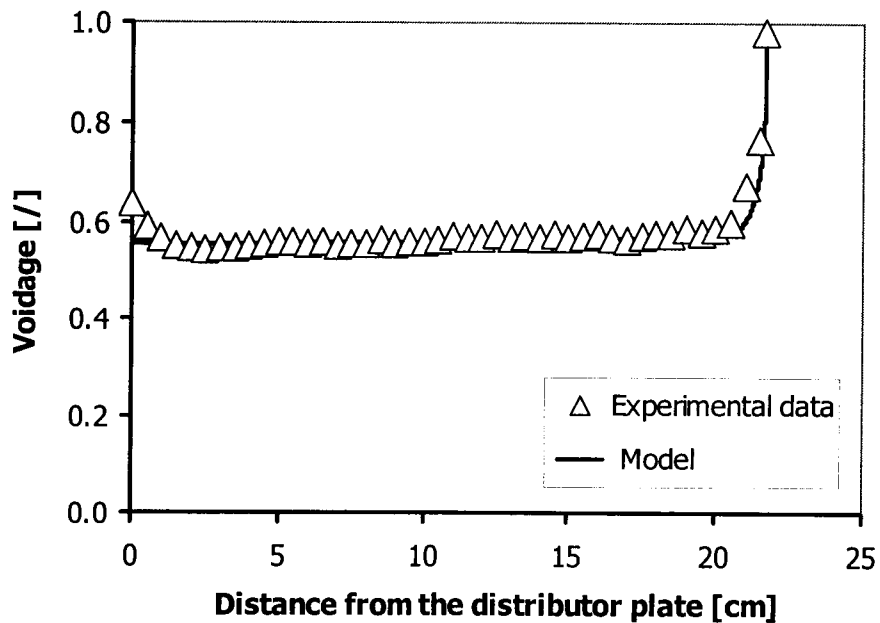


**Figure 5.17** Voidage distribution of particle B in the G-MAFB  $dH_z/dz = -20,543 \text{ A/m/m}$ ,  $U_o = 0.0222 \text{ m/s}$ , and  $h_{bed} = 0.217 \text{ m}$ .

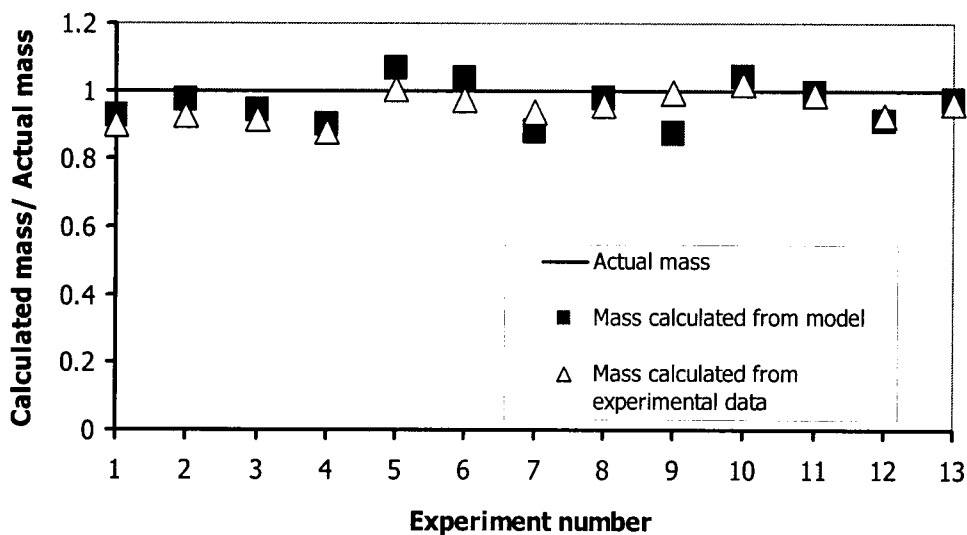


**Figure 5.18** Comparison of the calculated mass obtained from model and experiments with the exact mass.

#### 5.1.4 Experimental data on board NASA's KC-135 aircraft

In the experiments performed in the zero-g environment onboard the NASA-KC135 aircraft, the height of the bed is recorded at a fixed magnetic field strength for different flow rates. As previously mentioned in section 4.2, each maneuver provides only 25 seconds for an experimental run, therefore, the height of the bed and the position of the interface between packed and fluidized particles at any given liquid flow rate are the only experimental data that could be recorded. These experiments were conducted by the Chemical Engineering Flight Team onboard the NASA KC-135 aircraft, Ellington Field, Houston, TX. The

magnetic field intensity used in the zero-g experiment is provided in Appendix F. Table 5.2 represents the height of the bed at a fixed magnetic field strength for different flow rates.

**Table 5.2** Bed height at a fixed magnetic field strength for different flow rates

Particle	Flow Rate [m/s]	Packed Bed Height [m]	Fluidized Bed Height [m]
C	0.0000	0.160	0.160
C	0.0010	0.160	0.160
C	0.0055	0.160	0.195
C	0.0075	0.160	0.200
C	0.0110	0.160	0.210
D	0.0000	0.180	0.180
D	0.0010	0.180	0.210

Compositions and characteristics of particles C and D are presented in section 3.5.

#### 5.1.5 Experimental results on board NASA's KC-135 aircraft

In chapter 4, the voidage distribution model in the absence of the gravity is presented in Equations (4-21) to (4-24).

$$\frac{\partial \varepsilon}{\partial z} = \frac{-\alpha(1-\varepsilon) - \phi - \gamma H_z \varepsilon^3 \frac{dH_z}{dz}}{E \varepsilon^3} \quad (4-21)$$



$$\alpha = \frac{150\mu_f U_0}{d_p^2} \quad (4-22)$$

$$\varphi = \frac{1.75\rho_f U_0^2}{d_p} \quad (4-23)$$

$$\gamma = \mu_0 \chi \quad (4-24)$$

$$E = \frac{d_p}{A_p} \frac{12(\chi V_p \mu_0 H_z)^2 \pi r (8\pi^2 r^6 + 12\pi r^3 \chi V_p + \chi^2 V_p^2)}{\mu_0 (-2\pi r^3 + \chi V_p)^4} \quad (2-18)$$

$$r = d_p + \frac{d_p}{k} \sqrt{\frac{\pi}{6(1-\varepsilon)}} \quad (2-23)$$

$$k = \frac{m}{(\varepsilon - \varepsilon_0)^n} \quad (2-24)$$

Because of the change in cross-sectional area of the bed, the superficial fluid velocity at any location in the bed can be defined as:

$$U_0(z) = \frac{U_0(0)}{\left(1 + \frac{2h \tan \theta}{x_0}\right)} \quad (5-1)$$

where  $\tan(\theta)$  is the slope of the column,  $h$  is any height of the bed, and  $x_0$  is the width of the fluidization column at  $h = 0$ .

The values of  $m$  and  $n$ , (Equation 2-24) are found to be 1.75 and 0.50, respectively. The model prediction of the voidage distribution and the bed height in the MAFB in the 0g environment, including the experimentally observed bed heights, are shown in Figures 5.19 to 5.25. The height of the bed obtained from

the model prediction is compared to the height of the bed obtained experimentally in Figure 5.26. In addition, the calculated total mass of particles in the bed, using the model predicted voidage distribution, is compared to the actual mass of particles in the bed (Figure 5.27).

It is noted in the 0g experiments that all particles are not completely fluidized. Some particles are packed at the bottom of the bed up to a certain height due to the strength of the magnetic force in that region where the magnetic force is stronger than the drag force from the fluid. Notice, also that the strength of the fluid jets at the bottom of the bed is not sufficient to cause fluidization or even movement of the particles. Particles start to fluidize at the location where the drag force is in equilibrium with the magnetic force.

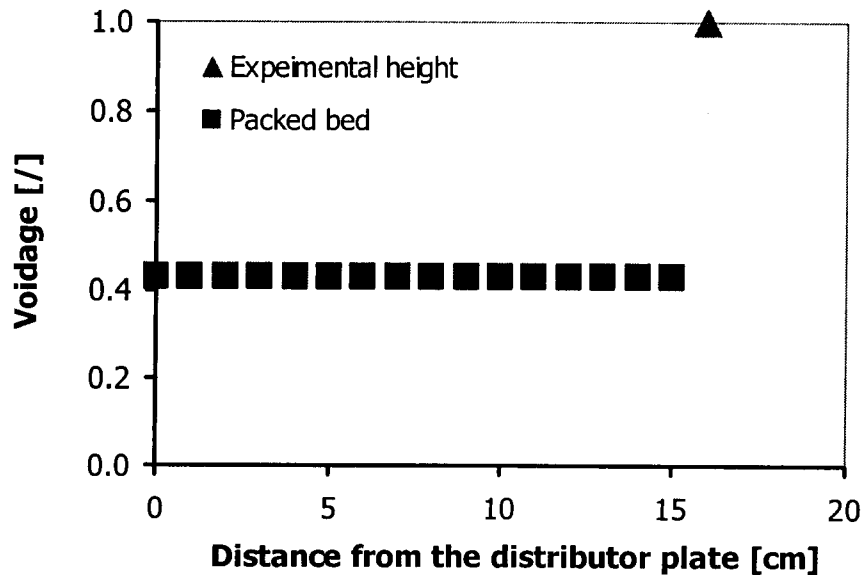


**Figure 5.19** Prediction of the voidage distribution of particle C in the 0g environment,  $U_{0,bottom} = 0.0000$  m/s,  $d_p = 0.0024$  m, and  $h_{bed} = 0.160$  m (magnetic profile, see Appendix F, Figure F.5).

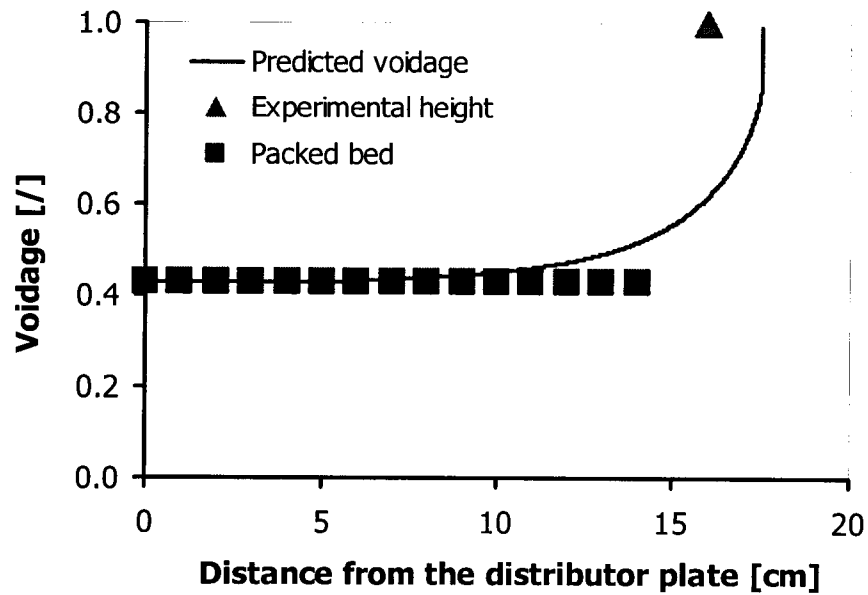


**Figure 5.20** Prediction of the voidage distribution of particle C in the 0g environment,  $U_{0,bottom} = 0.0010$  m/s,  $d_p = 0.0024$  m, and  $h_{bed} = 0.160$  m (magnetic profile, see Appendix F, Figure F.5).

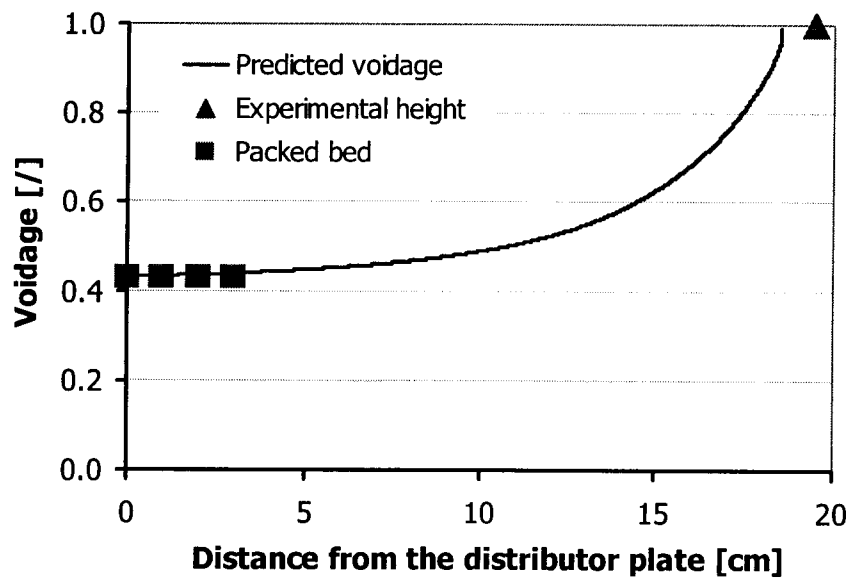


**Figure 5.21** Prediction of the voidage distribution of particle C in the 0g environment,  $U_{0,bottom} = 0.0055$  m/s,  $d_p = 0.0024$  m, and  $h_{bed} = 0.195$  m (magnetic profile, see Appendix F, Figure F.5).

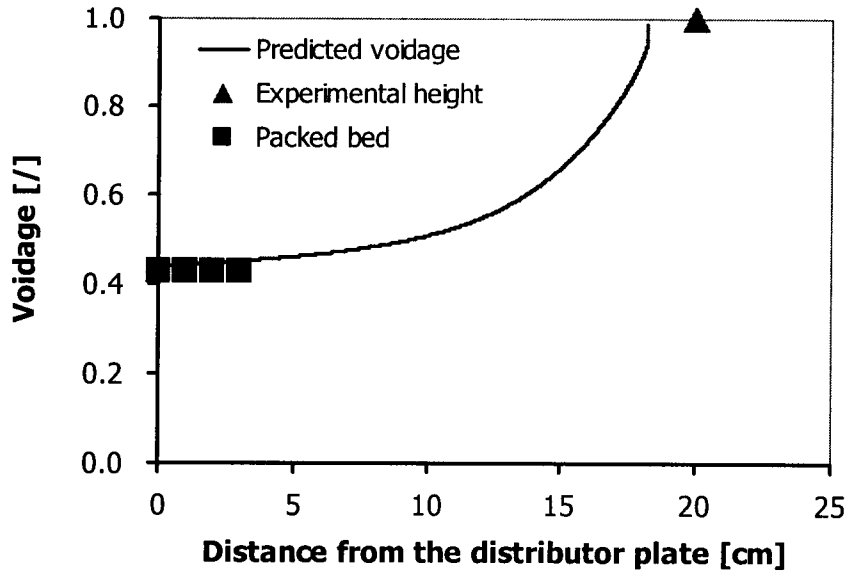


**Figure 5.22** Prediction of the voidage distribution of particle C in the 0g environment,  $U_{0,bottom} = 0.0076$  m/s,  $d_p = 0.0024$  m, and  $h_{bed} = 0.200$  m (magnetic profile, see Appendix F, Figure F.5).

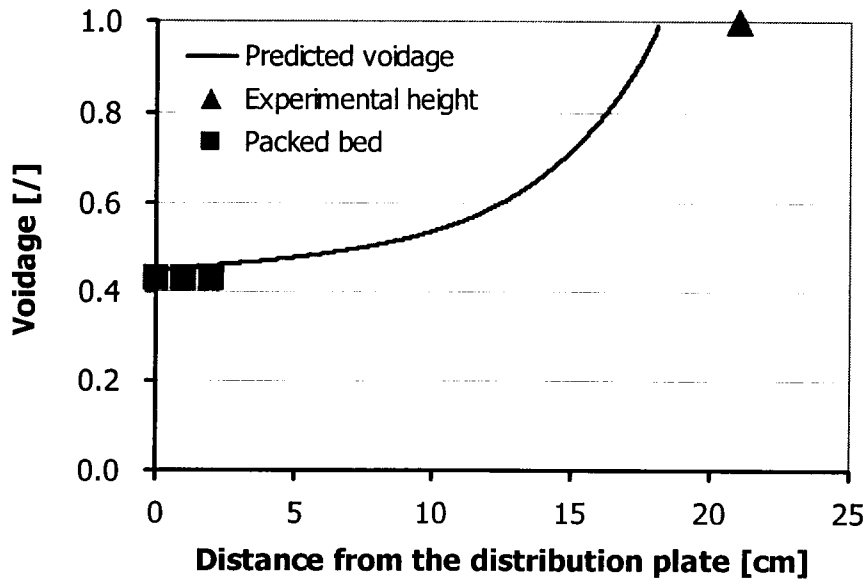


**Figure 5.23** Prediction of the voidage distribution of particle C in the 0g environment,  $U_{0,bottom} = 0.0110$  m/s,  $d_p = 0.0024$  m, and  $h_{bed} = 0.210$  m (magnetic profile, see Appendix F, Figure F.5).

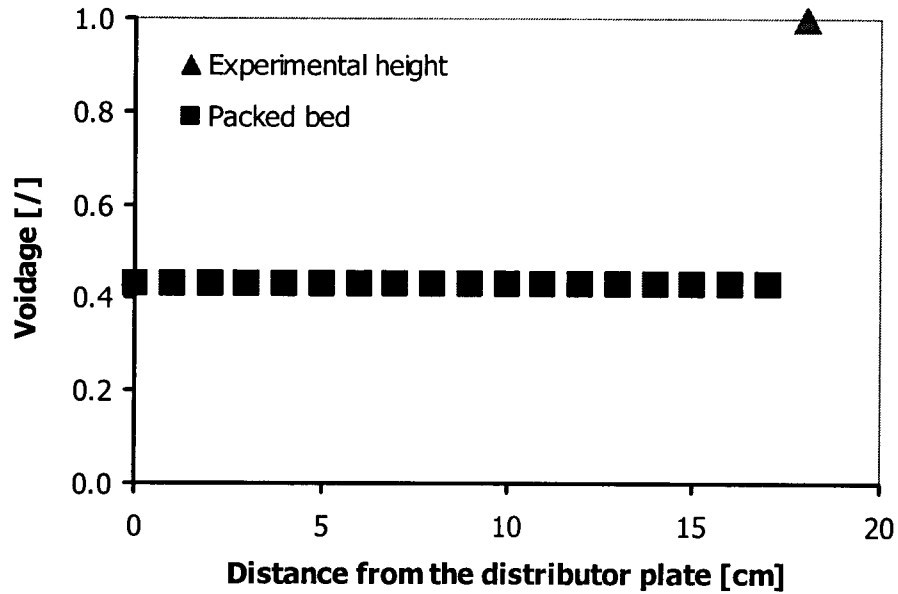


**Figure 5.24** Prediction of the voidage distribution of particle D in the 0g environment,  $U_{0,bottom} = 0.0000$  m/s,  $d_p = 0.0015$  m, and  $h_{bed} = 0.180$  m (magnetic profile, see Appendix F, Figure F.5).

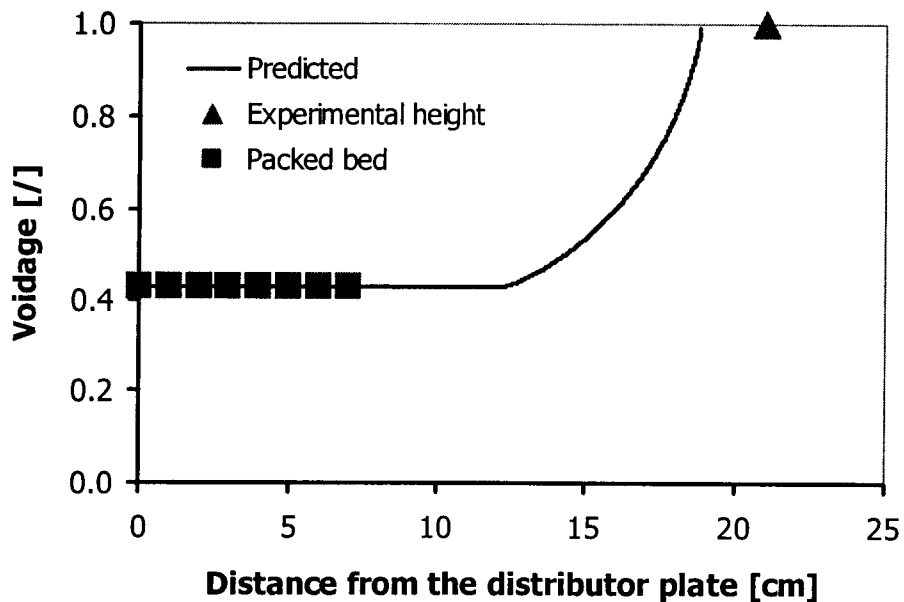


**Figure 5.25** Prediction of the voidage distribution of particle D in the 0g environment,  $U_{0,bottom} = 0.0010$  m/s,  $d_p = 0.0015$  m, and  $h_{bed} = 0.208$  m (magnetic profile, see Appendix F, Figure F.5).

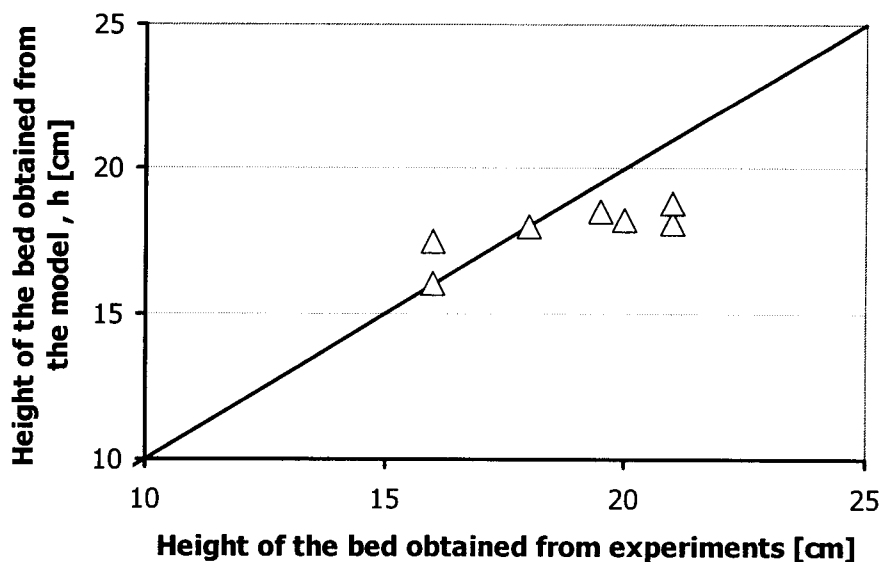


**Figure 5.26** Comparison between the height of the bed obtained from the model and the height of the bed obtained from experimental observations.

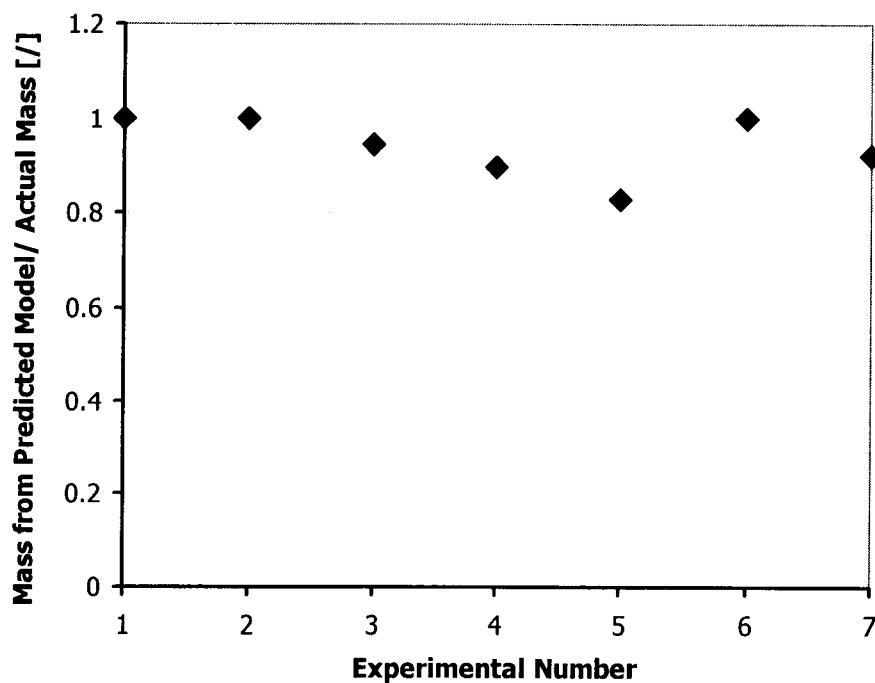


**Figure 5.27** Comparison between the predicted mass and the actual mass of particles in the bed.

The experimental results from the two very different experimental conditions, 1g environment and 0g environment, produced two sets of parameter  $m$  and  $n$  in Equation (2-24).

$$m = 4.14, n = 0.5 \quad \text{for 1g environment}$$

$$m = 1.75, n = 0.5 \quad \text{for 0g environment}$$

It is remarkable that constant “ $n$ ” in both cases has a numerical value of 0.5. This indicates the existence of an underlying fundamental principle that is characteristic for the liquid-solid fluidization, and that is unchanged for obviously dramatically different fluidization conditions prevailing in 1g and 0g environments.

During the development of the voidage model we did not anticipate this. However, we are now ready to incorporate this “discovery” into the equation describing the axial distance between two adjacent particles (Equation 2-24) in the following manner:

$$r = d_p + \frac{d_p}{m} \sqrt{\frac{\pi(\varepsilon - \varepsilon_0)}{6(1 - \varepsilon)}} \quad (5-2)$$

Thus, Equation (2-24) is not necessary anymore for model definition. This entire voidage model is now expressed in terms of single adjustable parameter “ $m$ ”. The rest of the terms in the model are consequence of the application of first principle and do not contain adjustable parameters.

We believe that parameter “ $m$ ” is reflecting the role of relative inertial effects of liquid and/or fluid phase with respect to all other forces in fluidized beds under the two dramatically different experimental environments (0g and 1g).

## **5.2 Filtration experimental *Data and Results***

### **5.2.1 Filtration experimental data**

A series of filtration experiments was conducted using a fixed magnetic field gradient (see Appendix F), and flow velocities varying between 0.54 and 1.34 cm/s. A magnetic field inside the filter column was created such that the field intensity was highest at the bottom of the bed, and then decreased toward the top of the column. The magnetic force on the ferromagnetic filter medium was orientated downward toward the distributor plate. Biomass waste particles (wheat straw particles) suspended in an aqueous stream were recirculated between a holding tank and the magnetically consolidated filter bed (see Figure 5.28) at a fixed flow rate and magnetic field intensity. The particulate concentration within the holding tank was recorded as a function of time to determine the loading of the filter. Particles E and F (composition and characteristics of particles E and F are presented in section 3.5) are used as the filter media. Figure 5.29 illustrates an example of the experimental data obtained in the filtration experiments. The complete filtration experimental data for different flow rates are provided in Appendix L.



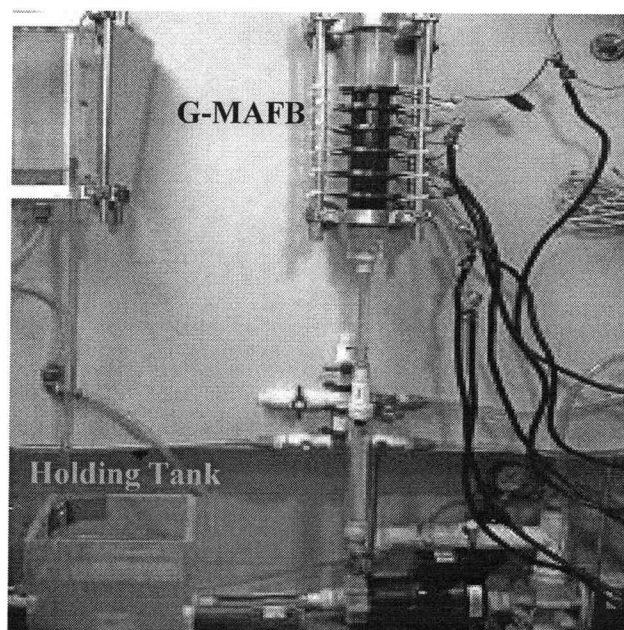


**Figure 5.28** G-MAFB apparatus used in filtration experiments.

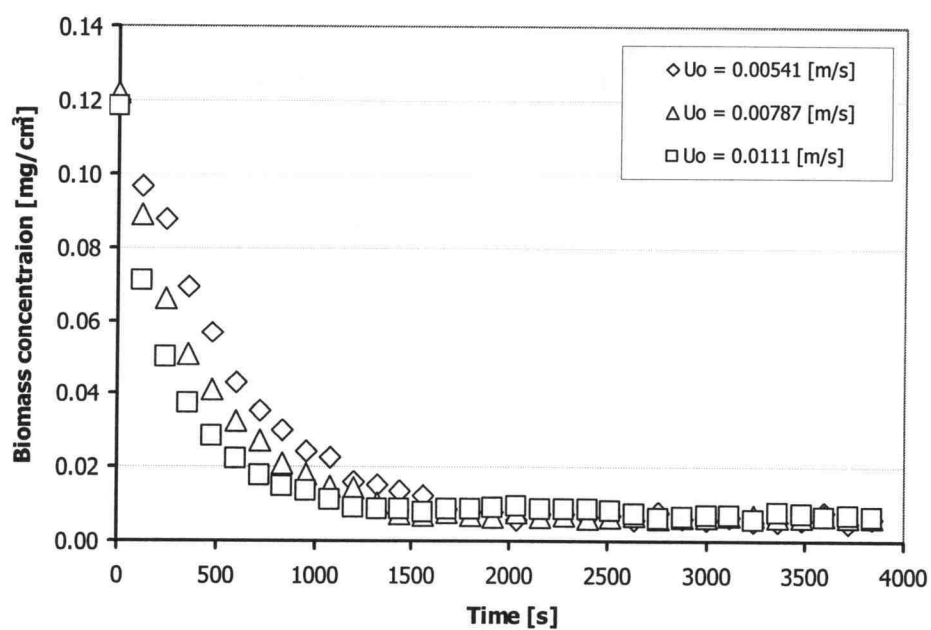


**Figure 5.29** Change of biomass concentration in the holding tank,  $d_p = 2.5$  mm,  $D_p = 73.52$   $\mu$ m,  $dH_z/dz = -38,817$  A/m/m and packed bed condition.

### 5.2.2 Filtration experimental results

The experimental results and model fitting with appropriate accumulation coefficient,  $k_1$ , and detachment coefficient,  $k_2$ , are presented in Figures 5.30 to 5.40. The nominal particle diameter, derived from centrifugal sedimentation measurements, was used to characterize the size of the biomass waste particles.

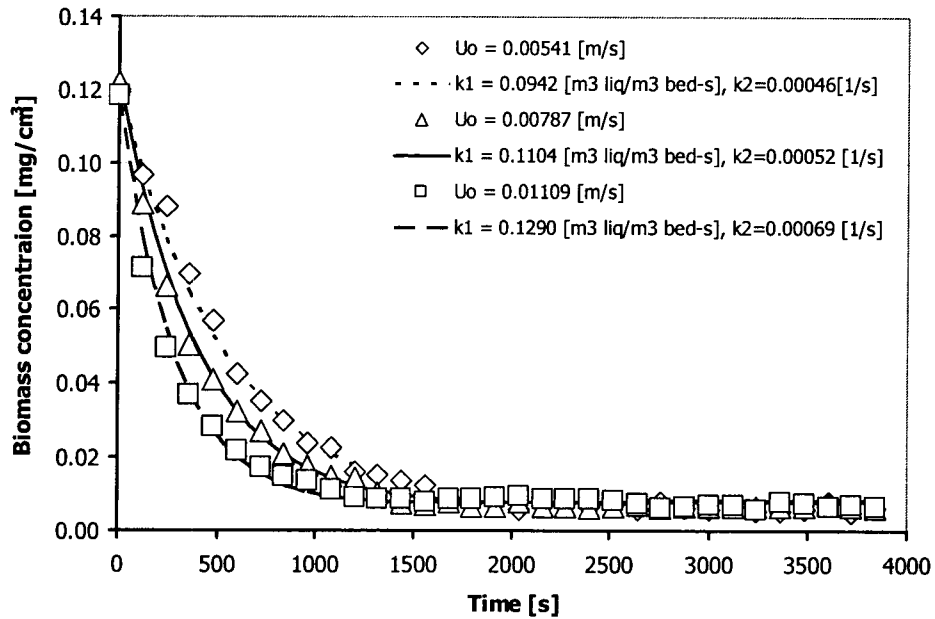


**Figure 5.30** Change of biomass concentration in the holding tank,  $d_p = 2.5$  mm,  $D_p = 73.52$   $\mu$ m,  $dH_z/dz = -38,817$  A/m/m,  $C_0 \sim 0.12$  [mg/cm<sup>3</sup>], and packed bed condition.

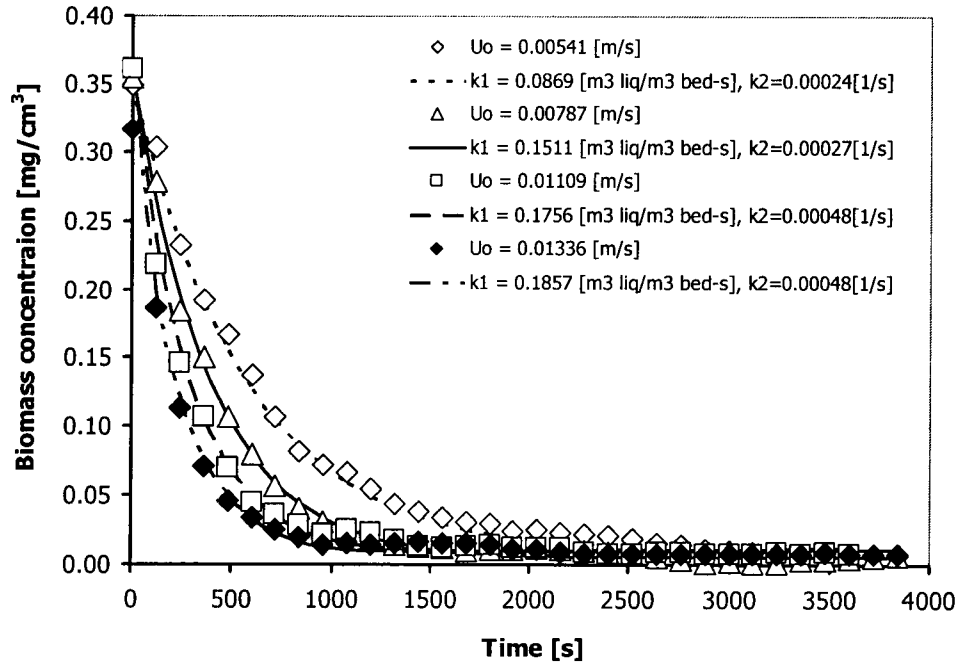


**Figure 5.31** Change of biomass concentration in the holding tank,  $d_p = 2.5$  mm,  $D_p = 73.52$   $\mu$ m,  $dH_z/dz = -38,817$  A/m/m,  $C_0 \sim 0.33$  [mg/cm³], and packed bed condition.

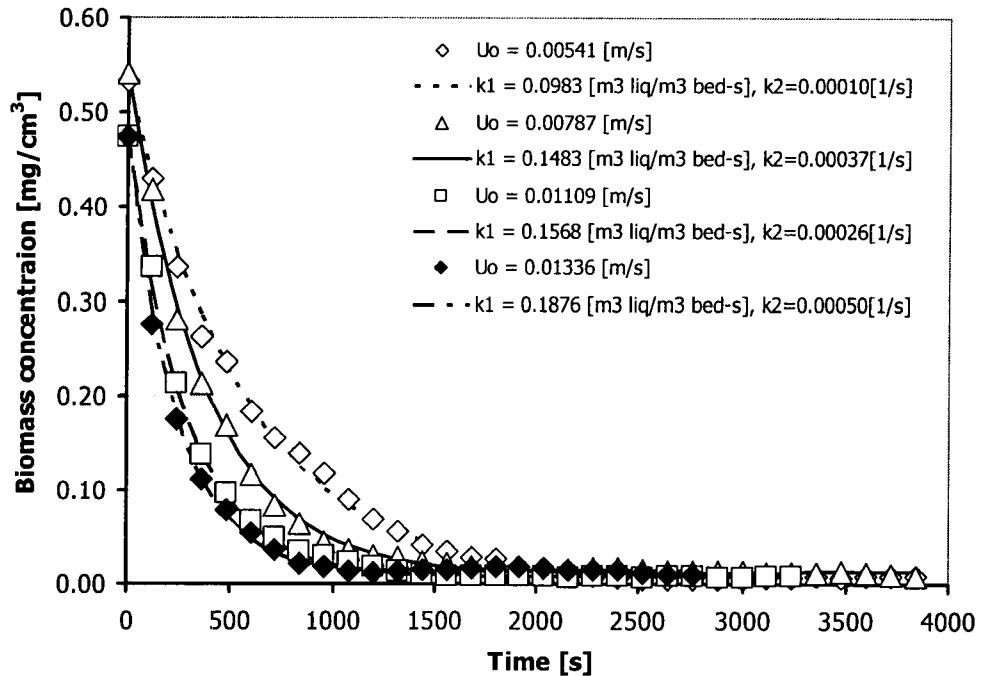


**Figure 5.32** Change of biomass concentration in the holding tank,  $d_p = 2.5$  mm,  $D_p = 73.52$   $\mu$ m,  $dH_z/dz = -38,817$  A/m/m,  $C_0 \sim 0.51$  [mg/cm³], and packed bed condition.

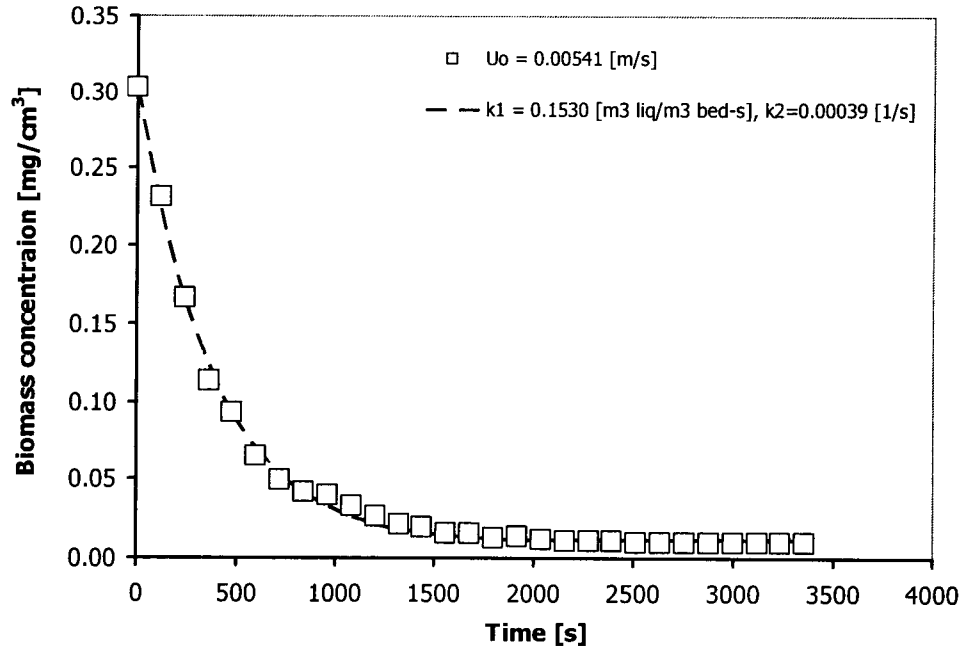


**Figure 5.33** Change of biomass concentration in the holding tank,  $d_p = 2.5$  mm,  $D_p = 114.68$   $\mu$ m,  $dH_2/dz = -38,817$  A/m/m,  $C_0 \sim 0.30$  [mg/cm³], and packed bed condition.

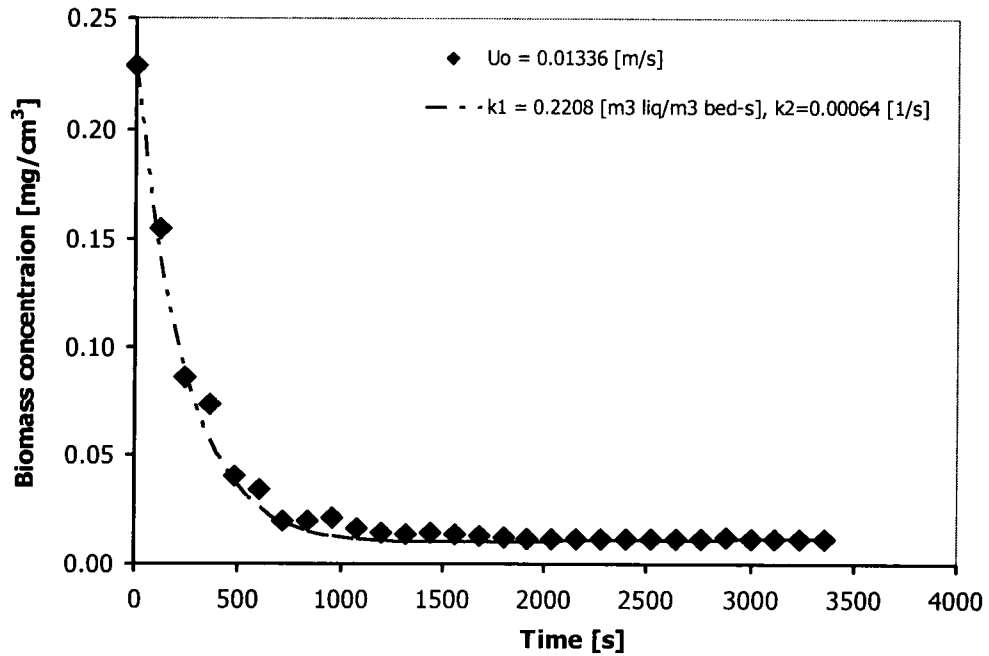


**Figure 5.34** Change of biomass concentration in the holding tank,  $d_p = 2.5$  mm,  $D_p = 114.68$   $\mu$ m,  $dH_2/dz = -38,817$  A/m/m,  $C_0 \sim 0.22$  [mg/cm³], and packed bed condition.

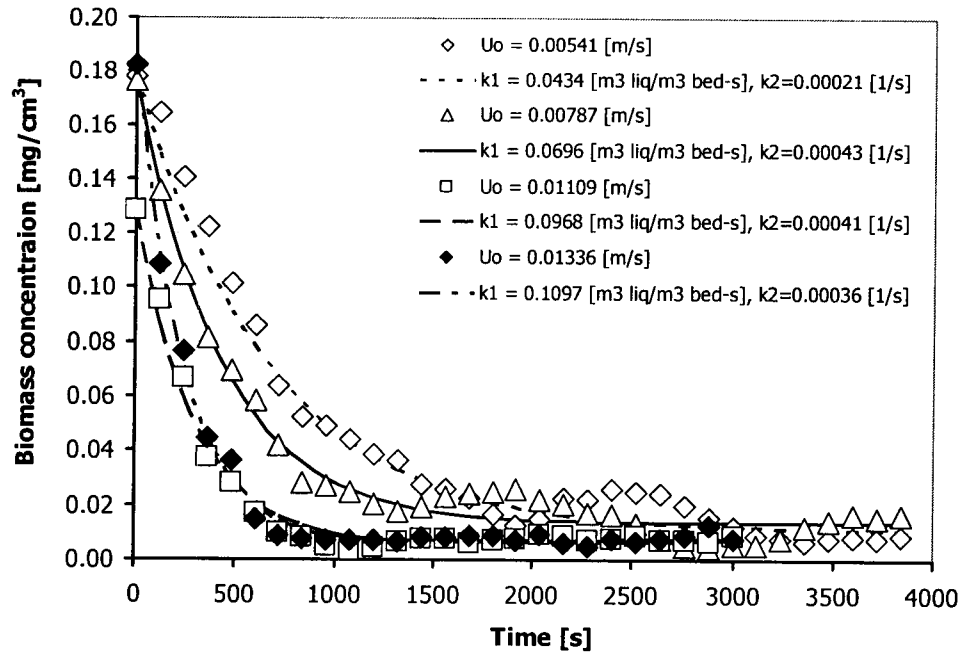


**Figure 5.35** Change of biomass concentration in the holding tank,  $d_p = 3.5$  mm,  $D_p = 73.52$   $\mu$ m,  $dH_z/dz = -38,817$  A/m/m,  $C_0 \sim 0.18$  [mg/cm³], and packed bed condition.

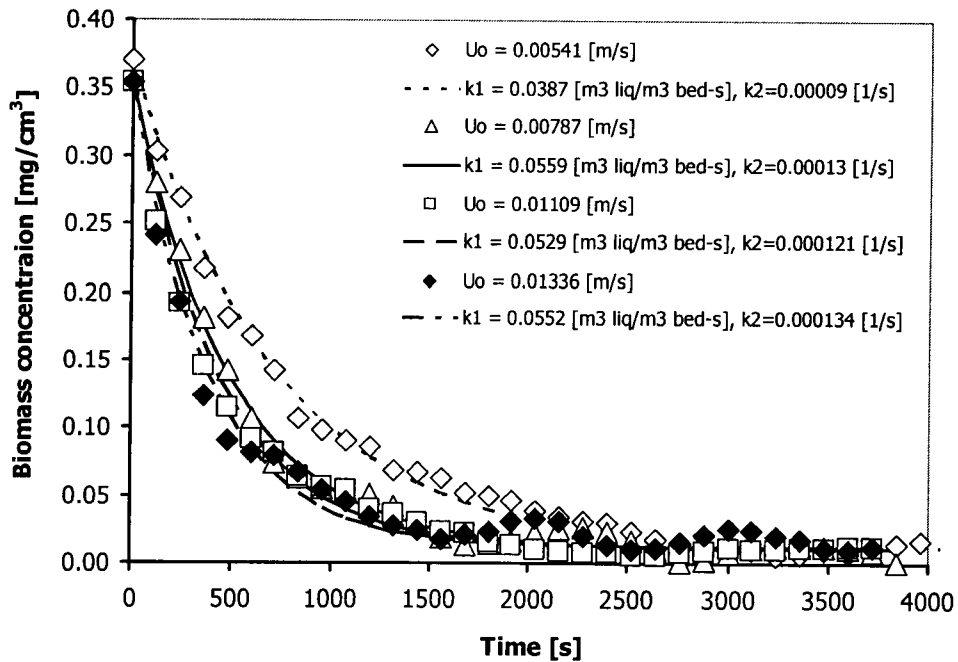


**Figure 5.36** Change of biomass concentration in the holding tank,  $d_p = 3.5$  mm,  $D_p = 73.52$   $\mu$ m,  $dH_z/dz = -38,817$  A/m/m,  $C_0 \sim 0.35$  [mg/cm³], and packed bed condition.

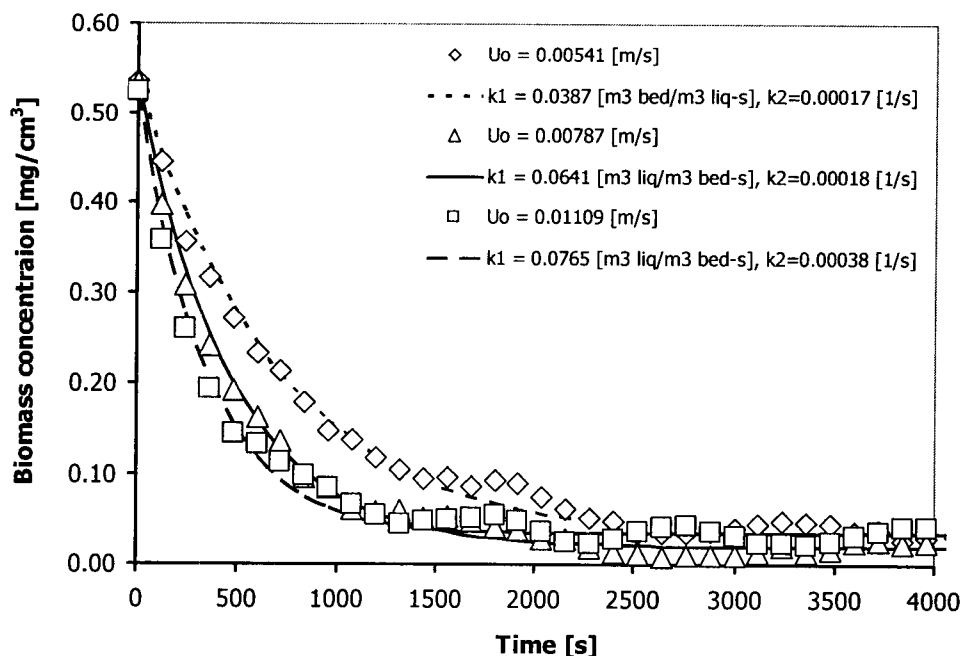


**Figure 5.37** Change of biomass concentration in the holding tank,  $d_p = 3.5$  mm,  $D_p = 73.52$   $\mu$ m,  $dH_z/dz = -38,817$  A/m/m,  $C_0 \sim 0.53$  [mg/cm³], and packed bed condition.

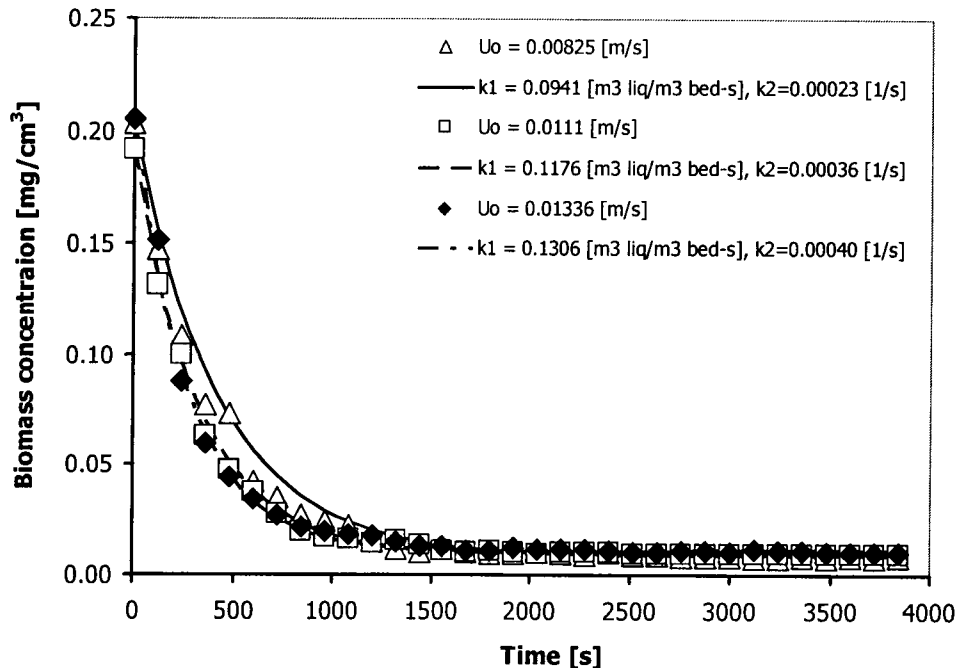


**Figure 5.38** Change of biomass concentration in the holding tank,  $d_p = 3.5$  mm,  $D_p = 114.68$   $\mu$ m,  $dH_z/dz = -38,817$  A/m/m,  $C_0 \sim 0.20$  [mg/cm³], and packed bed condition.

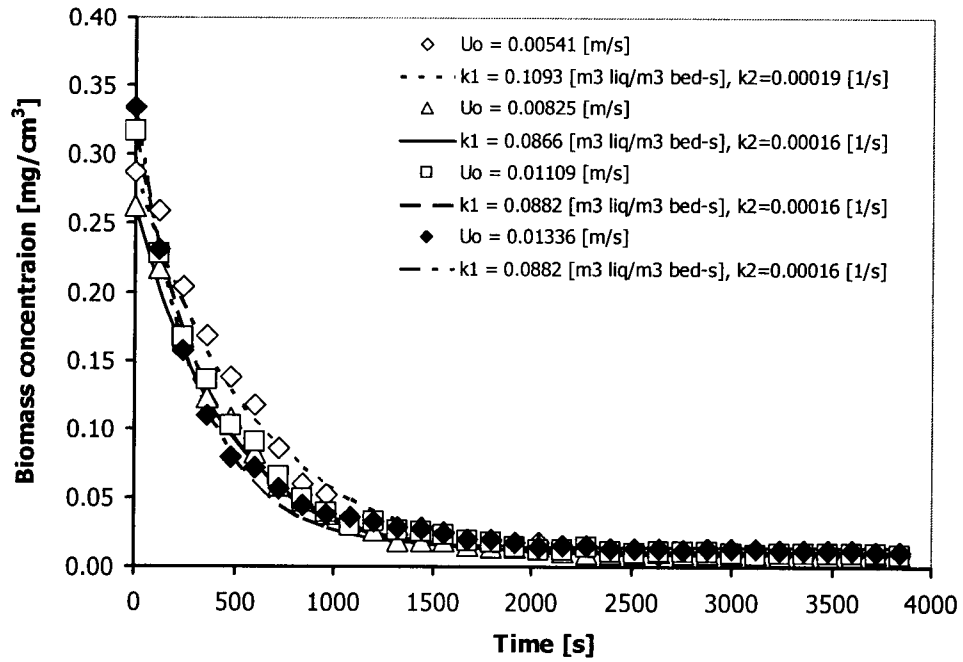


**Figure 5.39** Change of biomass concentration in the holding tank,  $d_p = 3.5$  mm,  $D_p = 114.68$   $\mu$ m,  $dH_z/dz = -38,817$  A/m/m,  $C_0 \sim 0.31$  [mg/cm³], and packed bed condition.

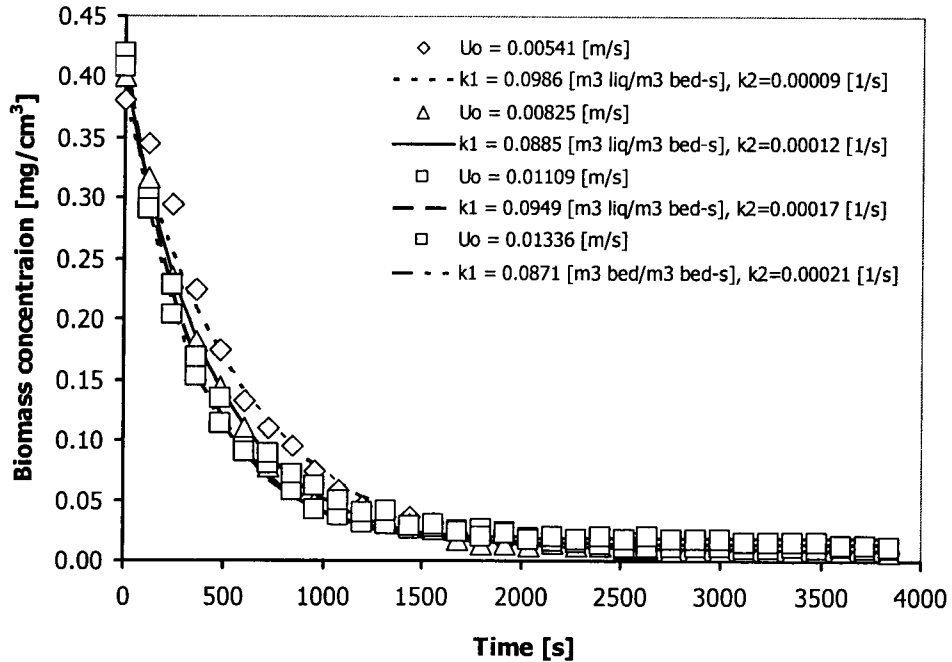


**Figure 5.40** Change of biomass concentration in the holding tank,  $d_p = 3.5$  mm,  $D_p = 114.68$   $\mu$ m,  $dH_z/dz = -38,817$  A/m/m,  $C_0 \sim 0.40$  [mg/cm³] and packed bed condition.

In this study, we found that the accumulation coefficient is related to two mechanisms involved in the deposition of straw particles, namely, direct interception and inertial impaction. The effect of electrostatic attraction mechanisms can be verified by adjusting the pH of deionized water (pH = 3.6, 7.0 and 9.8) in the filtration system, as shown in Figure 5.41. The changes in pH will vary the effective surface charges of the particles (Akse (2001)). The filtration experimental results show that there is no difference in the filtration rate at different pH. Therefore, there is no evidence of an electrostatic mechanism playing a role in this filtration process.

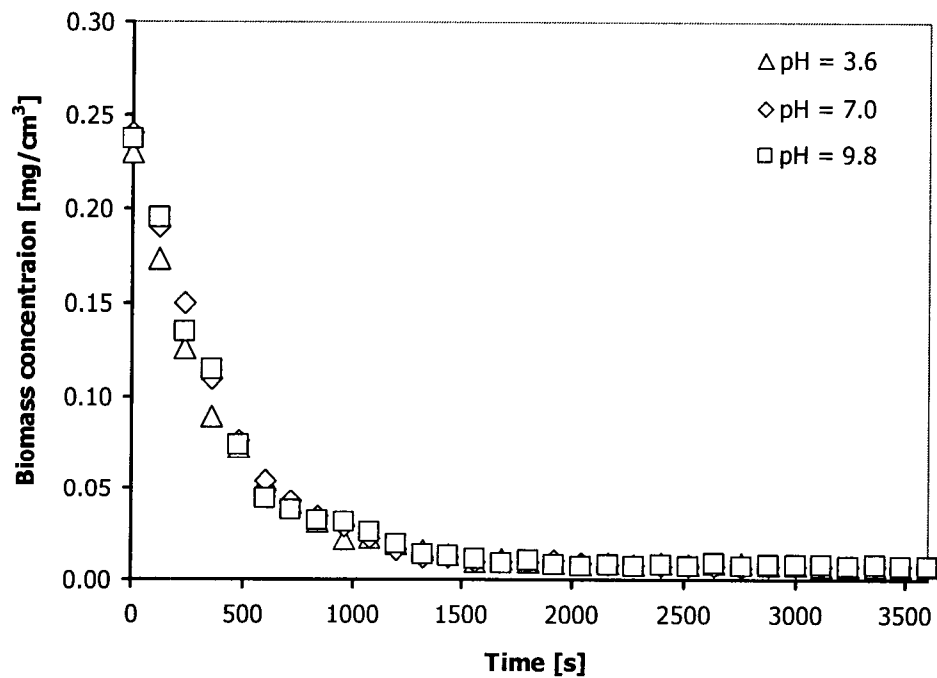


**Figure 5.41** Change of biomass concentration in the holding tank at different pH,  $d_p = 3.5$  mm,  $D_p = 73.52$   $\mu$ m,  $U_0 = 0.00825$  m/s,  $dH_z/dz = -38,817$  A/m/m and packed bed condition.



Black (1967) suggested that if the value of the Peclet number (in the Brownian diffusion mechanism) is much above 100, the collection efficiency by this mechanism can be ignored. Typically estimated Peclet number in our experiments is at the order of  $10^6$ , therefore; Brownian diffusion deposition mechanism is negligible.

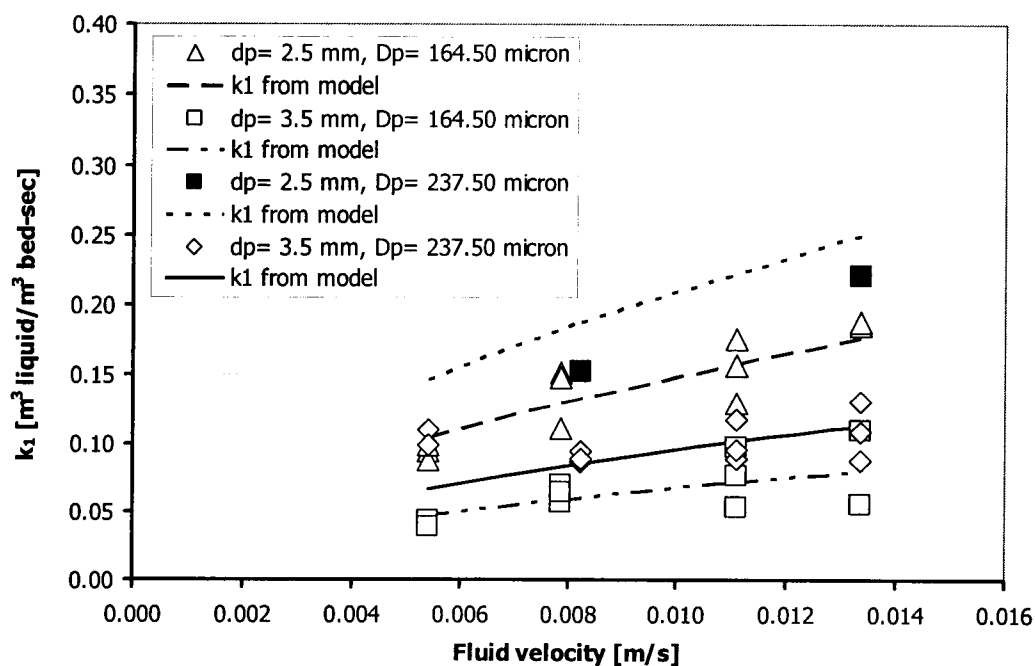
As previously mentioned in section 3.6, the three different methods for estimation of biomass particle diameter were employed in this study. The general form of the correlation for the accumulation coefficient ( $k_I$ ) derived from dimensional analysis (see Appendix I), as a function of hydrodynamic and geometric parameters of the filtration system is proposed as follows;

$$\frac{k_I D_p}{U_0} = a \left( \frac{D_p}{d_p} \right)^b \left( \frac{U_0 (\rho_{str} - \rho_f) D_p^2}{\mu_f d_p} \right)^c \quad (5-3)$$

The values of  $a$ ,  $b$ , and  $c$  depend on characteristic length scales  $D_p$  and  $d_p$ . The length scales  $d_p$  was measured with high accuracy. However, determining the characteristic nominal length scale of waste particles depends on the measuring technique as indicated in section 3.6. The values of  $a$ ,  $b$ , and  $c$ , within the range of our experimental results, are listed in Table 5.3. Figures 5.42 to 5.44 illustrate the values of  $k_I$  derived using the different particle diameter measurement methods.

**Table 5.3** Values of parameters in the accumulation correlation

Method	Parameter	Est. Value	Standard Error	T Statistic	P-Value
<b>Sieve Screen Analysis</b>	Ln (a)	-0.41	0.50	-0.82	0.4163
	b	2.77	0.24	11.43	0.0000
	c	-0.42	0.09	-4.48	0.0001
<b>Centrifugal Sedimentation</b>	Ln (a)	0.01	0.55	0.02	0.9867
	b	2.74	0.23	11.80	0.0000
	c	-0.45	0.09	-4.93	0.0000
<b>Microscope Analysis</b>	Ln (a)	-1.27	0.34	-3.71	0.0008
	b	2.77	0.25	11.29	0.0000
	c	-0.41	0.09	-4.35	0.0001

**Figure 5.42** Correlation for the accumulation coefficient ( $k_1$ ) obtained from intermediate size screen analysis.

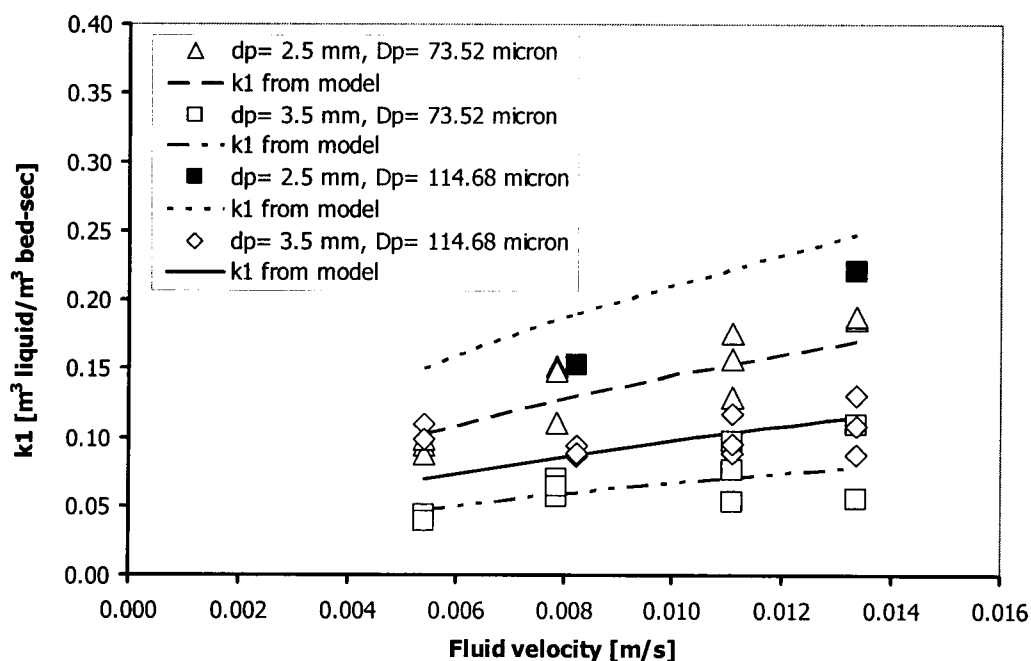


**Figure 5.43** Correlation for the accumulation coefficient ( $k_1$ ) obtained from centrifugal sedimentation particle size analysis.

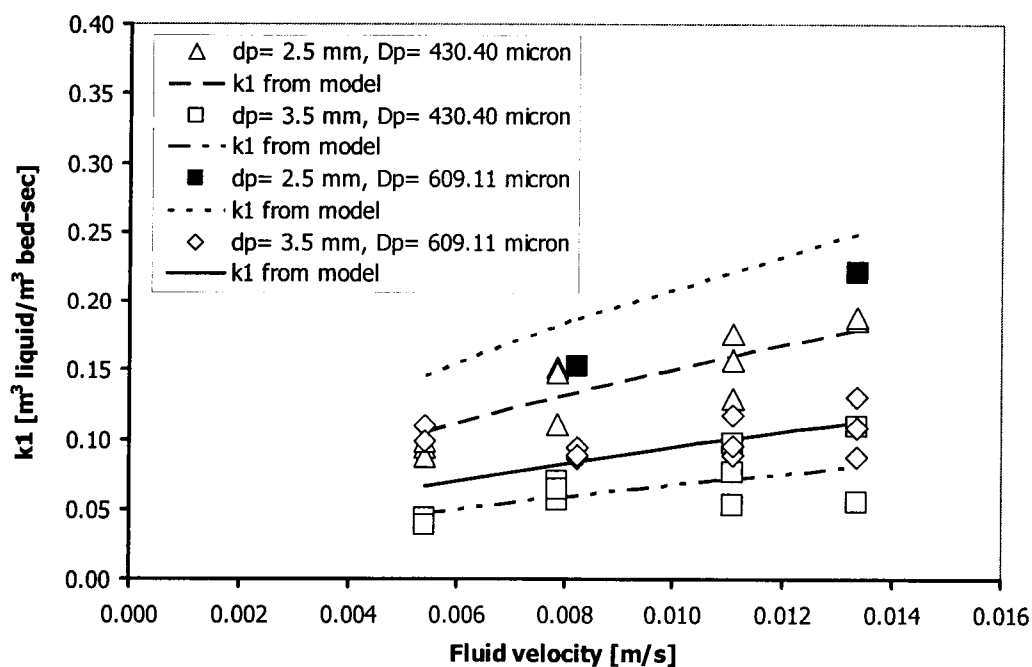


**Figure 5.44** Correlation for the accumulation coefficient ( $k_1$ ) obtained from optical microscope analysis.

The analysis leading toward the correlation for the detachment coefficient ( $k_2$ ) is somewhat different from the analysis related to the accumulation coefficient ( $k_1$ ). We experimentally observed that the deposited waste biomass is in the form of particle clumps and/or bio-waste film, which surrounds fluidization particle. Therefore, straw particles in the bio-waste film loose their 'identity' and they interact with the fluid as a solid bio-film. Consequently, we may assume that the nominal diameter of waste particles ( $D_p$ ) will not play an important role in the correlation for the detachment mechanism. Local fluid flow condition characterized by a local velocity ( $U_o$ ) and the size of the fluidization particles ( $d_p$ ), is much more likely to play a role in the detachment mechanism. Furthermore, the ratio between fluidization particle diameter ( $d_p$ ) and the fluidization column diameter ( $D_{col}$ ) may also play a role in the detachment mechanism. It is well accepted in the fluidization practice that column to particle ratio must be larger than 20 [ $(D_{col}/d_p) > 20$ ] if the influence of column walls on fluidization phenomena should be considered negligible. The  $(D_{col}/d_p)$  ratio in our experiments was in the range of 14.39 - 20.14 which is close to the recommended value. Unfortunately all our experiments were performed in a single column and we could not test the influence of this parameter on the correlation for the detachment coefficient.

We first investigated the interdependence between the coefficient  $k_2$  and the two fluidization parameters  $U_o$  and  $d_p$ ,

$$k_2 = e U_o^f d_p^g \quad (5-4)$$

and found relatively strong interdependence as represented through correlation statistics in Table 5.4.

**Table 5.4** Values of parameter in the detachment correlation

Method	Parameter	Est. Value	Standard Error	T Statistic	P-Value
<b>All Three Particle Size Analysis</b>	Ln (e)	-15.69	2.77	-5.67	0.0000
	f	0.75	0.22	3.44	0.0017
	g	-1.90	0.45	-4.23	0.0002

Therefore,

$$k_2 = 1.53 \times 10^{-7} U_0^{0.75} d_p^{-1.9} \quad (5-5)$$

The above correlation can be rewritten, without any loss of generality, in the following form:

$$\frac{k_2 d_p}{U_0} = 3.2 \times 10^{-5} \left( \frac{d_p}{D_{col}} \right)^{-0.65} \left( \frac{d_p U_0 \rho_f}{\mu_f} \right)^{-0.25} \quad (5-6)$$

Figure 5.45 illustrates how the above correlation fits the experimental data. Notice, that the nominal diameter of the bio-waste particle is not included in the definition of this correlation. The standard error of coefficient e, f, and g in the above correlation are larger than the corresponding errors obtained in the correlation for the accumulation coefficient  $k_1$ . This is a consequence of the fact that the accuracy of the correlation for the detachment coefficient  $k_2$  predominantly depends on the accuracy of data at the end of the filtration process. Since the concentration of the biomass waste at the end of the filtration process was typically very close to zero, the experimental 'noise' at this level of

concentrations was of the same order of magnitude as measured concentrations. Therefore, significant uncertainties are involved in the above correlation, thus its lower accuracy.

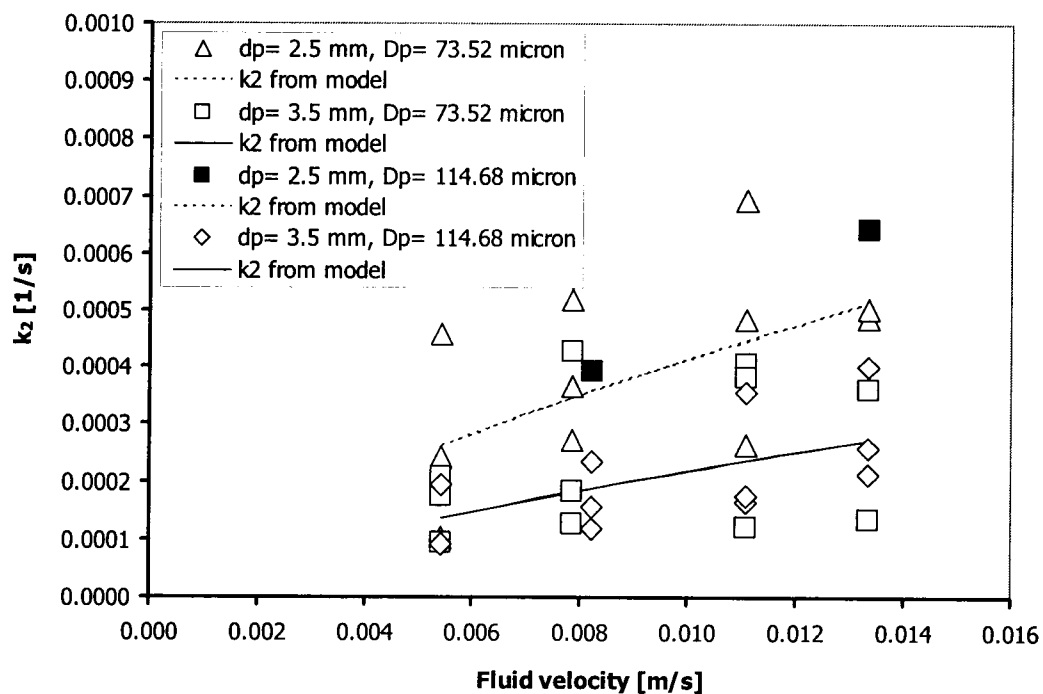


**Figure 5.45** Correlation for the detachment coefficient ( $k_2$ ).

## CHAPTER 6

### DISCUSSION, CONCLUSIONS AND RECOMMENDATIONS

#### 6.1 Discussion

##### 6.1.1 Discussion of voidage distribution experiments

From the experimental data and the voidage distribution model presented in Section 5.1, we can conclude the following:

(i) The experiments conducted with the Gradient-Magnetically Assisted Fluidized Bed (G-MAFB) under non-uniform magnetic field conditions proved that magnetic forces may be employed as a means for controlling bed voidage and height in normal gravity and for producing stable fluidization in a microgravity environment. The magnitude of the additional magnetic force is dependent on both the magnetic field intensity and the field gradient. Experimental observations demonstrate that the magnetic forces play a major role in keeping the ferromagnetic particles from escaping from the bed under microgravity conditions. Without the magnetic force, it is not possible to maintain the particles in the fluidized state. As shown in Figures 5.1 and 5.2, the height of the bed, at any given fluid velocity, decreases as the field intensity and the field gradient increase. As a result, the average bed porosity decreases as the magnetic field intensity and field gradient increase, for any given superficial fluid velocity. The previous studies

by Al-Mulhim (1995) and Rhee (1998) proved that decreasing the bed voidage results in a better particle-fluid mass transfer. Therefore, based on observed behavior, one may conclude that the magnetically fluidized bed will also enhance the mass transfer rate and improve the chemical conversion efficiency.

(ii) We are able to predict the voidage distribution in the G-MAFB in both 0g and normal 1g conditions. In the proposed model, the Discrete Particle Method (DPM) approach is successfully used as an investigative tool for the Two-Continuum Phase (TCP) representation of fluidized beds. In developing the model, the magnetic interparticle forces used in the DPM is transformed into a particle-phase modulus of elasticity which is then used in the TCP model. The proposed model describes very well the experimental data obtained from both laboratory and 0g experiments. An example of the typical corresponding elastic modulus at any location in the G-MAFB is shown in Figure 6.1. As expected, the elastic modulus is higher at the bottom of the bed and gradually decreases toward the top of the bed according to the magnitude of the magnetic force acting on the ferromagnetic particles.

(iii) The overall accuracy of the proposed model is verified by comparing the mass obtained from the voidage distribution predicted by the model to the actual mass, and it falls within 12.5% maximum error in the 1g experiments and 17.3% maximum error in the 0g experiments. It is noted that the calculated masses from the laboratory experiments are consistently lower than the exact masses. The calculated masses from the laboratory experiments are based on the dynamic pressure drop, which is difficult to measure and may involve an error up



to 4%. In addition, particles exchange momentum with the column wall and the distributor plate. This undoubtedly reduces the dynamic pressure drop. Therefore, the calculated mass from experiments is always lower than the actual mass.

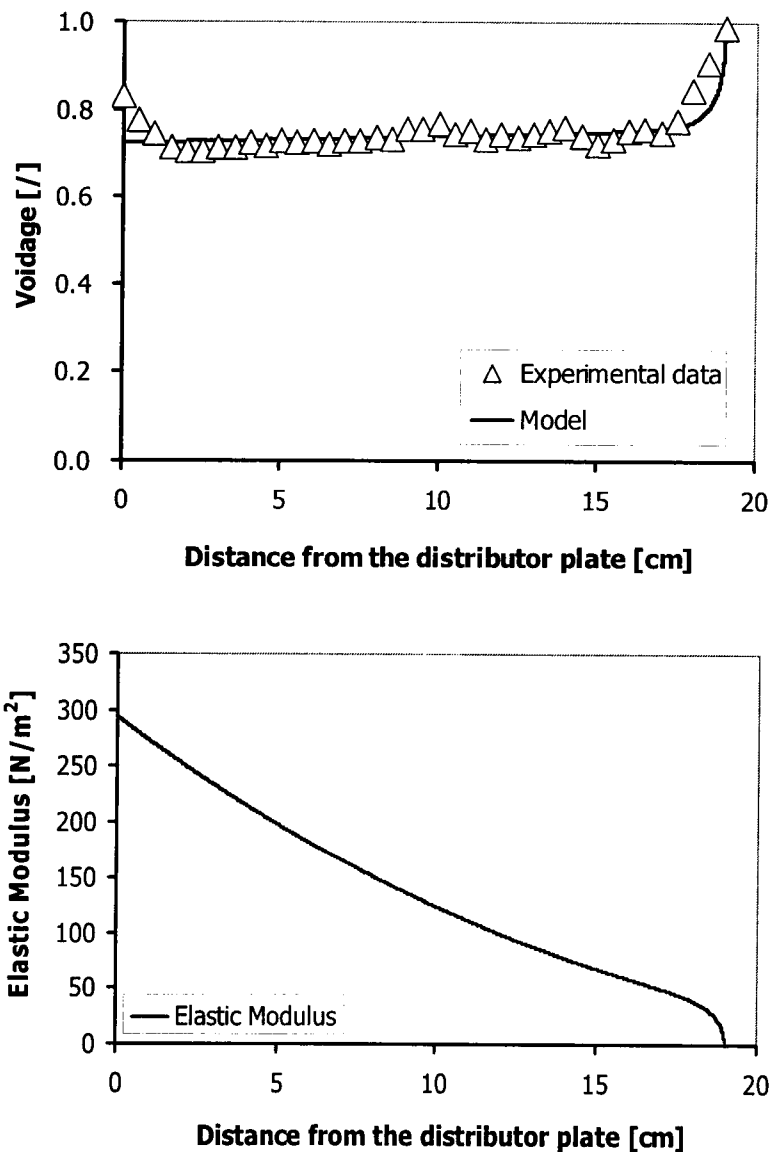


**Figure 6.1** Voidage distribution and elastic modulus of particle A in the G-MAFB,  $dH_z/dz = -20,543 \text{ A/m/m}$ ,  $U_o = 0.0222 \text{ m/s}$ , and  $h_{bed} = 0.190 \text{ m}$ .

### 6.1.2 Discussion of filtration experiments

From the experiment results shown in Figures 5.30 to 5.40, we can conclude the following:

(i) At a given magnetic field intensity and gradient, the filtration rate increases as the fluid superficial velocity increases. In these experiments, the concentration of the waste particles was substantially lowered during the filtration process. However, the concentration of waste particles remains constant after it reaches the steady state. The filtration process can be characterized by the rate of accumulation of waste particles in the bed and the rate of detachment of already-filtered particles. Figure 6.2 shows an example of our experimental results. Although we were not able to directly measure the change of the filtration media diameter and associated change of voidage distribution inside the bed, and the mass distribution of waste particle inside the bed, the developed model gave us an insight how these important variables were changing along the bed height. The data shown in Figures 6.3, 6.4, and 6.5 represent the corresponding changes in the filtration media diameter, waste particle mass deposited inside the G-MAFB, and voidage, respectively, as the filtration operation progresses. Figure 6.6 shows the comparison between actual mass and mass obtained from the proposed model.

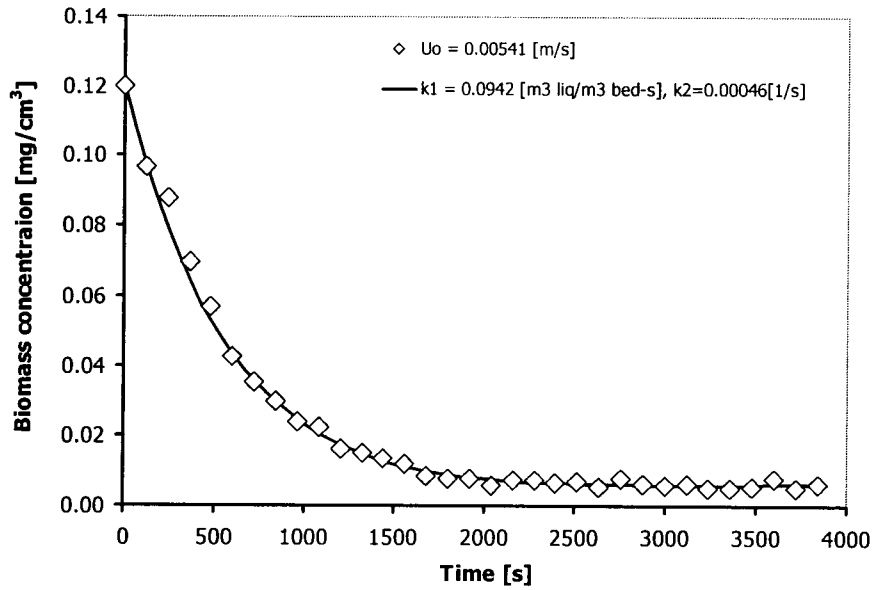


**Figure 6.2** Change of biomass concentration in the holding tank,  $d_p = 2.5$  mm,  $D_p = 73.52$   $\mu\text{m}$ ,  $dH_z/dz = -38,817$  A/m/m and packed bed condition.

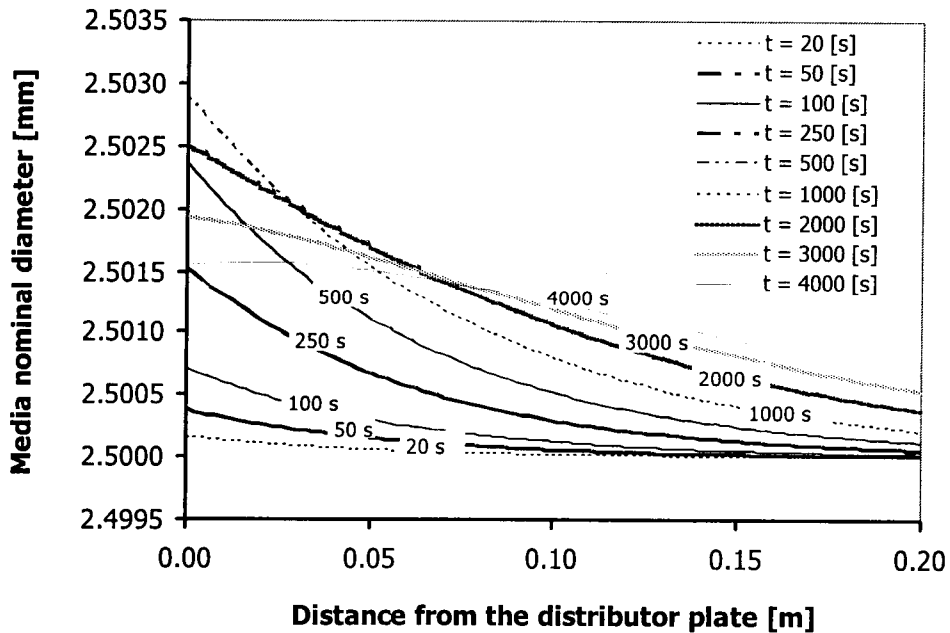


**Figure 6.3** Changes of media particle diameter inside the G-MAFB with time,  $d_{p,0} = 0.0025$  m.

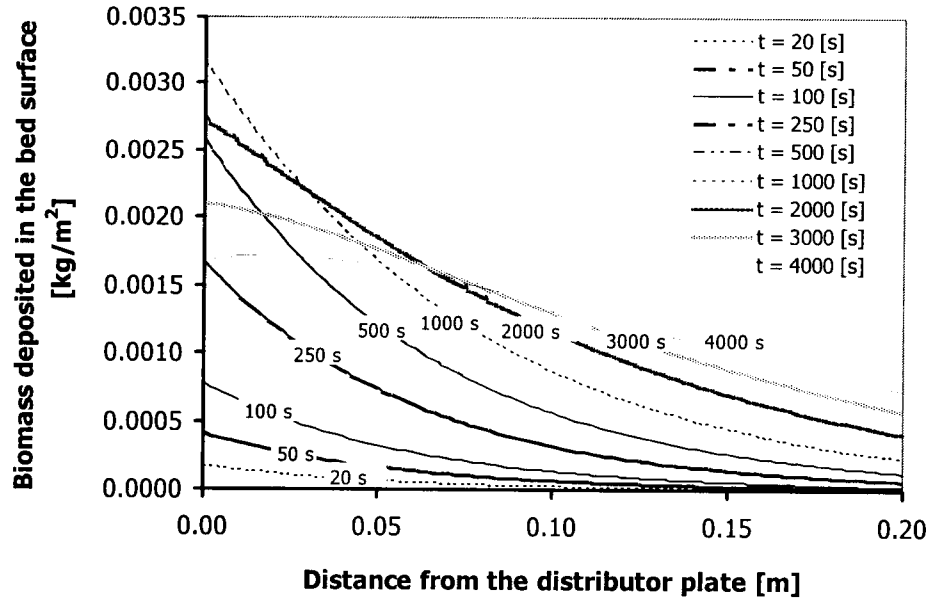


**Figure 6.4** Changes of biomass concentration deposited inside the G-MAFB with time.

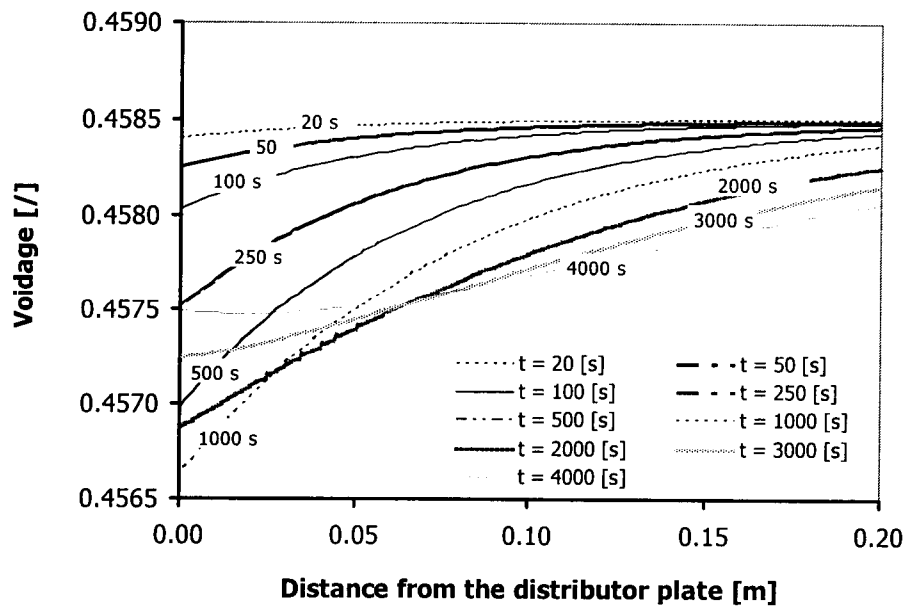


**Figure 6.5** Changes of voidage in the G-MAFB with time,  $\varepsilon_0 = 0.46$ .

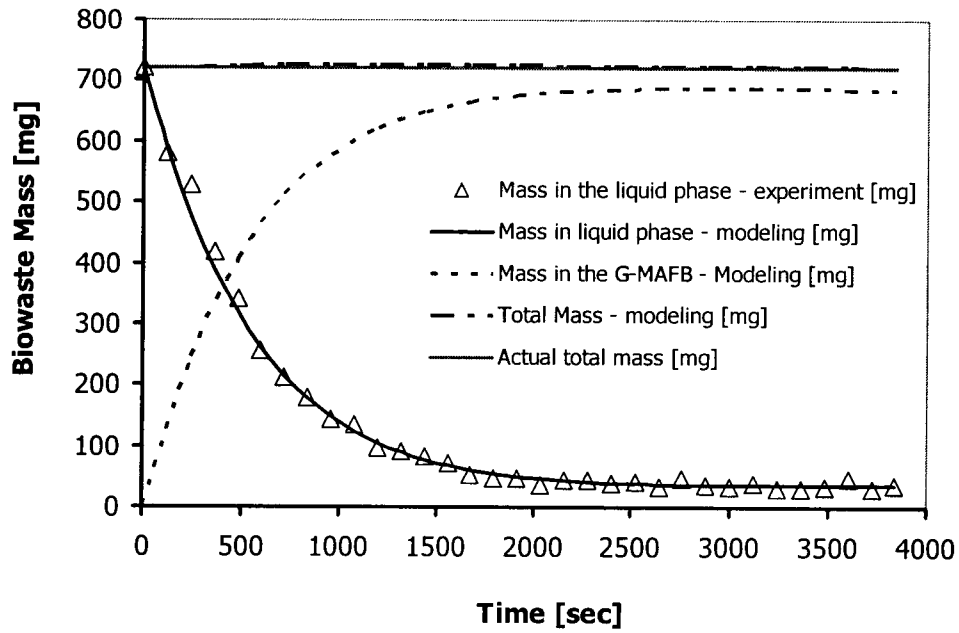


**Figure 6.6** Comparison of mass obtain from experiment and proposed model in the G-MAFB system.

(ii) In this study, the bench-scale G-MAFB was built as a part of a solid waste destruction process, as previously shown in Figure 2.7. With the proposed correlations for accumulation coefficient ( $k_1$ ) and detachment coefficient ( $k_2$ ), the changes of biomass particle concentration, media, and voidage of the G-MAFB, can be readily estimated.

In the filtration experiment in the bench-scale G-MAFB, the biomass waste particles,  $D_p = 73.52 \mu\text{m}$ , are filtered in fluidization media,  $d_p = 2.7 \text{ mm}$ , in bed height  $h_{\text{bed}} = 0.35 \text{ m}$ , at fluid velocity,  $U_0 = 0.01957 \text{ m/s}$ . The corresponding  $k_1$  and  $k_2$  from the correlations are found to be  $0.1764 [\text{m}^3\text{liquid}/\text{m}^3\text{bed-sec}]$  and

0.00059 [1/s], respectively. The predicted change in biomass concentration in the holding tank as the filtration progresses is shown in Figure 6.7. This figure clearly demonstrates that the predicted changes in biomass concentration in the holding tank are in good agreement with the experimental data. Figures 6.8, 6.9, and 6.10 represent the predicted changes in the filter media particle diameter, biowaste mass deposited within the G-MAFB, and voidage distribution, respectively, as the filtration progresses. Figure 6.11 shows the predicted changes in mass within the G-MAFB and in the holding tank obtained from the proposed model.

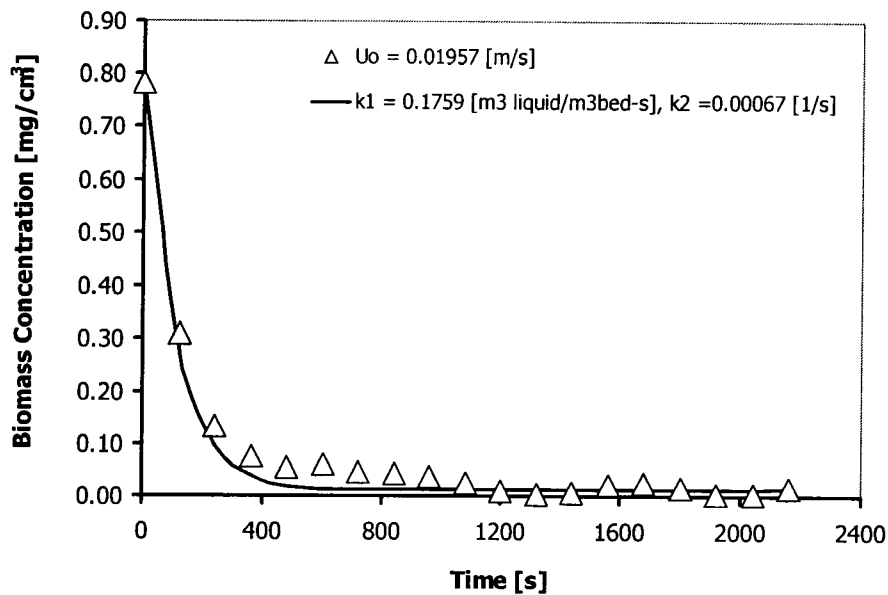


**Figure 6.7** Predicted changes of biomass concentration in the holding tank ( $d_p = 2.7$  mm,  $C_0 = 0.782$  mg/cm<sup>3</sup>,  $V_{\text{tank}} = 8,000$  cm<sup>3</sup>,  $U_0 = 0.01957$  m/s, and  $h_{\text{bed}} = 0.35$  m).

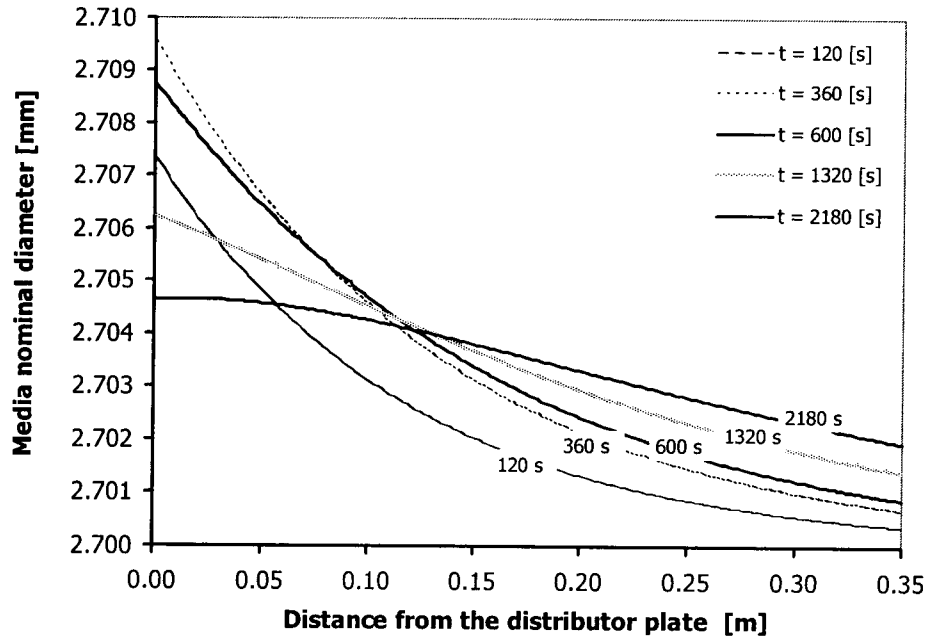


**Figure 6.8** Predicted changes of media particle diameter in the G-MAFB with time ( $d_p = 2.7$  mm,  $C_0 = 0.782$  mg/cm<sup>3</sup>,  $V_{\text{tank}} = 8,000$  cm<sup>3</sup>,  $U_0 = 0.01957$  m/s, and  $h_{\text{bed}} = 0.35$  m).

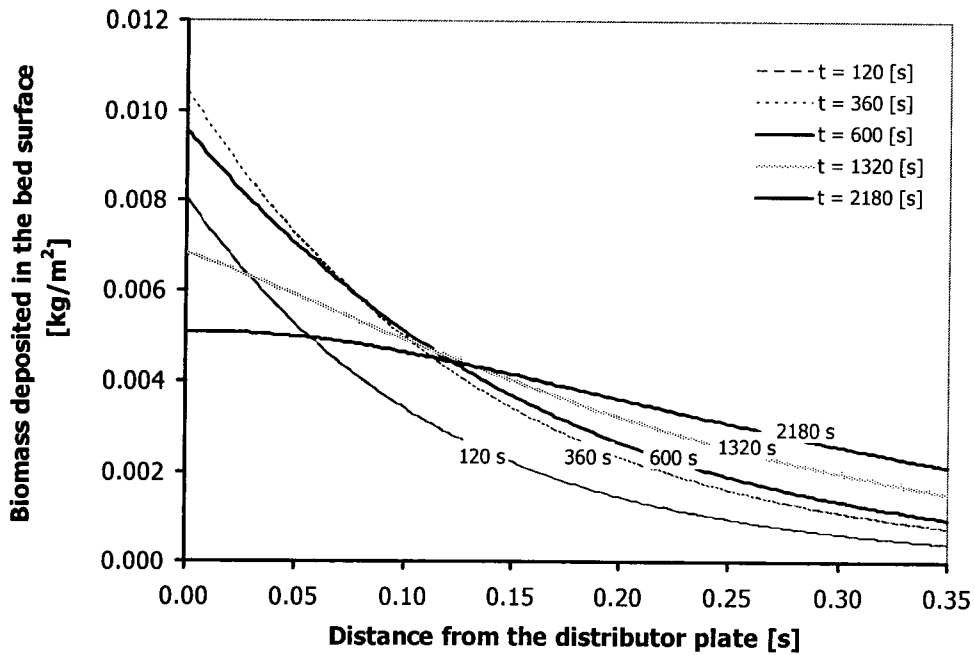


**Figure 6.9** Predicted changes of mass deposited in the G-MAFB with time ( $d_p = 2.7$  mm,  $C_0 = 0.782$  mg/cm<sup>3</sup>,  $V_{\text{tank}} = 8,000$  cm<sup>3</sup>,  $U_0 = 0.01957$  m/s, and  $h_{\text{bed}} = 0.35$  m).

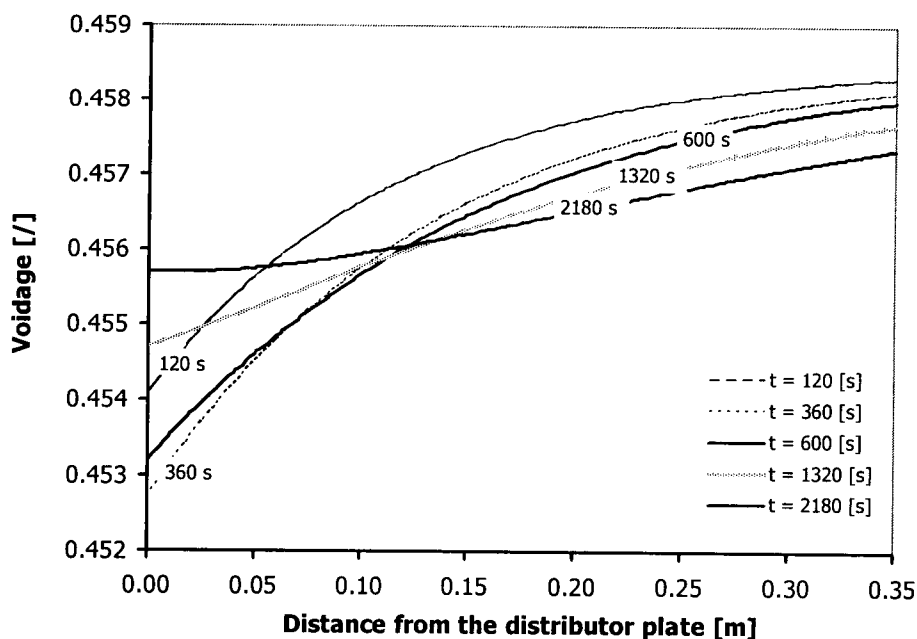


**Figure 6.10** Predicted changes of voidage distribution in the G-MAFB with time ( $d_p = 2.7$  mm,  $C_0 = 0.782$  mg/cm<sup>3</sup>,  $V_{\text{tank}} = 8,000$  cm<sup>3</sup>,  $U_0 = 0.01957$  m/s, and  $h_{\text{bed}} = 0.35$  m).

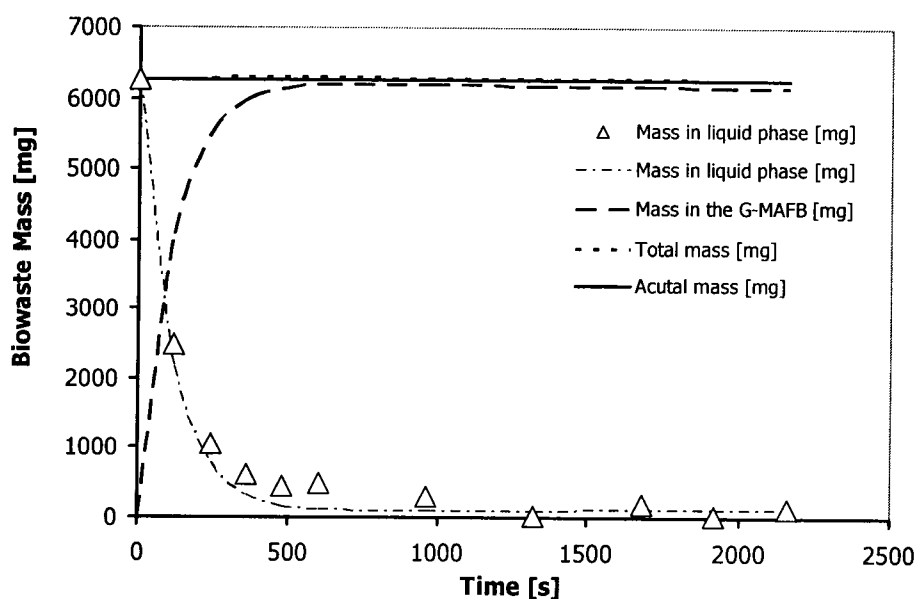


**Figure 6.11** Predicted changes of mass in the G-MAFB system with time ( $d_p = 2.7$  mm,  $C_0 = 0.782$  mg/cm<sup>3</sup>,  $V_{\text{tank}} = 8,000$  cm<sup>3</sup>,  $U_0 = 0.01957$  m/s, and  $h_{\text{bed}} = 0.35$  m).



## 6.2 Conclusions

The influence of the magnetic field and the field gradient on the G-MAFB observed in the laboratory experiments agrees well with the experiments performed in the 0g environment. The experiments showed that the magnetic force plays an important role in controlling the bed voidage and the height of the bed:

- (i) at a given magnetic field intensity,  $H_z$ , and field gradient, with  $dH_z/dz$  constant, the height of the bed increases as the superficial fluid velocity increases:
- (ii) at a given fluid superficial velocity,  $U_0$ , the height of the bed,  $h$ , decreases as the magnetic field intensity and its gradient increase.

The magnetic force is dependent on the magnetic field intensity and the field gradient. In our experiments, the magnetic field gradient was kept constant. The magnetic field intensity was greatest at the bottom of the column and gradually decreased toward the top. The magnetic force acting on particles, therefore, was directed downward toward the distributor plate and was most intense at the bottom decreasing with increasing height of the bed. As a result, the particle holdup (voidage) varies within the bed as a function of bed height.

The voidage distribution model developed in this study is based on the four governing equations, namely, the equations of motion and the equations of continuity in both liquid and particle phases. In addition, in the equation of motion for particle phase, the magnetic interparticle forces used in the DPM

approach are transformed into a particle-phase modulus of elasticity, representing the shear stress in the particle phase. The resulting expression of the voidage distribution is given as:

$$\frac{\partial \varepsilon}{\partial z/L} = \frac{\varepsilon^3 - \alpha(1 - \varepsilon) - \varphi - \gamma H_z \varepsilon^3}{\lambda E \varepsilon^3} \quad (4-20)$$

with boundary conditions:  $z/L = 1, \varepsilon = 1$

The parameters in Equation (4-20) are defined as:

$$\alpha = \frac{150 \mu_f U_0}{d_p^2 (\rho_p - \rho_f) g} \quad (4-16)$$

$$\varphi = \frac{1.75 \rho_f U_0^2}{d_p (\rho_p - \rho_f) g} \quad (4-17)$$

$$\lambda = \frac{1}{(\rho_p - \rho_f) g L} \quad (4-18)$$

$$\gamma = \frac{\mu_0 \chi}{(\rho_p - \rho_f) g} \frac{\partial H_z}{\partial z} \quad (4-19)$$

$$E = \frac{d_p}{A_p} \frac{12 (\chi V_p \mu_0 H_z)^2 \pi (8 \pi^2 r^6 + 12 \pi^3 \chi V_p + \chi^2 V_p^2)}{\mu_0 (-2 \pi^3 + \chi V_p)^4} \quad (2-18)$$

$$r = d_p + \frac{d_p}{m} \sqrt{\frac{\pi (\varepsilon - \varepsilon_0)}{6(1 - \varepsilon)}} \quad (5-2)$$

where  $m = 4.14$  for 1g environment

The experimental results derived in the laboratory agree well with the predictions derived from the model. The experiments in the 0g environment onboard the NASA KC-135 aircraft also proved that the magnetic force has a significant role in keeping the particles from escaping from the bed. The voidage distribution model in the absence of the gravity is expressed as:

$$\frac{\partial \varepsilon}{\partial z} = \frac{-\alpha(1-\varepsilon) - \varphi - \gamma H_z \varepsilon^3 \frac{\partial H_z}{\partial z}}{E \varepsilon^3} \quad (4-21)$$

$$\alpha = \frac{150 \mu_f U_0}{d_p^2} \quad (4-22)$$

$$\varphi = \frac{1.75 \rho_f U_0^2}{d_p} \quad (4-23)$$

$$E = \frac{d_p}{A_p} \frac{12(\chi V_p \mu_0 H_z)^2 \pi r (8\pi^2 r^6 + 12\pi^3 \chi V_p + \chi^2 V_p^2)}{\mu_0 (-2\pi^3 + \chi V_p)^4} \quad (2-18)$$

$$r = d_p + \frac{d_p}{m} \sqrt{\frac{\pi(\varepsilon - \varepsilon_0)}{6(1-\varepsilon)}} \quad (5-2)$$

where  $m = 1.75$  for 0g environment.

The proposed model describes very well the experimental data obtained from 0g experiments.

The feasibility of the G-MAFB as a renewable filter, utilizing magnetic force to achieve stable fluidization, has been successfully demonstrated in our study. This technology has many potential areas of application. Filtration experiments conducted in the laboratory have shown that the G-MAFB based methods can

successfully separate biomass waste particles from a recirculating liquid stream. Within the range of fluid velocities used in the filtration experiments, the rate of filtration increases with the fluid velocity. The correlation of the accumulation, as a function of hydrodynamic and geometric parameters of the filtration system, are proposed as:

Sieve Screen Analysis:

$$\frac{k_1 D_p}{U_0} = 0.67 \left( \frac{D_p}{d_p} \right)^{2.77} \left( \frac{U_0 (\rho_{str} - \rho_f) D_p^2}{\mu_f d_p} \right)^{-0.42} \quad (6-1)$$

Centrifugal Sedimentation Analysis:

$$\frac{k_1 D_p}{U_0} = 1.01 \left( \frac{D_p}{d_p} \right)^{2.74} \left( \frac{U_0 (\rho_{str} - \rho_f) D_p^2}{\mu_f d_p} \right)^{-0.45} \quad (6-2)$$

Microscope Analysis

$$\frac{k_1 D_p}{U_0} = 0.28 \left( \frac{D_p}{d_p} \right)^{2.77} \left( \frac{U_0 (\rho_{str} - \rho_f) D_p^2}{\mu_f d_p} \right)^{-0.41} \quad (6-3)$$

The correlation for detachment coefficient is proposed as;

$$\frac{k_2 d_p}{U_0} = 3.2 \times 10^{-5} \left( \frac{d_p}{D_{col}} \right)^{0.65} \left( \frac{d_p U_0 \rho_f}{\mu_f} \right)^{-0.25} \quad (5-6)$$

The contributions of this research to chemical engineering science can be summarized as follows:

1. There are two major approaches in modeling the fluid dynamic

behavior of the fluidization beds, discrete particle modeling (DPM) and two-continuum phase modeling. The DPM approach entails long computing time and is limited to the small number of particles that can be incorporated into numerical calculations. The two-continuum phase fluid model approach offers the advantage of less computing time than the DPM method. However, in the two-continuum phase model, the constitutive relationships of any terms that appear in the governing equations have to be defined explicitly in terms of fluid/particle properties. Other researchers (Rosensweig 1979 and Conan 1996) have studied the stability of the magnetically fluidized bed, but none of them incorporated the effect the interparticle force in their modeling. Even though Rietema (1977, 1990, 1993) investigated the interparticle force in a conventional fluidized bed and expressed the interparticle force in term of elastic modulus, his theoretical development is still not practical for use in fluidization simulation.

In our studies, the particle pressure and particle stress tensor, created by interparticle magnetic forces, are replaced explicitly with the elasticity term in the governing equations. The magnetic interparticle force developed and used in the Discrete Particle Method (Pinto-Espinoza, 2002) is transformed into the elastic modulus of the particulate phase used in the two-continuum phase model. This approach (combination of DPM and two-continuum phase modeling) in modeling fluidized beds could become a new paradigm for studying fluidization and processes performed in fluidized beds.

2. This study developed a new method for investigation of the

interparticle forces in fluidized beds. Unlike previous studies (Rietema (1977, 1990, 1993)) in which interparticle forces could not be readily controlled or even adjusted, in the present study, the magnitude and orientation of the interparticle forces could be controlled. The ability to generate any desired magnitude of interparticle forces allows us to study more precisely the influences of these forces on bed structure and bed performance.

3. This study generated the first experimental data ever recorded for fluidization in microgravity. It also provided new data and empirical correlations for filtration operations in the G-MAFB.

### **6.3 Recommendations**

For further studies, the following points are recommended:

1. In this study, the change of voidage distribution in the radius,  $r$ , direction due to the change of the magnetic force in that direction is negligible. However, one may want to investigate the variation of voidage in both the  $r$  and  $z$  directions.

2. The modeling of the fluid jets should be included in the equation of motion for the fluid and particle phases for 1g applications. For 0g application, this is not necessary.

3. In the filtration experiments, one may explore a wider range of particle sizes and experimental conditions to find an optimized state of this unit operation.

4. The filtration experiments with different media particle sizes deployed simultaneously in the fluidized bed (the larger diameter particles at the inlet and the smaller diameter particles at the outlet (stratification)) may provide very useful design of the filtration operation in G-MAFB.

5. In the filtration experiments, one may include a study of mass distribution inside the bed which would increase the predictability of the model.

## BIBLIOGRAPHY

Al-Mulhim, Mohammed (1995). Enhancement of Mass Transfer Coefficient in a Magnetically Stabilized Liquid-Solid Fluidized Bed. M.S. thesis, Chemical Engineering. Oregon State University. Corvallis, Oregon.

Anderson, T.B. and Roy Jackson (1967). "A Fluid Mechanical Description of Fluidized Bed." I&EC Fundamentals. **6** (4): 527-538.

Arnoldos, J., J. Casal, A. Lucus and L. Puigjaner (1985). "Magnetically Stabilized Fluidization: Modeling and Application to Mixture." Power Technology. **44**: 57-62.

Akse, J.R. and R. Dahl (2001), Sub-Micron Particle Removal from Gas-Water Mixtures without Flow Restrictions. Final Report, SBIR Phase I Contract NAS8-01024, National Aeronautics and Space Administration, Marshall Space Flight Center, Huntsville, Al.

Black, Charles Hartgraves (1966). Effectiveness of a Fluidized Bed in Filtration of Airborne Particulate of Submicron Size. Phd. Thesis, Mechanical Engineering. Oregon State University. Corvallis, Oregon.

Burns Mark A. and Graves David J. (1985). "Continuous Affinity Chromatography Using a Magnetically Stabilized Fluidized Bed." Biotechnology Progress. **1** (2): 95-103.

Burns Mark A. and Graves David J. (1988). "Structural Studies of A Liquid-Fluidized Magnetically Stabilized Bed." Chem. Eng. Comm. **67**: 315-330.

Conan J. Fee (1996). "Stability Of The Liquid-Fluidized Magnetically Stabilized Fluidized Bed." AIChE Journal. **42** (5): 1213-1219.

Cowley, M.D., and Rosensweig, R.E. (1967). "The Interfacial Stability of A Ferromagnetic Fluid." Journal of Fluid Mech. **30** (4): 671-688



Crowe, Clayton, Martin Sommerfeld and Yutaka Tsuji (1998). *Multiphase Flows with Droplets and Particles*. CRC Press.

Di Felice, R. (1994). "The Voidage Function for Fluid Particle Interaction System." Int. Journal of Multiphase Flow. **20**: 153-159

Ergun, S. (1952). "Fluid Flow through Packed Columns." Chem. Eng. Prog. **48**, 89

Espinoza, J. Pinto (2002). "Dynamic Behavior of Ferromagnetic Particles in a Liquid-Solid Magnetically Assisted Fluidized Bed (MAFB): Theory, Experiment and CFD-DPM simulation." PhD. Thesis, Chemical Engineering. Oregon State University. Corvallis, Oregon.

Graham, L. J. (1998), "Dechlorination of p-Chlorophenol on Bimetallic Pd/Fe Catalyst in a Magnetically Stabilized Fluidized Bed; Experiment and Theory." PhD. Thesis, Chemical Engineering. Oregon State University. Corvallis, Oregon.

Hinds, William C. (1999). Aerosol Technology, second edition, John Wiley & Sons, Inc.

Horiba. Instruction Manual for Particle Size Distribution Analyzer Model: CAPA-700. Horiba Ltd.

Hristov, Jordan Y. (1996). "Fluidization of Ferromagnetic Particles in a Magnetic Field Part 1: The Effect of Field Line Orientation on Bed Stability." Powder Technology. **87**: 59-66

Intelligent Instrumentation™ (1993). Visual Designer® Data Acquisition Application Software Generation System For Microsoft® Windows™. User Manual.

Jackson, R. (1985). Hydrodynamic Stability of Fluid-Particles Systems, Fluidization 2<sup>nd</sup> Edition, edited by J.F. Davidson, R.Clift and D.Harrison, Academic Press.

Jovanovic G., Sornchamni T., Atwater J., Akse J., Wheeler R. (2003a), "The Magnetically Assisted Liquid-Solid Fluidization in Normal and Microgravity Condition: Experiment and Theory." Paper submitted to Powder Technol.

Jovanovic G., Pinto Espinoza, J., Sornchamni, T., Reed, B., Wheeler, R., Atwater, J., Akse, J. (2003). "Development of Enabling Technologies for Magnetically Assisted Gasification of Solid Wastes." 33<sup>rd</sup> International Conference on Environmental Systems. Paper 2003-01-2374.

Jovanovic G., Sornchamni T., Yoo S., Atwater J., Aske J. , DeHart J. and Fisher J. (1999). "Magnetically Assisted Gasification of Solid Waste." 29<sup>th</sup> International Conference on Environmental Systems. Paper 1999-01-2183.

Kunii, Daizo and Octave Levenspiel (1991). Fluidization Engineering, second edition, Butterworth-Heinemann.

Levenspiel, Octave (1998). Engineering Flow and Heat Exchange, Revised Edition

Rhee, Brian Kanghee (1998). "Enhancement of Mass Transfer Coefficient in A Three-Phase Magnetic Stabilized Fluidized Bed." M.S. thesis, Chemical Engineering. Oregon State University. Corvallis, Oregon.

Rietema, K and Musters, S.M.D. (1977). "The Effect of Interparticle Forces on The Expansion of A Homogeneous Gas-Fluidized Bed." Powder Technology. **18**: 1493-1497.

Rietema, K and H.W. Piepers (1990). "The Effect of Interparticle Forces on The Stability of Gas-Fluidized Beds-I. Experimental Evidence." Chemical Engineering Science. **45** (9): 1627-1639.

Rietema, K., E.J.E. Cottaar and H.W. Piepers (1993). "The Effect of Interparticle Forces on The Stability of Gas-Fluidized Beds-II Theoretical Derivation of Bed Elasticity on The Basis of Van Der Waals Forces between Powder Particles." Chemical Engineering Science. **48** (9): 1687-1697.

Rosensweig, Ronald E. (1979). "Magnetic Stabilization of The State of Uniform Fluidization." Ind. Eng. Chem. Fundam. **18** (3): 260-269.

Rosensweig, R.E., M. Zahn, W.K. Lee and P.S. Hagan (1983). "Theory and Experiments In The Mechanics Of Magnetically Stabilized Fluidized Solids." Theory of Dispersed Multiphase Flow. Academic Press, Inc. 359-384.

Saxena S.C. and S. Shrivastava. (1991). "Some Hydronamic Investigations of A Magnetically Stabilized Air-Fluidized Bed of Ferromagnetic Particles." Powder Technology. **64**: 57-67.

Sergeev, Yu. A. and D.A. Dobritsyn (1995). "Linear, Nonlinear Small-Amplitude, Steady and Shock Waves in Magnetically Stabilized Liquid-Solid and Gas-Solid Fluidized Beds." Int. J. Multiphase Flow, **21** (1): 75-94.

Siegell, J. H (1987). "Liquid-Fluidized Magnetically Stabilized Beds." Powder Technology. **52**: 139-148

Sornchamni T., Jovanovic G., Atwater J., Akse J., Wheeler R. (2003). "Operation of Magnetically Assisted Fluidized Beds in Microgravity and Vairable Gravity: Experiment and Theory." Paper submitted to Advanced Space Research.

Terranova Brenda E. and Burns Mark A. (1991). "Continuous Cell Suspension Processing Using Magnetically Stabilized Fluidized Beds." Biotechnology and Bioengineering. **37**: 110

Tien, Chi (1989). Granular Filtration of Aerosols and Hydrosols. Butterworth Publishers.

Villers, Frantz (1998). "Bed Porosity in a Magnetically Stabilized Liquid-Solid Fluidized Bed." M.S. thesis, Chemical Engineering. Oregon State University. Corvallis, Oregon.

Wu, W.Y., A. Navada and S.C. Saxena (1997). "Hydrodynamic Character of A Magnetically Stabilized Air Fluidized Bed of An Admixture of Magnetic and Non-Magnetic Particles." Power Technology. **90**: 39-46.

Zhu, Qingshan and Hongzhong Li (1995). "Study on Magnetic Fluidization of Group C Powders." Powder Technology. **86**: 179-185.

## **APPENDICES**

## APPENDIX A

### THE DERIVATION OF MASS AND MOMENTUM EQUATIONS

#### A.1 Mass conservation equations

##### A.1.1 Mass conservation equation for the fluid phase

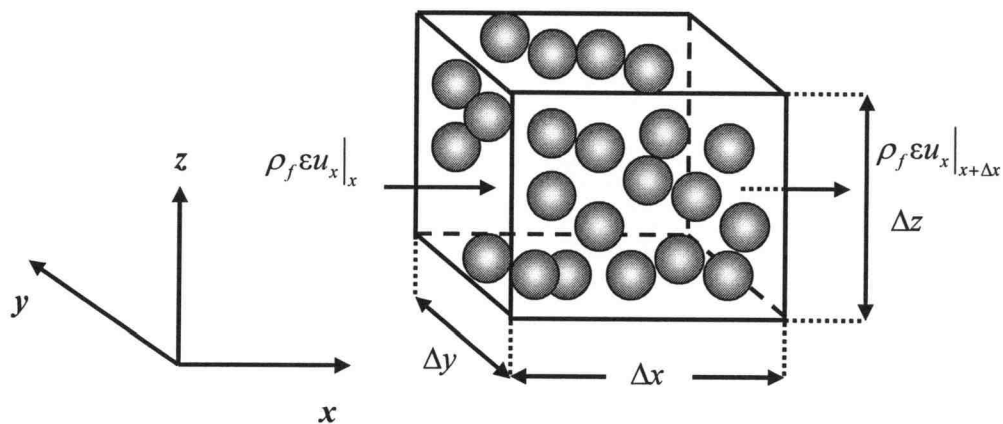


**Figure A.1** Stationary volume element  $\Delta x \Delta y \Delta z$  through which fluid and particles are flowing.

Consider the pair of faces perpendicular to the  $x$ -axis. The rate of mass in through the face at  $x$  is  $(\rho_f \varepsilon u_x)|_x \Delta y \Delta z$  and the rate of mass out through the face at  $x + \Delta x$  is  $(\rho_f \varepsilon u_x)|_{x+\Delta x} \Delta y \Delta z$ . Similar expressions may be written for the other two pairs of faces.

Hence, a mass balance over a stationary volume element  $\Delta x \Delta y \Delta z$  can be presented as the following:

$$\{\text{rate of mass accumulation}\} = \{\text{rate of mass input}\} - \{\text{rate of mass output}\} \quad (\text{A-1})$$

$$\begin{aligned} \frac{\partial \rho_f \varepsilon \Delta x \Delta y \Delta z}{\partial t} = & \Delta y \Delta z \left[ \left( \rho_f \varepsilon u_x \right) \Big|_x - \left( \rho_f \varepsilon u_x \right) \Big|_{x+\Delta x} \right] \\ & + \Delta x \Delta z \left[ \left( \rho_f \varepsilon u_y \right) \Big|_y - \left( \rho_f \varepsilon u_y \right) \Big|_{y+\Delta y} \right] + \Delta y \Delta z \left[ \left( \rho_f \varepsilon u_z \right) \Big|_z - \left( \rho_f \varepsilon u_z \right) \Big|_{z+\Delta z} \right] \end{aligned} \quad (\text{A-2})$$

By dividing Equation (A-2) by  $\Delta x \Delta y \Delta z$  and taking the limit as these dimensions approach zero, we get

$$\frac{\partial \rho_f \varepsilon}{\partial t} = - \frac{\partial \rho_f \varepsilon u_x}{\partial x} - \frac{\partial \rho_f \varepsilon u_y}{\partial y} - \frac{\partial \rho_f \varepsilon u_z}{\partial z} \quad (\text{A-3})$$

If  $\rho_f$  is constant, Equation A-2 can be reduced to

$$\frac{\partial \varepsilon}{\partial t} = - \frac{\partial \varepsilon u_x}{\partial x} - \frac{\partial \varepsilon u_y}{\partial y} - \frac{\partial \varepsilon u_z}{\partial z} \quad (\text{A-4})$$

It may be written in the vector form as

$$\frac{\partial \varepsilon}{\partial t} + \nabla \cdot \varepsilon \mathbf{U} = 0 \quad (\text{A-5})$$

### A.1.2 Mass conservation equation for the particle phase

The particle phase is treated as a continuous phase; therefore, the equation of continuity for the particle phase is obtained in a similar fashion:

$$\frac{\partial(1-\varepsilon)}{\partial t} + \nabla \cdot (1-\varepsilon) \mathbf{V} = 0 \quad (\text{A-6})$$

## A.2 Momentum conservation equations

### A.2.1 Momentum conservation equation for the fluid phase

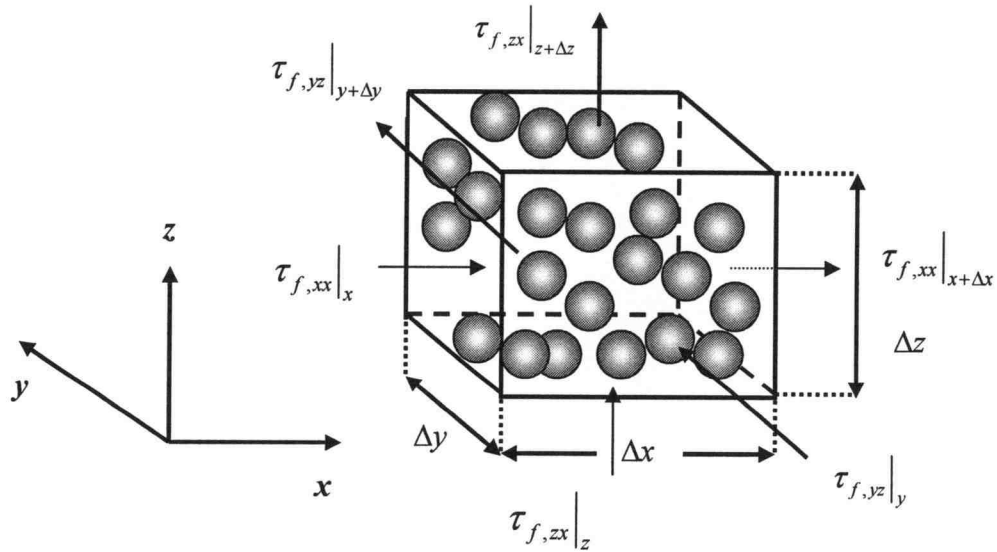


**Figure A.2** Stationary volume element  $\Delta x \Delta y \Delta z$  in which the x-momentum component is transported through the surface

The equation of motion for the liquid phase can be obtained as:

$$\{\text{rate of momentum accumulation}\} = \{\text{rate of momentum in}\} - \{\text{rate of momentum out}\} + \{\text{sum of forces acting on fluid in the system}\} \quad (\text{A-7})$$

In the  $x$ -direction, the momentum flows into and out of the control volume element by two mechanisms: convection (by virtue of the bulk fluid flow) and molecular transfer (by virtue of the velocity gradient)

The rate at which the  $x$ -momentum component comes in through the face at  $x$  by the convection flow is  $\rho_f \epsilon u_x u_x \big|_x \Delta y \Delta z$ , and the rate at which it departs through the face at  $x + \Delta x$  is  $\rho_f \epsilon u_x u_x \big|_{x+\Delta x} \Delta y \Delta z$ . The rate at which it flows in at  $y$  is  $\rho_f \epsilon u_y u_x \big|_y \Delta x \Delta z$ . Similar expressions may be written for the other three faces.

Therefore, the net convective  $x$ -momentum entering into the volume element is:

$$\begin{aligned} \Delta y \Delta z \left( \rho_f \epsilon u_x u_x \big|_x - \rho_f \epsilon u_x u_x \big|_{x+\Delta x} \right) + \Delta x \Delta z \left( \rho_f \epsilon u_y u_x \big|_y - \rho_f \epsilon u_y u_x \big|_{y+\Delta y} \right) \\ + \Delta y \Delta z \left( \rho_f \epsilon u_z u_x \big|_z - \rho_f \epsilon u_z u_x \big|_{z+\Delta z} \right) \end{aligned} \quad (\text{A-8})$$

The rate at which the  $x$ -component of momentum enters through the face at  $x$  by molecular transport is  $\tau_{f,xx} \big|_x \epsilon \Delta y \Delta x$  and the rate at which the  $x$ -component of momentum departs through the face at  $x + \Delta x$  is  $\tau_{f,xx} \big|_{x+\Delta x} \epsilon \Delta y \Delta x$ . The rate at which it enters the face at  $y$  is  $\tau_{f,yx} \big|_y \epsilon \Delta x \Delta z$ . The  $x$ -component of



momentum for the remaining three faces can be obtained by similar expressions. The net  $x$ -momentum entering the volume element through molecular transport is:

$$\varepsilon \Delta y \Delta z \left( \tau_{f,xx} \Big|_x - \tau_{f,xx} \Big|_{x+\Delta x} \right) + \varepsilon \Delta x \Delta z \left( \tau_{f,yx} \Big|_y - \tau_{f,yx} \Big|_{y+\Delta y} \right) + \varepsilon \Delta x \Delta y \left( \tau_{f,zx} \Big|_z - \tau_{f,zx} \Big|_{z+\Delta z} \right) \quad (\text{A-9})$$

The important forces acting on the fluid in the control volume element are fluid pressure,  $P_f$ , and the gravitational force,  $g$ . In addition, the fluid exerts a force on the particles in this control volume element. The sum of these forces is given by:

$$\varepsilon \Delta y \Delta z \left( P_f \Big|_x - P_f \Big|_{x+\Delta x} \right) + \rho_f g_x \varepsilon \Delta x \Delta y \Delta z - F_{1x} \varepsilon \Delta x \Delta y \Delta z \quad (\text{A-10})$$

The rate of  $x$ -momentum accumulation within the element is

$$\frac{\partial (\rho_f u_x \varepsilon \Delta x \Delta y \Delta z)}{\partial t} \quad (\text{A-11})$$

Dividing the resulting equation by  $\Delta x \Delta y \Delta z$  and taking the limit as  $\Delta x$ ,  $\Delta y$  and  $\Delta z$  approach zero, we obtain:

$$\begin{aligned} \frac{\partial (\rho_f \varepsilon u_x)}{\partial t} = & - \left( \frac{\partial (\rho_f \varepsilon u_x u_x)}{\partial x} + \frac{\partial (\rho_f \varepsilon u_y u_x)}{\partial y} + \frac{\partial (\rho_f \varepsilon u_z u_x)}{\partial z} \right) \\ & - \varepsilon \left( \frac{\partial \tau_{f,xx}}{\partial x} + \frac{\partial \tau_{f,yx}}{\partial y} + \frac{\partial \tau_{f,zx}}{\partial z} \right) - \varepsilon \frac{\partial P_{f,x}}{\partial x} + \rho_f \varepsilon g_x - F_{1x} \varepsilon \end{aligned} \quad (\text{A-12})$$

We can obtain the  $y$  and  $z$  momentum components using the same procedure.

$$\begin{aligned} \frac{\partial(\rho_f \varepsilon u_y)}{\partial t} = & - \left( \frac{\partial(\rho_f \varepsilon u_x u_y)}{\partial x} + \frac{\partial(\rho_f \varepsilon u_y u_y)}{\partial y} + \frac{\partial(\rho_f \varepsilon u_z u_y)}{\partial z} \right) \\ & - \varepsilon \left( \frac{\partial \tau_{f,xy}}{\partial x} + \frac{\partial \tau_{f,yy}}{\partial y} + \frac{\partial \tau_{f,zy}}{\partial z} \right) - \varepsilon \frac{\partial P_{f,y}}{\partial x} + \rho_f \varepsilon g_y - F_{1y} \varepsilon \end{aligned} \quad (\text{A-13})$$

$$\begin{aligned} \frac{\partial(\rho_f \varepsilon u_z)}{\partial t} = & - \left( \frac{\partial(\rho_f \varepsilon u_x u_z)}{\partial x} + \frac{\partial(\rho_f \varepsilon u_y u_z)}{\partial y} + \frac{\partial(\rho_f \varepsilon u_z u_z)}{\partial z} \right) \\ & - \varepsilon \left( \frac{\partial \tau_{f,xz}}{\partial x} + \frac{\partial \tau_{f,yz}}{\partial y} + \frac{\partial \tau_{f,zz}}{\partial z} \right) - \varepsilon \frac{\partial P_{f,z}}{\partial x} + \rho_f \varepsilon g_z - F_{1z} \varepsilon \end{aligned} \quad (\text{A-14})$$

By combining Equation (A-12) with (A-14), we obtain the single vector equation:

$$\frac{\partial(\rho_f \varepsilon \mathbf{U})}{\partial t} = -\nabla \rho_f \varepsilon U U - \varepsilon \nabla P_f - \varepsilon \nabla \cdot \boldsymbol{\tau}_f + \rho_f \varepsilon \mathbf{g} - \varepsilon \mathbf{F}_1 \quad (\text{A-15})$$

With the aid of the equation of continuity, Equation (A-15) can be written as:

$$\begin{aligned} \rho_f \varepsilon \frac{\partial \mathbf{U}}{\partial t} &= -\varepsilon \nabla P_f - \varepsilon \nabla \cdot \boldsymbol{\tau}_f + \rho_f \varepsilon \mathbf{g} - \varepsilon \mathbf{F}_1 \\ \rho_f \varepsilon \left( \frac{\partial \mathbf{U}}{\partial t} + (\mathbf{U} \cdot \nabla) \mathbf{U} \right) &= -\varepsilon \nabla P_f - \varepsilon \nabla \cdot \boldsymbol{\tau} + \rho_f \varepsilon \mathbf{g} - \varepsilon \mathbf{F}_1 \end{aligned} \quad (\text{A-16})$$

The stress tensors can be written in terms of the velocity gradients and fluid properties as:

$$\tau_{f,xx} = -2\mu \left( \frac{\partial u_x}{\partial x} \right) + \frac{2}{3} \mu (\nabla \cdot \mathbf{U})$$

$$\begin{aligned}
\tau_{f,yy} &= -2\mu \left( \frac{\partial u_y}{\partial y} \right) + \frac{2}{3}\mu (\nabla \cdot \mathbf{U}) \\
\tau_{f,zz} &= -2\mu \left( \frac{\partial u_z}{\partial z} \right) + \frac{2}{3}\mu (\nabla \cdot \mathbf{U}) \\
\tau_{f,xy} &= \tau_{f,yx} = -\mu \left( \frac{\partial u_x}{\partial y} + \frac{\partial u_y}{\partial x} \right) \\
\tau_{f,yz} &= \tau_{f,zy} = -\mu \left( \frac{\partial u_y}{\partial z} + \frac{\partial u_z}{\partial y} \right) \\
\tau_{f,zx} &= \tau_{f,xz} = -\mu \left( \frac{\partial u_z}{\partial x} + \frac{\partial u_x}{\partial z} \right)
\end{aligned} \tag{A-17}$$

### A.2.2 Momentum conservation equation for the particle phase

By using the same analogy as that for the fluid phase, the momentum conservation equation for the particle phase can be given as:

$$\begin{aligned}
\rho_p (1-\varepsilon) \left( \frac{\partial \mathbf{V}}{\partial t} + (\mathbf{V} \cdot \nabla) \mathbf{V} \right) &= -(1-\varepsilon) \nabla P_f - (1-\varepsilon) \nabla P_p - (1-\varepsilon) \nabla \cdot \boldsymbol{\tau}_p \\
&\quad + \rho_p (1-\varepsilon) \mathbf{g} + \varepsilon \mathbf{F}_1 + \mathbf{F}_m
\end{aligned} \tag{A-18}$$

The term  $\mathbf{F}_m$  is the magnetic force on the particles, and the term  $(1-\varepsilon) \nabla P_f$  shown in the momentum conservation equation for the particle phase is the buoyancy reaction of the fluid on the particles.

## APPENDIX B

### DERIVATION OF THE ATTRACTIVE INTERPARTICLE MAGNETIC FORCES

Pinto-Espinoza (2002) developed a model of both total repulsive and attractive interparticle magnetic forces in his study. However, in this study, I focus only on the attractive interparticle magnetic forces to be used in the voidage distribution modeling. The details of Pinto-Espinoza's development of attractive forces are as follows:

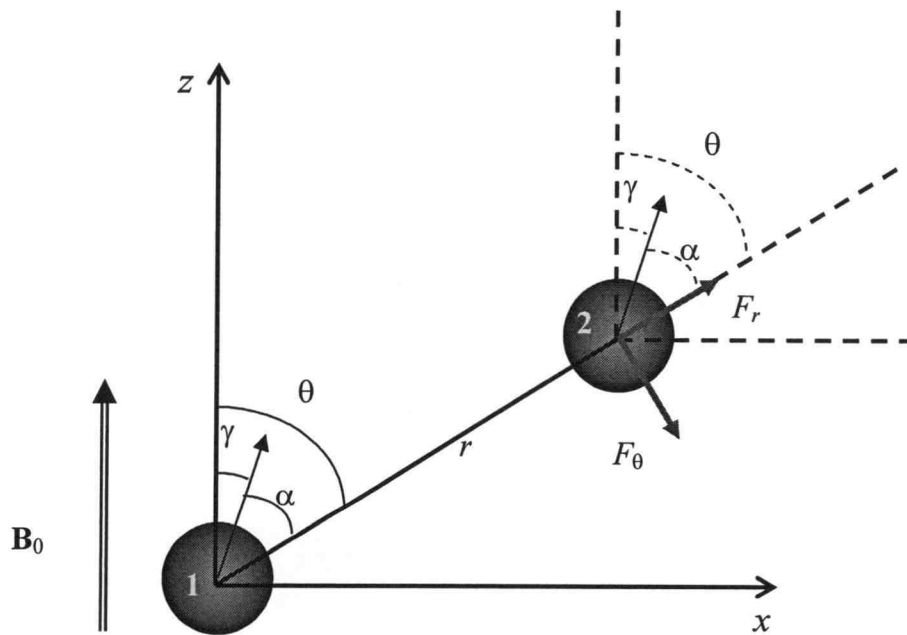


**Figure B.1** Repulsive and attractive magnetic forces between two ideal dipoles under the influence of a uniform external magnetic field,  $B_0$ . The forces  $F_r$  and  $F_\theta$  acting on particle 1 are of the same magnitude but of opposite direction.

We assume that two identical magnetically susceptible particles are located side-by-side in a uniform magnetic field  $B_0$ . They are separated by a distance  $r$ , as shown in Figure B.1. Two magnetically susceptible particles are also assumed to have ideal dipoles in the calculation of the attractive forces.

The magnetization of each particle is caused by the magnetic field at the particle position. In addition, each particle is considered as a magnetic dipole producing a magnetic field expressed in Equation (B-1).

$$\mathbf{B}(r, \theta) = \frac{\mu_0 m}{4\pi r^3} [3 \sin \theta \cos \theta \hat{\mathbf{x}} + (2 - 3 \sin^2 \theta) \hat{\mathbf{z}}] \quad (\text{B-1})$$

In this case, the particles are aligned along the vertical axis ( $z$ -direction) and the orientation of the dipoles is also in the  $z$  direction. The angle between the particles,  $\theta$ , measured from the  $z$ -axis, is zero and the fields produced by the particles, simplified from Equation (B-1), are:

$$\mathbf{B}_1(r) = -\frac{\mu_0 m_1}{2\pi r^3} \hat{\mathbf{z}} \quad (\text{B-2})$$

$$\mathbf{B}_2(r) = -\frac{\mu_0 m_2}{2\pi r^3} \hat{\mathbf{z}} \quad (\text{B-3})$$

The total dipole moment of the particles, considering the influence of the external magnetic field and the field induced by the other particle, can be expressed as:

$$\mathbf{m}_1 = \frac{\chi_e V_p}{\mu_0} \left( B_0 + \frac{\mu_0 m_2}{2\pi r^3} \right) \hat{\mathbf{z}} \quad (\text{B-4})$$

$$\mathbf{m}_2 = \frac{\chi_e V_p}{\mu_0} \left( B_0 + \frac{\mu_0 m_1}{2\pi r^3} \right) \hat{\mathbf{z}} \quad (\text{B-5})$$

With the symmetry assumption, we can conclude that  $m_1 = m_2 = m$ . The equation relating the dipole moment to the external field  $B_0$  and the distance  $r$  can be written as:

$$m = \frac{\chi_e V_p}{\mu_0} \left( B_0 + \frac{\mu_0 m}{2\pi r^3} \right) \quad (\text{B-6})$$

Rearranging Equation (B-6) in terms of  $m$ , we can get

$$m = \frac{2\pi\chi_e V_p B_0}{\mu_0} \left[ \frac{r^3}{(2\pi r^3 - \chi_e V_p)} \right] \quad (\text{B-7})$$

The potential energy of the two dipoles at the  $\theta = 0$  position (both particles are at the  $z$ -axis) is expressed as:

$$U = -\frac{\mu_0 m^2}{2\pi r^3} \quad (\text{B-8})$$

Substituting for  $m$ ,

$$U = \frac{-2\pi(\chi_e V_p B_0)^2}{\mu_0} \left[ \frac{r^3}{(2\pi r^3 - \chi_e V_p)^2} \right] \quad (\text{B-9})$$

The attractive magnetic force between the two particles can be found by taking the negative of the derivative of  $U$  with respect to  $r$ ,

$$F_{attractive} = -\frac{6(\chi_e V_p B_0)^2}{\mu_0} \left[ \frac{2\pi^2 r^5 + \chi_e V_p \pi r^2}{(2\pi r^3 - \chi_e V_p)^3} \right] \quad (\text{B-10})$$

The negative sign in this equation indicates that the particles are attracted to each other.

## **APPENDIX C**

### **PREPARATION OF FERRO-SODIUM ALGINATE MIXTURE**

In this section, the general procedure for preparing the ferro-sodium alginate mixture is described. Particle A is composed of the following materials:

Ferromagnetic Powder	20%
Microsphere Balloons	8%
1.75 % Sodium Alginate Solution	72%

In order to obtain the most uniform distribution of composition in the mixture, only 100 g of the suspension is prepared for each production run. The preparation of the ferromagnetic sodium alginate is given by the following instructions:

1. First, weigh 70.74 g of water and pour it into a 250 cm<sup>3</sup> beaker. Place the beaker under the mixer.
2. Weigh 1.26 g of sodium alginate powder. Start mixing the water and slowly add sodium alginate powder into the beaker. Continue mixing until all of the alginate powder is dissolved into the water. This is the 1.75 % sodium alginate solution.



3. Weigh 20 g of ferromagnetic powder and 8 g of microsphere balloons and add them to the sodium alginate solution in small increments.
4. Continue mixing all components for about 4 hours. When the suspension is well mixed, pour it into the particle generator.
5. Repeat step 1 to 4 for particles B, C, D, E and F by using the weight percents of components as shown in Table 3-4.

## APPENDIX D

### PROPERTIES OF MATERIALS

The physical and chemical properties of sodium alginate, microsphere balloons, ferromagnetic powder, and Gellan gum are tabulated in Tables D.1 to D.4, respectively.

**Table D.1** Properties of sodium alginate powder\*

Chemical Name	Algin (Sodium Alginate)
Chemical Family	Polysaccharide gum
Bulk Density	0.8 g/cm <sup>3</sup>
pH as a 1% Solution	approximately neutral
Solubility in water	soluble, forming a viscous solution, becoming a paste at a concentration of about 5%
Molecular Weight	range from approx. 10,000 to 200,000

\* Sodium alginate, KELTONE® HV, was obtained from the NutraSweet Kelco Co.

**Table D.2** Physical and chemical properties of microsphere balloons\*\*

Chemical Compositions	70% SiO <sub>2</sub> , 25%Na <sub>2</sub> O, 5% B <sub>2</sub> O <sub>3</sub>
Density (g/cm <sup>3</sup> )	0.35
Median Particle Size (μm)	55

\*\* Microsphere balloons were obtained from Emerson & Cuming™

**Table D.3** Composition and properties of ferromagnetic powder\*\*\*

Chemical Composition	MnOFe <sub>2</sub> O <sub>3</sub> 45-70% Fe <sub>2</sub> O <sub>3</sub> 22-55% FeOFe <sub>2</sub> O <sub>3</sub> 0-0.5%
Bulk Density (g/cm <sup>3</sup> )	2.2
Median Particle Size ( $\mu$ m)	2
Surface Area (cm <sup>2</sup> /g)	2.286
Moisture %	0.01
Solubility in water	Negligible
Reactivity in water	Negligible
Melting Point	> 1500 C

\*\*\* Ferromagnetic powder was obtained from Steward™ Co.

**Table D.4** Properties of Gellan Gum\*\*\*\*

Chemical Name	Gellan Gum
Chemical Family	Polysaccharide gum
Bulk Density	(50 lb/cu. Ft.) 0.8 g/cm <sup>3</sup>
pH as a 1% Solution	approximately neutral
Solubility in water	soluble, forming a viscous solution, becoming a paste at concentration greater than about 5%
Molecular Weight	approximately 1,000,000

\*\*\*\* Food grade Gellan Gum, KELCOGEL® F, was obtained from CP Kelco™

## **APPENDIX E**

### **CALIBRATION OF INSTRUMENTS**

Every instrument used in this study was calibrated for accuracy and reliability. The following are the calibration procedures for each instrument.

#### **E.1 Gaussmeter Calibration**

The axial probe is sent to Lake Shore Cryotronics<sup>®</sup>, Inc. every two years for probe calibration.

#### **E.2 G-MAFB flowrate calibration**

The corresponding flowrates at each point on the rotameter scale are listed in Table E.1. Figure E.1 represents the plot of flow velocity against the rotameter scale reading used in the voidage distribution experiments. Figure E.2 shows the plot of the measured flow velocity from a special flow rotameter vs. the rotameter scale reading. Figure E.3 shows the relationship of flow velocity and the rotameter scale reading used in the filtration experiments.

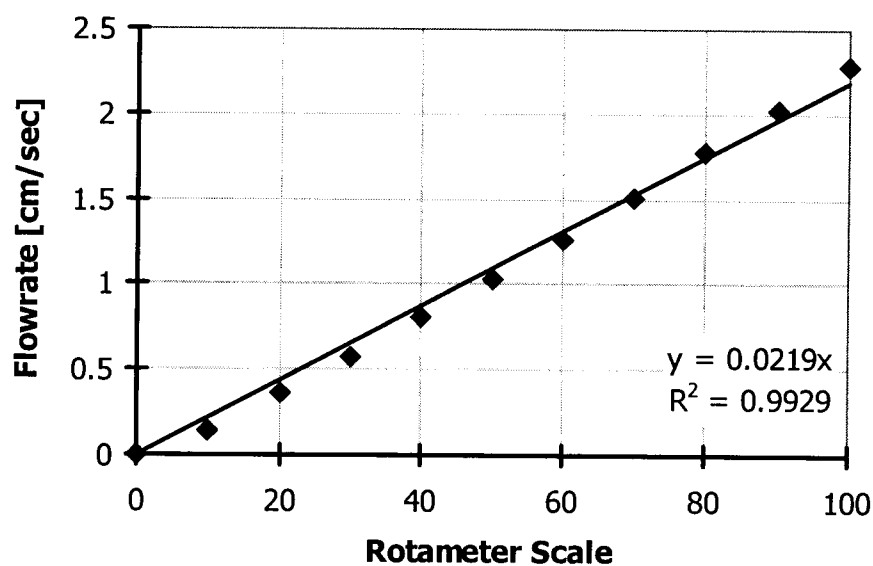


**Figure E.1** Flow rotameter calibration for voidage distribution experiments.

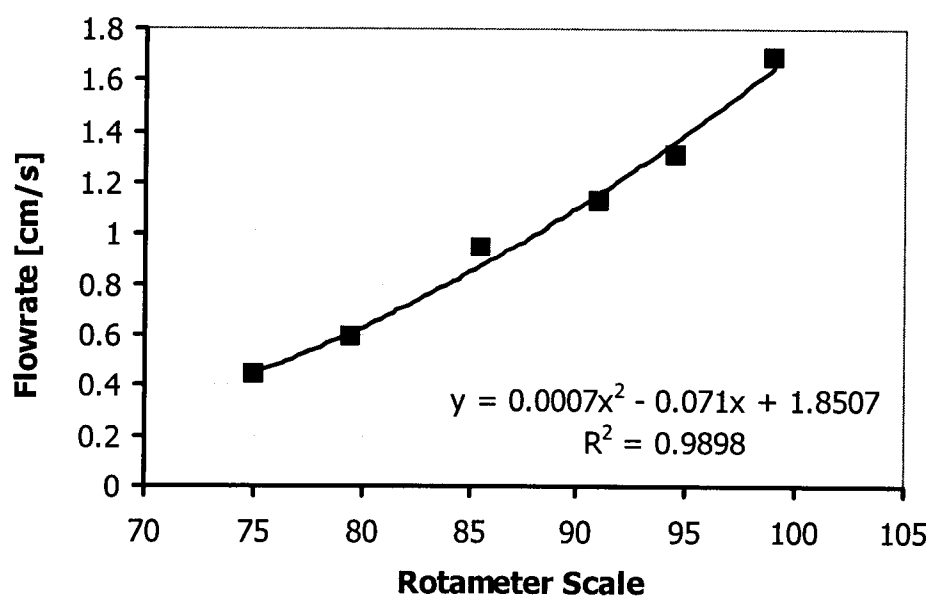


**Figure E.2** Flow rotameter calibration curve from a special flow meter used on board NASA's KC-135 aircraft.

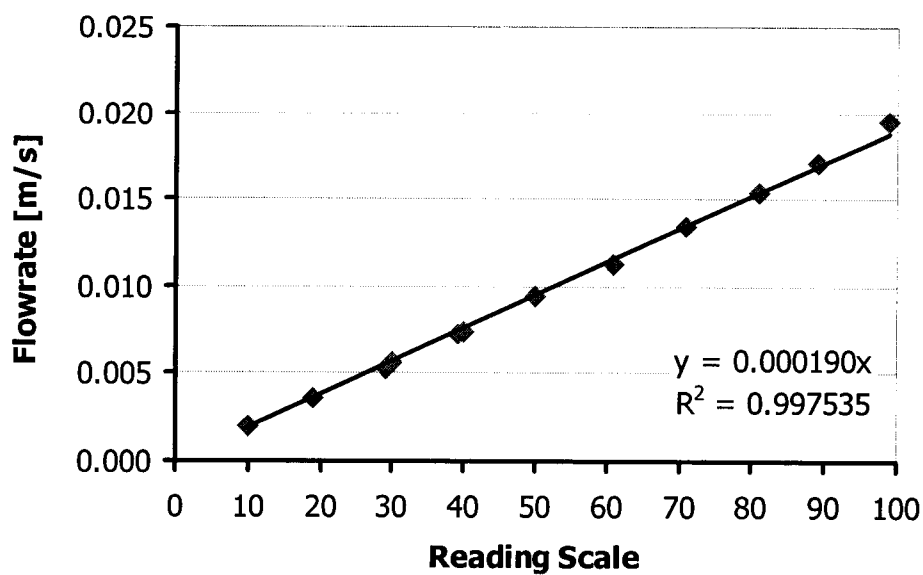


**Figure E.3** Flow rotameter calibration curve for filtration experiments.

### E.3 Rheostat resistance calibration

The rheostat resistance at any reading scale was measured and Figure E.4 represents the plot of the resistance calibration.

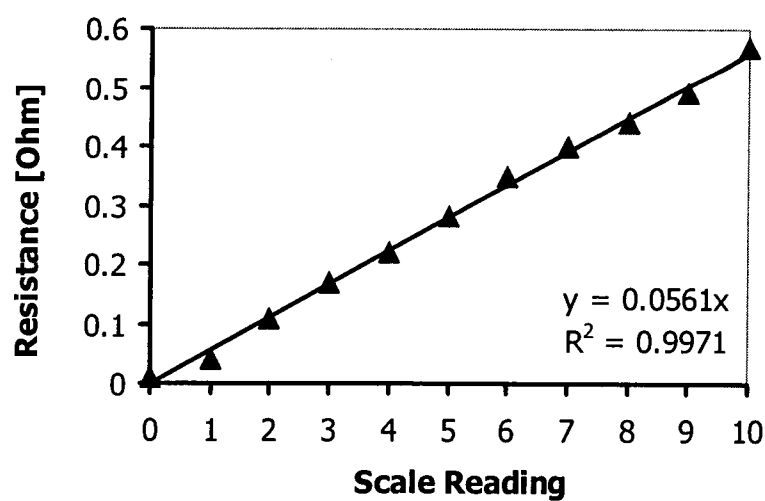


**Figure E.4** Rheostat resistance calibration curve.

#### E.4 Laser photo-diode detector calibration

The calibration curve of concentration and voltage response is shown in Figure E.5.

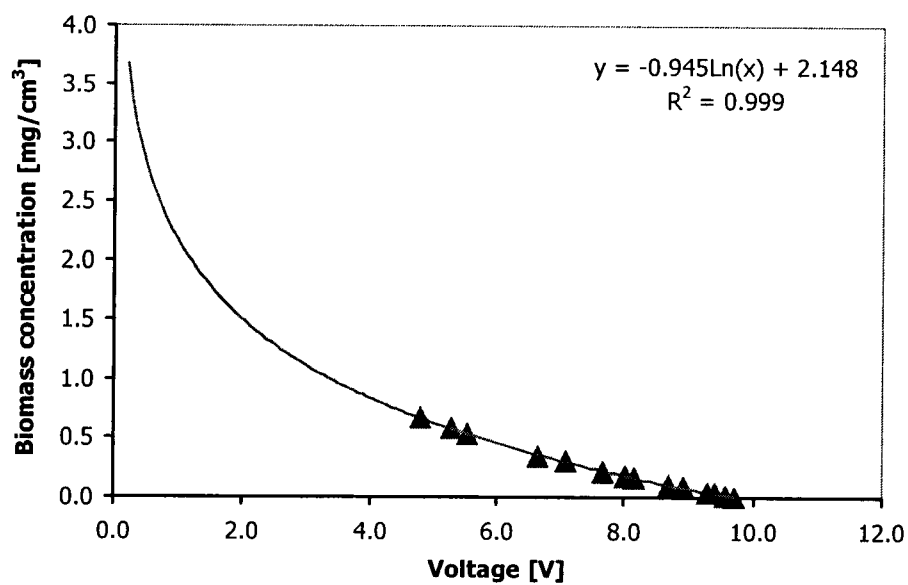


**Figure E.5** Laser photo-diode detector calibration curve.

## APPENDIX F

### MAGNETIC FIELD INTENSITY

In the voidage distribution and filtration experiments, the magnetic field intensity variation along the centerline was measured. By varying the voltage across the power supply, different magnetic field intensities and magnetic field gradients were obtained. These are summarized in Figures F.1 through F.6.

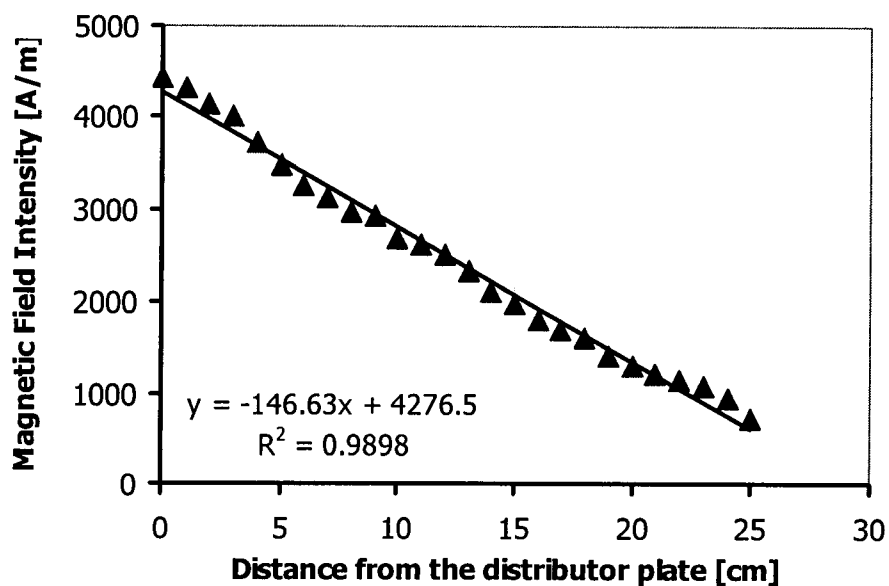


**Figure F.1** Magnetic field intensity in the bed used in the voidage distribution experiments at 1.0 volt across power supply.



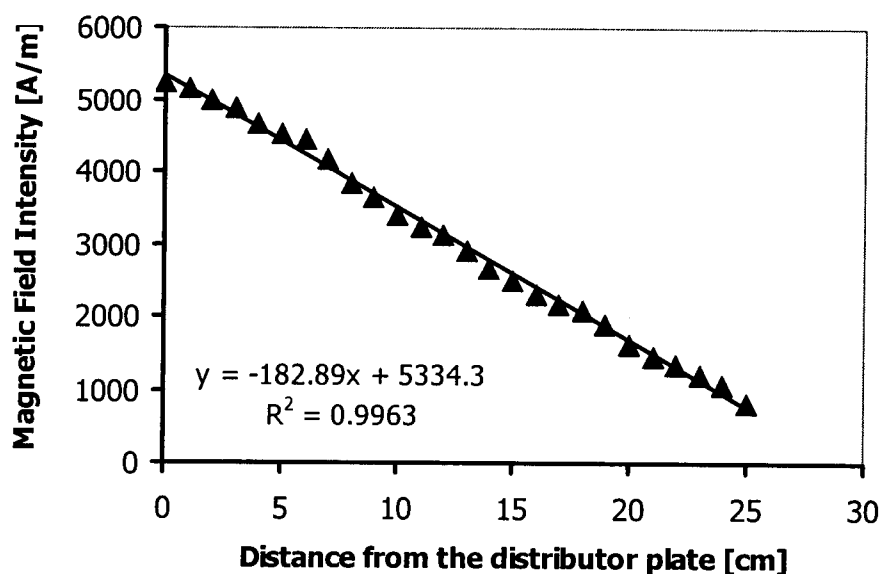


**Figure F.2** Magnetic field intensity in the bed used in the voidage distribution experiments at 2.0 volts across power supply.

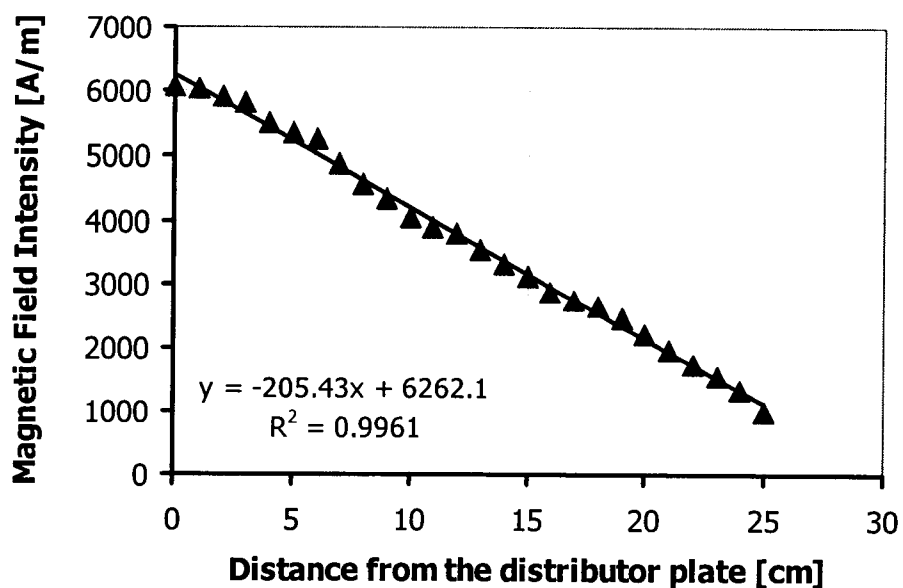


**Figure F.3** Magnetic field intensity in the bed used in the voidage distribution experiments at 3.0 volts across power supply.

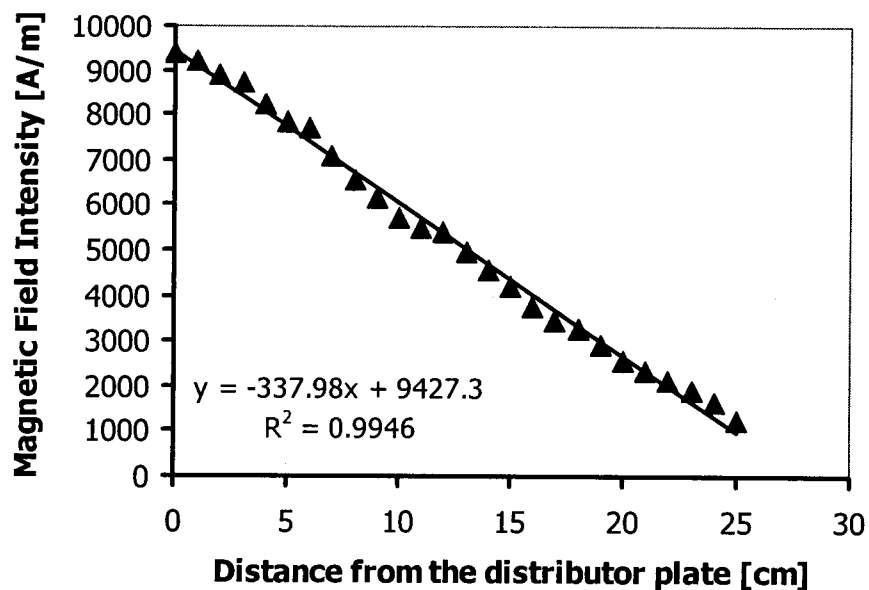


**Figure F.4** Magnetic field intensity in the bed used in the voidage distribution experiments at 4.0 volts across power supply.

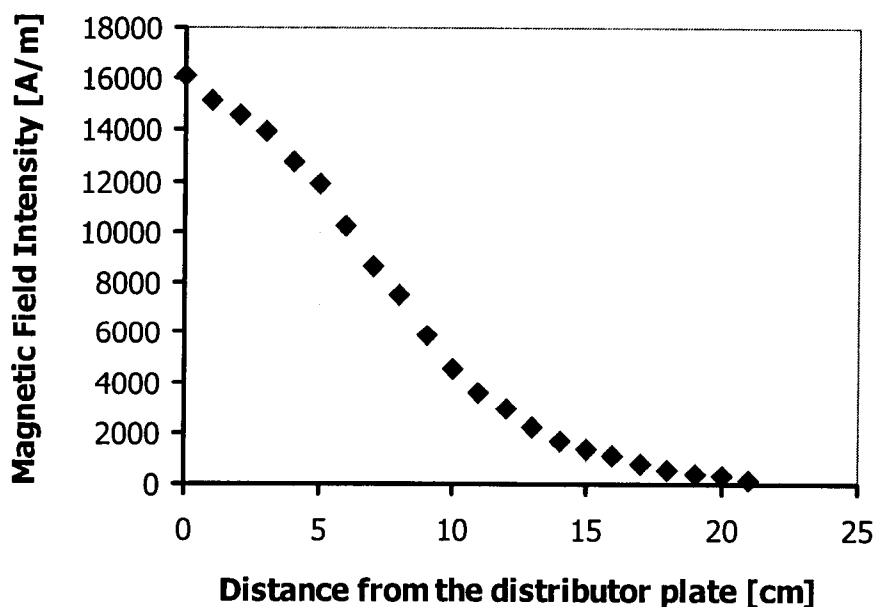


**Figure F.5** Magnetic field intensity used for the experiments on board NASA's KC-135 aircraft at 1.0 volt across power supply.

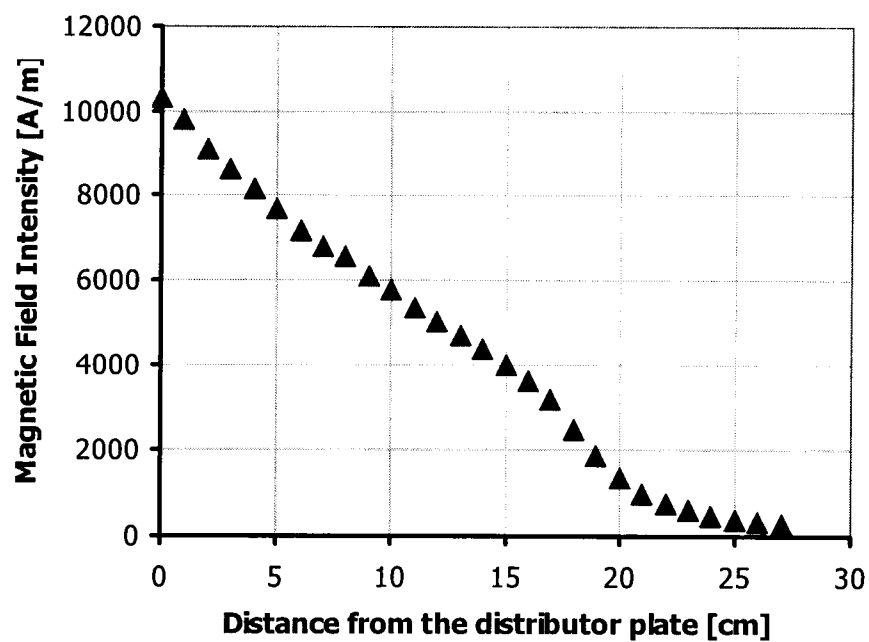


**Figure F.6** Magnetic field intensity in the bed used in the filtration experiment.

## APPENDIX G

### MAGNETIC SUSCEPTIBILITY MEASUREMENT

The ferrite powder magnetic susceptibility is one of the most important parameters in our voidage distribution modeling. Therefore, we carefully measured the magnetic susceptibility using a modified Thermogravimetric analyzer (TGA), TA Instrument™, Inc. Model 2950. Normally, the TGA is used to trace the sample weight change due to decomposition, oxidation, or dehydration under controlled conditions (ramping temperature or isothermal temperature with constant gas or air purging). The microbalance in the TGA has a resolution of 1  $\mu\text{g}$  and can measure the weight of samples up to 1g. The magnetic susceptibility measurement procedures are as follows:

1. Load a small ceramic canister and a small basket to the weight support and set to zero weight (tared).
2. Place a ferromagnetic particle ( $d_p = 1 \text{ mm}$ , 20% Fe, 9% Microsphere balloon and 71% of 1.75% alginate solution) on the ceramic canister and note the original weight.
3. Insert a single solenoid coil beneath the canister and turn on the DC power supply to generate the magnetic field. Measure the distance from the canister to the center of the solenoid and note the total

weight due to the magnetic force acting on the particle toward the center of the solenoid.

4. Vary the distance between canister and solenoid and note the total weight.

The magnetic force is simply calculated by subtracting the weight of the ferromagnetic particle in the presence of the magnetic field from the original weight. The magnetic force is converted to the susceptibility of the ferromagnetic particle.

A series of experiments shows that the average magnetic susceptibility of ferromagnetic particles is 2.74, which translates to a ferromagnetic powder susceptibility of 31.98. The magnetic susceptibility for different ferrite contents can be obtained by the following equation:

$$\chi_{\text{particle}} = \text{volume fraction of ferromagnetic powder} \times \chi_{\text{ferro. powder}} \quad (\text{G-1})$$

The calculation of magnetic susceptibility of ferromagnetic particles is shown in Table G-1 and the field intensity used in this measurement is shown in Figure G-1.

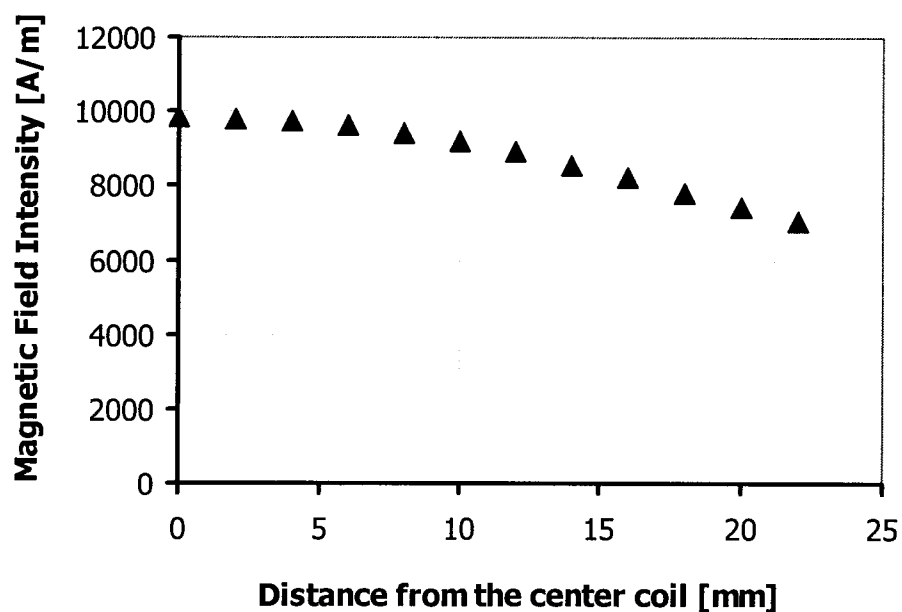


**Figure G.1** Magnetic field intensity used with the TGA

**Table G.1** Calculation of magnetic susceptibility of ferromagnetic particles

Number of particles	Axial distance from the center of the coil [mm]	Magnetic Force [N]	Susceptibility $\chi$
1	4	0.00000755	3.18
1	6	0.00000961	2.71
1	8	0.00001128	2.42
1	10	0.00001285	2.25
3	4	0.00002286	3.21
3	6	0.00003169	2.98
3	8	0.00003659	2.61
3	10	0.00004346	2.54

## APPENDIX H

### VISUAL DESIGNER *FLOWGRAM*

The *FlowGram* created in the Visual Designer® Software is used to process a voltage signal from a DASport parallel port. The schematic diagram of *FlowGram* used in this study is shown in Fig. H-1. The descriptions of each icon are as follows:

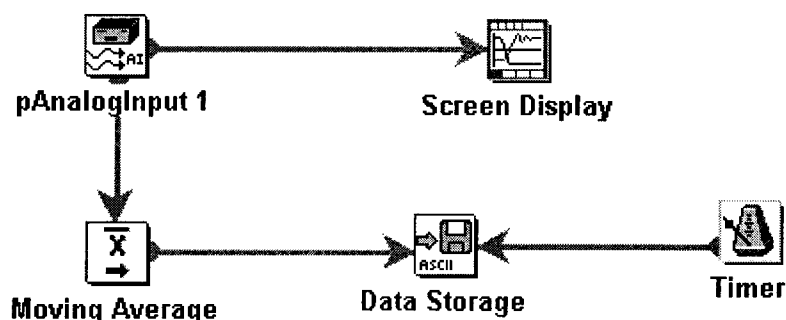


**Figure H.1** Schematic diagram of *FlowGram* in Visual Designer® software

**pAnalogInput 1:** This icon represents a unit that performs analog input data acquisition. The parameter selections, including gain, range and input configuration are listed in Table H.1.

**Table H.1** Parameter setting on pAnalogInput 1

Name	Device	Unit	Channel	Gain	Range [V]	Configuration
PCI-20450P-3x	LPT1	1	0	1	0-10	Differential

**Screen Display:** This icon is used to graphically display input buffer data in an  $x$ - $y$  format. In this study, the  $y$  scale represents the value of analog data voltages and  $x$  represents time.

**Moving Average:** This icon is used to reduce the amount of noise from an input signal by averaging the past  $N$  data points. The number of average points was set equal to the number of data points obtained in one second, 516 points.

**Data Storage:** This block function is used to store data input to hard disk in tab-delimited ASCII format file. This file can be opened for rewrite or append.

**Timer:** This timer icon allows us to set the sample period and the initial time delay for the **Data Storage** icon. In this study, we set the sample period at one second with no time delay.



## APPENDIX I

### DIMENSIONAL ANALYSIS

The variables controlling the accumulation coefficient  $k_I$  in the magnetic fluidized bed are fluid velocity  $U_0$ , straw diameter  $D_p$ , ferromagnetic particle diameter  $d_p$ , density of fluid  $\rho_f$ , density of straw  $\rho_{\text{straw}}$ , and viscosity  $\mu_f$ . The dimensions of the variables are shown in Table G.1.

**Table I.1** Dimensions of variables

Unit	$k_I$	$\rho_{\text{straw}}$	$\rho_f$	$d_p$	$D_p$	$\mu_f$	$U_0$
<b>Mass [M]</b>	0	1	1	0	0	1	0
<b>Length [L]</b>	0	-3	-3	1	1	-1	1
<b>Time [T]</b>	-1	0	0	0	0	-1	-1

The dependent variable is  $k_I$ . The repeating variables could be  $U_0$ ,  $D_p$  and  $\rho_f$ .

The total number of variables,  $p = 7$

Number of fundamental dimensions,  $q = 3$

Number of dimensionless groups to be formed  $= p - q = 4$

The dimensionless group can be written as

$$\delta_1 = a(\delta_2 \delta_3 \delta_4) \quad (\text{I-1})$$

The first term,  $\delta_1$ , includes the dependent variable  $k_I$ . Because  $k_I$  contains only the dimensions length and time, it must be combined to form a dimensionless group with the repeating variables that do not contain mass, namely  $U_0$  and  $D_p$ .

$$\delta_1 = k_1 [U_0]^i [d_p]^j \quad (\text{I-2})$$

Replacing the variables with their dimensions, and finding the values of i and j:

$$[L, T]^0 = [T]^{-1} [L^1 T^{-1}]^i [L]^j \quad (\text{I-3})$$

Equating powers of L and T, we get i = -1 and j = 1.

Therefore,  $\delta_1$  can be written as

$$\delta_1 = \frac{k_1 D_p}{U_0} \quad (\text{I-4})$$

In a similar manner, we can obtain  $\delta_2$ ,  $\delta_3$ , and  $\delta_4$  as follows:

$$\delta_2 = \frac{\rho_p}{\rho_f} \quad (\text{I-5})$$

$$\delta_3 = \frac{D_p}{d_p} \quad (\text{I-6})$$

$$\delta_4 = \frac{\mu_f}{U_0 D_p \rho_f} \quad (\text{I-7})$$

The correlation of  $k_1$  can be written as:

$$\frac{k_1 D_p}{U_0} = a \left( \frac{D_p}{d_p} \right) \left( \frac{\rho_{straw}}{\rho_f} \right) \left( \frac{\mu_f}{U_0 D_p \rho_f} \right) \quad (\text{I-8})$$

Rearranging Equation (G-8), one may get

$$\frac{k_1 D_p}{U_0} = a \left( \frac{D_p}{d_p} \right)^b \left( \frac{U_0 D_p^2 (\rho_{straw} - \rho_f)}{\mu_f d_p} \right)^c \quad (\text{I-9})$$

Replacing the repeating variable  $D_p$  with  $d_p$  and the controlling variable  $\rho_{\text{straw}}$  with  $D_{col}$ , the correlation for  $k_2$  can be written as:

$$\frac{k_1 d_p}{U_0} = e \left( \frac{d_p}{D_{col}} \right)^f \left( \frac{d_p U_0 \rho_f}{\mu} \right)^g \quad (\text{I-10})$$

## APPENDIX J

### OPTIMIZATION PROGRAM FOR EVALUATING $K_1$ AND $K_2$

A Fortran program linked with IMSL was used to find the optimized values of  $k_1$  and  $k_2$ . The example of Fortran program is as follows:

```

PROGRAM filtration
C
C   This program is used to calculate the change of biomass waste particles concentration
C   in the G-MAFB
C
  IMPLICIT NONE
C
  INTEGER N
  PARAMETER (N=2)
C
  INTEGER MAXFCN, IBTYPE
  REAL FTOL, FVALUE, X(N), XGUESS(N), XLB(N), XUB(N)
  EXTERNAL BCPOL, FCN
C
C   Initializations
  DATA XGUESS/0.001,0.003/,XLB/0.0, 0.0/, XUB/0.9, 0.01/
C
  FTOL = 1.0E-20
  IBTYPE = 0
  MAXFCN = 150
C
  CALL BCPOL (FCN,N,XGUESS, IBTYPE, XLB, XUB,FTOL,MAXFCN, X,FVALUE)
C
C   PRINT RESULT
  PRINT 90, X(1),X(2)
90  FORMAT (1x,F25.20,1x,F25.20)

```

END

c\*\*\*\*\*

SUBROUTINE FCN (N, X, F)

IMPLICIT NONE

INTEGER N

REAL F,X(N)

REAL cdum(3535)

INTEGER i,j,tm,it

REAL C(101,130001), D(101,130001)

REAL Dp(101,130001), e(101,130001), a(101,130001)

REAL delx, delt, length, v, vol, flow, area, k1, k2, e0, Dp0, Co, F0

REAL straw

INTEGER K, M, num

c

c Declare variables

c t = time [s]

c x = location in x-direction [m]

c C(x,t) = biomass concentration in liquid at any x and t

c D(x,t) = biomass concentration on the ferromagnetic surface at any x and t

c delx = small interval in x

c delt = small interval in z

c Dp = ferromagnetic particle diameter [m]

c e = voidage

c v = fluid velocity [m/s]

c vol = volume of holding tank [m]

c a = specific surface [m<sup>2</sup>/m<sup>3</sup> bed]

c area = cross-sectional of the column [m]

c Co = initial concentration [mg/m<sup>3</sup>]

c F = volumetric flow rate [m<sup>3</sup>/sec]

c k1 = the accumulation coefficient [m<sup>3</sup> liquid/m<sup>3</sup> bed-s]

c k2 = the detachment coefficient [1/s]

c N = number of points in x-direction

c M = number of points in time

c straw = density of straw [kg/m<sup>3</sup>]

c

c General Information

length = 0.15

delx = 0.002

```

delt  = 0.05
Dp0   = 0.0025
e0    = 0.4585
v      = 0.013362642526
vol    = 0.006
area   = 3.14159265358979*0.05036**(2.0)/4.0
flow   = area*v
Co     = 0.117916184
straw  = 1089.6
k1     = X(1)
k2     = X(2)
K      = 76
M      = 70700

c
c  Initial condition at t = 0 for any 0<x<0.15 [m]
C(1,1)=Co
D(1,1)=0.0
DO 30 i=2,K
    C(i,1)=0.0
    D(i,1)=0.0
30  CONTINUE

c
DO 101 i=1,K
    Dp(i,1)=0.0025
    e(i,1) =0.4585
    a(i,1) =6.0*(1.0-0.4585)/0.0025
101  CONTINUE

c
DO 40 j=2,M
    DO 50 i=2,K-1

c
        D(i,j)=D(i,j-1)+delt*(k1/a(i,j-1)*C(i,j-1)-k2*D(i,j-1))
        D(1,j)=D(1,j-1)+delt*(k1/a(1,j-1)*C(1,j-1)-k2*D(1,j-1))
        D(76,j)=D(76,j-1)+delt*(k1/a(76,j-1)*C(76,j-1)-k2*D(76,j-1))

c
        C(i,j)=C(i,j-1)-delt*v/e(i,j-1)/delx*(C(i,j-1)-C(i-1,j-1))
&      +(3.0*C(i,j-1)*(1.0-0.4585)*Dp(i,j-1)**2.0/Dp0**3.0
&      /straw-a(i,j-1))/e(i,j-1)*(D(i,j)-D(i,j-1))

```

```

      C(76,j)=C(76,j-1)-delt*v/e(76,j-1)/delx*(C(76,j-1)-C(75,j-1))
&    +(3.0*C(76,j-1)*(1.0-0.4585)*Dp(76,j-1)**2.0/Dp0**3.0
&    /straw-a(76,j-1))/e(76,j-1)*(D(76,j)-D(76,j-1))
      C(1,j)=C(1,j-1)+delt/vol*flow*(C(76,j-1)-C(1,j-1))
C
      Dp(i,j)=0.0025+D(i,j)/1089.6
      Dp(1,j)=0.0025+D(1,j)/1089.6
      Dp(76,j)=0.0025+D(76,j)/1089.6
      e(i,j)=1.0-(1.0-e0)*(Dp(i,j)/0.0025)**3.0
      e(1,j)=1.0-(1.0-e0)*(Dp(1,j)/0.0025)**3.0
      e(76,j)=1.0-(1.0-e0)*(Dp(76,j)/0.0025)**3.0
      a(i,j)=6.0*(1-e(i,j))/Dp(i,j)
      a(1,j)=6.0*(1-e(1,j))/Dp(1,j)
      a(76,j)=6.0*(1-e(76,j))/Dp(76,j)
C
50  CONTINUE
40  CONTINUE
      F=0.0
      OPEN (unit=1,file='data1.txt')
      OPEN (unit=2,file='info.txt')
C
      READ (1,*) num
      DO 1 j=1,num
        READ (1,*)tm,cdum(j)
C
1  CONTINUE
      REWIND (unit=1)
C
      DO 60 i=1,num
        it = i*20
        F0=(cdum(i)-C(1,it))**(2.0)
        F=F+F0
60  CONTINUE
C
      WRITE (2,80) k1, k2, F
80  FORMAT (F15.13, 2x, F15.13, 2x, F30.10)
      RETURN
      END

```

## APPENDIX K

### DYNAMIC PRESSURE DROP AND VOIDAGE DATA

**Table K.1** Experimental dynamic pressure drop and voidage of particle A in the G-MAFB,  $dH_z/dz = -20,543 \text{ A/m/m}$ ,  $U_0 = 0.0176 \text{ m/s}$ ,  $h_{\text{bed}} = 0.220 \text{ m}$ , and  $h_{\text{in}} = 0.135 \text{ m}$

Height of the bed [cm]	Dynamic Pressure Drop [Pa]	Voidage
0	97.28	0.747
0.5	96.09	0.703
1	94.30	0.671
1.5	91.91	0.660
2	89.28	0.650
2.5	86.41	0.645
3	83.42	0.645
3.5	80.44	0.650
4	77.57	0.665
4.5	75.06	0.660
5	72.43	0.671
5.5	70.04	0.671
6	67.65	0.665
6.5	65.14	0.671
7	62.75	0.676
7.5	60.48	0.682
8	58.33	0.676
8.5	56.06	0.676
9	53.79	0.682
9.5	51.64	0.676
10	49.37	0.671
10.5	46.98	0.671
11	44.59	0.660
11.5	41.96	0.671
12	39.57	0.665
12.5	37.06	0.682
13	34.91	0.676
13.5	32.64	0.689
14	30.61	0.696
14.5	28.70	0.682
15	26.55	0.682
15.5	24.40	0.682
16	22.25	0.676
16.5	19.98	0.682
17	17.83	0.682
17.5	15.68	0.682
18	13.53	0.689



18.5	11.49	0.682
19	9.34	0.689
19.5	7.31	0.689
20	5.28	0.696
20.5	3.37	0.719
21	1.82	0.747
21.5	0.62	0.828
22	0.10	0.968

**Table K.2** Experimental dynamic pressure drop and voidage of particle A in the G-MAFB,  $dH_z/dz = -14,663 \text{ A/m/m}$ ,  $U_0 = 0.0222 \text{ m/s}$ ,  $h_{\text{bed}} = 0.220 \text{ m}$ , and  $h_{\text{in}} = 0.135 \text{ m}$

Height of the bed [cm]	Dynamic Pressure Drop [Pa]	Voidage
0	66.28	0.769
0.5	64.85	0.743
1	63.02	0.732
1.5	60.99	0.721
2	58.77	0.732
2.5	56.75	0.728
3	54.66	0.739
3.5	52.76	0.739
4	50.87	0.743
4.5	49.04	0.747
5	47.28	0.739
5.5	45.38	0.760
6	43.81	0.747
6.5	42.05	0.760
7	40.48	0.739
7.5	38.59	0.760
8	37.02	0.747
8.5	35.26	0.760
9	33.69	0.755
9.5	32.06	0.769
10	30.62	0.755
10.5	28.99	0.755
11	27.35	0.751
11.5	25.66	0.747
12	23.89	0.751
12.5	22.19	0.751
13	20.50	0.764
13.5	18.99	0.760
14	17.43	0.760
14.5	15.86	0.769
15	14.42	0.769
15.5	12.99	0.779
16	11.68	0.774
16.5	10.31	0.779
17	9.00	0.774
17.5	7.63	0.784
18	6.39	0.790
18.5	5.21	0.801
19	4.17	0.808
19.5	3.19	0.808
20	2.21	0.814
20.5	1.29	0.837
21	0.57	0.886
21.5	0.18	0.957
22	0.08	0.982

**Table K.3** Experimental dynamic pressure drop and voidage of particle A in the G-MAFB,  $dH_z/dz = -18,289$  A/m/m,  $U_o = 0.0222$  m/s,  $h_{bed} = 0.205$  m, and  $h_{in} = 9.5$  cm

Height of the bed [cm]	Dynamic Pressure Drop [Pa]	Voidage
0	68.57	0.829
0.5	67.79	0.790
1	66.61	0.743
1.5	64.78	0.718
2	62.50	0.735
2.5	60.54	0.735
3	58.58	0.747
3.5	56.81	0.728
4	54.72	0.735
4.5	52.76	0.728
5	50.67	0.728
5.5	48.58	0.725
6	46.43	0.732
6.5	44.40	0.739
7	42.51	0.747
7.5	40.74	0.735
8	38.79	0.751
8.5	37.09	0.751
9	35.39	0.769
9.5	33.95	0.760
10	32.38	0.755
10.5	30.75	0.764
11	29.25	0.755
11.5	27.62	0.755
12	25.98	0.739
12.5	24.09	0.747
13	22.33	0.751
13.5	20.63	0.764
14	19.12	0.747
14.5	17.36	0.751
15	15.66	0.743
15.5	13.83	0.747
16	12.07	0.735
16.5	10.11	0.747
17	8.35	0.755
17.5	6.71	0.774
18	5.34	0.779
18.5	4.04	0.779
19	2.73	0.779
19.5	1.42	0.814
20	0.51	0.879
20.5	0.08	0.982

**Table K.4** Experimental dynamic pressure drop and voidage of particle A in the G-MAFB,  $dH_z/dz = -20,543 \text{ A/m/m}$ ,  $U_0 = 0.0222 \text{ m/s}$ ,  $h_{\text{bed}} = 0.190 \text{ m}$ , and  $h_{\text{in}} = 9.5 \text{ cm}$

Height of the bed [cm]	Dynamic Pressure Drop [Pa]	Voidage
0	70.10	0.829
0.5	69.31	0.774
1	67.94	0.743
1.5	66.11	0.715
2	63.76	0.706
2.5	61.22	0.706
3	58.67	0.712
3.5	56.25	0.715
4	53.90	0.725
4.5	51.74	0.718
5	49.46	0.728
5.5	47.37	0.725
6	45.21	0.728
6.5	43.12	0.721
7	40.90	0.728
7.5	38.81	0.728
8	36.72	0.735
8.5	34.76	0.732
9	32.74	0.755
9.5	31.10	0.755
10	29.47	0.769
10.5	28.03	0.743
11	26.21	0.751
11.5	24.51	0.732
12	22.48	0.743
12.5	20.65	0.735
13	18.69	0.743
13.5	16.86	0.751
14	15.17	0.760
14.5	13.60	0.739
15	11.70	0.721
15.5	9.48	0.732
16	7.46	0.751
16.5	5.76	0.755
17	4.13	0.747
17.5	2.36	0.774
18	0.99	0.845
18.5	0.34	0.908
19	0.05	0.988

**Table K.5** Experimental dynamic pressure drop and voidage of particle A in the G-MAFB,  $dH_z/dz = -14,663 \text{ A/m/m}$ ,  $U_0 = 0.0176 \text{ m/s}$ ,  $h_{\text{bed}} = 0.130 \text{ m}$ , and  $h_{\text{in}} = 6.5 \text{ cm}$

Height of the bed [cm]	Dynamic Pressure Drop [Pa]	Voidage
0	46.46	0.746
0.5	45.25	0.717
1	43.68	0.698
1.5	41.80	0.702
2	39.99	0.694
2.5	38.05	0.675
3	35.76	0.669
3.5	33.34	0.681
4	31.16	0.681
4.5	28.98	0.688
5	26.93	0.688
5.5	24.87	0.702
6	23.05	0.681
6.5	20.88	0.672
7	18.52	0.694
7.5	16.58	0.688
8	14.53	0.681
8.5	12.35	0.681
9	10.17	0.702
9.5	8.36	0.709
10	6.66	0.709
10.5	4.97	0.713
11	3.34	0.751
11.5	2.19	0.757
12	1.10	0.806
12.5	0.44	0.855
13	0.05	0.982

**Table K.6** Experimental dynamic pressure drop and voidage of particle A in the G-MAFB,  $dH_z/dz = -18,289 \text{ A/m/m}$ ,  $U_o = 0.0176 \text{ m/s}$ ,  $h_{\text{bed}} = 0.125 \text{ m}$ , and  $h_{\text{in}} = 6.5 \text{ cm}$

Height of the bed [cm]	Dynamic Pressure Drop [Pa]	Voidage
0	49.00	0.718
0.5	47.43	0.689
1	45.41	0.686
1.5	43.32	0.672
2	40.97	0.655
2.5	38.22	0.649
3	35.35	0.660
3.5	32.74	0.672
4	30.39	0.672
4.5	28.03	0.660
5	25.42	0.666
5.5	22.94	0.666
6	20.46	0.660
6.5	17.84	0.672
7	15.49	0.686
7.5	13.40	0.693
8	11.44	0.693
8.5	9.48	0.701
9	7.66	0.701
9.5	5.83	0.709
10	4.13	0.701
10.5	2.30	0.749
11	1.12	0.790
11.5	0.34	0.878
12	0.05	0.981
12.5	0.03	0.981

**Table K.7** Experimental dynamic pressure drop and voidage of particle A in the G-MAFB,  $dH_z/dz = -20,543 \text{ A/m/m}$ ,  $U_0 = 0.0176 \text{ m/s}$ ,  $h_{\text{bed}} = 0.110 \text{ m}$ , and  $h_{\text{in}} = 6.5 \text{ cm}$

Height of the bed [cm]	Dynamic Pressure Drop [Pa]	Voidage
0	50.21	0.711
0.5	48.54	0.691
1	46.55	0.667
1.5	44.08	0.650
2	41.21	0.651
2.5	38.39	0.647
3	35.44	0.658
3.5	32.77	0.650
4	29.90	0.656
4.5	27.19	0.665
5	24.69	0.667
5.5	22.22	0.671
6	19.83	0.669
6.5	17.40	0.676
7	15.13	0.672
7.5	12.78	0.678
8	10.55	0.674
8.5	8.24	0.687
9	6.17	0.693
9.5	4.21	0.691
10	2.22	0.734
10.5	0.87	0.786
11	0.05	0.983

**Table K.8** Experimental dynamic pressure drop and voidage of particle A in the G-MAFB,  $dH_z/dz = -20,543$  A/m/m,  $U_0 = 0.0199$  m/s,  $h_{bed} = 0.130$  m, and  $h_{in} = 6.5$  cm

Height of the bed [cm]	Dynamic Pressure Drop [Pa]	Voidage
0	51.81	0.735
0.5	50.18	0.713
1	48.18	0.683
1.5	45.57	0.666
2	42.55	0.668
2.5	39.57	0.666
3	36.55	0.677
3.5	33.81	0.669
4	30.87	0.676
4.5	28.09	0.688
5	25.60	0.694
5.5	23.24	0.713
6	21.24	0.708
6.5	19.15	0.713
7	17.15	0.711
7.5	15.11	0.715
8	13.15	0.717
8.5	11.23	0.717
9	9.32	0.725
9.5	7.52	0.747
10	6.05	0.747
10.5	4.58	0.759
11	3.27	0.763
11.5	2.01	0.785
12	0.99	0.834
12.5	0.38	0.882
13	0.03	0.990



**Table K.9** Experimental dynamic pressure drop and voidage of particle A in the G-MAFB,  $dH_z/dz = -33,798 \text{ A/m/m}$ ,  $U_o = 0.0199 \text{ m/s}$ ,  $h_{\text{bed}} = 0.115 \text{ m}$ , and  $h_{\text{in}} = 6.5 \text{ cm}$

Height of the bed [cm]	Dynamic Pressure Drop [Pa]	Voidage
0	68.357	0.727
0.5	66.593	0.661
1	63.436	0.641
1.5	59.691	0.635
2	55.751	0.640
2.5	51.962	0.639
3	48.130	0.644
3.5	44.472	0.631
4	40.379	0.651
4.5	36.939	0.643
5	33.238	0.645
5.5	29.624	0.644
6	25.966	0.657
6.5	22.700	0.673
7	19.848	0.675
7.5	17.061	0.674
8	14.230	0.695
8.5	11.879	0.682
9	9.245	0.683
9.5	6.632	0.698
10	4.346	0.704
10.5	2.190	0.742
11	0.662	0.827
11.5	0.004	0.997

**Table K.10** Experimental dynamic pressure drop and voidage of particle B in the G-MAFB,  $dH_z/dz = -14,663 \text{ A/m/m}$ ,  $U_o = 0.0222 \text{ m/s}$ ,  $h_{\text{bed}} = 0.187 \text{ m}$ , and  $h_{\text{in}} = 13.5 \text{ cm}$

Height of the bed [cm]	Dynamic Pressure Drop [Pa]	Voidage
0	236.10	0.641
0.5	232.45	0.606
1	227.56	0.589
1.5	221.90	0.575
2	215.50	0.572
2.5	208.97	0.564
3	201.93	0.560
3.5	194.65	0.558
4	187.23	0.570
4.5	180.58	0.562
5	173.42	0.570
5.5	166.76	0.566
6	159.85	0.577
6.5	153.57	0.570
7	146.91	0.566
7.5	140.01	0.568
8	133.22	0.570
8.5	126.56	0.566
9	119.66	0.564
9.5	112.62	0.566
10	105.71	0.570
10.5	99.06	0.564
11	92.02	0.572
11.5	85.49	0.577
12	79.21	0.572
12.5	72.68	0.570
13	66.02	0.570
13.5	59.36	0.575
14	52.96	0.575
14.5	46.55	0.577
15	40.27	0.587
15.5	34.49	0.579
16	28.34	0.582
16.5	22.31	0.577
17	16.03	0.572
17.5	9.50	0.592
18	3.97	0.659
18.5	0.83	0.812
18.7	0.05	0.986

**Table K.11** Experimental dynamic pressure drop and voidage of particle B in the G-MAFB,  $dH_z/dz = -18,289 \text{ A/m/m}$ ,  $U_o = 0.0222 \text{ m/s}$ ,  $h_{\text{bed}} = 0.178 \text{ m}$ , and  $h_{\text{in}} = 13.5 \text{ cm}$

Height of the bed [cm]	Dynamic Pressure Drop [Pa]	Voidage
0	237.18	0.646
0.5	233.66	0.606
1	228.76	0.582
1.5	222.73	0.572
2	216.20	0.570
2.5	209.54	0.568
3	202.76	0.556
3.5	195.22	0.556
4	187.69	0.550
4.5	179.77	0.560
5	172.49	0.562
5.5	165.33	0.560
6	158.04	0.556
6.5	150.51	0.554
7	142.84	0.562
7.5	135.68	0.560
8	128.40	0.562
8.5	121.24	0.562
9	114.08	0.562
9.5	106.92	0.566
10	100.01	0.568
10.5	93.23	0.568
11	86.44	0.570
11.5	79.79	0.579
12	73.63	0.572
12.5	67.10	0.575
13	60.69	0.568
13.5	53.91	0.572
14	47.38	0.570
14.5	40.72	0.570
15	34.07	0.568
15.5	27.28	0.570
16	20.63	0.566
16.5	13.72	0.570
17	7.06	0.613
17.5	2.41	0.695
17.8	0.10	0.974

**Table K.12** Experimental dynamic pressure drop and voidage of particle B in the G-MAFB,  $dH_z/dz = -20,543$  A/m/m,  $U_0 = 0.0222$  m/s,  $h_{bed} = 0.165$  m, and  $h_{in} = 13.5$  cm

Height of the bed [cm]	Dynamic Pressure Drop [Pa]	Voidage
0	237.35	0.636
0.5	233.54	0.600
1	228.37	0.570
1.5	221.70	0.563
2	214.62	0.559
2.5	207.27	0.554
3	199.65	0.550
3.5	191.76	0.546
4	183.60	0.552
4.5	175.84	0.550
5	167.95	0.559
5.5	160.60	0.561
6	153.39	0.559
6.5	146.04	0.554
7	138.42	0.561
7.5	131.21	0.554
8	123.59	0.556
8.5	116.10	0.548
9	108.07	0.554
9.5	100.45	0.556
10	92.97	0.548
10.5	84.94	0.548
11	76.91	0.554
11.5	69.29	0.552
12	61.53	0.548
12.5	53.51	0.550
13	45.61	0.559
13.5	38.27	0.554
14	30.64	0.559
14.5	23.30	0.568
15	16.49	0.559
15.5	9.14	0.588
16	3.43	0.652
16.5	0.11	0.972

**Table K.13** Experimental dynamic pressure drop and voidage of particle B in the G-MAFB,  $dH_z/dz = -20,543 \text{ A/m/m}$ ,  $U_o = 0.0222 \text{ m/}$ ,  $h_{\text{bed}} = 0.217 \text{ m}$ , and  $h_{\text{in}} = 17.0 \text{ cm}$

Height of the bed [cm]	Dynamic Pressure Drop [Pa]	Voidage
0	292.90	0.635
0.5	289.07	0.591
1	283.49	0.568
1.5	276.70	0.554
2	269.04	0.548
2.5	261.03	0.546
3	252.84	0.548
3.5	244.83	0.548
4	236.81	0.554
4.5	229.15	0.556
5	221.66	0.559
5.5	214.35	0.559
6	207.03	0.556
6.5	199.54	0.559
7	192.22	0.551
7.5	184.39	0.556
8	176.90	0.556
8.5	169.41	0.562
9	162.27	0.556
9.5	154.78	0.559
10	147.46	0.559
10.5	140.14	0.562
11	133.00	0.571
11.5	126.38	0.568
12	119.59	0.568
12.5	112.80	0.577
13	106.53	0.568
13.5	99.74	0.571
14	93.12	0.568
14.5	86.32	0.574
15	79.88	0.568
15.5	73.09	0.571
16	66.47	0.574
16.5	60.02	0.568
17	53.23	0.565
17.5	46.26	0.571
18	39.64	0.577
18.5	33.37	0.574
19	26.93	0.587
19.5	21.18	0.580
20	15.08	0.587
20.5	9.34	0.599
21	4.11	0.673
21.5	1.32	0.763
21.7	0.07	0.981

## APPENDIX L

## FILTRATION EXPERIMENTAL DATA

**Table L.1** Filtration experimental data in Figure 5.30,  $d_p = 2.5$  mm,  $D_p = 73.52$   $\mu\text{m}$ ,  $C_0 \sim 0.12$  [mg/cm<sup>3</sup>], and  $h_{\text{bed}} = 0.20$  m

Time [sec]	Biomass waste concentration [mg/cm <sup>3</sup> ]		
	$U_0 = 0.00541$ m/s	$U_0 = 0.00787$ m/s	$U_0 = 0.01109$ m/s
0	0.1200	0.1219	0.1184
120	0.0966	0.0888	0.0712
240	0.0879	0.0662	0.0497
360	0.0695	0.0504	0.0370
480	0.0569	0.0408	0.0282
600	0.0427	0.0322	0.0219
720	0.0353	0.0270	0.0173
840	0.0297	0.0209	0.0148
960	0.0239	0.0178	0.0134
1080	0.0224	0.0147	0.0112
1200	0.0161	0.0143	0.0090
1320	0.0150	0.0104	0.0085
1440	0.0136	0.0073	0.0086
1560	0.0121	0.0071	0.0076
1680	0.0087	0.0079	0.0084
1800	0.0076	0.0067	0.0084
1920	0.0076	0.0066	0.0090
2040	0.0058	0.0079	0.0095
2160	0.0072	0.0066	0.0087
2280	0.0073	0.0067	0.0088
2400	0.0066	0.0063	0.0088
2520	0.0068	0.0064	0.0082
2640	0.0056	0.0068	0.0073
2760	0.0077	0.0062	0.0062
2880	0.0062	0.0064	0.0065
3000	0.0057	0.0067	0.0069
3120	0.0064	0.0068	0.0071
3240	0.0052	0.0067	0.0059
3360	0.0052	0.0066	0.0079
3480	0.0055	0.0066	0.0073
3600	0.0076	0.0068	0.0064
3720	0.0050	0.0064	0.0068
3840	0.0060	0.0063	0.0067

**Table L.2** Filtration experimental data in Figure 5.31,  $d_p = 2.5$  mm,  $D_p = 73.52$   $\mu\text{m}$ ,  $C_0 \sim 0.33$  [mg/cm<sup>3</sup>] and  $h_{\text{bed}} = 0.20$  m

Time [sec]	Biomass waste concentration [mg/cm <sup>3</sup> ]			
	$U_0 = 0.00541$ m/s	$U_0 = 0.00787$ m/s	$U_0 = 0.01109$ m/s	$U_0 = 0.01336$ m/s
0	0.3491	0.3542	0.3610	0.3166
120	0.3033	0.2784	0.2176	0.1864
240	0.2318	0.1843	0.1459	0.1129
360	0.1919	0.1502	0.1063	0.0703
480	0.1669	0.1067	0.0696	0.0454
600	0.1377	0.0791	0.0448	0.0333
720	0.1073	0.0562	0.0358	0.0254
840	0.0820	0.0407	0.0280	0.0194
960	0.0724	0.0306	0.0219	0.0140
1080	0.0663	0.0225	0.0248	0.0155
1200	0.0547	0.0181	0.0233	0.0144
1320	0.0441	0.0142	0.0179	0.0148
1440	0.0379	0.0130	0.0135	0.0159
1560	0.0340	0.0115	0.0119	0.0150
1680	0.0306	0.0104	0.0132	0.0151
1800	0.0298	0.0109	0.0136	0.0139
1920	0.0242	0.0107	0.0122	0.0111
2040	0.0248	0.0121	0.0115	0.0104
2160	0.0232	0.0111	0.0124	0.0087
2280	0.0213	0.0094	0.0088	0.0080
2400	0.0210	0.0090	0.0077	0.0074
2520	0.0184	0.0071	0.0073	0.0074
2640	0.0148	0.0051	0.0085	0.0075
2760	0.0140	0.0029	0.0083	0.0080
2880	0.0111	0.0009	0.0073	0.0074
3000	0.0099	0.0026	0.0078	0.0078
3120	0.0086	0.0014	0.0077	0.0081
3240	0.0082	0.0015	0.0082	0.0074
3360	0.0070	0.0028	0.0081	0.0076
3480	0.0065	0.0033	0.0089	0.0083
3600	0.0058	0.0039	0.0080	0.0078
3720	0.0067	0.0054	0.3610	0.0075
3840	0.0066	0.0060	0.2176	0.0079

**Table L.3** Filtration experimental data in Figure 5.32,  $d_p = 2.5$  mm,  $D_p = 73.52$   $\mu$ m,  $C_0 \sim 0.51$  [mg/cm<sup>3</sup>] and  $h_{bed} = 0.20$  m

Time [sec]	Biomass waste concentration [mg/cm <sup>3</sup> ]			
	$U_0 = 0.00541$ m/s	$U_0 = 0.00787$ m/s	$U_0 = 0.01109$ m/s	$U_0 = 0.01336$ m/s
0	0.5333	0.5417	0.4745	0.4745
120	0.4292	0.4183	0.3366	0.2760
240	0.3361	0.2800	0.2132	0.1749
360	0.2629	0.2133	0.1383	0.1122
480	0.2358	0.1690	0.0962	0.0780
600	0.1832	0.1172	0.0672	0.0537
720	0.1555	0.0834	0.0497	0.0355
840	0.1394	0.0643	0.0348	0.0217
960	0.1183	0.0437	0.0302	0.0184
1080	0.0895	0.0355	0.0225	0.0130
1200	0.0681	0.0293	0.0178	0.0115
1320	0.0553	0.0279	0.0127	0.0137
1440	0.0417	0.0222	0.0102	0.0155
1560	0.0338	0.0209	0.0089	0.0145
1680	0.0274	0.0180	0.0082	0.0163
1800	0.0265	0.0152	0.0078	0.0179
1920	0.0176	0.0145	0.0083	0.0181
2040	0.0146	0.0146	0.0079	0.0160
2160	0.0122	0.0154	0.0074	0.0148
2280	0.0078	0.0163	0.0082	0.0143
2400	0.0062	0.0162	0.0079	0.0140
2520	0.0048	0.0146	0.0074	0.0109
2640	0.0049	0.0129	0.0076	0.0096
2760	0.0052	0.0123	0.0079	0.0092
2880	0.0049	0.0128	0.0073	
3000	0.0055	0.0123	0.0069	
3120	0.0064	0.0117	0.0083	
3240	0.0069	0.0112	0.0075	
3360	0.0083	0.0112		
3480	0.0073	0.0124		
3600	0.0084	0.0107		
3720	0.0085	0.0095		
3840	0.0077	0.0089		



**Table L.4** Filtration experimental data in Figure 5.33,  $d_p = 2.5$  mm,  $D_p = 114.68$   $\mu\text{m}$ ,  $C_0 \sim 0.30$  [mg/cm<sup>3</sup>], and  $h_{\text{bed}} = 0.15$  m

Time [sec]	Biomass waste concentration [mg/cm <sup>3</sup> ]
	$U_0 = 0.00541$ m/s
0	0.3022
120	0.2313
240	0.1666
360	0.1134
480	0.0931
600	0.0650
720	0.0489
840	0.0412
960	0.0393
1080	0.0333
1200	0.0260
1320	0.0212
1440	0.0195
1560	0.0158
1680	0.0158
1800	0.0130
1920	0.0132
2040	0.0115
2160	0.0110
2280	0.0109
2400	0.0103
2520	0.0098
2640	0.0099
2760	0.0097
2880	0.0098
3000	0.0095
3120	0.0099
3240	0.0095
3360	0.0095

**Table L.5** Filtration experimental data in Figure 5.34,  $d_p = 2.5$  mm,  $D_p = 114.68$   $\mu\text{m}$ ,  $C_0 \sim 0.22$  [mg/cm<sup>3</sup>], and  $h_{\text{bed}} = 0.15$  m

Time [sec]	Biomass waste concentration [mg/cm <sup>3</sup> ]
	$U_0 = 0.00541$ m/s
0	0.2298
120	0.1489
240	0.1155
360	0.0758
480	0.0460
600	0.0343
720	0.0239
840	0.0172
960	0.0173
1080	0.0133
1200	0.0117
1320	0.0108
1440	0.0100
1560	0.0080
1680	0.0083
1800	0.0077
1920	0.0078
2040	0.0080
2160	0.0082
2280	0.0079
2400	0.0079
2520	0.0077
2640	0.0076
2760	0.0078
2880	0.0076
3000	0.0078
3120	0.0076
3240	0.0076
3360	0.0076

**Table L.6** Filtration experimental data in Figure 5.35,  $d_p = 3.5$  mm,  $D_p = 73.52$   $\mu\text{m}$ ,  $C_0 \sim 0.18$  [mg/cm<sup>3</sup>], and  $h_{\text{bed}} = 0.20$  m

Time [sec]	Biomass waste concentration [mg/cm <sup>3</sup> ]			
	$U_0 = 0.00541$ m/s	$U_0 = 0.00787$ m/s	$U_0 = 0.01109$ m/s	$U_0 = 0.01336$ m/s
0	0.1780	0.1765	0.1282	0.1825
120	0.1641	0.1358	0.0955	0.1086
240	0.1406	0.1046	0.0664	0.0764
360	0.1225	0.0815	0.0373	0.0447
480	0.1012	0.0696	0.0282	0.0366
600	0.0859	0.0581	0.0169	0.0148
720	0.0642	0.0416	0.0100	0.0088
840	0.0521	0.0281	0.0081	0.0079
960	0.0491	0.0271	0.0052	0.0071
1080	0.0443	0.0249	0.0031	0.0074
1200	0.0383	0.0203	0.0045	0.0069
1320	0.0364	0.0178	0.0064	0.0065
1440	0.0273	0.0194	0.0079	0.0084
1560	0.0256	0.0233	0.0076	0.0082
1680	0.0226	0.0242	0.0062	0.0086
1800	0.0167	0.0248	0.0074	0.0086
1920	0.0128	0.0258	0.0078	0.0072
2040	0.0150	0.0221	0.0092	0.0091
2160	0.0228	0.0204	0.0089	0.0062
2280	0.0220	0.0171	0.0073	0.0052
2400	0.0258	0.0165	0.0079	0.0076
2520	0.0246	0.0135	0.0087	0.0067
2640	0.0243	0.0076	0.0074	0.0076
2760	0.0201	0.0049	0.0070	0.0087
2880	0.0156	0.0042	0.0064	0.0129
3000	0.0120	0.0057	0.0085	0.0075
3120	0.0087	0.0057		
3240	0.0078	0.0077		
3360	0.0066	0.0124		
3480	0.0077	0.0143		
3600	0.0082	0.0167		
3720	0.0078	0.0156		
3840	0.0088	0.0167		

**Table L.7** Filtration experimental data in Figure 5.36,  $d_p = 3.5$  mm,  $D_p = 73.52$   $\mu\text{m}$ ,  $C_0 \sim 0.35$  [mg/cm<sup>3</sup>], and  $h_{\text{bed}} = 0.20$  m

Time [sec]	Biomass waste concentration [mg/cm <sup>3</sup> ]			
	$U_0 = 0.00541$ m/s	$U_0 = 0.00787$ m/s	$U_0 = 0.01109$ m/s	$U_0 = 0.01336$ m/s
0	0.3702	0.3546	0.3629	0.3533
120	0.3028	0.2803	0.2790	0.2416
240	0.2686	0.2300	0.1911	0.1932
360	0.2168	0.1812	0.1558	0.1233
480	0.1810	0.1418	0.1193	0.0902
600	0.1679	0.1064	0.0893	0.0821
720	0.1419	0.0742	0.0814	0.0791
840	0.1073	0.0633	0.0634	0.0673
960	0.0976	0.0550	0.0601	0.0535
1080	0.0907	0.0538	0.0558	0.0450
1200	0.0865	0.0511	0.0427	0.0339
1320	0.0679	0.0420	0.0391	0.0275
1440	0.0676	0.0283	0.0325	0.0238
1560	0.0625	0.0189	0.0267	0.0182
1680	0.0520	0.0134	0.0235	0.0204
1800	0.0493	0.0140	0.0159	0.0231
1920	0.0461	0.0162	0.0116	0.0306
2040	0.0391	0.0217	0.0103	0.0326
2160	0.0346	0.0252	0.0085	0.0304
2280	0.0308	0.0259	0.0091	0.0202
2400	0.0295	0.0234	0.0074	0.0137
2520	0.0233	0.0171	0.0066	0.0104
2640	0.0178	0.0103	0.0062	0.0115
2760	0.0140	0.0014	0.0082	0.0149
2880	0.0112	0.0017	0.0093	0.0214
3000	0.0087	0.0081	0.0108	0.0248
3120	0.0099	0.0108	0.0101	0.0239
3240	0.0058	0.0116	0.0094	0.0202
3360	0.0064	0.0127	0.0103	0.0175
3480	0.0101	0.0119	0.0117	0.0108
3600	0.0072	0.0108	0.0125	0.0094
3720	0.0123	0.0093	0.0114	0.0120
3840	0.0145	0.0015	0.3629	0.3533
3600	0.0166		0.2790	0.2416
3720	0.0140		0.1911	0.1932
3840	0.0164			
3960	0.0138			
4080	0.3702			
4200	0.3028			
4320	0.2686			

**Table L.8** Filtration experimental data in Figure 5.37,  $d_p = 3.5$  mm,  $D_p = 73.52$   $\mu\text{m}$ ,  $C_0 \sim 0.53$  [mg/cm<sup>3</sup>], and  $h_{\text{bed}} = 0.20$  m

Time [sec]	Biomass waste concentration [mg/cm <sup>3</sup> ]		
	$U_0 = 0.00541$ m/s	$U_0 = 0.00787$ m/s	$U_0 = 0.01109$ m/s
0	0.5363	0.5340	0.5242
120	0.4449	0.3973	0.3571
240	0.3553	0.3075	0.2596
360	0.3152	0.2412	0.1940
480	0.2709	0.1915	0.1432
600	0.2325	0.1614	0.1329
720	0.2125	0.1348	0.1130
840	0.1781	0.0961	0.0979
960	0.1474	0.0848	0.0838
1080	0.1377	0.0611	0.0661
1200	0.1178	0.0572	0.0543
1320	0.1042	0.0598	0.0439
1440	0.0945	0.0517	0.0482
1560	0.0955	0.0535	0.0492
1680	0.0867	0.0486	0.0514
1800	0.0927	0.0416	0.0542
1920	0.0892	0.0372	0.0474
2040	0.0739	0.0287	0.0359
2160	0.0618	0.0281	0.0253
2280	0.0512	0.0187	0.0224
2400	0.0482	0.0139	0.0279
2520	0.0353	0.0109	0.0368
2640	0.0349	0.0091	0.0408
2760	0.0346	0.0107	0.0437
2880	0.0366	0.0095	0.0363
3000	0.0395	0.0094	0.0310
3120	0.0448	0.0138	0.0237
3240	0.0474	0.0198	0.0227
3360	0.0457	0.0129	0.0219
3480	0.0439	0.0164	0.0250
3600	0.0358	0.0243	0.0321
3720	0.0373	0.0263	0.0369
3840	0.0272	0.0238	0.0417
3600	0.0297	0.0247	0.0417
3720	0.0223	0.0265	0.0375
3840	0.0241	0.0259	0.0295
3960	0.5363	0.5340	0.0222
4080	0.4449	0.3973	0.5242
4200	0.3553	0.3075	0.3571
4320			0.2596

**Table L.9** Filtration experimental data in Figure 5.38,  $d_p = 3.5$  mm,  $D_p = 114.68$   $\mu\text{m}$ ,  $C_0 \sim 0.20$  [mg/cm<sup>3</sup>], and  $h_{\text{bed}} = 0.15$  m

Time [sec]	Biomass waste concentration [mg/cm <sup>3</sup> ]		
	$U_0 = 0.00825$ m/s	$U_0 = 0.01109$ m/s	$U_0 = 0.01336$ m/s
0	0.2030	0.1915	0.2048
120	0.1476	0.1317	0.1515
240	0.1086	0.0995	0.0878
360	0.0773	0.0630	0.0599
480	0.0730	0.0474	0.0446
600	0.0423	0.0374	0.0340
720	0.0345	0.0272	0.0268
840	0.0266	0.0196	0.0212
960	0.0241	0.0169	0.0194
1080	0.0224	0.0163	0.0180
1200	0.0150	0.0142	0.0173
1320	0.0117	0.0153	0.0148
1440	0.0103	0.0134	0.0129
1560	0.0115	0.0109	0.0130
1680	0.0102	0.0104	0.0111
1800	0.0097	0.0110	0.0109
1920	0.0093	0.0098	0.0122
2040	0.0098	0.0096	0.0115
2160	0.0093	0.0098	0.0117
2280	0.0086	0.0102	0.0117
2400	0.0098	0.0098	0.0108
2520	0.0090	0.0096	0.0104
2640	0.0089	0.0096	0.0103
2760	0.0078	0.0094	0.0108
2880	0.0081	0.0096	0.0107
3000	0.0083	0.0096	0.0103
3120	0.0077	0.0093	0.0114
3240	0.0076	0.0093	0.0105
3360	0.0081	0.0094	0.0106
3480	0.0076	0.0093	0.0099
3600	0.0084	0.0094	0.0100
3720	0.0076	0.0093	0.0100
3840	0.0080	0.0094	0.0102
3600		0.1915	0.2048
3720		0.1317	0.1515
3840		0.0995	0.0878

**Table L.10** Filtration experimental data in Figure 5.39,  $d_p = 3.5$  mm,  $D_p = 114.68$   $\mu\text{m}$ ,  $C_0 \sim 0.31$  [mg/cm<sup>3</sup>], and  $h_{\text{bed}} = 0.15$  m

Time [sec]	Biomass waste concentration [mg/cm <sup>3</sup> ]			
	$U_0 = 0.00541$ m/s	$U_0 = 0.00825$ m/s	$U_0 = 0.01109$ m/s	$U_0 = 0.01336$ m/s
0	0.2875	0.2623	0.3162	0.3344
120	0.2590	0.2171	0.2274	0.2304
240	0.2039	0.1664	0.1665	0.1572
360	0.1678	0.1221	0.1356	0.1093
480	0.1378	0.1072	0.1019	0.0789
600	0.1171	0.0823	0.0902	0.0714
720	0.0852	0.0584	0.0654	0.0561
840	0.0592	0.0482	0.0492	0.0448
960	0.0518	0.0385	0.0394	0.0375
1080	0.0360	0.0328	0.0288	0.0362
1200	0.0322	0.0263	0.0321	0.0325
1320	0.0224	0.0180	0.0265	0.0286
1440	0.0278	0.0180	0.0254	0.0273
1560	0.0252	0.0186	0.0224	0.0239
1680	0.0199	0.0148	0.0184	0.0195
1800	0.0188	0.0142	0.0168	0.0191
1920	0.0176	0.0137	0.0138	0.0173
2040	0.0173	0.0154	0.0124	0.0145
2160	0.0128	0.0111	0.0124	0.0154
2280	0.0117	0.0100	0.0138	0.0153
2400	0.0122	0.0099	0.0107	0.0131
2520	0.0107	0.0102	0.0101	0.0133
2640	0.0084	0.0104	0.0108	0.0134
2760	0.0086	0.0096	0.0108	0.0122
2880	0.0077	0.0096	0.0110	0.0129
3000	0.0080	0.0100	0.0101	0.0128
3120	0.0086	0.0101	0.0090	0.0131
3240	0.0077	0.0092	0.0100	0.0115
3360	0.0081	0.0092	0.0098	0.0120
3480	0.0075	0.0084	0.0098	0.0116
3600	0.0080	0.0090	0.0097	0.0123
3720	0.0073	0.0094	0.0093	0.0113
3840	0.0083	0.0087	0.0089	0.0108
3600	0.2875	0.2623	0.3162	0.3344
3720	0.2590	0.2171	0.2274	0.2304
3840	0.2039	0.1664	0.1665	0.1572

**Table L.11** Filtration experimental data in Figure 5.40,  $d_p = 3.5$  mm,  $D_p = 114.68$   $\mu\text{m}$ ,  $C_0 \sim 0.40$  [mg/cm<sup>3</sup>], and  $h_{\text{bed}} = 0.15$  m

Time [sec]	Biomass waste concentration [mg/cm <sup>3</sup> ]			
	$U_0 = 0.00541$ m/s	$U_0 = 0.00825$ m/s	$U_0 = 0.01109$ m/s	$U_0 = 0.01336$ m/s
0	0.3805	0.4009	0.4186	0.4083
120	0.3445	0.3170	0.2991	0.2910
240	0.2940	0.2344	0.2288	0.2034
360	0.2250	0.1820	0.1534	0.1677
480	0.1741	0.1439	0.1351	0.1136
600	0.1325	0.1102	0.0939	0.0903
720	0.1099	0.0783	0.0808	0.0891
840	0.0952	0.0618	0.0583	0.0717
960	0.0747	0.0478	0.0417	0.0620
1080	0.0578	0.0393	0.0369	0.0499
1200	0.0442	0.0399	0.0314	0.0401
1320	0.0360	0.0332	0.0303	0.0406
1440	0.0355	0.0291	0.0262	0.0279
1560	0.0311	0.0262	0.0275	0.0293
1680	0.0229	0.0169	0.0241	0.0231
1800	0.0185	0.0131	0.0258	0.0194
1920	0.0144	0.0135	0.0231	0.0227
2040	0.0143	0.0129	0.0185	0.0174
2160	0.0152	0.0147	0.0163	0.0195
2280	0.0145	0.0129	0.0150	0.0168
2400	0.0132	0.0123	0.0142	0.0196
2520	0.0101	0.0109	0.0113	0.0172
2640	0.0097	0.0107	0.0116	0.0198
2760	0.0085	0.0090	0.0115	0.0171
2880	0.0095	0.0084	0.0108	0.0174
3000	0.0088	0.0084	0.0107	0.0176
3120	0.0089	0.0088	0.0104	0.0154
3240	0.0084	0.0085	0.0099	0.0150
3360	0.0077	0.0088	0.0112	0.0146
3480	0.0072	0.0086	0.0098	0.0144
3600	0.0071	0.0082	0.0110	0.0129
3720	0.0071	0.0083	0.0099	0.0123
3840	0.0074	0.0078	0.0100	0.0106
3600	0.3805	0.4009	0.4186	0.4083
3720	0.3445	0.3170	0.2991	0.2910
3840	0.2940	0.2344	0.2288	0.2034